University Of Bahrain

College of Engineering

Department of Mechanical Engineering

Study of the effect of surface roughness difference between upper and lower surfaces on aerodynamic characteristics of a NACA 4412 airfoil

A Thesis submitted in Partial Fulfillment of the Requirements of the Doctorate Degree in Mechanical Engineering

Submitted by

Ebrahim Kamal Seddiq

University number: 20121003

Supervised by

Dr. Mohamed Nabhan
(Associate Professor)

Dr. Omar Al-Abasi
(Associate Professor)

University of Bahrain
Kingdom of Bahrain
June, 2023

University Of Bahrain

College of Engineering

Department of Mechanical Engineering

Study of the effect of surface roughness difference between upper and lower surfaces on aerodynamic characteristics of a NACA 4412 airfoil

A Thesis submitted in Partial Fulfillment of the Requirements of the Doctorate Degree in Mechanical Engineering

Submitted by

Ebrahim Kamal Seddiq

University number: 20121003

Supervised by

Dr. Mohamed Nabhan
(Associate Professor)

Dr. Omar Al-Abasi
(Associate Professor)

University of Bahrain
Kingdom of Bahrain
June, 2023

Defense Committee's approval

University of Bahrain

College: Engineering

Department: Mechanical Engineering

Doctorate's program: Doctorate's Degree in Mechanical Engineering

Student: Ebrahim Kamal Hasan Mohamed Seddiq ID number: 20121003 defended his thesis by which he fulfilled the requirement for the degree of Doctorate in Mechanical Engineering entitled: " Study of the effect of surface roughness difference between upper and lower surfaces on aerodynamic characteristics of a NACA 4412 airfoil on this day of June 5, 2023.

The committee recommends awarding of PhD. Degree with the grade of:A

(Defense Committee)

Name		Signature
Dr. Mohammed Nabhan	Supervisor	
Dr. Omar Al-Abbasi	Supervisor	
Prof. Walid Chakroun	External examiner	
Prof. Ahmed Yousif	Internal examiner	

Declaration

I declare that this work is the result of my investigation and that it has not already been accepted in substance for any degree, nor is it being submitted for any degree.



Signed: ..... Date: 8/6/2023

Abstract

This study has traced the surface Roughness effect on NACA 4412 airfoil. In addition, research revised Aerodynamic characteristics with and without the impact of applied surface roughness at different heights on the lower surface of the Airfoil and investigated the differences. This study employed Numerical and Experimental approaches to affirm the results.

Numerical solution was performed using Fluent Ansys code. Two sets of spherical aligned surface roughness patterns were applied to the lower surface face of the NACA 4412 airfoil and then compared the first and second sets to a smooth Airfoil. The first set has ten designed surface roughness heights (ks) from 0.05 mm to 0.5 mm. The second set possesses four different surface roughness with ks from 1 mm to 4 mm. The simulation was conducted in turbulent high subsonic incompressible flow with $4.39 \times 10^6 \geq \text{Re} \geq 8.79 \times 10^6$, 10 km Altitude, and $k - \omega$ model. Each model was tested at 0°, 5°, and 10° angles of attack (α) and run-in velocities: 150 m/s, 200 m/s, 250 m/s, and 300 m/s at steady level flight.

The experimental study was conducted in a horizontal low subsonic wind tunnel at sea level air properties. Four models were tested with a smooth upper surface and a lower surface with roughened ks = 0.258 mm, ks =0.45 mm, ks =0.125 mm, and ks =0.129 mm. Each model sampled at α= 0°, 5°, 10° for speeds V= 20 m/s, 23 m/s, 27 m/s, 30 m/s, and 35 m/s. Boundary Layer Thickness (BL) was also measured for each model Experimentally to indicate the effect of surface roughness on BL thickness.

Airfoil models compared to the smooth Airfoil ($k_s \cong 0mm$) numerically. The ks =0.05 mm (first set) and ks=1 mm (second set) had shown the best outcomes. Lift Coefficient C_L increased at α=0° but decreased at α= 5° and 10°. The drag coefficient C_D decreased for the first

set but increased significantly for the second. For the First set model with ks = 0.05 mm, the C_L/C_D at $\alpha = 5^o$ increased compared to the smooth airfoil model by 13.08%, 13.73%, 14.3%, and 12.2% at velocities: 150 m/s, 200 m/s, 250 m/s, and 300 m/s. For the second set model of ks = 1 mm, C_L/C_D decreased at $\alpha = 5^o$ compared to the smooth airfoil by: 4.91%, 5.9%, 6.35%, 7.52% at velocities: 150 m/s, 200 m/s, 250 m/s, and 300 m/s. Power required to operate the airfoil with ks=0.05 mm at $\alpha = 5^o$ decreased by 12.78%, 13.53%, 13.95%, and 12.50% for velocities: 150 m/s, 200 m/s, 250 m/s, and 300 m/s respectively.

Roughened experimental models were compared with a smooth model ($k_s \cong 0$mm). The airfoil model with ks = 0.125 mm revealed C_L's best results at $\alpha = 0^o$. Airfoil with ks = 0.045 mm had the slightest decrease in C_L values for all angles of attack 0^o, 5^o, and 10^o and recorded the best values at 10^o with 2.32%, 4.24%, 4.98%, 5.53%, and 6.28% for wind tunnel velocities: 20 m/s, 23 m/s, 27 m/s, 30 m/s, and 35 m/s. C_D values decreased the lowest for ks=0.125 mm at $\alpha = 0^o$ by 11.95%, 11.67%, 11.39%, 11.18%, 10.88% for velocities: 20 m/s, 23 m/s, 27 m/s, 30 m/s, and 35 m/s. C_L/C_D improved the best at $\alpha = 0^o$ by 1.288%, 12.76%, 12.31%, 12.30%, and 12.29% for velocities: V = 20 m/s, 23 m/s, 27 m/s, 30 m/s and 35 m/s respectively. Power conservation improved the best for Airfoil with ks=0.125 mm compared to the smooth Airfoil and documented 12.53%, 12.54%, 12.04%, 12.16%, and 12.32% for velocities of 20 m/s, 23 m/s, 27 m/s, 30 m/s, and 35 m/s respectively. Finally, BL thickness is proven to be sensitive to surface roughness change. By increasing ks, the transition from laminar to turbulent BL shifts upstream.

These results suggested that low-cost designated rounded surface roughness film be applied at the lower surface of NACA 44the 12 Airfoil to get better aerodynamic characteristics.

Publication

Journal name: Aerospace

Manuscript ID: aerospace-2208482

Type of manuscript: Article

Title: NACA 4412 Airfoil's Lift and Drag Coefficients Influenced by Applied

Surface Roughness on the Lower Surface at High Subsonic Speeds

Authors: Ebrahim Kamal Seddiq *, Mohammed Nabhan, Omar Al-Abbasi

Received: 24 January 2023

E-mails: ebrahimseddiq@gmail.com, mnabhan@uob.edu.bh, omabbasi@uob.edu.bh

Submitted to section: Aeronautics,

https://www.mdpi.com/journal/aerospace/sections/aeronautics

Advanced Flow Diagnostic Tools

https://www.mdpi.com/journal/aerospace/special_issues/flow_diagnostic_tools

You can follow the progress of your manuscript at the following link (l.Requireduired):

https://susy.mdpi.com/user/manuscripts/review_info/5c73d7ec9120c64296dd3c63013645db

Dedication

I dedicate my dissertation work to my father, Dr Kamal Seddiq, who inspired me never to stop believing in myself.

Acknowledgement

I want to sincerely thank my thesis supervisors, Dr Mohammed Nabhan and Dr Omar Al-Abasi, for their assistance, direction, and inspiration during the thesis research process. I also want to thank the faculty and staff at the mechanical engineering college for helping me accomplish the thesis.

I especially want to thank Allah (swt), who gave me a wonderful family who supported me and inspired me to become where I am now.

Table of Contents

Defense Committee's approval ..... A
Declaration ..... B
Abstract C
Publication ..... E
Dedication ..... F
Acknowledgement ..... G
Table of Contents ..... H
List of Tables L
List of Figures ..... P
List Appendices ..... U
Nomenclature V
Chapter One Introduction to the Study 1
1.1 Introduction 2
1.2 Research Problem 6
1.3 Research Questions 6
1.4 Research Objectives 7
1.5 Research Significance 7
1.6 Study Setting 7
1.7 Research Terminology 8
Chapter Two Theoretical Framework and Literature Review 11
2.1 Introduction 12
2.2 The Airfoil Quality 12
2.3 Viscous Flow 13
2.4 Solutions to Viscous Flows 21
2.4.1 Continuity Equation 21
2.4.2 Momentum Equation 21
2.4.3 Viscous Flow Equations 21
2.5 Boundary Layers 22

2.5.1 Laminar Boundary Layers 23
2.5.2 Turbulent Boundary Layers 24
2.6 Surface Roughness 24
2.6.1 Effect of Wall Roughness 25
2.6.2 Wind Farms Blade Roughness 27
2.6.3 Effect of Frost on Airfoil Upper Surface 27
2.6.4 Effect of Frost on Airfoil Lower Surface 28
2.6.5 Surface Roughness influence 28
i. Heat Transfer 29
ii. Reynolds Number 29
iii. Roughness Location 30
iv. Lift and Drag 30
2.6.6 Roughness Model Implementation 31
i. Approach Methodologies 31
ii. Moody Diagram 32
iii. Overflow 32
iv. Bowyer's Grid Generator 32
v. Multi-Domain Spectral Difference Method 33
2.7 Literature Review 33
2.8 Commentary on Literature Review 45
2.9 Research Hypothesis 46
Chapter Three 47
Methods and Procedures 47
3.1 Introduction 48
3.2 Flow Field Characteristics 49
3.2.1 Boundary Conditions 51
3.2.2 Air Flow Behavior 52
3.2.3 Steady Level Flight 52
3.3 Lift Theory 53
3.4 Geometry Selection 55
3.4.1 Airfoil Selection 55

3.4.2 Surface Roughness 56
3.5 Numerical Approach 58
3.5.1 Ansys 2020 R1 Fluent Space Claim 59
3.5.2 Meshing 64
i. Smooth Airfoil 66
ii. Airfoil with Applied Roughness 0.05mm up to 0.5mm 67
iii. Airfoil with Applied Roughness set 2 of 1mm up to 4mm. 68
iv. Bounding Box 69
v. Meshing Grid Independency Study 70
3.5.3 Fluent 71
i. Turbulence Models 73
ii. Boundary Conditions 78
iii. Solution Setup 81
3.6 Experimental Approach 83
3.6.1 Design of the Model 84
3.6.2 Manufacture of Objects 85
3.6.3 Wind Tunnel Setup 86
i. Wake Survey Rake 87
ii. Electronic Manometer Bank 88
iii. Lift and Drag Electronic Balance Device 88
iv. Calibrating the Models 89
vi. Testing of the Rig 97
3.7 Experimental Procedures and Uncertainty 97
3.7.1 Experimental Procedures 98
i. Lift and Drag Experiment 98
ii. Boundary Layer Experiment 99
3.7.2 Uncertainty Analysis 102
3.8 Summary 103
Chapter Four Results, Discussions, Conclusions and Recommendations 104
4.1 Introduction 105

4.2 Results 105
4.2.1 Numerical Results 105
i. The Lift coefficient (C_L) 106
ii. Drag Coefficient (C_D) 110
iii. Lift to Drag Ratio (C_L/C_D) 114
iv. Power Analysis 118
4.2.2 Experimental Results 122
i. Lift Coefficient (C_L) 122
ii. Drag Coefficient (C_D) 124
iii. Lift to Drag Ratio (C_L/C_D) 126
iv. Power Analysis 128
v. Results Verification 130
vi. Experimental Boundary Layer Thickness (BL Thickness) 131
4.3 Discussions 134
4.3.1 Numerical Lift Coefficient Discussion 134
i. First Set of Applied Roughness C_L 134
ii. Second Set of Applied Roughness C_L 139
iii. Turbulent Flow Behavior 141
4.3.2 Numerical Drag Coefficient Discussion 144
i. First Set of Applied Roughness C_D 144
ii. Second Set of Applied Roughness C_D 147
4.3.3 Numerical Lift-to-Drag Coefficient Discussion 149
i. First Set of Applied Roughness C_L/ C_D 149
ii. Second Set of Applied Roughness C_L/ C_D 152
4.3.4 Numerical Power Analysis Discussion 153
4.3.5 Experimental Lift Coefficient Discussion 156
4.3.6 Experimental Drag Coefficient Discussion 159
4.3.7 Experimental Lift-to-Drag Coefficient Discussion 161
4.3.8 Boundary Layer Thickness Measurement Discussion 162
4.3.9 Experimental Power Analysis Discussion 164
4.4 Conclusions 165

List of Tables

Table (3.1): Set 1 Roughness Height $\boldsymbol{ks}$ Effect on Boundary Layer 57
Table (3.2): Set 2 Roughness Height $\boldsymbol{ks}$ Effect on Boundary Layer 57
Table (3.3): Meshing Properties for Smooth Airfoil NACA 4412..... 67
Table (3.4): Meshing Properties of ks = 0.05mm Applied to the Airfoil NACA 4412 Compared to ks = 0.5mm Model..... 68
Table (3.5): Meshing Properties of ks = 1mm Applied to the Airfoil NACA 4412 Model Compared to ks = 4mm Model 69
Table (3.6): Grid Independency Study for Smooth Airfoil 71
Table (3.7) Sandpaper Sizes Used for the Models..... 91
Table (3.8): Average Surface Roughness Calibration 91
Table (3.9): C-15 Wind Tunnel Inlet Fan Speed Equivalent Inlet Velocities..... 97
Table (4.1): Experimental Results Verification at α=0° 131
Table (4.2): Experimental Results Verification at α=5° 131
Table (4.3): C_L Percentage Variation for Different Roughness of First Set models to the Smooth Airfoil at α= 0°..... 135
Table (4.4): C_L Percentage Variation for Different Roughness of First Set models to the Smooth Airfoil at α= 5°..... 135
Table (4.5): C_L Percentage Variation for Different Roughness of First Set models to the Smooth Airfoil at α= 10°..... 136
Table (4.6): C_L Percentage for Differences of Airfoils with Applied Roughness of Second Set of ks to the Smooth Airfoil α= 0°..... 140
Table (4.7): C_L of Percentage Differences of Airfoils with Applied Roughness of Second Set of k_s to the Smooth Airfoil α= 5° 140
Table (4.8): C_L Percentage Differences of Airfoils with Applied Roughness of Second set of ks to the Smooth Airfoil α= 10° 141

Table (4.9): C_D Percentage Difference of Airfoils with Applied Roughness of First set of ks to the Smooth Airfoil α= 0° 145
Table (4.10): C_D Percentage Differences of Airfoils with Applied Roughness of First Set of ks to the Smooth Airfoil α= 5° 146
Table (4.11): C_D Percentage Differences of Airfoils with Applied Roughness of First Set of ks to the Smooth Airfoil α= 10° 147
Table (4.12): C_D Percentage Differences of Airfoils with Applied Roughness of Second Set of ks to the Smooth Airfoil α= 0° 148
Table (4.13): C_D Percentage Differences of Airfoils with Applied Roughness of Second Set of ks to the Smooth Airfoil α= 5° 148
Table (4.14): C_D Percentage Differences of Airfoils with Applied Roughness of Second Set of ks to the Smooth Airfoil α= 10° 149
Table (4.15): C_L/ C_D Percentage Differences of Airfoils with Applied Roughness of First Set of ks to the Smooth Airfoil α= 0° 150
Table (4.16): C_L/ C_D Percentage Differences of Airfoils with Applied Roughness of First Set of ks to the Smooth Airfoil α= 5° 151
Table (4.17): C_L/ C_D Percentage Differences of Airfoils with Applied Roughness of First Set of ks to the Smooth Airfoil α= 10° 151
Table (4.18): C_L/ C_D Percentage Differences of Airfoils with Applied Roughness of Second set of ks to the Smooth Airfoil α= 0° 152
Table (4.19): C_L/ C_D Percentage Differences of Airfoils with Applied Roughness of Second Set of ks to the Smooth Airfoil α= 5° 153
Table (4.20): C_L/ C_D Percentage Differences of Airfoils with Applied Roughness of Second set of ks to the Smooth Airfoil α= 10° 153
Table (4.21): Power Analysis CL3/2CD Percentage Variation for Different Roughness of First Set models to Smooth Airfoil at α= 0° 154
Table (4.22): Power Analysis CL3/2CD Percentage Variation for Different Roughness of First Set models to Smooth Airfoil at α= 5° 154

Table (4.23): Power Analysis CL3/2CD Percentage Variation for Different Roughness of First Set models to Smooth Airfoil at α= 10°.. 155
Table (4.24): Power Analysis CL3/2CD Percentage Difference of Airfoils with Applied Roughness of Second set of ks to the Smooth Airfoil α= 0° 156
Table (4.25): Power Analysis CL3/2CD Percentage Difference of Airfoils with Applied Roughness of Second set of k_s to the Smooth Airfoil α= 5° 156
Table (4.26): Power Analysis CL3/2CD Percentage Difference of Airfoils with Applied Roughness of Second set of ks to the Smooth Airfoil α= 10° 156
Table (4.27): C_L Percentage Difference of Airfoils with Applied Roughness of k_s to the Smooth Airfoil at α= 0° 158
Table (4.28): C_L Percentage Difference of Airfoils with Applied Roughness of ks to the Smooth Airfoil at α= 5° 158
Table (4.29): C_L Percentage Difference of Airfoils with Applied Roughness of k_s to the Smooth Airfoil at α= 10° 159
Table (4.30): C_D Percentage Difference of Airfoils with Applied Roughness of ks to the Smooth Airfoil at α= 0° 159
Table (4.31): C_D Percentage Difference of Airfoils with Applied Roughness of ks to the Smooth Airfoil at α= 5° 160
Table (4.32): C_D Percentage Difference of Airfoils with Applied Roughness of k_s to the Smooth Airfoil at α= 10° 160
Table (4.33): C_L/C_D Percentage Difference of Airfoils with Applied Roughness of ks to the Smooth Airfoil at α= 0° 161
Table (4.34): C_L/C_D Percentage Difference of Airfoils with Applied Roughness of ks to the Smooth Airfoil at α= 5° 162
Table (4.35): C_L/C_D Percentage Difference of Airfoils with Applied Roughness of ks to the Smooth Airfoil at α= 10° 162

Table (4.36): Power Analysis CL3/2CDPercentage Difference of Airfoils with Applied Roughness of ks to the Smooth Airfoil at α= 0° 164
Table (4.37): Power Analysis CL3/2CDPercentage Difference of Airfoils with Applied Roughness of ks to the Smooth Airfoil at α= 5° 165
Table (4.38): Power Analysis CL3/2CDPercentage Difference of Airfoils with Applied Roughness of ks to the Smooth Airfoil at α= 10° 165

List of Figures

Figure (1.1): Forces Acting on an Aircraft in Horizontal Flight 2
Figure (1.2): A Flowchart Describing Sources of Drag Force 4
Figure (1.3): Flight Envelope.....4
Figure (2.1): Viscous Flow Around Airfoil (Anderson J. D., 2017)..... 14
Figure (2.2): Boundary Layer Changes from Laminar to Turbulent (Anderson J. D., 2017)..... 15
Figure (2.3): Pressure Difference Between Viscous and Inviscid Flows 16
Figure (2.4): Different between Slender and Blunt Body's Drag..... 17
Figure (2.5): Turbulent and Laminar Flow Streamlines..... 18
Figure (2.6): Velocity Profiles for Laminar and Turbulent Flows 18
Figure (2.7): Transition of the Flow from Laminar to Turbulent on a Flat Plate (Anderson J. D., 2017)..... 19
Figure (2.8): The Boundary Layer Thickness on Flat Plate (Anderson J. D., 2017)..... 23
Figure (2.9): Variation of Rivet Drag Relative to Position of Forward Rows (Hood, 1939)..... 31
Figure (3.1): Methodology Process..... 49
Figure (3.2): Cruising Altitude for Commercial Airplanes (Bahr et al.). 50
Figure (3.3): Cruising Speed for Commercial Airplanes (Bahr et al.) 51
Figure (3.4): Aircraft Loads in Level Flight (Megson, 2022) 53
Figure (3.5): NACA 4412 Airfoil..... 56
Figure (3.6): NACA 4412 Airfoil Drawn in Space Claim..... 60
Figure (3.7): The Elliptic Face Around NACA 4412 Airfoil 61
Figure (3.8): Envelope Box Face Around the Elliptic Face 61
Figure (3.9): The two Faces Creating the Surface of the Project 62

Figure (3.10): Overview of the Scripts Screen in ANSYS Fluent 2020 R1 63
Figure (3.11): Close View of the Applied Roughness Drawn in Space Claim 63
Figure (3.12): Main Screen of Meshing Program 64
Figure (3.13): Triangular Meshing for Set1 Applied Roughness 65
Figure (3.14): Quadrilateral Meshing for Set2 Applied Roughness 66
Figure (3.15): Named Selection for the Models 70
Figure (3.16): Setup Launching Screen 72
Figure (3.17): General Options and Materials in Fluent Screen 73
Figure (3.18): Models Applied to the Solution in Fluent 74
Figure (3.19): Airflow Properties at 10,000m Altitude 75
Figure (3.20): Viscous Model Applied to the Project 77
Figure (3.21): Boundary Conditions of the Project 78
Figure (3.22): Velocity Inlet Boundary Conditions 79
Figure (3.23): Pressure Outlet Options in Fluent 80
Figure (3.24): Wall Boundary Conditions in Fluent 81
Figure (3.25): Lift and Drag Coefficients Setup in Fluent 82
Figure (3.26): The Convergence of Solution Accuracy with the Assigned Residuals 83
Figure (3.27): Experiment Process 84
Figure (3.28): Front and Top View of the Model 85
Figure (3.29): C15-20 Computer Controlled Subsonic Wind Tunnel 86
Figure (3.30): Stainless Steel Wake Rake Tubes Arrangement 87
Figure (3.31): Electronic Manometer Bank 88
Figure (3.32) Lift and Drag Balance Device 89
Figure (3.33): Testing Models of 400 Grits Upper Surface and (400, 60 Grits) Lower Surfaces 90

Figure (3.34): Surface Roughness measurement locations at lower and upper surfaces of NACA 4412 Airfoil 92
Figure (3.35): Depth Gauge Used to Measure Surface Smoothness 92
Figure (3.36): C15-20: Lift and Drag Airfoil Model Calibration Test 93
Figure (3.37): Boundary Layer Experiment Set 94
Figure (3.38): Boundary Layer Probe Used in BL Experiments 94
Figure (3.38): Boundary Layer Probe Used in BL Experiments 95
Figure (3.39): Surface Roughness Effect on Boundary Layer (Kadivar, Tormey, & McGranaghan, 2021) 96
Figure (3.39): Airfoil inside Wind Tunnel's Duct 99
Figure (3.40): BL Experiment Setup 100
Figure (3.41): BL Experiment Fixture 101
Figure (3.42): BL Experiment Model Setup 101
Figure (3.43): Model Placement in BL Experiment 102
Figure (4.1): First Set Lift Coefficient C_L at $\alpha=0^o$ 106
Figure (4.2): First Set Lift Coefficient C_L at $\alpha=5^o$ 107
Figure (4.3): First Set Lift Coefficient C_L at $\alpha=10^o$ 108
Figure (4.4): Second Set Lift Coefficient C_L at $\alpha=0^o$ 109
Figure (4.5): Second Set Lift Coefficient C_L at $\alpha=5^o$ 109
Figure (4.6): Second Set Lift Coefficient C_L at $\alpha=10^o$ 110
Figure (4.7): First Set Drag Coefficient C_D at $\alpha=0^o$ 111
Figure (4.8): First Set Drag Coefficient C_D at $\alpha=5^o$ 111
Figure (4.9): First Set Drag Coefficient C_D at $\alpha=10^o$ 112
Figure (4.10): Second Set Drag Coefficient C_D at $\alpha=0^o$ 113
Figure (4.11): Second Set Drag Coefficient C_D at $\alpha=5^o$ 113
Figure (4.12): Second Drag Coefficient Set C_D at $\alpha=10^o$ 114
Figure (4.13): First Set Lift to Drag Ratio (C_L/C_D) at $\alpha=0^o$ 115
Figure (4.14): First Set Lift to Drag Ratio (C_L/C_D) at $\alpha=5^o$ 115
Figure (4.15): First Set Lift to Drag Ratio (C_L/C_D) at $\alpha=10^o$ 116

Figure (4.16): Second Set Lift to Drag Ratio (C_L/C_D) at $\alpha=0^o$ 117
Figure (4.17): Second Set Lift to Drag Ratio (C_L/C_D) at $\alpha=5^o$ 117
Figure (4.18): Second Set Lift to Drag Ratio (C_L/C_D) at $\alpha=10^o$ 118
Figure (4.19): Power Analysis CL3/2CD for First Set of ks at $\alpha=0^o$..... 119
Figure (4.20): Power Analysis CL3/2CD for First Set of ks at $\alpha=5^o$..... 119
Figure (4.21): Power Analysis CL3/2CD for First Set of ks at $\alpha=10^o$... 120
Figure (4.22): Power Analysis CL3/2CD for Second Set of ks at $\alpha=0^o$ 120
Figure (4.23): Power Analysis CL3/2CD for Second Set of ks at $\alpha=5^o$ 121
Figure (4.24): Power Analysis CL3/2CD for Second Set of ks at $\alpha=10^o$ 121
Figure (4.25): Experimental Lift Coefficient C_L at $\alpha=0^o$..... 123
Figure (4.26): Experimental Lift Coefficient C_L at $\alpha=5^o$..... 123
Figure (4.27): Experimental Lift Coefficient C_L at $\alpha=10^o$..... 124
Figure (4.28): Experimental Drag Coefficient C_D at $\alpha=0^o$..... 125
Figure (4.29): Experimental Drag Coefficient C_D at $\alpha=5^o$..... 125
Figure (4.30): Experimental Drag Coefficient C_D at $\alpha=10^o$..... 126
Figure (4.31): Experimental Lift to Drag Ratio (C_L/C_D) at $\alpha=0^o$..... 127
Figure (4.32): Experimental Lift to Drag Ratio (C_L/C_D) at $\alpha=5^o$..... 127
Figure (4.33): Experimental Lift to Drag Ratio (C_L/C_D) at $\alpha=10^o$..... 128
Figure (4.34): Power Analysis CL3/2CD for Experimental Models of ks at $\alpha=0^o$ 129
Figure (4.35): Power Analysis CL3/2CD for Experimental Models of ks at $\alpha=5^o$ 129
Figure (4.36): Power Analysis CL3/2CD for Experimental Models of ks at $\alpha=10^o$ 130
Figure (4.37): BL Thickness δ at 0.7C for ks =0.0258mm..... 132
Figure (4.38): BL Thickness δ at 0.7C for ks =0.045mm..... 133
Figure (4.39): BL Thickness δ at 0.7C for ks =0.125mm..... 133
Figure (4.40): BL Thickness δ at 0.7C for ks =0.19mm..... 134

Figure (4.41): Static Pressure Contours of NACA 4412 at α= 5° and V=250m/s (ks =0.05mm) 137
Figure (4.42): Skin Friction Comparison Between Smooth Airfoil and Airfoil with ks =0.05mm 137
Figure (4.43): Static Pressure Contours of NACA 4412 at α= 5° and V=250m/s (Smooth Airfoil) 138
Figure (4.44): Total Pressure Comparison Between Smooth Airfoil and Airfoil with ks =0.05mm 139
Figure (4.45): Turbulent Energy of NACA 4412 at α= 0° and V=250m/s (Smooth Airfoil) 142
Figure (4.46): Turbulent Energy of NACA 4412 at α= 0° and V=250m/s (ks =0.05mm) 142
Figure (4.47): Turbulent Energy of NACA 4412 at α= 0° and V=250m/s (ks =3mm) 143
Figure (4.48): Turbulent Intensity comparison between Smooth Airfoil and Airfoil with ks =0.05mm 144

List Appendices

Appendix (A)	Meshing Properties for the Models
Appendix (B)	Grid Independency Study
Appendix (C)	Fluent Ansys 2020 R1 Solution Iteration
Appendix (D)	Dimension 1200es 3-D Printer Specifications
Appendix (E)	C15-20 Computer Controlled Subsonic Wind Tunnel
Appendix (F)	Uncertainty Analysis
Appendix (G)	Wind Tunnel Results
Appendix (H)	Experimental Results Verification

Nomenclature

A	Planform Area of Wing, m^2
AR	The Aspect Ratio, m
c	Chord Length of Airfoil at any Point Along the Wingspan, m
C_D	The Drag Coefficient, $(D/0.5\rho V_\infty^2 A)$
C_{Df}	The Skin Friction Drag Coefficient
C_f	Skin Friction
C_L	The Lift Coefficient, $(L/0.5\rho V_\infty^2 A)$
C_{Lmax}	Maximum Lift Coefficient at Stall Speed
C_L/C_D	Lift Coefficient to Drag Coefficient Ratio
D	The Drag Force, N
e	Wing Geometry Factor, m^{-1}
f_i	The Body Force of Micro Unit
ks	Roughness Thickness, m
L	The Lift Force, N
L/D	Lift Force to Drag Force Ratio
M	Mach Number, M
P	Pressure, Pa
Re	Reynolds Number, $(\rho V_\infty L/\mu)$
Re_{cr}	Critical Reynolds Number
U	The Velocity of Micro Unit $U = u_i + v_j + w_k$
U_R	The Uncertainty of the Measured value R
U_{x_i}	The Uncertainty of a Given Variables x_i
V_{stall}	Stall Velocity at Maximum Angle of Attack, m/s
V_∞	Uniform Free Air Stream Velocity, m/s
V_w	Velocity at the Wall (Adjacent to the Wall), m/s

V_*	Shear Velocity at Boundary-Layer Displacement Thickness, m/s

Greek Symbols:

α	Angle of Attack, *degree*
ρ	Density of Air flow, kg/m^3
δ	Boundary Layer Thickness, m
δ_T	The Thermal Boundary Layer Thickness, m
τ_w	Wall Shear Stress, Pa
τ_{ij}	The Viscosity Stress Component of Micro Unit
μ	Dynamic Viscosity, kg/ms
ε	Downwash Angle, deg
ω	Specific Turbulent Dissipation Rate (or Turbulence Frequency), 1/s
ν	Kinematic Viscosity, m^2/s

Abbreviations:

BL	Boundary Layer
CFD	Computational Fluid Dynamics
CFX	Ansys Software Solver for Fluid Dynamic, which uses the Control Volume Finite Element Method
DNS	Direct Numerical Simulation
GPGPU	The process of doing Computation by the Central Processor Unit using a Graphics Processing Unit (GPU), which typically solely handles calculation for Computer Graphics
LE	The Leading Edge of the Wing
LES	Large Eddy Simulation
PIV	Particle Image Velocimetry
P_r	Prandtl Number
RSTT	Reynolds Stress Transport Turbulence Models

SST K- ω	Shear-Stress Transport K- ω Model
TE	The Trailing Edge of the Wing
T	Flow Temperature
T_w	Flow Temperature at Wall
RANS	Reynolds Averaged Navier-Stokes

Chapter One
Introduction to the Study

1.1 Introduction

1.2 Research Problem

1.3 Research Question

1.4 Research Objectives

1.5 Research Significance

1.6 Research Setting

1.7 Research Terminology

Chapter One
Introduction to the Study

1.1 Introduction

Aerodynamic forces are the main forces that act on bodies while they move through the air. These forces are mainly due to the following:

1- Pressure distribution over the body surface.

2- Shear stress distribution over the body surface.

The resultant aerodynamic force R consists of two main components, the lift force L, which is vertical to the free stream velocity line, and the drag force D, which is opposite to the free stream velocity line (Anderson J. D., 2005). The thrust T and the weight W forces are counter to the aerodynamic forces, as shown in Figure (1.1).

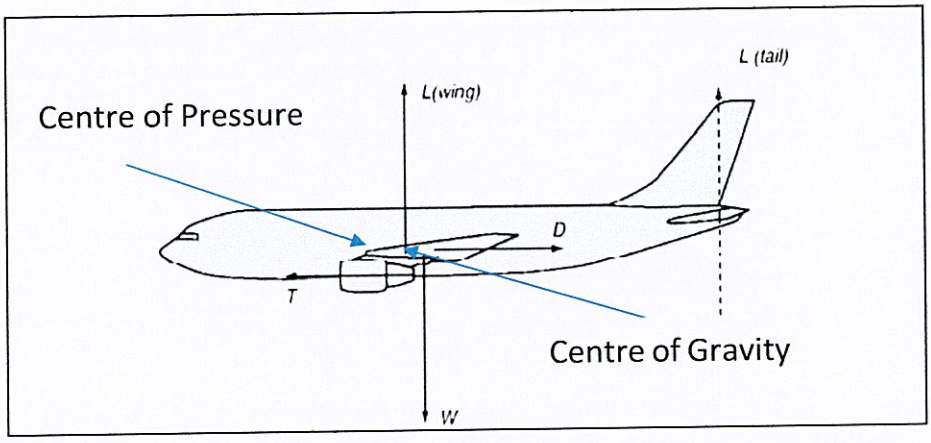


Figure (1.1): Forces Acting on an Aircraft in Horizontal Flight

The design of an aircraft passes through a long journey of primary and secondary design steps and constraints (McCormick, 1995).

Aerodynamics is the most crucial sector for external flow because it deals with the main forces affecting the aircraft on its flight. Scientists highlighted these forces below:

1- Lift Force.
2- Drag Force.
3- Thrust Force.
4- Weight Force.

An area of low pressure exists on the airfoil's upper surface, while higher pressure forms on the lower surface of the airfoil. This difference in pressure between the upper and lower surfaces of the airfoil is called lift force. Seventy-five per cent 75% of the total lift force of an airfoil is the result of the decrease in pressure over the upper surface, while twenty-five per cent 25% of the lift force by higher pressure on the lower surface (Anderson J. D., 2005).

Drag is the force resisting the thrust force of an aircraft. It acts in the same direction as the relative airflow. The total drag divided into two main types; parasite drag and induced drag during subsonic Flight. Furthermore, Parasite drag divided into three types: skin friction drag, pressure (form or profile drag), and interference drag, as shown in Figure (1.2). The interference drag arises when the components of an aircraft are combined. Therefore, one component or part of the aircraft can affect the flow field as well as the drag of the whole aircraft (Moran, 2003).

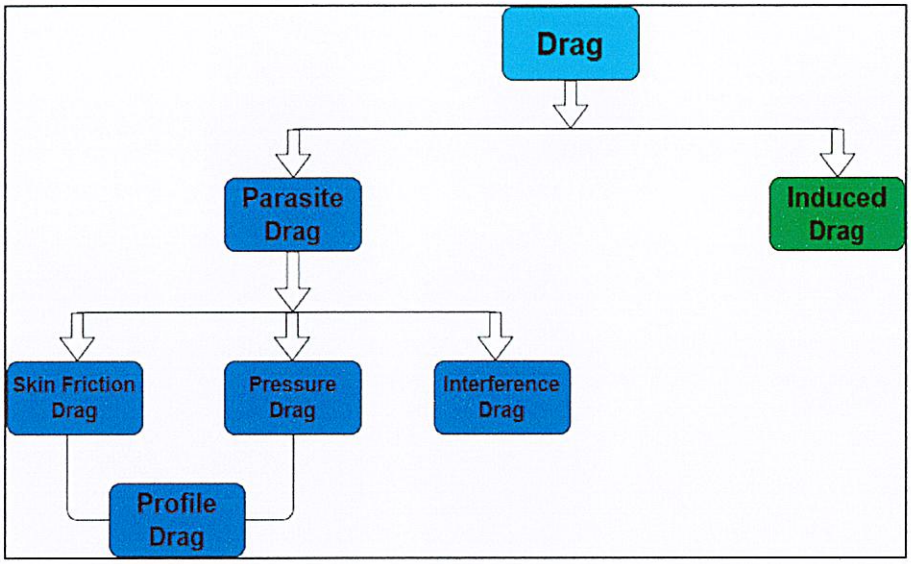


Figure (1.2): A Flowchart Describing Sources of Drag Force

The aircraft was set in equilibrium in steady-level flight at a constant speed. In this situation, thrust force equals the drag force, and the weight equals the lift force. Therefore, each pair is equal and opposite in direction. Figure (1.3) anointed the flight envelope. It elaborates on the association between drag force and the aircraft's velocity, which determines the cruising speed of the aircraft (Kazimieras, 2017).

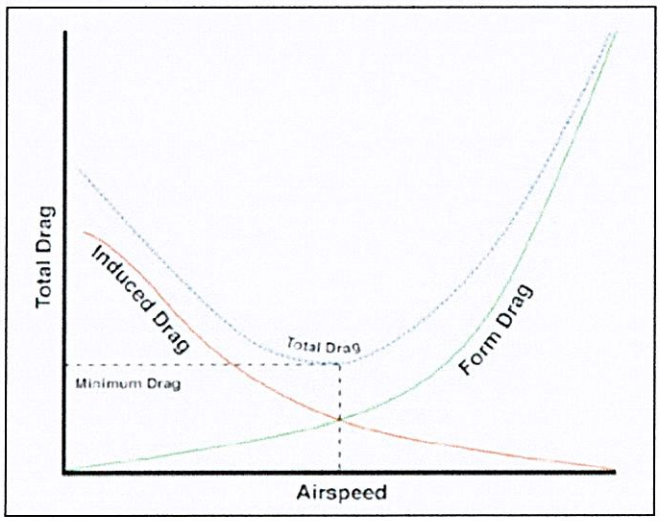


Figure (1.3): Flight Envelope

The influence of body surface roughness in the flow field generally provokes the Flow near the surface of that body to convert from laminar to turbulent. By augmenting the surface roughness, the transition point at which laminar Flow diverts into turbulent will shift upstream along the surface of the airfoil. The Reynolds number and body surface roughness deliver a share in demarcating the transition from laminar to turbulent Flow. Another vital factor triggering that transition is the flow field pressure gradient. The skin friction force, referred to as the Viscosity of the Flow over the surface, generates an aerodynamic shear force, which leans on the three mentioned factors: Reynolds number, body surface roughness and Flow field pressure gradient (Talay, 1975).

Scientists considered the structural design a significant factor, as the aircraft's structure should withstand all these aerodynamic forces and their corresponding reactions, such as vibrations with different categories and vortices. Designing a structure that can resist all these forces with the mandated aerodynamic shape and surface roughness takes work. Design optimization figured weight reduction constraints to maintain feasible, economical flying with consideration of all aerodynamic forces and moments.

The safety of Flight should be the primary concern in all aerodynamic studies. Any practical design with a high risk of accidents or incidents is prohibited. A good and complete literature review embellishes new designs concerning the field's noteworthy studies. These studies should preferably cover the following three main verification methods:

1- Analytical Methods.
2- Experimental methods.
3- Numerical Methods.

1.2 Research Problem

Changing the wing's surface roughness will result in variation of aerodynamic characteristics. These changes are optimistic, but some are considered harmful. The desired outcome of applied roughness determines the type, height, and location of applied roughness. This study will debate in Chapter two that recent studies consolidated in designing and studying surface roughness test patterns in areas: Leading edge, trailing edge, middle or at 25% of the chord for both sides of the wings simultaneously or on the upper surface only. Nevertheless, what will happen if surface elements added to the lower surface to implement Bernoulli's equation theory (Anderson J. D., 2005)? Most of the research in this field is either experimentally or numerically verified. However, they still need to complete the same research's numerical and experimental verification.

Increasing the lift coefficient while keeping the drag coefficient at the expected levels, accompanied by reasonable control of boundary layer transition, is an area to be evaluated and studied in this research.

1.3 Research Questions

1. Could we increase the lift coefficient by increasing the surface roughness of the lower side of the wing?
2. Could decrease the drag coefficient by increasing the surface roughness of the lower side of the wing?
3. Could we enhance lift to drag ratio of the airfoil by applying surface roughness to the lower surface of the airfoil?
4. By changing surface roughness, could we control the boundary layer transition from laminar to turbulent?

5. Could we increase the aircraft power by adding surface roughness to the lower surface of the airfoil?

1.4 Research Objectives

Employ CFD simulation program, namely Ansys Fluent 2020 and 2-D wind tunnel C-15 Computer Controlled Subsonic Wind Tunnel, to predict the effect of raising the wing's lower surface roughness in cruise flight regime and compare the progress in aerodynamic characteristics to another similar plain model.

1.5 Research Significance

Previous research experimentally ascertained many typical models. Researchers tested these models utilizing different surface roughness patterns applied to both wing's sides or solely the upper side. The only difference was changing the location and height of the applied patterns. Our significance to this field will be changing the surface roughness height of the whole lower surface only to enrich the pressure of the lower surface to convey an enormous pressure difference between the lower and upper surfaces. This pressure distinction will add more lift to our wing, while the other aerodynamic aspects will remain within accepted limits. Numerical simulation and Experimental work adopted to verify the solution.

1.6 Study Setting

This study proposed a Numerical simulation and Experimental work to study the fluid flow characteristics, namely surface roughness, for different models of Aircraft wings. The wings will be simulated using CFD

code and exposed to a varying upstream air velocity at assorted angles of attack. After that, different surface roughness patterns will be applied to the wing's lower surface and measure the aerodynamic parameters in each position for all models. Finally, the Boundary layer will be studied and lift parameters at various angles of attack and velocities. Earlier experimentally verified models will be verified at the onset of the research. The thesis will consist of four chapters, namely:

1. Introduction to the Study.

2. Theoretical Framework and Literature Review

3. Methods and Procedures.

4. Results, Discussion, Conclusions, and Recommendations.

1.7 Research Terminology

In aerodynamics, various concepts and technologies are used, namely:

1- Aerodynamics: A branch of fluid dynamics concerned with studying the motion of air, mainly when it interacts with a solid object, such as an airplane wing.
2- Fluid mechanics: the branch of physics concerned with the mechanics of fluids (liquids, gases, and plasmas) and the forces on them. It has applications in various disciplines, including mechanical, civil, chemical, and biomedical engineering, geophysics, astrophysics, and biology.
3- Surface roughness: often shortened to roughness, is a component of surface texture. The deviations quantify it in the direction of the average

vector of an actual surface from its ideal form. If these deviations are large, the surface is rough; if they are small, the surface is smooth. In surface metrology, roughness is typically considered a measured surface's high-frequency, short-wavelength element.

4- Lift: A fluid flowing past the surface of a body exerts a force on it. The component of this force perpendicular to the oncoming flow direction is called lift.

5- Drag: A fluid flowing past the surface of a body exerts a force, which is the component of the resultant surface force parallel to the flow direction.

6- Computational fluid dynamics: CFD is a branch of fluid mechanics that uses numerical methods and algorithms to solve and analyze fluid flow problems. Computers are used to perform the calculations required to simulate the interaction of liquids and gases with surfaces defined by boundary conditions.

7- Aerodynamics Characteristics: In Aerodynamics, the four main forces which act on aircraft during the Flight are Lift, Drag, Thrust and Weight. Drag is one of the most critical phenomena and is the opposing force of an aircraft's forward motion. It could be divided mainly into parasite drag (not due to lift) and lift-induced drag. The performance of a given airfoil profile is related to lift drag, angle of attack, velocity, density, Viscosity, compressibility, and geometry of the airfoil.

8- Airfoil: An airfoil is the shape of a wing, the blade of a propeller, the rotor blade, the windmill blade, etc.

9- Airfoil Shape: It is the cross-section of the wing. The lift force depends on the airfoil's shape, especially the amount of camber (curvature such that the upper surface is more convex than the lower surface). Increasing the camber generally increases lift.

10- NACA Airfoils: These are airfoil shapes for aircraft wings developed by the National Advisory Committee for Aeronautics (NACA). The shape of the NACA airfoils is described using a series of digits following the word "NACA". The parameters in the numerical code can enter equations to precisely generate the airfoil cross-section and calculate its properties.

11- Subsonic Aircraft: An aircraft with a maximum speed less than the speed of sound (Mach 1). The term is sometimes, but not always, used to describe an aircraft that flies below Mach 0.8. General Aviation aircraft, helicopters, and all modern airliners are subsonic aircraft.

12- Inviscid Flow: Fluid flow in an idle situation where Viscosity is assumed to be zero, with no friction force and other related aerodynamic parameters.

13- Viscous Flow: Fluid flow in an actual situation where Viscosity is applied, and all related aerodynamics parameters are included in the calculations.

14- Boundary layer: A thin fluid flows adjacent to the moving object. The velocity right on the surface is zero and increases until it reaches free stream velocity. Also, the temperature changes until it reaches free stream temperature.

15- Boundary Layer Separation: BLS is the detachment of a boundary layer from contacting surface of a moving object. This phenomenon happens because of the shear stress of the velocity element moving downstream, which decreases the velocity due to high adverse pressure.

16- Laminar Flow: Parallel and homogeneous streamlines moving in the flow field. We find it in low velocities and low Re.

17- Turbulent Flow is an inhomogeneous flow field where flow particles move in irregular streamlines. We find it in high velocities and high-caph Re.

18- Shear velocity: This is a format for expressing shear stress in velocity units. Comparing realistic speeds, such as the Flow in a stream, to ones that indicate shear between flow layers is a helpful technique in fluid mechanics.

19- Turbulent Viscosity: also goes by the name Eddy viscosity. The proportionality factor describes how moving eddies cause an energy transfer that is turbulent and causes tangential forces.

20- Strouhal number: In dimensional analysis, the Strouhal number is a dimensionless number describing oscillating flow mechanisms.

Chapter Two
Theoretical Framework and Literature Review

2.1 Introduction to the Theory

2.2 Airfoil Quality

2.3 Viscous Flow

2.4 Solutions of Viscous Flows

2.5 Boundary Layers

2.6 Surface Roughness

2.7 Literature Review

2.8 Commentary on Literature Review

2.9 Research Hypothesis

Chapter Two

Theoretical Framework and Literature Review

2.1 Introduction

Aerodynamic forces act on bodies while they are moving through the flow field. The resultant aerodynamic force, R, is resolved into two main components: lift force, which is vertical to the free stream velocity, and drag force, contrary. Classifications divided airflow into two consequential types: Inviscid flow and viscous flow.

Jean LeRond d'Almbert, (1768) stated that he could not justify the resistance of fluids by theory precisely because of the neglection of the resistance, which is inaccurate. This statement countered his theory: d'Alembert's paradox. This theory assumed leads to predict zero drag on closed two-dimensional bodies (Anderson J. D., 2017).

In reality, different drag forms influence anybody moving in a fluid. Inviscid theory brought drag and supersonic wave drag but could not compute other forms of drag existed due to viscosity. Inviscid flow rounds out the overall fundamentals of natural aerodynamics into simplified boundary conditions.

2.2 The Airfoil Quality

Lift generation is the fundamental purpose of airfoils. Simply, the best lift differentiae required to be obtain, two preliminary parameters are aimed to evaluate:

1- The lift force: $L = C_L \frac{1}{2} \rho V^2 A$ (1)

2- The drag force: $D = C_D \frac{1}{2} \rho V^2 A$ (2)

Where C_L is the Lift coefficient. The maximum lift coefficient C_{Lmax} which also regulates the stalling speed of the aircraft (Anderson J. D., 2005), is:

$$V_{stall} = \sqrt{\frac{2W}{\rho_\infty A C_{Lmax}}} \quad (3)$$

Researchers conduct different approaches to raising the surface of the airfoils concerning the boundary layer nature to oversee the flow near the airfoil's surface. Demarcating optimum aerodynamic attributes for every flight regime is a detailed process. However, focusing on obtaining the highest L/D with minimum V_{stall} is a common pursuit.

2.3 Viscous Flow

Viscous flow is a type of flow affected by viscosity, mass diffusion and thermal conductivity. When a solid object moves through a fluid, the influence of the friction between the surface and the adjacent flow develops frictional force, diminishing the relative motion. This force influences fluid and the surface and is measured by force per unit area, dubbed shear stress. The influence of this force causes zero velocity at the surface adjacent to the flow, V=0, called the no-slip condition, which distinguishes the viscous flow, as Figure (2.1) illustrates. The flow just over the surface is finite but retreats and gradually increases as locomote away from the adjacent surface in a normal direction (n) until it bears free stream velocity. This phenomenon ensues due to shear stress. As seen in Figure (2.1), in insert (a), the velocity profile gradient ∂V/∂n increases gradually in the upstream region, but in insert (b), it retreated after the separation point.

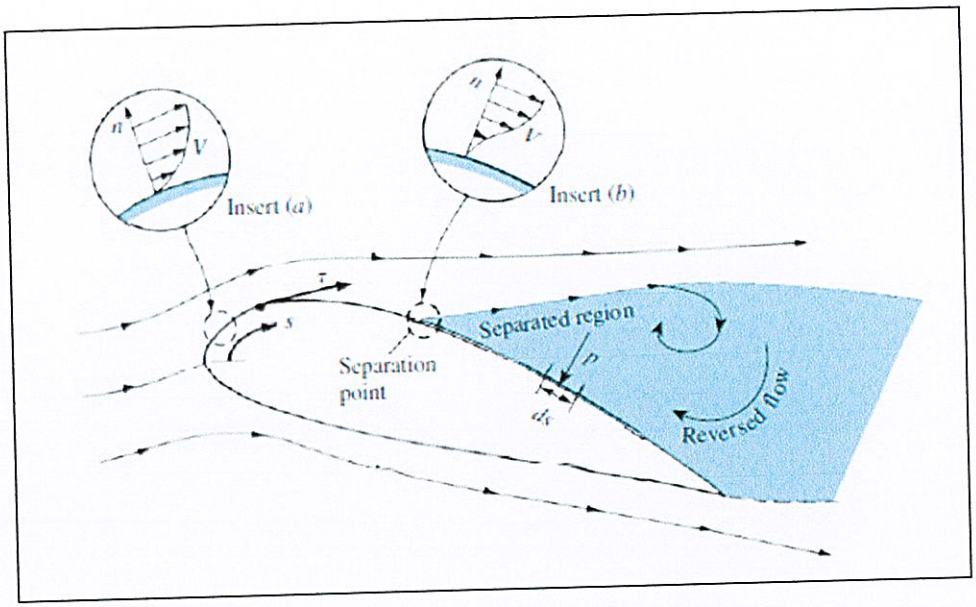


Figure (2.1): Viscous Flow Around Airfoil (Anderson J. D., 2017)

In addition to the shear stress generation, the friction force develops adverse pressure. This pressure increased during advancing downstream. In Figure (2.2), as adverse pressure accumulates, the velocity decreases—the negative pressure increases causing decay in the velocity. Figure (2.2) shows how the speed of an element decreases as while moving downstream from V_1 to V_2 until it reaches V_3, during observing the initiation of reversed flow. This phenomenon separates the flow from the adjacent surface and creates a wake of circulating flow downstream. Figure (2.1) in insert (b) depicts the point of separation where $\partial V/\partial n=0$ at the surface. So, in addition to the shear stress, friction compels the flow over the body to separate. This separation disturbs the pressure over the surface. As a result, the flow over the body downstream in Figure (2.1) will not take the body's shape in the upstream shape after the separation point. Because of that, the influential body that forges lift force decreases, or an effective body.

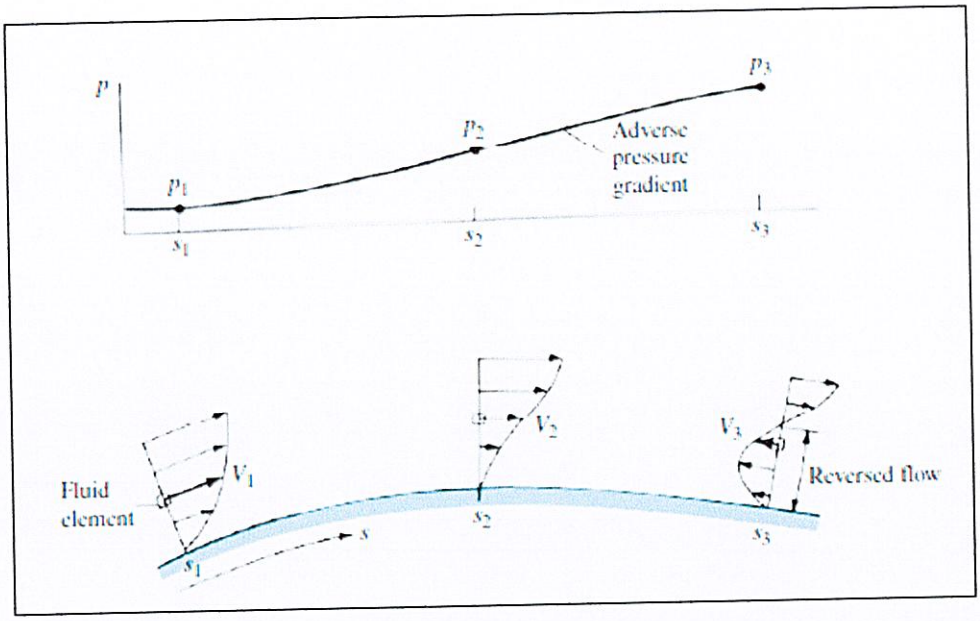


Figure (2.2): Boundary Layer Changes from Laminar to Turbulent (Anderson J. D., 2017)

This phenomenon builds disturbed pressure over the body's actual shape, resulting in further force in the free stream direction of anointed drag. For example, the dashed curve in Figure (2.3) presents the pressure of the flow of the attached flow, which can only be conveyed downstream in inviscid flow as embroidered in d'Alembert's paradox theory. However, in viscous flow, separated flow acquired as a persisted curve in the exact Figure, which is lower pressure for the same body. This drag state is called the drag pressure due to flow separation, denoted by D_P.

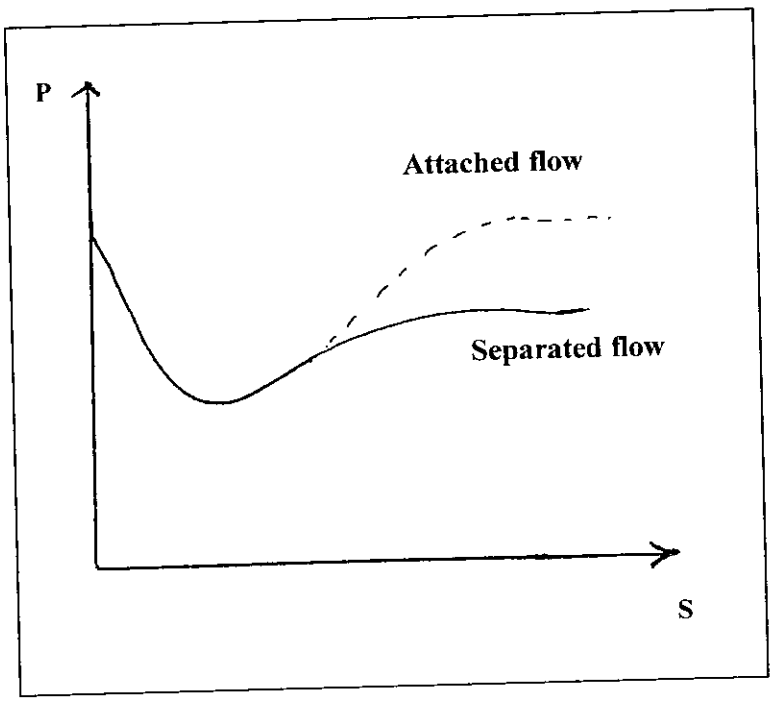


Figure (2.3): Pressure Difference Between Viscous and Inviscid Flows

In summary, the impact of viscosity leads to two prominent types of pressure:

1- Friction drag D_f is the skin friction drag, the drag force created because of the shear stress created by the friction.
2- Form drag D_p, which is the pressure drag due to separation; this drag component is due to pressure diffusion around the body shape.

The summation of $D_f + D_f$ is called profile drag for two-dimensional and parasite drag for three-dimensional bodies. Figure (2.4) explains the relationship between slender, blunt bodies with drag. DP is the most drag force contributor for flow past blunt bodies, and D_f is the dominating drag force contributor for slender bodies.

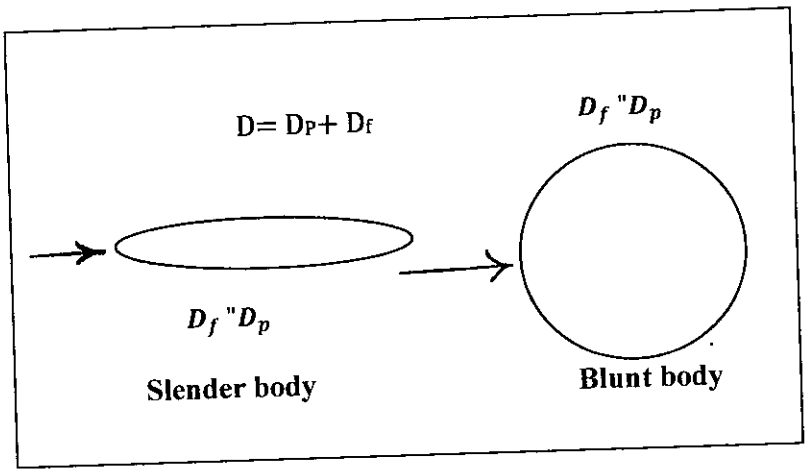


Figure (2.4): Different between Slender and Blunt Body's Drag

The flow separation boosts the negative pressure over the body, which boosts the drag force and results in a substantial loss of lift force, which can compel the airfoil to stall.

The impact of thermal conductivity is another physical feature of the viscous flow in addition to friction. The moving fluid has kinetic energy, which reduces due to the friction force. This loss leads to a lowering of the kinetic energy as well. When the kinetic energy lowers, it will transform to heat energy, provoking an increment in the temperature of the moving body—the heat transfers from the fluid to the moving body via viscous dissipation. As flow velocity grows, the mechanism of aerodynamic heating grows, friction dissipates additional kinetic energy, and hence the overall temperature disparity between the cold surface of the body and the warmer flow proliferation.

After the main characteristics of viscous flow discussed, shear stress, separation, and aerodynamic heating, the flow can be classified into laminar and turbulent flow. Assume viscous flow over a body as sketched in Figure (2.5). Insert (a) shows steady and smooth streamlines, while

insert (b) shows unstable flow. The first is laminar flow and the second is turbulent flow.

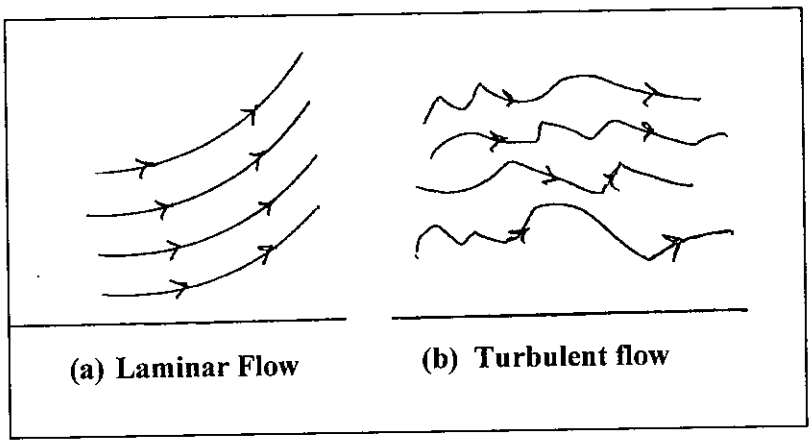


Figure (2.5): Turbulent and Laminar Flow Streamlines

The irregular motion of flow particles in turbulent flow pumped the flow close to the surface, causing an increase in the flow velocity compared to the laminar flow.

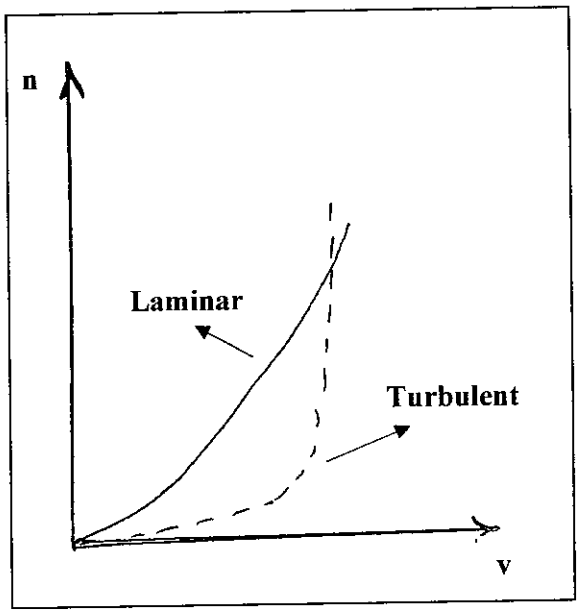


Figure (2.6): Velocity Profiles for Laminar and Turbulent Flows

Figure (2.6) depicts the velocity profile comparison between the laminar and turbulent flow. The turbulent flow velocity gradient at the surface compared to the laminar flow can be depicted as follow:

$$\left(\left(\frac{\partial V}{\partial n}\right)_{n=0}\right)_{turbelent} > \left(\left(\frac{\partial V}{\partial n}\right)_{n=0}\right)_{laminar} \quad (4)$$

Due to this contrast, the turbulent flow produces more frictional force and aerodynamic heating than the laminar flow. Nevertheless, a valued advantage counted to the turbulent flow over the laminar flow in that the flow does not separate from the adjacent surface effortlessly as laminar flow. Moreover, the separated region will be more diminutive if it has occurred. Then less D_P for turbulent flow obtained.

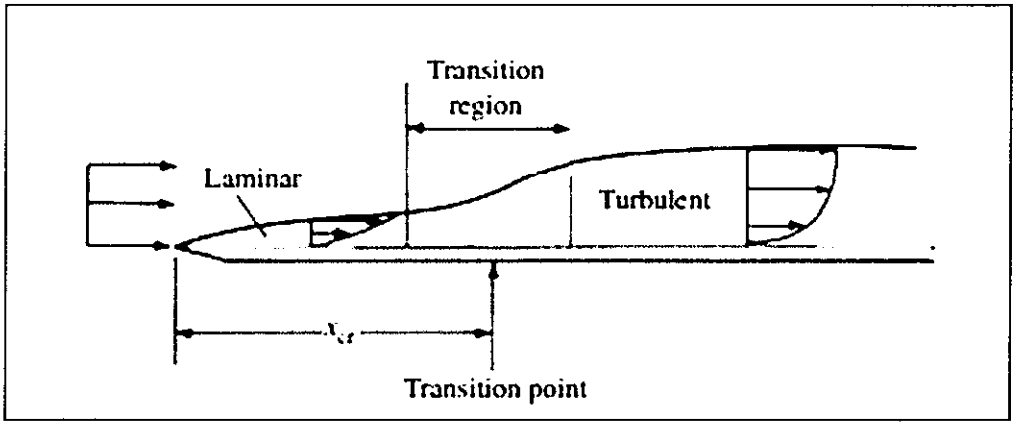


Figure (2.7): Transition of the Flow from Laminar to Turbulent on a Flat Plate (Anderson J. D., 2017)

The flow transition from laminar to turbulent cannot comprehensively controled. However, generally, the flow adjacent to the body's surface initiates laminar in the upstream region, as portrayed in Figure (2.7) and converts through the transition region because of the effect of the friction force, which retard the flow as proceeding downstream.

After some distance, the serenity of the laminar flow alters the flow into turbulent flow. Therefore, this region is simplified into a transition point between upstream laminar flow and downstream turbulent flow denoted by x_{cr}. The value of x_{cr} depends on features that promote the flow to translate from laminar to turbulent and then bring x_{cr} upstream toward the leading edge. The factors influencing the flow transition are:

1- Augmented surface roughness stimulates turbulent flow over the body. Laying rough grit on the surface can trigger the laminar flow to become turbulent flow prematurely.
2- Augmented turbulence in the freestream, especially in wind tunnels, may significantly modify the transition point location

3- Negative pressure gradients instigate the transition to turbulent flow early as the flow separates too.
4- Heating of the fluid by the surface if its temperature is higher than the flow, which encourages the laminar flow to change to turbulent flow. In contrast, a colder wall favors laminar flow.
5- High values of Mach number M_∞ and low values of Reynolds number Re tend to maintain laminar flow. Hence, for hypersonic flow, the laminar flow is extensive. Referring to Figure (2.7) is monopolizing factor in the flow transition from laminar to turbulent on a flat plate. Critical Reynolds number Re_{cr} defined as:

$$Re_{cr} \equiv \frac{\rho_\infty V_\infty x_{cr}}{\mu_\infty} \tag{5}$$

The value of $Re_{cr} \approx 500{,}000$. If the Re of the flow is nearby below it, it is considered a laminar flow. Moreover, the flow considered a turbulent flow if Re is higher than 500,000 (Anderson J. D., 2017).

2.4 Solutions to Viscous Flows

The continuity equation, momentum, and energy equations govern the viscous flow for a general unsteady, compressible, viscous, three-dimensional flow.

2.4.1 Continuity Equation

This equation expresses the movement of finite fluid. It typically covers the three-dimensional, unsteady flow of all flow types; inviscid or viscous, compressible, or incompressible and is expressed by:

$$\frac{\partial \rho}{\partial t} + \nabla.(\rho V) = 0 \tag{6}$$

2.4.2 Momentum Equation

The momentum equation depicts the law of conservation of momentum for moving fluid. The rate of change of momentum of any micro-unit in the flow field is identical to the equivalent summation force of all external forces acting on the micro-unit. The force exerted by the fluid can be calculated using Newton's 2nd Law. The force is equal to the rate of change of momentum (Munson & Roy, 2013). So, Force = rate of change of momentum The following formulas represent fluid momentum (Singirsu, 2018):

$$F = \dot{m}\,(u_2 - u_1) \tag{7}$$

$$F = Q\rho(u_2 - u_1) \tag{8}$$

where $\dot{m}$ is mass flow rate, u is velocity of the fluid, and Q is u*A

2.4.3 Viscous Flow Equations

Navier-Stokes equations are partial differential equations fetched from momentum equation. The following equations are a general state of unsteady, compressible, three-dimensional viscous flow:

$$\rho\frac{\partial u}{\partial t}+\rho u\frac{\partial u}{\partial x}+\rho v\frac{\partial u}{\partial y}+\rho w\frac{\partial u}{\partial z}=-\frac{\partial p}{\partial x}+\frac{1}{Re}\left[\frac{\partial \tau_{xx}}{\partial x}+\frac{\partial \tau_{xy}}{\partial y}+\frac{\partial \tau_{xz}}{\partial z}\right] \quad (9)$$

$$\rho\frac{\partial v}{\partial t}+\rho u\frac{\partial v}{\partial x}+\rho v\frac{\partial v}{\partial y}+\rho w\frac{\partial v}{\partial z}=-\frac{\partial p}{\partial y}+\frac{1}{Re}\left[\frac{\partial \tau_{xy}}{\partial x}+\frac{\partial \tau_{yy}}{\partial y}+\frac{\partial \tau_{yz}}{\partial z}\right] \quad (10)$$

$$\rho\frac{\partial w}{\partial t}+\rho u\frac{\partial w}{\partial x}+\rho v\frac{\partial w}{\partial y}+\rho w\frac{\partial w}{\partial z}=-\frac{\partial p}{\partial z}+\frac{1}{Re}\left[\frac{\partial \tau_{xz}}{\partial x}+\frac{\partial \tau_{yz}}{\partial y}+\frac{\partial \tau_{zz}}{\partial z}\right] \quad (11)$$

Incompressible viscous flow formulas employ Navier stokes Equations (9, 10 and 11) and the continuity equation (6). However, for compressible flow, the energy equation should be counted. Navier-Stokes equations deliver an exact solution for laminar flow. The turbulent flow parameters in equations (9,10, and 11) can be assumed to be time-mean values over the turbulent oscillations and substitute μ by $\mu + \varepsilon$.

Viscous flow equations can be employed to acquire practical outcomes in the following approaches (Anderson J. D., 2017):

1. There are very few viscous flow geometrical conditions that can use Navier-Stokes solution to get an exact solution or precise solution to downsize the equations. These solutions examples are Couette flow and Poiseuille flow.
2. The viscous flow equations can be simplified by selecting boundary conditions to neglect many parameters. Nevertheless, the solutionwill be obtained if we carefully choose the boundary conditions as an approximate solution, not an exact solution.
3. The solution can be fulfilled of the equations by using modern computational fluid codes that use advanced algorithms to obtain exact solutions.

2.5 Boundary Layers

The boundary layer is a narrow flow region adjacent to the surface, where the flow is retreated due to friction between the flow and the surface.

The boundary layer is skinny compared to the body's surface but significantly contributes to flow characteristics such as drag and heat transfer. Figure (2.8) depicts velocity at the surface where there is no-slip condition is $V = V_w = 0$ and gradually rises until it reaches free stream velocity at the outer edge of the boundary layer, which called velocity boundary layer height δ to be $V = V_\infty$. The temperature T at the wall is also $T = T_w$ and reaches the outer flow temperature at a vertical distance dubbed thermal boundary layer δ_T. In general, $\delta_T \neq \delta$. That depends on Prandtl number P_r. When P_r=1 $\delta_T = \delta$, but for air P_r=0 at $\delta_T > \delta$.

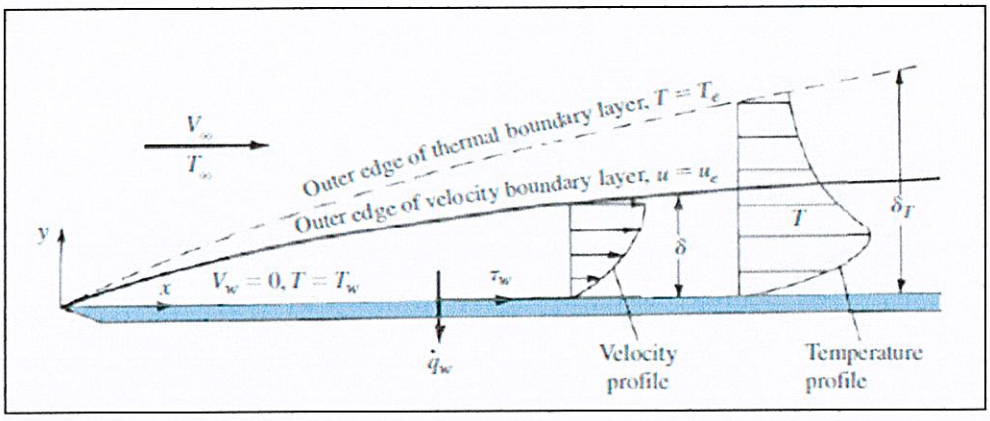


Figure (2.8): The Boundary Layer Thickness on Flat Plate (Anderson J. D., 2017)

2.5.1 Laminar Boundary Layers

For incompressible laminar flow over a flat plate, the boundary layer is simplified into equations and consolidate them into one equation named the Blasius equation:

$$2f''' + ff' = 0 \qquad (12)$$

where $f' = \frac{u}{u_e}$. Where u is the inner boundary layer's velocity, and u_e is the outer boundary layer's velocity. A numerical solution for the equation

delivers these results, which can precisely describe the flow properties inside the laminar boundary layer as follow:

Local skin friction coefficient c_f:

$$c_f = \frac{\tau_w}{\frac{1}{2}\rho_\infty V_\infty^2} = \frac{0.664}{\sqrt{Re_x}} \tag{13}$$

Integrated friction drag coefficient:

$$C_{Df} = \frac{1.328}{\sqrt{Re_c}} \tag{14}$$

Boundary layer thickness:

$$\delta = \frac{5.0x}{\sqrt{Re_x}} \tag{15}$$

2.5.2 Turbulent Boundary Layers

Getting an exact solution for the turbulent, incompressible flow over the plate takes much work. empirical relations show that;

Integrated friction drag coefficient:

$$C_{Df} = \frac{0.074}{\sqrt{Re_x^{\frac{1}{5}}}} \tag{16}$$

Boundary layer thickness:

$$\delta = \frac{0.37x}{\sqrt{Re_x^{\frac{1}{5}}}} \tag{17}$$

2.6 Surface Roughness

Roughness, as a terminology, in aerodynamics, has a broad meaning covering all types of irregularities and imperfections as well as rough paint,

grooves, waves, insects, rivets, excrescences, and the like. Surface roughness affects lift and drag forces and, consequently, airfoil lifting efficiency. They also change the roughness area and location and impact the airfoil stall angle (Schlichting & Gersten, 2016). For wings, the roughness of the surface usually occurs from natural phenomena such as ice, frost, snow, ageing from a long time in service, or pitting due to sandstorms. Due to their roughness and shape on the airfoil, rain and ice yield many accidents yearly (Finnigan & Gersten, 2000).

Among large-scale parameters that influence the aircraft during take-off or landing, such severe parameters include crosswind, wind shear, heavy rain, runway accumulated water or ice, and bird strikes. In these anticipated flying conditions, accidents frequently happen as the time is insufficient for the aircraft to recover velocity or altitude for safe operation. Due to this reason, attention should be paid to the methodology that the flight environmental contribution can influence aircraft performance during various flying regimes, particularly in take-off and landing. Numerous examples consider that surface roughness plays a curious role in the operation and performance of all aeronautical systems (Rauparch & Thom, 1981).

2.6.1 Effect of Wall Roughness

Turbulent boundary layers are sensitive to wall roughness, specifically at high Reynolds numbers. This sensitivity is because of the roughness element that may stand out through the viscous sublayer modifies the smoothness of the wall. The impact of wall roughness on the boundary layer relies on the roughness elements' dimensions, shape, and spacing. (Nikradze, 1950) matched every type of roughness against a

similar sand-grain roughness having a roughness of height ks. As V_* is friction velocity obtained by:

$$V_* = \sqrt{\frac{\tau_w}{\rho}} \tag{18}$$

Moreover, kinematic viscosity is derivative of dynamic viscosity:

$$\nu = \frac{\mu}{\rho} \tag{19}$$

Nikradze classified these roughness heights into three cases:

1- Hydraulically smooth: If $\frac{k_s V_*}{\nu} \leq 5$, the roughness elements lie completely inside the viscous sublayer; the roughness will not impact the velocity profile, skin friction, or drag.

2- Completely rough If $\frac{k_s V_*}{\nu} \geq 50$, the roughness elements interfere with the wholly developed turbulence. Therefore, the local skin-friction and drag coefficients are independent of Reynolds number and are given by

$$Cf = (2.87 + 1.58 log_{10}\left(\frac{x}{ks}\right))^{-2.5} \tag{20}$$

$$CDf = (1.89 + 1.62 log_{10}\left(\frac{L}{ks}\right))^{-2.5} \tag{21}$$

3- Transitional roughness If $5 \leq \frac{k_s V_*}{\nu} \leq 50$, the surface roughness affects both local skin friction and drag coefficients, which they depend on both Reynolds number and relative roughness ks/δ.

The degree of roughness is considered reasonable in engineering research if the surface remains hydraulically smooth along the surface of contact. The roughness element's height may remain within the boundary layer along the trailing edge.

The expression of the aerodynamic effects of a surface utilizing sand-grain roughness needs to be more precise. It is mandatory to remember that the aerodynamic effects of a specific type of roughness may be distinguishable from the sand-grain roughness scale of the same size (Houghton, Carpenter, Collicott, & Valentine, 2013).

2.6.2 Wind Farms Blade Roughness

Wind farms experience underperformance compared to the manufacturer's predictions, and performance drops over time. This phenomenon happens because capacity factors usually overestimate 10% to 15% (Boccard, 2009). The only possible aerodynamic reason is the blade roughness due to erosion, foreign deposits (such as insects), and coating. All these factors diminish performance by diminishing section maximum lift and raising drag (White et al., 2011). Hagen investigated Turbulent flow fields over rough surfaces (Hagen, 1854), and Darcy (Darcy, 1857) performed early works regarding pressure changes in water conduits. Experimental proof regarding turbulent flows over rough walls revealed that there are two critical parameters: the roughness Reynolds number, which reckons the roughness effect on buffer layers, and the ratio of the thickness of the boundary layer to the height of roughness (Raupach, Antonia, & Rajagopalan, 1991) (Jime'nez, 2004).

2.6.3 Effect of Frost on Airfoil Upper Surface

Many scientists have investigated the aerodynamic effect of roughness on wings and aircraft performance. Ljungstroem (Ljungstroem, 1972) investigated the effect of frost on the upper surface on two-

dimensional airfoils performance experimentally. Although these airfoils got high-lift devices, Ljungstroem investigated only the upper surface and leading-edge frost. Bragg and Gregorek (BRAGG & GREGOREK, 1989) studied the effect of roughness due to several different sources for laminar flow airfoils, including specific considerations of the overall aircraft performance, but only they considered leading-edge roughness. Brumby (Brumby, 1991) proposed a correlation of roughness consequences for maximum lift considering only the upper surface as well as leading-edge roughness. Valarezo (Valarezo, Lynch, & McGhee, 1993) performed investigations for high Reynolds numbers about the performance effects of frost formed on upper surface simulations.

2.6.4 Effect of Frost on Airfoil Lower Surface

Dietenberger (Dietenberger, 1983), along with van Hengst and Boer (Hengst & Boer, 1991), used empirical methods based on experimental data as an infusion to computational take-off analysis to study the effect of frost (roughness) on take-off performance of an aircraft. Under different flight situations, the fuel in wing tanks (at lower surfaces) reaches low temperatures. The fuel, in this case, is often called" cold-soaked." After landing, the remaining fuel in the tanks may cool the wing's lower surface to below freezing. The involved wing area depends on the location of the wing tank, the fuel temperature, the amount of fuel remaining, and the wing structure design. If the humidity at ground level is high, moisture in the air condenses on aircraft wings near the cold fuel forming frost. Ice may also develop if the frost melts partially, and the resulting water streams toward the fuselage and freezes in the case of wing dihedral (Bragg, Heinrich, Valarezo, McGhee, & McGhee, 1994).

2.6.5 Surface Roughness influence

The parameterization process of roughness is one of the many hurdles encountered in surface roughness influence investigations. Roughness definition is generally as random or uniform.

i. Heat Transfer

Sheldahl (Sheldahl & CKlimas, 1981) showed that applying roughness to the airfoil surface causes the heat transfer to increase downstream of the stagnation region.

ii. Reynolds Number

Achenbach (Achenbach, Influence of surface roughness on the cross-flow around a circular cylinder, 1971) performed wind tunnel experiments on cylinders wrapped with sandpaper around their perimeter and found that this causes a much quicker thickening of the boundary layer by increasing the Reynolds number. Additionally, he (Achenbach, 1974) showed that reducing the critical Reynolds number increases the roughness element's size. In particular interest, by increasing the Reynolds number, the transition and separation points move upstream, consequently increasing the drag. Also, Sheldahl (Sheldahl & CKlimas, 1981) indicated that surface roughness increases the subsequent flow Reynolds number beyond the critical value. Generally, boundary layer thickness becomes thinner with increasing Reynolds number drag coefficient and Strouhal number change. The Strouhal number is defined as St = fstD/U, where fst is the vortex shedding frequency (or the Strouhal frequency) of a body at rest, D is the diameter of the circular cylinder and U is the velocity of the ambient flow.

iii. Roughness Location

Bloch and Miller (Bloch & Mueller, 1986) tested rough airfoils at low Reynolds numbers. They concluded that roughness distribution caused the separation bubbles to shift forward, which changed the airfoil's aerodynamic characteristics. When Under-wing frost exists forward enough to influence the boundary layer at the upper surface, it shows its most significant influence on airfoil performance (Bragg, Heinrich, Valarezo, McGhee, & McGhee, 1994).

iv. Lift and Drag

Chakroun (Abdel-Rahman & Chakroun, 1997) investigated the effect of various surface roughness at a low chord Reynolds number on drag and lift coefficients for a flapped airfoil (NACA 2412). Later, Abdel-Rahman and Chakroun (Abdel-Rahman & Chakroun, 1997) announced that the pressure difference between the airfoil's lower and upper surfaces rises by increasing surface roughness, especially near the leading edge. Roughness results in a slight lift decrease and a gradual drag increase. Nonetheless, roughness increases the lift in the stall region. Finally, Chakroun (Chakroun, Al-Mesri, & Al-Fahad, 2004) performed experimental testing on NACA 0012 to realize the influence of surface roughness location and size on the airfoil aerodynamic characteristics. They observed that roughness location influences the minimum drag value. Also, applying surface roughness at the leading edge increases the lift near the stall region and the stall angle.

NACA has experimented (Hood, 1939) to measure the increase in drag coefficient provoked by rivet heads in wings compared with smooth wing drag (no rivets). The results showed that using rivets with the most miniature practicable heads is desirable. Also, the adequate method for

reducing rivet drag is by eliminating the rivets from the wing forward part. Figure (2.9) displays the significance of this way.

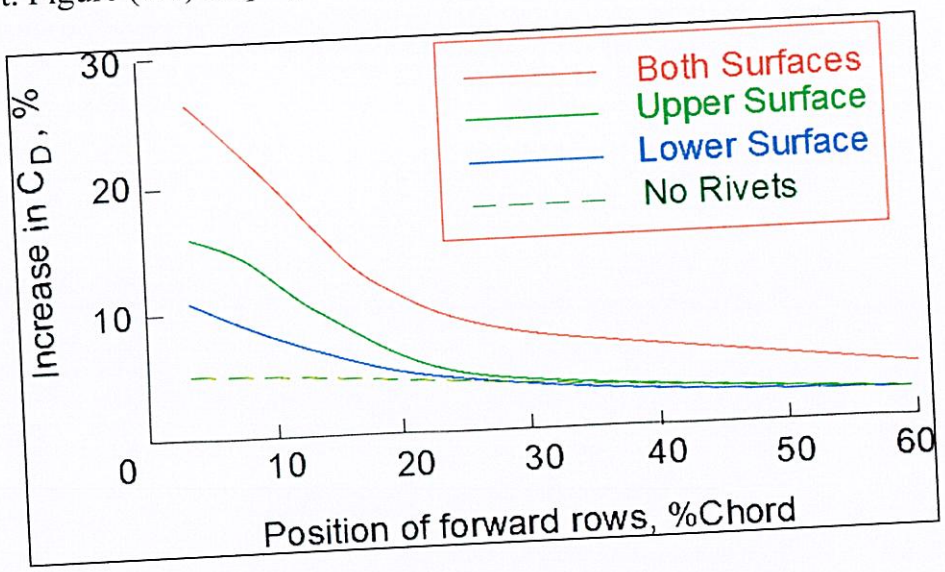


Figure (2.9): Variation of Rivet Drag Relative to Position of Forward Rows (Hood, 1939)

Haosheng carried out an experiment using a rotary rheometer with notched grooves in longitudinal, transverse, and isotropic directions to examine the patterns of the surface roughness effect. The experiment results showed that higher drag force occurred in the case of transverse grooves analogised with smooth surfaces, while lower drag force appeared in the case of longitudinal grooves. The drag force in the case of isotropic grooves was between them (Haosheng, Darong, & Yongjian, 2006).

2.6.6 Roughness Model Implementation

i. Approach Methodologies

Two methods of approach to the methodology are roughness, which creates drag: no separation flow fields and slight local separations flow

fields. The second flow field is much more noteworthy because the flow fields without separation lead to only minor drag increases (Smith & Kaups, 1968).

ii. Moody Diagram

It is an applicable engineering method developed by Nikuradse (Nikuradse, 1950), Colebrook (Colebrook et al., 1939), and Moody (Moody, 1944) to predict frictional losses in pipes. The Moody diagram is still prominently applied in undergraduate studies and utilized by practising engineers even 75 years after its development. However, its use requires determining an equivalent roughness height for the studied surface and the physical roughness scale for uniform, close-packed sand (Flack, Schultz, & Volino, 2020).

iii. Overflow

Overflow is a structured flow solver overset (CFD) based on Reynolds-averaged Navier Stokes. It is very robust and comprehensive, permitting the selection of various turbulence models, numerical schemes, boundary conditions, and time advancement schemes (Beam & Warming, 1978).

iv. Bowyer's Grid Generator

Bowyer's scheme is generally a point-adding method that delivers the boundary points (inner and outer boundary points). Then by using these points, initial grids are generated and added to circumscribed circle centre of the triangles that do not conform to the specified conditions and delete those that do not fit the circle criterion. Outward usable edges are

found, erasing edges and triangles that do not fit the specified conditions, and new triangles are locally regenerated.

v. Multi-Domain Spectral Difference Method

The method utilizes the three-dimensional nonlinear compressible Navier–Stokes equations in the conservation form as the governing equations. Then all physical segments in the governing equations are transformed into standard cubic elements to achieve an efficient implementation. The solution points and the flux points appear as two sets of points defined in the standard element. After using the conserved variables at the solution points, the conserved variables translated at the flux points and computed the inviscid fluxes at the interior. The method calculated inviscid flux and definitive viscous flux at element interfaces. After that, they obtained the fluxes derivatives at all the solution points, and the DOFs were Updated using a multistage total-variation-diminishing scheme for time integration (Zhou & Wang, 2011), (Zhou & Wang, 2012). (Latin & Bowersox, 2002) Similar CFD solvers have developed over time, such as the Riemann solver (Latin & Bowersox, 2002), the Roe solver (Roe, 1981), and the Russanov solver (Sun, Wang, & Liu, 2006).

2.7 Literature Review

An experimental study concerning the effect of surface roughness on aerodynamic characteristics is under review. Controlling the flow separation is a prominent aerodynamic concern, especially at low velocities. Andreas Hövelmann et al. (Hövelmann, Knoth, & Breitsamter, 2016) revealed a relationship between flow separation onset and surface roughness. They examined a 53-degree leading-edge sweep diamond wing configuration with a rounded leading-edge contour to monitor and control

the onset of flow separation by spreading different roughness to the leading edge to trigger the boundary layer. They went through an experimental approach using a wind tunnel at low speed to examine flow separation to correspond with the CFD model based on fully-turbulent Reynolds–Averaged Navier–Stokes (RANS) equations. They referred to aforesaid experimental and numerical investigations, which demonstrate a delay in the vortex formation with augmenting leading-edge bluntness. They observed the same behavior for high Reynolds number, Mach number, and leading-edge sweep. As a result, they validated the flow separation onset. They performed the experiments in the Göttingen-type low-speed wind tunnel W/T facility A of TUM-AER in Germany. The maximum speed of the wind tunnel is 65 m/s. They performed uncertainty calculations to ensure precision and that all atmospheric conditions were within limits. They designed an aluminum alloy model, and all sensors and pressure controllers were installed, including aerodynamic forces and moments sensors. After that, they applied different surface roughness on the leading edge with different angles of attack. The results highlight that the flow separation onset and consequences leading edge vortex are sensitive to the surface roughness height and the contour alignment and shape at the diamond wing leading edge. These outcomes open the door to handling the onset of the boundary layer separation to oversee specific characteristics for this type of wing and other wing geometries. This study's disadvantage is concentrating only on low velocities and low Re, then comparing it to a fully turbulent CFD model.

Another experimental study raised attention to the aerodynamic stall delay and controlling the effect of disturbance wake (Zhang Y., 2018). He used two roughness patterns: Aligned and staggered, with two roughness heights of k=0.25mm and k=0mm. The large k will lay outside the

boundary layer, while the small k will lay inside the boundary layer. He manufactured a tape with a height of $\sim 0.1mm$ and stuck it on the mentioned airfoil, with a maximum thickness of 17% chord length and a maximum camber of 2.4% at 65% chord. This airfoil features a sizeable leading edge which fosters a higher lift and a gentler stall characteristic compared to NACA 65 series. He ran the experiment at three different low Re values: 78000 (11m/s), 16900 (24 m/s) and 260000 (37 m/s). He computed the boundary layer thickness using the formula $\frac{0.37x}{Re_x^{0.2}}$ to get the boundary layer height $\delta \sim 0.36mm$. His experimental study relies on Surface pressure and particle image velocimetry (PIV) picturing system. He runs the test at ten different angles of attack from 0° to 18° under specific temperature, humidity, and pressure conditions. Yan Zhang extrapolated that applying roughness enriches the drag and diminishes the lift. Also, more influential roughness advances the aerodynamic stall, but minor roughness precludes deep stalls. Finally, PIV results declared that a staggered distribution pattern induces higher pulses of weak distribution than aligned patterns, especially at high angles of attack.

Then moved to a numerical study that elaborated the fundamentals of numerical validation of aerodynamic models, which assisted us in generating our numerical CFD model setup as explained in chapter three of Caryroglua and Kilicb (Cayiroglua & Kilicb, 2017). They assumed that the designing process, aerodynamic and structural analysis were crucial to obtaining maximum lift, minimum drag, and high stall performance. At the same time should be light, robust, and resist vibrations. In this paper, optimization of the wing aerodynamic analysis of an airplane was the main objective. They conducted wing simulation with the Ansys-Fluent program using with built-in genetic algorithm. The design was written in Python, inside the Ansys-Workbench and assisted by JavaScript and Journaling.

The developed method, as they stated, can be used in various design applications. In the optimization process, one cycle of the design process consists of five stages: Generation, evaluation, selection, crossover, and mutation. The generation of genes is automatic to a solid geometric model inside the Design Modeler, and then they are meshed in the Mechanical Modeler according to the given criteria. Boundary conditions apply in the Fluent module and then run to get the solution. Python code then reads the results; if they are not converged, the analysis process runs again with the modified program-controlled gene. Finally, the objective function is set, which describes the output design and considers the constraints which vary according to the aircraft type and critical aerodynamic parameters.

The designing process pays attention to the structure and the loads affecting the aircraft, including the vibration phenomenon. Tawfiq Khatir et al. (Khatir, Djillali, Khatir, Abdelkader, & Wahab, 2017) investigated the non-damped oscillations on aircraft's wings named flutter. The generation of oscillations occurs at specific velocities, which can destroy the structure. Floating is a fatal consequence of flutter and usually ends with plane rupture. It identifies a dynamic instability of the structure. The flutter phenomenon often occurs due to an interaction between aerodynamics, elasticity, and inertial forces. It appears at a certain velocity of flight called critical floating speed. This study seeks to decide whether an aircraft is floating at critical velocity experimentally and numerically using the Finite Element Analysis package ANSYS CFX. The experimental outcomes are in good agreement with those obtained numerically. They found that the amplitude of the second vibration mode is more destructive and severer than the first mode. The critical flutter speed decreases with the increasing angle of attack. Above the critical

speed, the amplitudes of vibrations lessen. So, they identified critical speed considerations in designing the wings to avoid fatalities.

As discussed earlier in this chapter, the changeover in roughness can be obtained naturally or by designing roughness patterns. The natural surface roughness due to ice creation, rain, frost, and dust is hazardous and may cause accidents. In contrast with designated roughness, the natural roughness appearance is unpredictable. Most of the investigations were experimental and hardly linked to each other because of differences in circumstances and test conditions. However, by developing numerical methods using digital codes and massive software, prediction models appeared to be close to reality. Yihua Cao et al. introduced controlled models with specific boundary layers and obtained encouraging results (Cao, Ma, Zhang, & Sheridan, 2012) designed a model which simulates various ice accretion types and stages using the Euler flow computation model. Several codes for simulating ice accretion have originated internationally, such as LEWICE (USA), CAPTA (France), TRAJICE2 (UK), FENSAP-ICE (Canada), and MULTIICE (Italy). They split the numerical simulation of ice accretion into four modules: air flow field solution, droplets collection, efficiency calculation, boundary layer characteristics evaluation and finally, ice amount evaluation via thermodynamic model. They demonstrated the ice accretion phenomenon and the interface with boundary layer properties in three major areas:

1- Roughness on an iced surface: The roughness on the iced surface is irregular, and the accretion process was difficult to predict. Simulating the process and obtaining the roughness precisely in numerical simulation of ice accretion is challenging. The equivalent sand-grain roughness was devoted to describing the roughness effect. The surface

roughness for equivalent sand grain roughness formulated from the experimental data:

$$ks = 0.0008C.(0.047.T_C - 11.27).(0.5714 + 0.2457.LWC + 1.2571.LWC^2 \quad (22)$$

where c denotes the airfoil chord, and T_c denotes the ambient temperature. While L is the average height of the roughness and W is the average width.

2- Thermodynamic model: The thermodynamic model from the Messinger model is accredited by most ice accretion codes and evaluated through the balance of mass and energy values.

3- Prediction of ice shape: For airfoils, the following formula calculates the ice volume in every iced control volume mathematically :

$$V_{ice} = \frac{\dot{m}_{ice}.\Delta T}{\rho_i} \quad (23)$$

where ΔT is the time step, ρ_i is ice density, and $\dot{m}_{ice}$ are the mass flow rate of the ice.

Yihua Cao et al. expressed the ice amount and the ice shape after a time step, assuming that ice builds in the direction perpendicular to the airfoil surface. However, the airflow field is altered simultaneously as the airfoil shape evolves by ice accretion. Therefore, the airflow field requires to be solved again. For wings, the rime ice accretion is simulated using the assumption that the water droplets immediately freeze when they touch the wing surface. In 3-D application, the ice volume can be calculated as:

$$V_{ice} = \frac{LWC.v_\infty.\beta.\acute{A}\Delta T}{\rho_i} \quad (24)$$

where the symbol Á denotes the impingement area of a 3-D control volume.

Yihua Cao et al. extrapolated that using Euler numerical model for NACA 0012 airfoil and a GLC-305 wing model could effectively simulate the droplet impingement on the iced surface with specific wall conditions

that resulted in numerical computation of the droplet flow field. The heat transfer coefficient on the iced surface is assessed using the modified Messinger model to sidestep a complete N-S equation solution. They ascertained that Ice accretions deteriorate the designed aerodynamic shapes of the airfoil and wing. Finally, the deformed aerodynamic shapes yielded by glaze ice are more severe than that of rime ice.

Walid Chakroun, Issa Al-Mesri and Sami Al-Fahad (Chakroun, Al-Mesri, & Al-Fahad, 2004) executed an experimental examination to understand the effect of surface roughness size and location on the aerodynamic characteristics of NACA 0012 symmetrical airfoil. Their examination aims to investigate the impact of surface roughness on lift, drag and stall angle by adjusting the roughness type and location on the wind turbine blade's aerodynamic characteristics. This examination was conducted on roughness sizes; smooth, 200 μm roughness, 500 μm roughness and wire roughness of 2 mm diameter distributed along the upper and the lower surfaces of the airfoil at 1 cm distance from each other in the region $0° < \alpha < 10°$ Where α is the angle of attack. They found that leading-edge roughness provides higher drag than trailing-edge roughness when applying the roughness to both airfoil sides. They also found that the lift coefficient is influenced by surface roughness location. As the applied roughness moved toward the trailing edge, the stall behavior enhanced, and a high lift was obtained up to the stall angle; it delayed the stall condition in some cases. Nevertheless, because of the high upsurge in drag, the optimum performance of the wind turbine can be obtained by a smooth surface. Finally, they uncovered that the boundary layer thickness (δ) of rough surface is thicker than the smooth surface.

Mingyang Wang et al. (Wang, Lu, Yang, Zhao, & Zhang, 2021) disseminated a numerical study about surface roughness's effect on

compressor airfoil aerodynamic performance at low Reynolds number Re = 1.5 -105. Four roughness locations were applied, covering 10%, 30%, 50%, and 100% of the suction surface from the leading edge and seven roughness values from 52 to 525 μm. Results demonstrated that the surface roughness magnitude regulated the loss efficiency of the airfoil by triggering the structure of the Laminar Separation Bubble LSB and the turbulence level near the wall. For all the roughness locations, the variation trend for the profile loss led to a maximum decrease of 14.6%, 16.04%, 16.45% and 10.20% in the profile loss at k = 157 μm for the four roughness locations, respectively. This effect amplifies the wake and produces a more substantial turbulent flow region. However, the growth of the turbulent boundary layer was enhanced, and the compressor airfoil's aerodynamic performance deteriorated. Controlling the surface roughness leads to controlling boundary layer development and improving airfoil performance significantly at low Re. Surface roughness control can be applied to fixed wings, whereas the turbulent boundary layer is desirable in high Re flight regimes.

To manufacture a prototype airfoil, there is a need to get adequate surface roughness using a 3-D printer. O. Gülcan, K. Günaydın, and A. Çelik (Gülcan, Günaydın, & Çelik, 2022) experimentally ascertained that the direction of printing the airfoil has an immediate effect on surface roughness finishing values of airfoil geometries printed in PolyJet 3-D printer. The numerical part of the study focused on the aerodynamic performance of those printed in different velocities and angles of attack. They found that airfoil printing in the X direction will deliver smoother surface roughness than in the Y direction. Therefore, they proposed printing the airfoil horizontally for lower irregularities and a better surface finish. Furthermore, they found that the higher roughness of vertically

printed models produced in PolyJet for fixed-wing UAV wings affects the drag coefficient by 7.5% at high-velocity cruises. These outcomes supported our hypothesis of the consequence of surface roughness in the means of production but did not investigate the corresponding effects on aerodynamic characteristics.

The surface roughness with Reynold number Re effect governs the transition of the boundary layer from laminar to turbulent. In order to comprehend this transition and control it, referred to S. Özçakmak et al. (Özçakmak et al., 2018) study that embroidered on the relationship between surface imperfections and wind turbine aerodynamic performance. The experimental study carried out on the DAN-AERO wind tunnel for NACA 63-418 airfoil was used. Under the pre-set operating condition, Reynolds numbers, turbulence grid and boundary layer control devices, the results demonstrate a high correlation of the transition process on these parameters. The analyses reveal that rising leading edge roughness moves the stagnation point upstream. Also, the transition location moves more proximate to the leading edge with increasing Re when the roughness height is smaller than the critical roughness height. They stated that inflow turbulence has a more significant effect (experimentally) on the transition location than the numerical results.

M. Costes and F. Moen performed numerical research on the numerical simulation model for ice accretion on aircraft wings (Costes & Moens, 2019). The paper suggests a numerical investigation of simulated flow around a NACA 23012 airfoil with two ice patterns, a spanwise ridge and leading-edge roughness. Reynold Averaged-Navier Stokes RANS and Unsteady Reynold Averaged-Navier Stokes URANS simulations with various turbulence models (Spalart-Allmaras, Menter SST, EARSM, DRSM) for a specific range of the airfoil polar. The developments are

verified experimentally in the ONERA F-1 wind tunnel. The Spalart-Allmaras model is the only RANS model converged in all flow conditions. Also, DRSM provides a precise prediction of performance degradation due to ice accretion. These numerical methods provide us with a prediction of flow behavior, which is mandatory to identify the aerodynamic parameters of the airfoil.

A numerical validation explained the mechanism of vortex shedding of a high roughness cylinder in the below critical flow regime ($Re \approx 10^5$). A. Bimbato, L. Alcântara Pereira, and M. Hirata (Bimbato, Alcântara Pereira, & Hirata, 2019) used a mesh-free vortex method with local turbulence effects during the vorticity diffusion process. Simultaneous measurements of the aerodynamic forces and time-averaged local surface are investigated to reach the above-critical Reynolds number flow patterns from below-critical flows. A clear relation between surface roughness and aerodynamic forces was verified.

Y. Liu, K. Zhang, K. Tian, and H. Hu (Liu, Zhang, Tian, & Hu, 2020) conducted an experimental study to evaluate the effects of surface roughness formed around the leading edge of an airfoil model due to ice accretion over the airfoil surface. Two identical airfoil models were manufactured. One model had embedded ice roughness, and the other had a smooth airfoil leading edge. A high-speed and infrared (IR) thermal imaging system was used. The airflow characteristics and heat transfer process were affected due to changing the roughness reportedly.

The sensitive roughness height is further detailed in a numerical study on the S834 airfoil from National Renewable Energy Laboratory. The results of the lift and drag with the smooth or rough surface using *the* $K-\omega$ SST turbulence model were affirmed experimentally. Results

suggest that the sensitive roughness and the pressure surface are not correlated. The important outcome from the breakdown is that the lift coefficient and the maximum lift-to-drag $\frac{L}{D}$ ratio increase for the rough airfoil and reduce the sensitivity of the airfoil to roughness height for the modified blunt trailing edge model (Zhang, Wang, Zhang, Liu, & W., 2017)

Discrete roughness on wings influences the boundary layer. As the roughness height increases, the transition point of the boundary layer from laminar to turbulent shifts upstream. Kurz utilized Direct Numerical Simulations (DNS) in the laminar boundary layer region to ensure that the convective instability phenomenon minimizes when the flow disturbance level is low and advances to a higher level when the flow is disturbed for a limited time, and then flow remains turbulent (Kurz, B., & Kloker, 2015).

Zarketa-Astigarraga, A. et al. (Zarketa-Astigarraga, Penalba, Martin-Mayor, & Martinez-Agirre, 2022) discussed the flow behavior in critical Reynolds number Reflow. Experimental work was carried out on NACA 0021 airfoil to review lift, drag and moment forces in transitional Reynolds numbers. Airfoils operate in transition Re show extreme sensitivity to surrounding flow. Uncertainty calculation was carefully carried out and proved the difficulty of controlling Boundary Layer Separation in this situation.

A straightforward way to study the presence of roughness on an aircraft's wing experimentally called: the speckle method for measuring surface roughness. Using the angular speckle correlation technique (ASC), any surface irregularities can be detected and measured. Any change in surface regularity may compel erosion to the surface, especially in junction areas and leading edges (Salazar & Barrientos, 2013). Salazar and

Barrientos concluded that any increment in surface roughness would raise the parasite drag and loss in the momentum of the boundary layer. This study gives us a supplemental experimental technique for calculating the surface roughness height. A complete uncertainty deconstruction verified that the error was acceptable (Salazar & Barrientos, 2013).

Roughness height, naturally found, is not regularly distributed in patterns. However, conceived roughness heights are program controlled in CFD software design. Sand grain equivalent can substitute natural and artificial surface roughness in calculation with sand grain equivalent. Numerical, Experimental and Empirical methods are valid to predict the correct equivalent heights (Toth & Bobok, 2017) and (Adams & Grant, 2012).

Surface roughness can dramatically impact the fluid dynamics and heat transmission in convective flows. While surface roughness frequently has a detrimental impact on a system's performance, it may sometimes have a positive impact, like in convective flows where roughness components have been demonstrated to boost heat transfer. The main subjects of this study are the structure of the mean flow profile over rough surfaces and its relationship to the mean flow profile over smooth walls. Despite tremendous advancement, the research gathers that turbulent flow structure needs to be fully understood. This spectacle is a reason for the need for more systematic research on turbulent flow structure and the variety of roughness that affects the flow dynamics in roughness sublayers. In many instances, the present roughness scale (sand-grain roughness height) must accurately describe roughness. Therefore, a universal roughness scale is required, one that can be applied in rough and transitionally rough regimes and describes all types of roughness (Kadivar, Tormey, & McGranaghan,

A review on turbulent flow over rough surfaces: Fundamentals and theories, 2021).

2.8 Commentary on Literature Review

Previous studies elaborated on the correlation between surface roughness and the transformation in aerodynamic attributes. In addition, researchers emphasized the disadvantages of incrementing surface roughness, either naturally or artificially.

Naturally applied surface roughness occurs due to many causalities. The agreed resultant is the tribulation of prediction and the disturbed aerodynamic parameters near the flying object's surface. Consolidating on evaluating the negative effect of this roughness overcomes the utilization of the advantages. Many models are designed to predict this phenomenon numerically, employing mega software codes. The configuration of these codes varies regarding the intention of the flight and the test. The formal verification for this natural roughness is experimental with different wind tunnels or advanced picturing systems.

Designated surface roughness is the other trend in investigating the effect of aerodynamic aspects, which adopted in this study. Various patterns with different heights and locations are applied mainly to the leading edge of the airfoil, upper and lower surfaces simultaneously or only on the upper surface. CFD codes numerically simulated the flow behavior over the airfoil. Many numerical models based on different equations were chosen to simulate the precise aerodynamic parameters. Also, 2-D and 3-D wind tunnels are utilized to verify the results with specific boundary conditions and are gauged with different sensors. After that, the uncertainty calculations should keep the errors at adequate margins.

Researchers sought to study surface roughness's consequence to evaluate and specify the precise negative effect to eliminate and foresee it and then counter it if possible. During these studies, they discovered some positive reactions of the flow, summarized in; reducing stall speed and diminishing the wake and boundary layer separation. In contrast, raising the drag was a common disadvantage.

Benefited from previous investigations that it is possible to verify the results in numerical and experimental ways with reasonable accuracy. Furthermore, while reviewing past studies, focusing on the possible advantages of the surface roughness effect may lead us to enhance the aerodynamic characteristics of viscous flow instead of resisting it and eliminating it or limiting our studies to inviscid flow, which is unreal.

2.9 Research Hypothesis

Proof that applying designated surface roughness to the lower surface of a 2-D flying object (an airfoil: NACA4412) will enhance aerodynamic characteristics and improve flow properties. Despite the expected drag force increment, the lift force is expected to increase slightly due to the kinetic portion of Bernoulli's equation (Anderson J. D., 2005). Other characteristics, such as a lift-to-drag ratio, boundary layer separation and stall speed, are predicted to vary and will be observed.

Upon this hypothesis, low-cost designated rounded surface roughness can be applied at the lower surface of NACA 44the 12 Airfoil to get better aeraerodynamic characteristics.

Chapter Three
Methods and Procedures

3.1 Introduction

3.2 Flow Field Characteristics

3.3 Lift Theory

3.4 Geometry Selection

3.5 Numerical Approach

3.6 Experimental Approach

3.7 Experimental Procedures and Uncertainty

3.8 Summary

Chapter Three
Methods and Procedures

3.1 Introduction

As discussed earlier in chapter (2), surface roughness significantly impacts flow parameters and aerodynamic characteristics of flying objects. Early aerodynamic flight researchers trusted highly smooth surfaces to get the most reasonable aerodynamics. Then, researchers proclaimed that subsequent developments of surface roughness might be considered negative.

Adequate assigning flow parameters, verification methods, geometry selection and boundary conditions will smooth our pathway to get the optimum consequences with the most satisfactory accuracy.

This chapter will discuss our methodology to fulfil our theory by using central theoretical governing equations. In addition, a numerical solver, namely Ansys Fluent 2020 R1, and 2-D C-15 Wind Tunnel are employed to study the performance of the chosen airfoil. Figure (3.1) clarifies the methodological roadmap.

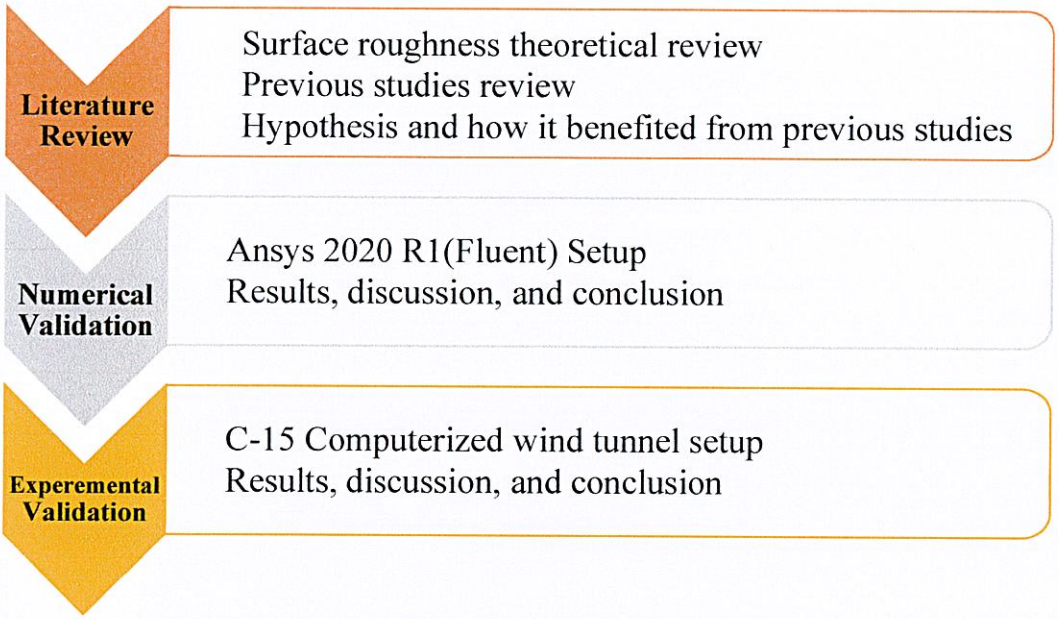


Figure (3.1): Methodology Process

3.2 Flow Field Characteristics

Enhancing aerodynamic characteristics translates into more extended ranges, longer durations, and better fuel consumption rates. The most prolonged flying regime in those flights is the steady flight phase. Most airplanes cruise at an altitude of between 30,000 and 42,000 feet (FINLAY, 2022). The reason is that at this altitude, the air density is very low $\rho \approx, 0.41369\ kg/m^3$, compared to the sea level value $of\ 1.22528\ kg/m^3$. Those flying conditions boost the aeroplane's speed and reduce fuel consumption. Figure (3.2) embellishes the cruising altitude evolution for significant transportation airplanes from 1938 to 2000 (Bahr et al.).

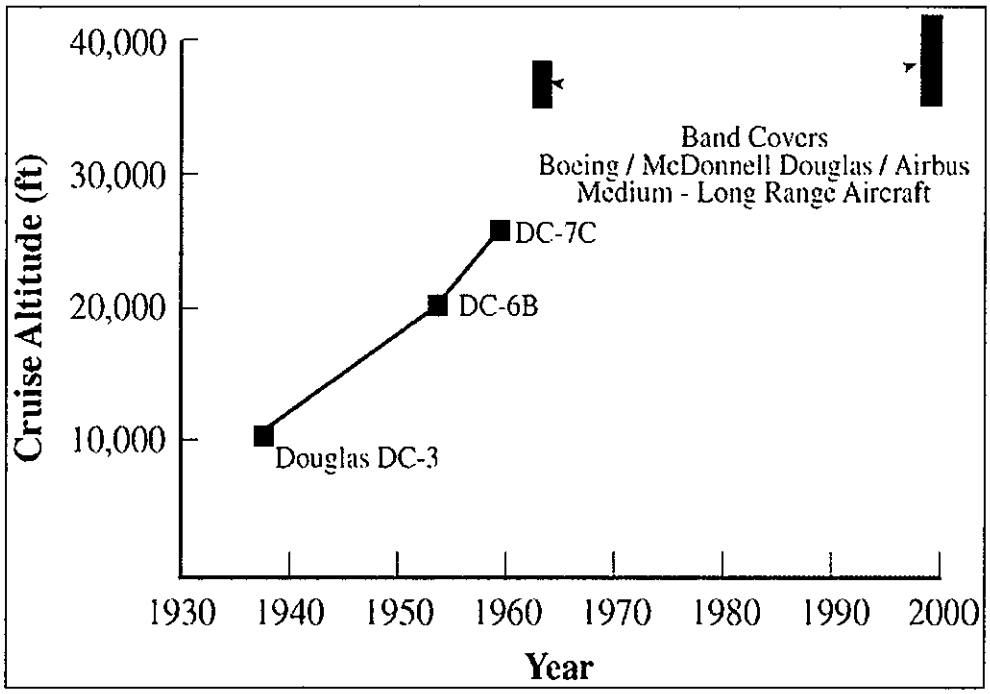


Figure (3.2): Cruising Altitude for Commercial Airplanes (Bahr et al.)

At cruising altitude of $10{,}000\,m$ for our study, the dynamic viscosity μ value is $1.4124 \times 10^{-5}\ \mathrm{N-s/m^2}$, and the kinematic viscosity ν is $3.4133 \times 10^{-5}\ \mathrm{m^2/s}$ (NASA, n.d.).

This study designated four different speeds for Numerical work. These present the standard cruising speed for some famous passengers and cargo airplanes: 150, 200, 250, and 300 m/s. In addition, various cruising speeds are used in commercial airplanes, as displayed in Figure (3.3) (Bahr et al.)

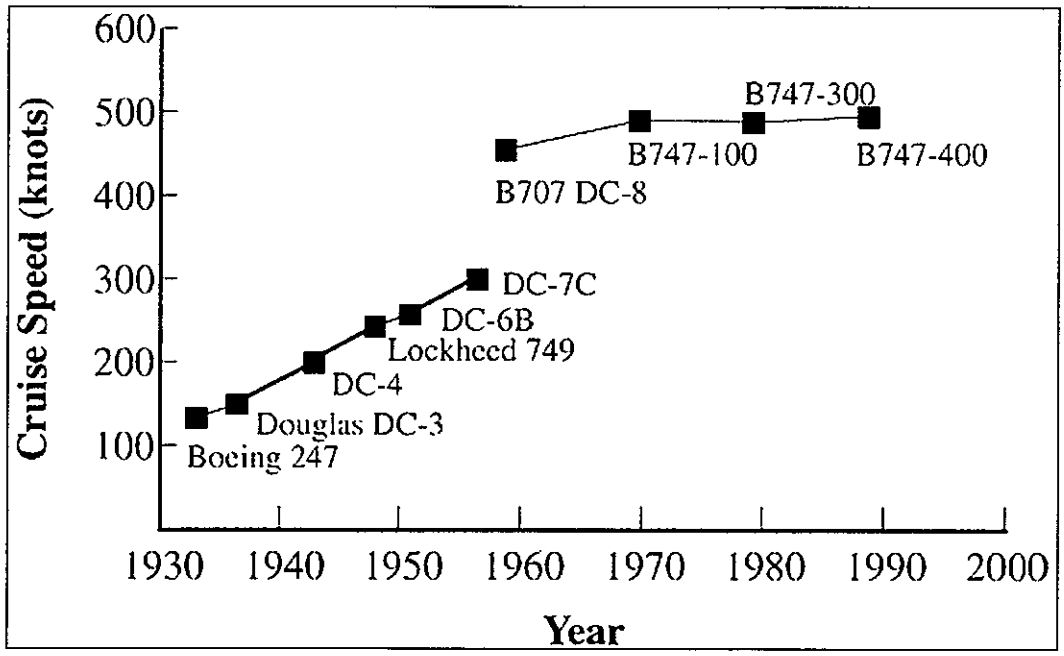


Figure (3.3): Cruising Speed for Commercial Airplanes (Bahr et al.)

3.2.1 Boundary Conditions

As mentioned in chapter (2), viscous flow is the free flow passing around our airfoil. On the other hand, viscous flow is the actual airflow in the atmosphere and wind tunnels. This type was selected to simulate real-state airflow conditions. This study implemented this flow type for wind tunnels and the options of simulation code flow parameters. Viscous flow permits us to execute different solutions of the trusted fluid dynamics regulating principles for the models precisely. On the other hand, Inviscid flow is applicable for special conditions, which may not be helpful in the study.

Another selection considers the airflow as turbulent rather than laminar flow. In chapter (2), discussed that fully turbulent flow has favorable characteristics over laminar flow in high subsonic velocities that operates airplanes. High Reynolds numbers also exist at these speeds, and the boundary layer is easily triggered to transform from laminar to

turbulent because of the effect of shear stress. The turbulent boundary layer has a better influence on adjacent flow behavior indeed.

3.2.2 Air Flow Behavior

Flying at high subsonic velocities of 150, 200, 250, and 300 m/s means Re > 500,000, which indicates a fully turbulent incompressible flow. The tests will run at 4,395,090 < Re < 8,790,181 (NASA, n.d.) This flow type is selected for its desired characteristics, as described in chapter (2).

3.2.3 Steady Level Flight

Steady-level flight dominates flight regimes in commercial flights as it contributes 80-90% of total flight duration. Since it establishes an equilibrium condition of all forces and moments, it will be easier to study the relations between flying objects and flow differentiae in this case. Also, the steady flight condition operates at cruising altitude and cruising speed, which this study assigned earlier. The main forces, lift, drag, weight, and thrust, are in static equilibrium as long as the aircraft is in a steady and unaccelerated level flight condition (Megson, 2022). Hence, for vertical equilibrium:

$$L + P - W = 0 \tag{25}$$

for horizontal equilibrium:

$$T - D = 0 \tag{26}$$

Moreover, taking moments around the aircraft's CG in the plane of symmetry:

$$La - Db - Tc - M0 - Pl = 0 \tag{27}$$

The loads acting on an aircraft in steady flight are shown in Figure (3.4) with the following notation:

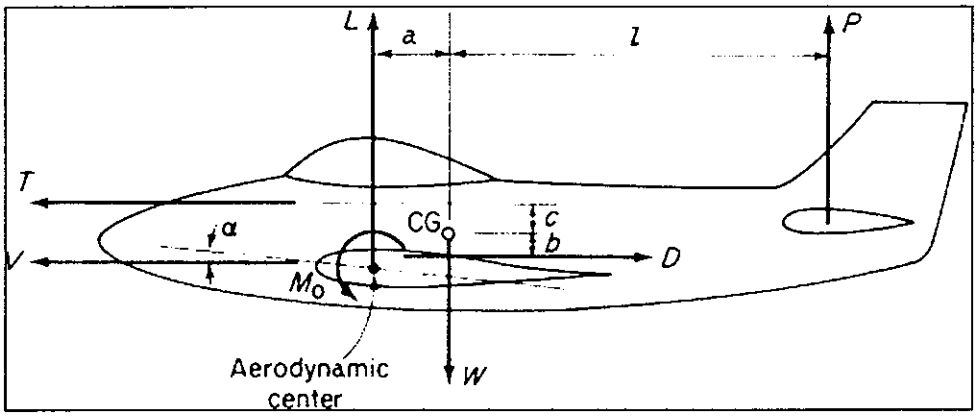


Figure (3.4): Aircraft Loads in Level Flight (Megson, 2022)

where L is the lift acting at the aerodynamic center of the wing, D is the aircraft drag, M_0 is the aerodynamic pitching moment of the aircraft, P is the vertical load on the horizontal tail acting at the aerodynamic center of the tail, W is the aircraft weight acting at its CG, and T is the engine thrust (parallel to the flight direction).

3.3 Lift Theory

Our study relies on Newton's first law, which states that an object will not alter its motion unless a force acts. Bernoulli's basic principle is translating this law into the following equation:

$$P + \frac{\rho}{2}V^2 + \rho gh = \text{constant} \qquad (28)$$

where P is the static pressure which denotes Pressure Energy, $\frac{\rho}{2}V^2$ is the dynamic pressure which represents Kinetic Energy. Finally, ρgh is the

hydrostatic pressure which means Static or Potential Energy. This summation of energies presents Bernoulli's equation's principle of energy conservation and is assumed constant along the streamline. Therefore, the streamlined energy passing through the first and last points of the airflow passing the airfoil should be the same. When compared these two points of the same streamline, we find:

$$P_1 + \frac{\rho}{2}V_1^2 + \rho g h_1 = P_2 + \frac{\rho}{2}V_2^2 + \rho g h_2 \quad (29)$$

As the start and end points of the incompressible flow circulate an airfoil, the mass flow rate will not change, and we get the following formula:

$$P_1 - P_2 = \frac{\rho}{2}(V_2^2 - V_1^2) \quad (30)$$

From the previous formula, we obtain the continuity equation, which expresses the mass conservation theory in continuity equation:

$$\rho A_1 V_1 = \rho A_2 V_2 \quad (31)$$

Solving equation (31) in equation (30) gives us this formula:

$$P_1 - P_2 = \frac{\rho}{2}V_1^2\left(\frac{A_1}{A_2} - 1\right) \quad (32)$$

This result concludes that: For horizontal flow, an increase in velocity must lead to a decrease in pressure. However, in airfoils, the flow passes at a higher velocity in the upper section than in the lower section due to airfoil geometry. This phenomenon mainly happens due to the difference in areas between these two surfaces. As a result, a high-pressure region on the lower surface and a low-pressure region on the upper surface. This pressure dissimilarity forms lift force. So, increasing this pressure disparity will increase lift force.

We aim to enhance lift force L, lift-to-drag ratio L/D and decrease drag force. Earlier main objectives may be considered but not limited to that only. Our study observations demand a decrease in stall speed, an increase in maximum lift, and a delay in stall angle.

3.4 Geometry Selection

3.4.1 Airfoil Selection

In this chapter, we present our methodology proposed to achieve our hypothesis earlier highlighted in the chapter (2). Then, explain the steps of our study, including numerical and experimental validation and introduce our problem setup and the basis for assigning main parameters and boundary conditions.

NACA 4412 airfoil is nominated to be our 2-D airfoil model. NACA 4412 and NACA 2412 are famous in aviation. The reason for that is their uncomplicated geometry and high lift characteristics, even close to ground conditions (Ockfen & Matveev, 2009). NACA 4412 has lower pressure on the lower surface than NACA 2411, which means lower lift. Also, a lower stall angle of 8° compared to 12° for the other airfoil.

Furthermore, finally, the maximum Y velocity reaches 45m/s for NACA 2412 and 32m/s for NACA 4412 (Gowda, 2019). Because of the lower aerodynamic efficiency of NACA 4412 in the previous comparison, we specified it to study the consequence of applying surface roughness with the expectation of significantly improving the main aerodynamic features. NACA 4412 has a maximum cumber of 4% of the airfoil chord line C and is located at 0.4 of C, while the maximum thickness is 12% of C, as pictured in Figure (3.5).

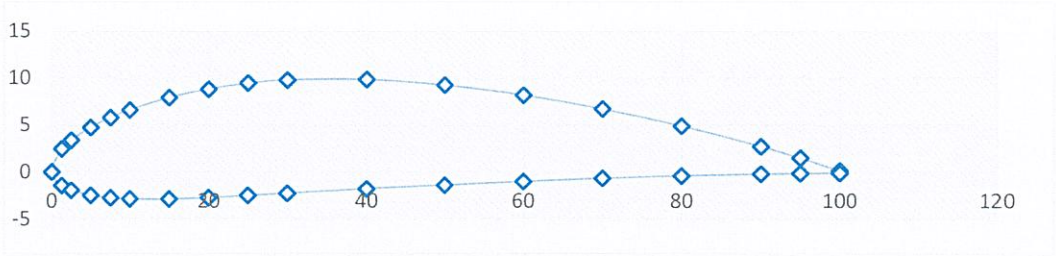


Figure (3.5): NACA 4412 Airfoil

3.4.2 Surface Roughness

We selected different roughness heights ks along the whole lower surface of the airfoil to examine lowering the velocity or altering the pressure in the bottom of the airfoil and its impact on lift theory. Rounded roughness was selected after the initial flat plate model tested in Ansys 2020 R1 with added different shapes and patterns of surface roughness; Rectangular, trapezoidal, triangle and rounded. The round shape was the best shape that positively interacted with flow parameters and roughened pattern. Then based on Yan Zhang's rounded pattern in his study, he used a pattern with 1×D diameter per element and 2×D spacing between every two sequences of sphere centers in aligned and staggered patterns (Zhang Y., 2018). Table (3.1) indicates various ks : values: (0.05, 0.1, 0.15, 0.2, 0.25, 0.3, 0.35, 0.4, 0.45, and 0.5) mm named the first set. This set lies in the hydraulically smooth region mostly where $5 \geq \frac{k_s V_*}{\nu}$ and the starting of transition region $5 \leq \frac{k_s V_*}{\nu} \leq 50$. While the second set ks are: (1, 2, 3, and 4) mm lay mostly in an entirely rough region $50 \leq \frac{k_s V_*}{\nu}$ as shown in Table (3.2).

Table (3.1): Set 1 Roughness Height *ks* Effect on Boundary Layer

Roughness height *ks* (mm)	$\frac{k_s V_*}{\nu}$ for $V_* = 150\ m/s$	$\frac{k_s V_*}{\nu}$ for $V_* = 200\ m/s$	$\frac{k_s V_*}{\nu}$ for $V_* = 250\ m/s$	$\frac{k_s V_*}{\nu}$ for $V_* = 300\ m/s$
0.05	0.751	0.834	0.916	0.988
0.10	1.502	1.667	1.831	1.977
0.15	2.253	2.501	2.747	2.965
0.20	3.004	3.335	3.662	3.954
0.25	3.755	4.168	4.578	4.942
0.30	4.507	5.002	5.494	5.931
0.35	5.258	5.836	6.409	6.919
0.40	6.009	6.670	7.325	7.908
0.45	6.760	7.503	8.240	8.896
0.50	7.511	8.337	9.156	9.885

Table (3.2): Set 2 Roughness Height *ks* Effect on Boundary Layer

Roughness height *ks* (mm)	$\frac{k_s V_*}{\nu}$ for $V_* = 150\ m/s$	$\frac{k_s V_*}{\nu}$ for $V_* = 200\ m/s$	$\frac{k_s V_*}{\nu}$ for $V_* = 250\ m/s$	$\frac{k_s V_*}{\nu}$ for $V_* = 300\ m/s$
1.0	15.022	16.674	18.312	19.77
2.0	32.775	36.364	39.964	43.127
3.0	52.6	53.35	64.1	69.2
4.0	73.97	82.09	90.15	97.35

Hydraulically smooth and transitional roughness are the most suitable regions to conduct our study. Larger *ks* will interfere with the fully developed turbulence flow, and the airfoil's aerodynamic shape is significantly changed. These small values of applied roughness claimed to fulfil the required improvement to our models.

3.5 Numerical Approach

We cannot accurately describe the fluid behavior using straightforward equations for complex scenarios like flow past an airfoil. So instead, we recommend using either experimentation, numerical methods, or a combination of the two to analyze the flow. Modelling flow using numerical methods is the field of Computational Fluid Dynamics CFD. It utilizes computational power to solve the Navier-Stokes equations, a system of partial differential equations that describes the fluid behavior but is challenging to solve.

To do this, the fluid domain modeled around the airfoil as a mesh of discrete elements, define boundary conditions and fluid properties, and apply an appropriate assessment technique to find a solution. One of the main challenges when dealing with turbulence is capturing the wide range of length scales associated with turbulent eddies. Three main techniques to simulate flow in CFD differ mainly in how they treat turbulence on these scales.

First, we have Direct Numerical Simulation DNS. This technique involves solving the Navier-Stokes equations to even the most minor scales and explicitly resolves all turbulent eddies. Unfortunately, this is very computationally expensive and needs to be a practical solution for most flow problems.

Next, we have Large Eddy Simulation LES. This technique resolves the large-scale eddies explicitly, but small-scale eddies are filtered out and modelled using what is known as a sub-grid-scale model. As a result, LES is much less computationally expensive than DNS.

Finally, we have the Reynolds Averaged Navier-Stokes RANS technique, which is the least computationally expensive of the three

techniques. This technique is a time-averaged method that does not resolve eddies explicitly at all. Instead, it models the effect of eddies using the concept of turbulent viscosity. Several turbulence models exist, like the $k-\varepsilon$ or $k-\omega$ models, with different models being better suited to different problem types.

We utilized the RANS technique in this study for the previously stated reason. ANSYS 2020 R1 is our software to simulate the flow field around NACA 4412 airfoil, specifically, Fluent code, a sub-program in ANSYS. This software runs Navier-Stokes, Euler's, and Bernoulli's equations with many sub-equations covering many operating conditions under the principles of finite element methods. The Genetic Algorithm prepares the solution through a long optimization process (Cayiroglua & Kilicb, 2017).

3.5.1 Ansys 2020 R1 Fluent Space Claim

Space Claim is the latest drawing co-program included in the Fluent package. The previous versions were Gambit and Design Modeler. This version of drawing software has better compatibility with importing different design formats drawn from other codes. Defining nodes, edges, vertices, surfaces, and bodies could be done with various options and less time and setup required. The program controls every step and automatically updates the preferences to design readable objects to pass to the meshing program.

Firstly, we selected the 2-D drawing scheme as we drew airfoils and all our calculations in 2-D. International dimensions standards apply throughout the project, neglecting the weight and settling for program

definition. The chord line was set to 1m as standard unit to ease the calculations of the prototype airfoil.

NACA 4412 airfoil data was imported from the Airfoil Tools website (NACA 4412 (naca4412-il), 2022). Connected Upper airfoil points in a line and lower airfoils in a separate line. That is to make different curves in order to get different edges needed for following setups and calculations. The curves were connected without gaps and smoothed to get the best curvature as shown in Figure (3.6).

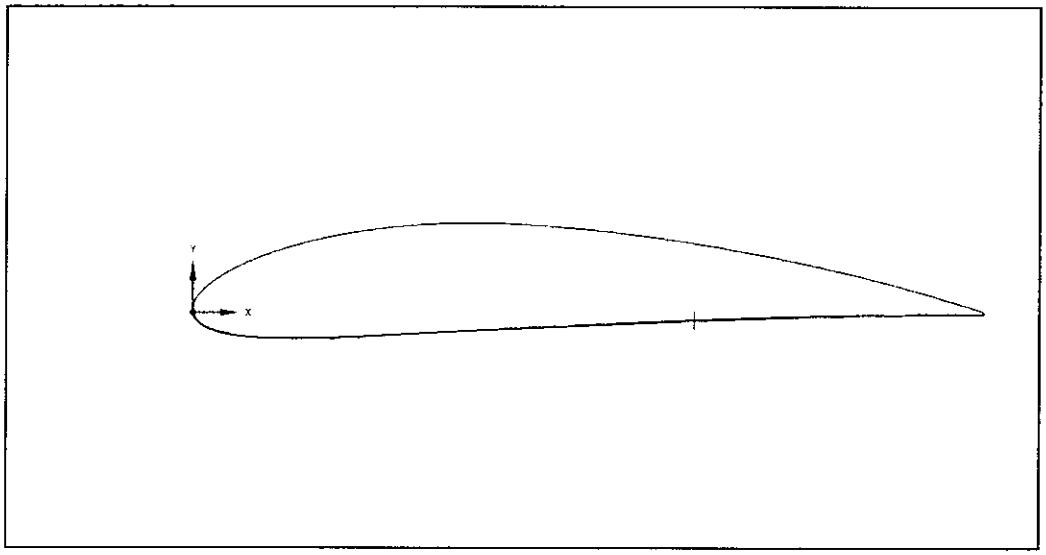


Figure (3.6): NACA 4412 Airfoil Drawn in Space Claim

Two surfaces generated around the airfoil. An elliptic surface with dimensions $6m \times 3m$ and an envelope box of $90m \times 50m$, as illustrated in Figure (3.7) and Figure (3.8).

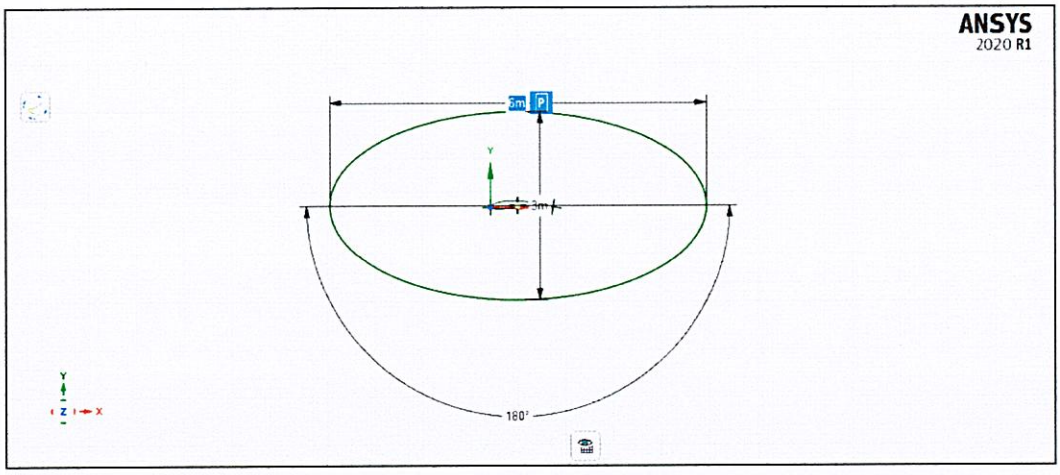


Figure (3.7): The Elliptic Face Around NACA 4412 Airfoil

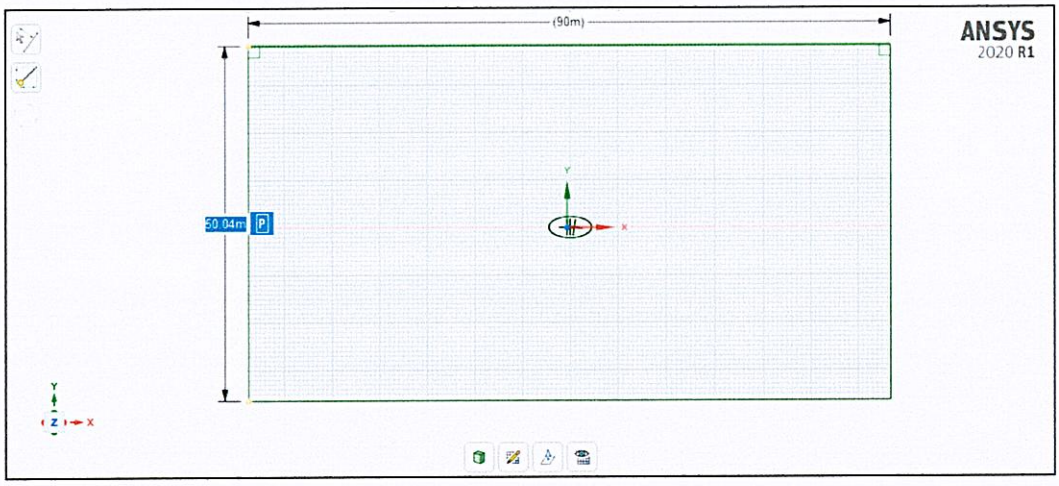


Figure (3.8): Envelope Box Face Around the Elliptic Face

The airfoil upper and lower walls are solid, while the two inner surfaces are fluids. The elliptic and envelope box surfaces dimensions are revised many times to get the best results and realistic for the model after meshing and during the setup process. Plain NACA, 4412 airfoil with known output data of C_d, C_l *and* C_m are compared in these trials to get a convergent solution for simple laminar flow as standardized in airfoil library data (NACA 4412 (naca4412-il), 2022). The surface splits into two

faces to concentrate the meshing cells near the airfoil surface and decrease it in the far field. Figure (3.9) elaborates on the two faces of the project.

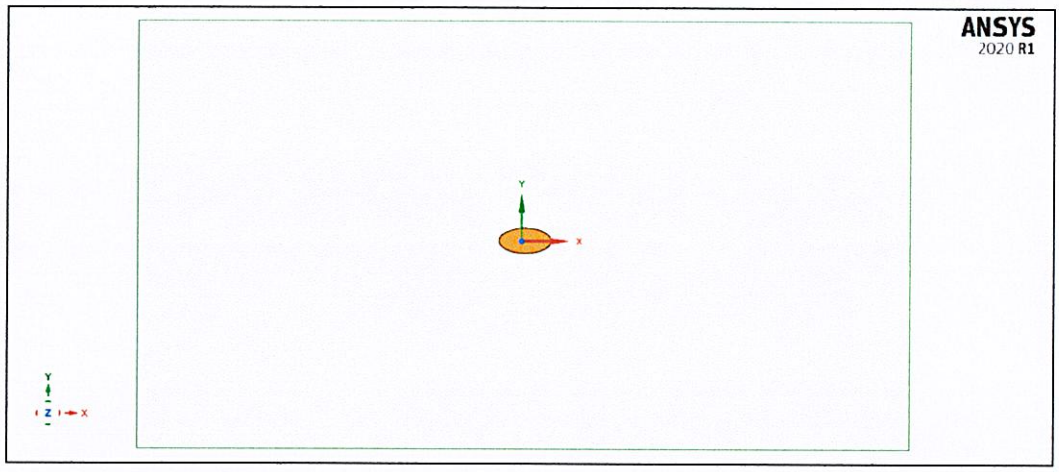


Figure (3.9): The two Faces Creating the Surface of the Project

The airfoil is drawn in fifteen different scripts to cover all models required for our project, as displayed in Figure (3.10):

1- Smooth airfoil with $0mm$ surface roughness,
2- Ten (10) different radii applied rounded roughness along the entire lower airfoil surface: 0 mm, 0.05 mm, 0.1 mm, 0.15 mm, 0.2 mm, 0.25 mm, 0.3 mm, 0.35 mm, 0.4 mm, 0.45 mm, and 0.5 mm as shown in Figure (3.11).
3- Five (5) different radii applied rounded roughness along the entire lower airfoil surface 1mm, 2mm, 3mm, and 4mm.

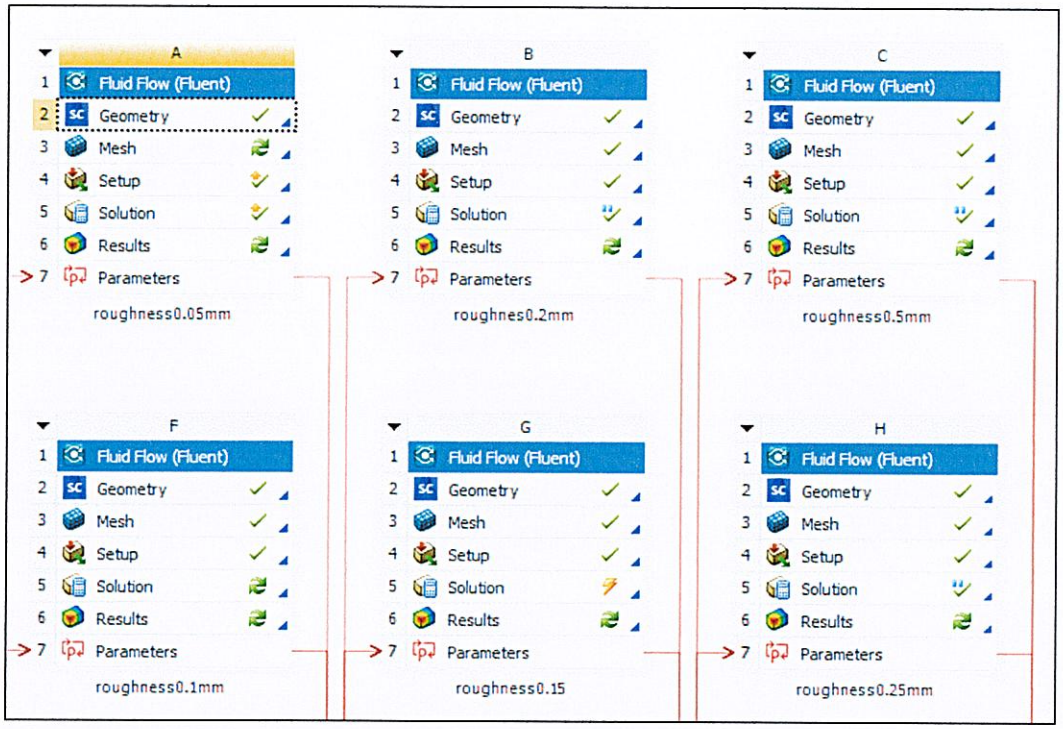


Figure (3.10): Overview of the Scripts Screen in ANSYS Fluent 2020 R1

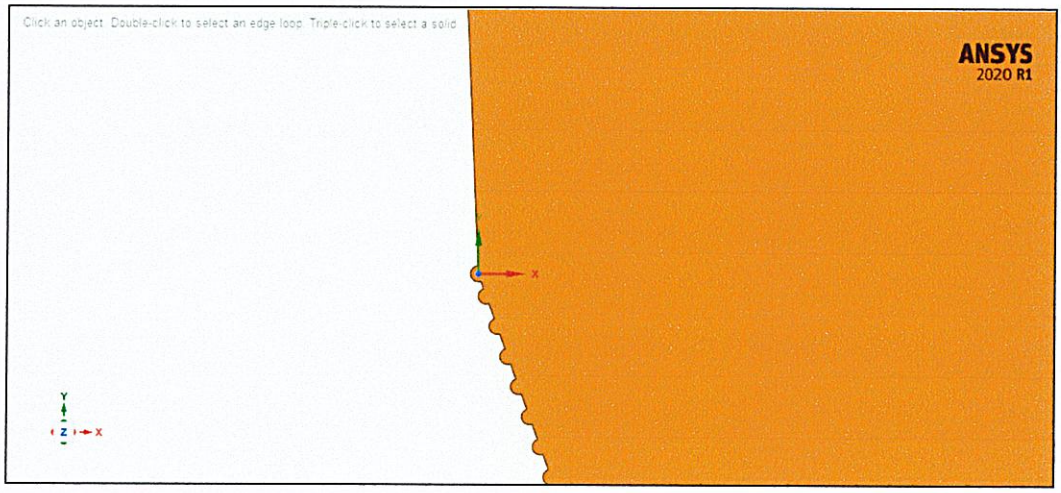


Figure (3.11): Close View of the Applied Roughness Drawn in Space Claim

3.5.2 Meshing

Meshing ANSYS (AUTODYN PrepPost) is the meshing sub-program in Fluent. We exported the models from Space Claim to this program to set up adequate grid for all the models in our project. Different meshing properties used for each model depend on the geometry of the airfoil and the number of edges generated, which differ due to the numbers and sizes of applied roughness. Figure (3.12) demonstrates the main screen of the meshing program.

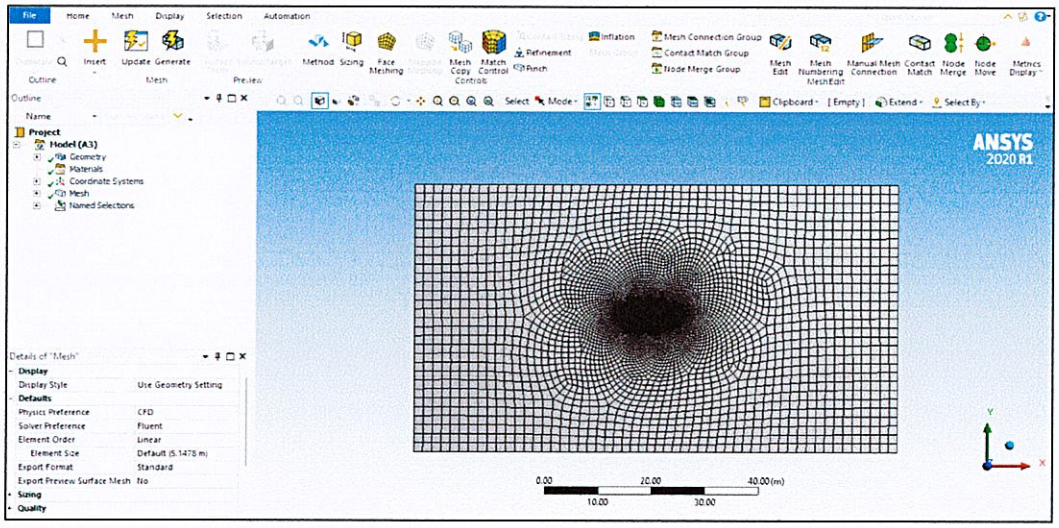


Figure (3.12): Main Screen of Meshing Program

The meshing of airfoils depends mainly on the quality of the grids, which varies according to airflow properties and airfoil geometry. We obtained perfect results when we applied triangular grids to the airfoil models in a set1 of applied roughness, as shown in Figure (3.13).

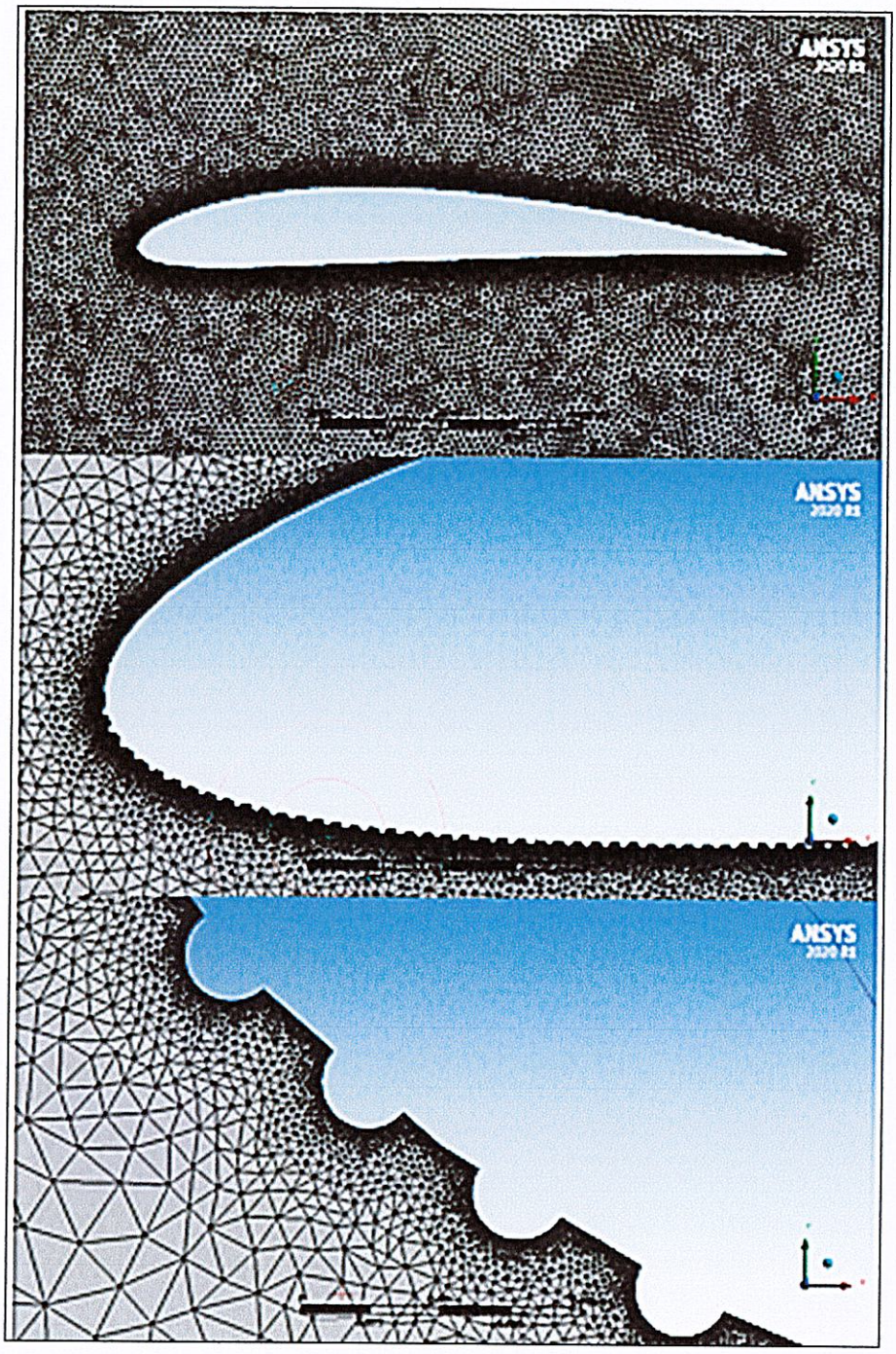


Figure (3.13): Triangular Meshing for Set1 Applied Roughness

Smooth airfoil and set2 applied roughness to the models performed sufficiently in homogenous quadrilateral grids, as shown in Figure (3.14).

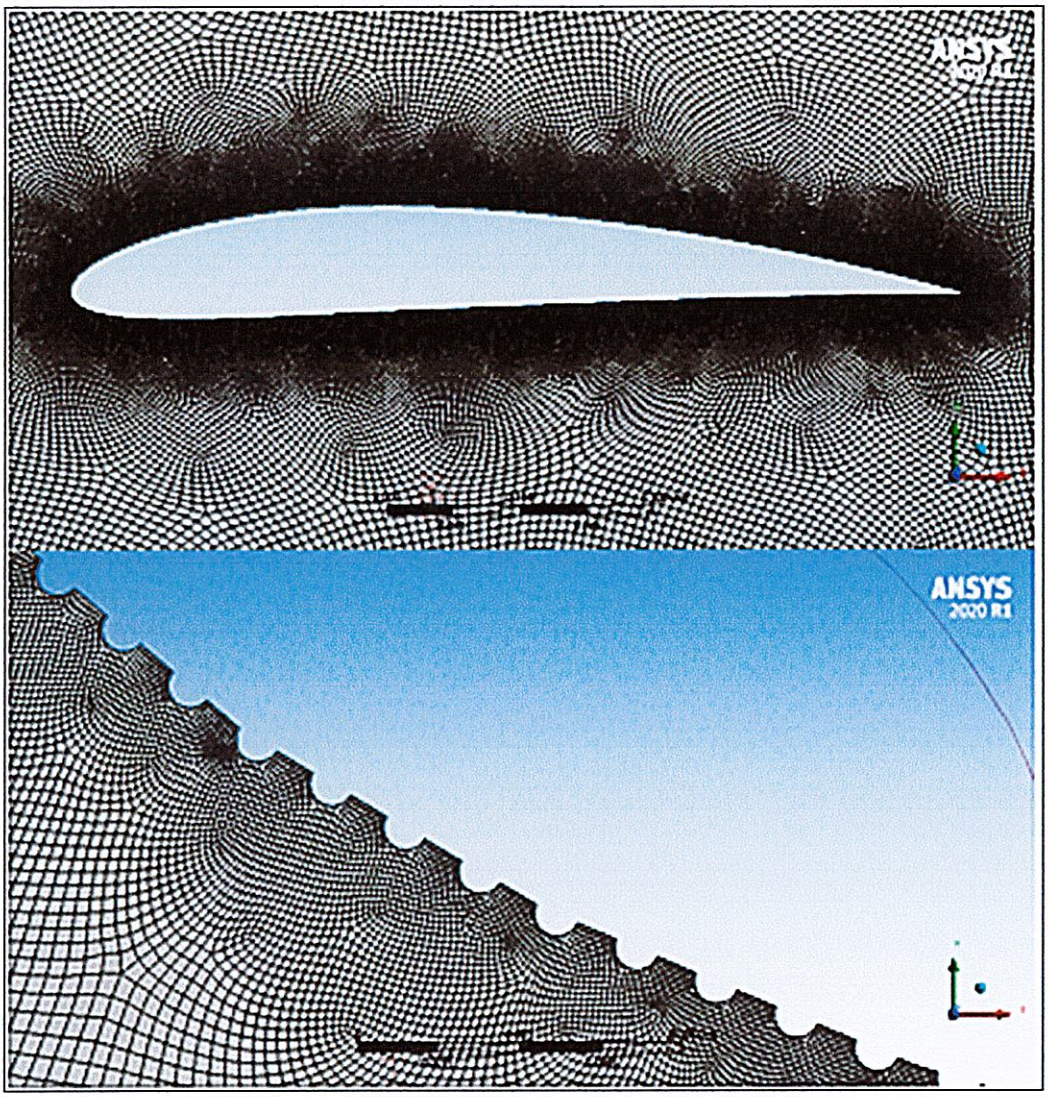


Figure (3.14): Quadrilateral Meshing for Set2 Applied Roughness

i. Smooth Airfoil

Setting up the smooth airfoil was straightforward in selecting the mesh properties because of the simplicity of the geometry compared to the other models. Table (3.3) lists the meshing properties for the smooth airfoil NACA 4412.

Table (3.3): Meshing Properties for Smooth Airfoil NACA 4412

Properties	Smooth airfoil NACA 4412
Element order	Linear
Element size	Standard (5.1478 m)
Growth rate	1.2
Mesh defeaturing	$2.5739 \times 10^{-2} m$
Capture curvature	5.1478×10^{-2}
Boundary box diagonal	102.96m
Average surface area	$2250\ m^2$
Minimum edge length	1.0105 m
Mesh quality	High smoothing
Inflation option	Smooth transition
Nodes	75225
Elements	73631
Meshing method	Quadrilateral dominant
Free face mesh type	Quad/Tri
Airfoil edges Sizing	Two edges divided to 2000 with minimum size 5.1478×10^{-2} and bias factor 1.2
Elliptic face sizing	One face with element size 4×10^{-2} and 1.2 growth rate
Refinement	Elliptic face (2)

ii. Airfoil with Applied Roughness 0.05mm up to 0.5mm

We introduce this set with very small ks, which lay inside the boundary layer. We can understand that the flow is hydraulically smooth as elaborated in Table (3.1). Some ks values barely entered the transitional flow margin, but we found the flow behavior is likely hydraulically smooth in the results revealed in chapter (4). Table (3.4) compares the meshing properties of $the\ ks = 0.05mm$ model to $the\ ks = 0.5mm$ model. Appendix (A) lists a complete range comparison between all models.

Table (3.4): Meshing Properties of $ks = 0.05mm$ Applied to the Airfoil NACA 4412 Compared to $ks = 0.5mm$ Model

Properties	$ks = 0.05mm$ NACA 4412	$ks = 0.5mm$ NACA 4412
Growth rate	1.2	1.2
Minimum edge length	5.040510^{-5}	$1.7079 \times 10^{-5}m$
Mesh quality	High smoothing	High smoothing
Inflation option	Smooth transition	Smooth transition
Nodes	106987	622976
Elements	1980694	612393
Meshing method	All Triangles Method	Quadrilateral Dominant
Free face mesh type	Triangles	Quad/Tri
Airfoil edges Sizing	10052 edges with element size $1 \times 10^{-5}m$ with the same proximity size and bias factor of 1.2	10099 edges with element size $1 \times 10^{-4}m$ with the same proximity size and bias factor of 1.2
face sizing	Oval face with element size 1×10^{-2}m and 1.2 growth rate. The box with an element size of 1.0m	Element size 5×10^{-2}m
Refinement	null	3

iii. Airfoil with Applied Roughness set 2 of 1mm up to 4mm.

This set of applied ks contains models of 1 mm, 2 mm, 3 mm, and 4 mm. As clarified in Table (3.2), this set lies mostly in an entirely rough region at the end of the transition region. We also aim to study this type of flow effect on the flow characteristics. Table (3.5) compares the meshing properties of 1 mm ks to 4 mm ks. Appendix (A) lists a complete range comparison between all models.

Table (3.5): Meshing Properties of $ks = 1mm$ Applied to the Airfoil NACA 4412 Model Compared to $ks = 4mm$ Model

Properties	$ks = 1\ mm$ NACA 4412	$ks = 4mm$ NACA 4412
Growth rate	1.2	1.2
Minimum edge length	4.7948×10^{-6}	2.6229×10^{-2}
Mesh quality	High smoothing	High smoothing
Inflation option	Smooth transition	Smooth transition
Nodes	478590	377578
Elements	909903	719835
Meshing method	All Triangles Method	All Triangles Method
Free face mesh type	Triangles	Triangles
Airfoil edges Sizing	601 edges with element size $5 \times 10^{-5}m$ with the same proximity size and bias factor of 1.2	126 edges with element size $5 \times 10^{-5}m$ with the same proximity size and bias factor of 1.2
face sizing	Oval face with element size 1×10^{-2}m and 1.2 growth rate. The box with an element size of 1.0m	Oval face with element size 1×10^{-2}m and 1.2 growth rate. The box with an element size of 1.0m.
Refinement	null	null

iv. Bounding Box

We chose a colossal boundary box of $90m \times 50m$ after several trial. This dimension was in the best size that did not interfere with the flow type or direction. Unfortunately, that also caused an enormous number of cells to carry out the calculation in the finite elements processing. We detected that naming the boundary box edges affects the results iteration, convergence/ divergence, and significantly changes the results. We achieved the best-named selection when we selected the upper edge, lower edge, and frontal edge as velocity inlets. The backward edge is named pressure outlet. These names apply to all sets' whole models and are illustrated in Figure (3.15).

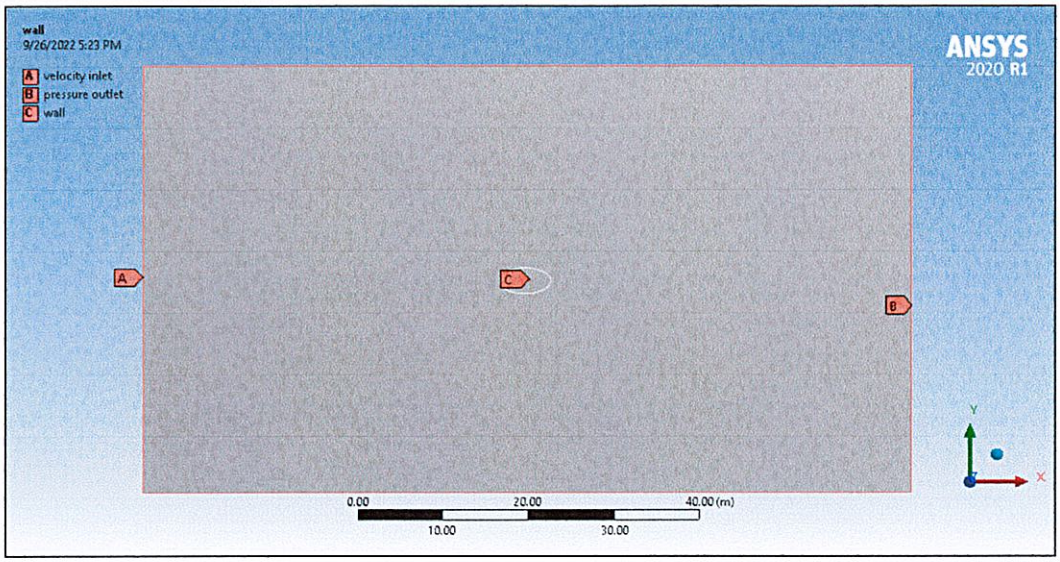


Figure (3.15): Named Selection for the Models

v. Meshing Grid Independency Study

Before performing the CFD simulations, we conducted a grid independence study to eliminate the influence of the number of the grid's size on the computational analysis outcomes. To estimate the lowest grids required to achieve grid independence, we adopted the following procedure: Sanjay considered the solution to be grid independent if the absolute values of the solution of the grid points in two successive trials do not exceed a difference of more than 0.5% (P.Sanjay, T.N, & Bharadwaj, 2016).

We began our grid independency study by coarse mesh, but we fixed the elements' size and the number of divisions for the exact model in the entire model's independence tests. Due to the tiny size of the edges of the applied roughness, especially for less than 1mm radius, the coarse and medium meshing was inapplicable to the models. Therefore, we started the study using fine meshing. We changed the quality of the meshing by using the program controlled smoothing and the Refinement option developed

into ANSYS 2020 R1. This option is a program-controlled option to supplement the overall meshing quality measured in the number of refining processes per model. This process adjusts the mesh sensitivity and grid sizes and controls the cells' rate of expansion or shrinkage near the body edges. The technique states that the selected mesh for every model is getting less than a 5% contrast in lift and drag coefficients results between the best two meshes. Table (3.6) presents the lift and drag forces coefficients difference at 250 m/s velocity for the smooth airfoil. Appendix (B) delivers a full-range Grid Independency Study.

Table (3.6): Grid Independency Study for Smooth Airfoil

Setup	Bounding box 90*50m/ Nodes 53069/ Elements 51480/High-quality smoothing/smooth transition/ element size of face 1 =0.05 / refinement 0 /v=250m/s	High quality/smooth transition/ element size of face 1 =0.05 / refinement 1	Percentage
LIFT COEFF	4.5556e-01	4.5555e-01	0.000002 %
DRAG COEFF	9.2872e-03	9.3317e-03	0.004 %

3.5.3 Fluent

We were modelling a turbulent flow project in Fluent onsets in correctly selecting all setup parameters in the code. Figure (3.16) demonstrates the setup launching options as the significant edit is choosing eight solver's parallel processes for our operating device as multi-General-purpose computing on graphics processing units GPGpU solver does not apply to our device. Also, we applied a double precision solver option to get the most relevant results.



Figure (3.16): Setup Launching Screen

We selected a 2-D planner solver with a pressure-based steady time model applied to the project. It is the best pre-setup option for a single airfoil to pass through the air with neglected gravity contribution. Figure (3.17) demonstrates our selection in the general menu.

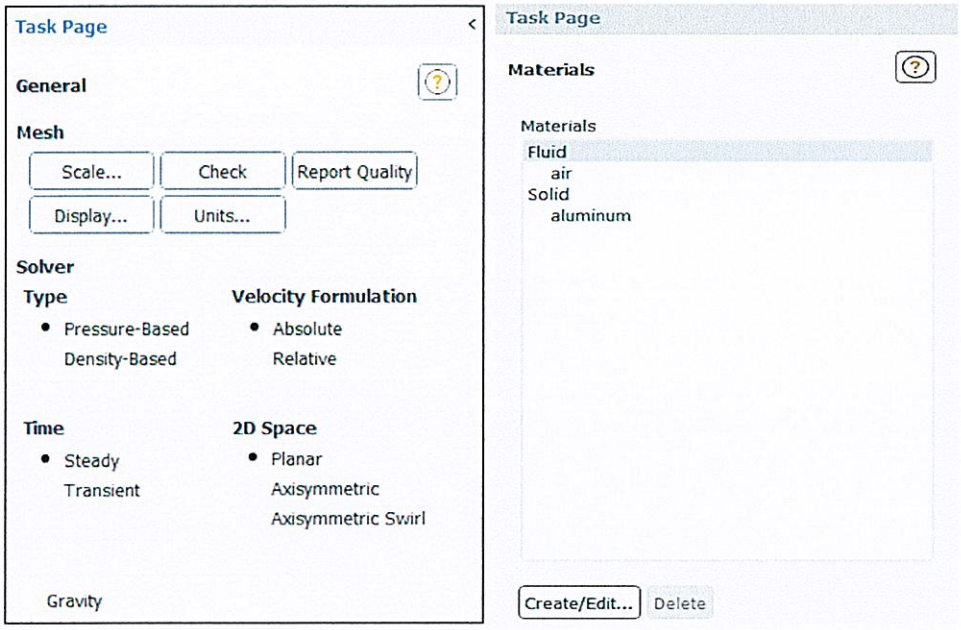


Figure (3.17): General Options and Materials in Fluent Screen

The materials of the surfaces are air as a fluid medium and Aluminum as the airfoil wall's solid surface. The usage of aluminum alloys is widespread in commercial jets structure because of their lightweight, sustainability against corrosion and erosion, low static electricity conductivity and elasticity. Figure (3.17) presents our selection in the Fluent list.

i. Turbulence Models

We demonstrated earlier in chapter (2) the necessity of employing viscous flow in our project as we study the relationship between the airfoil and adjacent flow by applying all main governing equations. Furthermore, the viscous flow enlarges our perception of the complex friction force and adverse pressure phenomenon, presenting the total aerodynamic forces acting on the airfoil. Therefore, we can precisely dissect the effect of different heights applied surface roughness on the airfoil. Figure (3.18)

shows the selected viscous flow model and enabled energy equation contribution in the solution iterations.

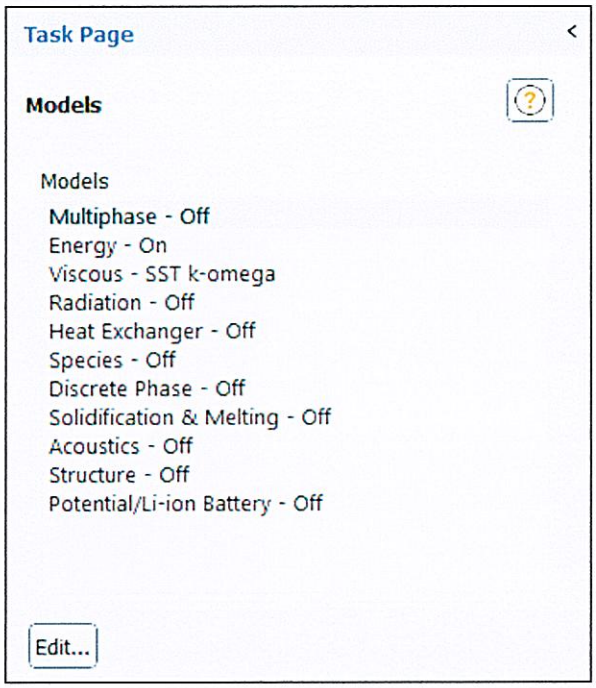


Figure (3.18): Models Applied to the Solution in Fluent

We defined the density and viscosity of the air at 10,000m, referring to NASA as the values considerably change with altitude. These values in Figure (3.19) demonstrate the viscous flow state at steady-level flight (NASA, n.d.).

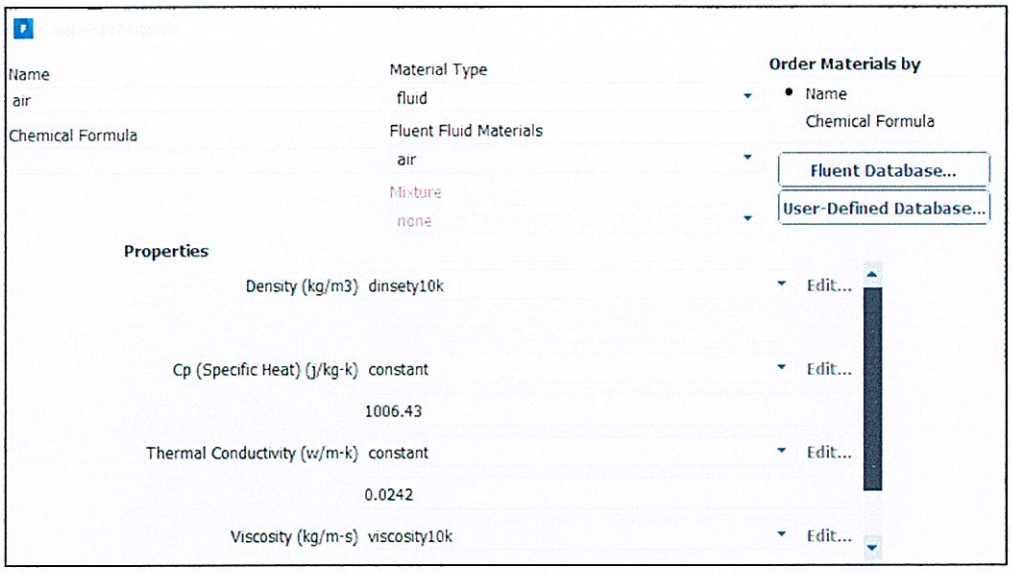


Figure (3.19): Airflow Properties at 10,000m Altitude

Main RNAS Turbulence Models available in Fluent:

a) One-Equation Models:

• Spalart-Allmaras: A low-cost RANS model for computing single transport equations with a revised eddy viscosity method called Spalart-Allmaras. Resolving the eddy viscosity is simple when adjusted near the wall. This model supplies solutions for aerodynamic/ turbomachinery applications requiring moderate separation, such as boundary-layer flows and supersonic/transonic flows over airfoils. However, this model is relatively new and valid for complicated engineering flows. Indeed, the lack of studies verifying this model raises the issue.

b) Two-Equation Models:

- Standard k–ε: The most popular engineering turbulence model for commercial use. Compressibility, buoyancy, and combustion have their submodules in this model. However, we cannot compute a factor in the equation called wall functions. These functions must always be employed to acquire good results. This model performs

poorly for flows with significant negative pressure gradients, considerable separation, and substantially streamlined curvature.

- RNG k–ε: The k- ε equations are the same as the conventional ones, except constants are determined using renormalization group theory.
- Realizable k–ε: Anticipates both planar and spherical jet spreading rates more precisely. Flows, including rotation, boundary layers under high unfavorable negative pressure gradients, separation, and recirculation, are also likely to perform effectively.
- Standard k–ω: The model equations do not have wall-undefined terms. Without applying wall features, they incorporate them into the wall. As a result, they are reliable and precise for various pressure gradient-driven boundary layer flows. Most often used in the turbomachinery and aerospace industries. Compressibility effects, transitional flows, and shear-flow corrections include a few k- ω sub-models or alternatives also defined in this model.
- SST k–ω: The SST k- ω model utilizes a combining function to progressively switch from the common k- ω model close to the wall to a high Reynolds number k- ω model in the boundary layer's outermost region. This method contains an advanced formulation for turbulent viscosity to consider the impact of the principal turbulent shear stress affecting transport.

For our project, two variations were used of the k–ω two-equation turbulence model—the Jones-Launder model for free shear layers and the conventional model, which are nearly similar. The new update of the model, known as the Shear- Stress Transport (SST) model, has the added capability of accounting for the dominant shear stress transport in boundary layers with negative pressure gradients. The eddy-viscosity definition

emphasizes Bradshaw's concept that the primary shear stress is proportional to turbulent kinetic energy as the basis for the model. The SST model's predictions for unfavorable pressure gradient boundary-layer flows are entirely unrelated to the freestream values and possess reasonable agreement with the available experimental data (Menter, 1992). Therefore, we chose to employ the SST k-model in our project while focusing on near-the-wall region precision. Figure (3.20) illustrates the viscous model selection applied throughout the project.

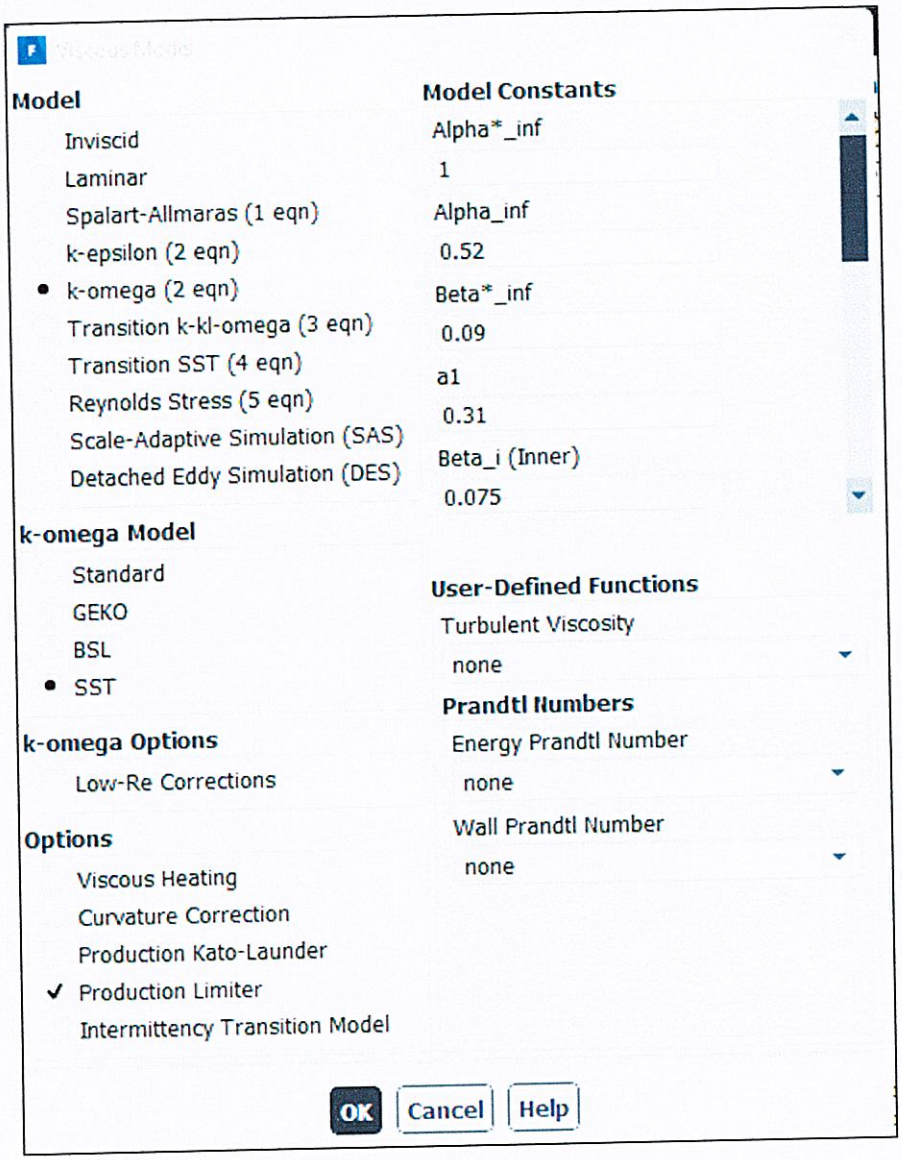


Figure (3.20): Viscous Model Applied to the Project

ii. Boundary Conditions

All edges in the study were highlighted in section (3.5.2) Bounding Box and pictured in Figure (3.15). Fluent imports the named selections, process them and numbers them progressively. Solid surfaces recognized are accompanied by airfield surfaces to be considered as interiors; id =1 and 2, respectively, as displayed in Figure (3.21).

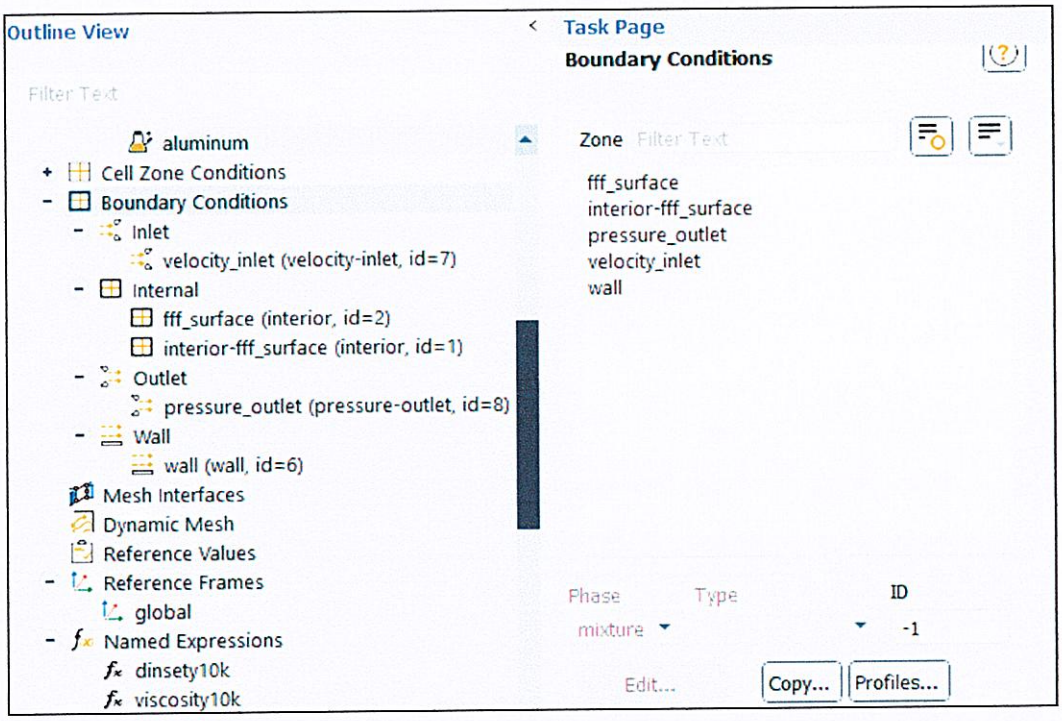


Figure (3.21): Boundary Conditions of the Project

We used four values for the velocity inlet: $150\text{m/s}, 200\text{m/s}, 250m/s$ and $300m/s$. In addition, we assigned a definition for every velocity by magnitude and direction. As a result, the incident angles appear in three different directions at $\alpha = 0^o, 5^o, and\ 10^o$. These are the collaborative setting angles of the wings in commercial airplanes in steady-level flight. The turbulence specification used is Turbulent Intensity is 5%

and a Viscosity Ratio of 10 programs controlled, as depicted in Figure (3.22).

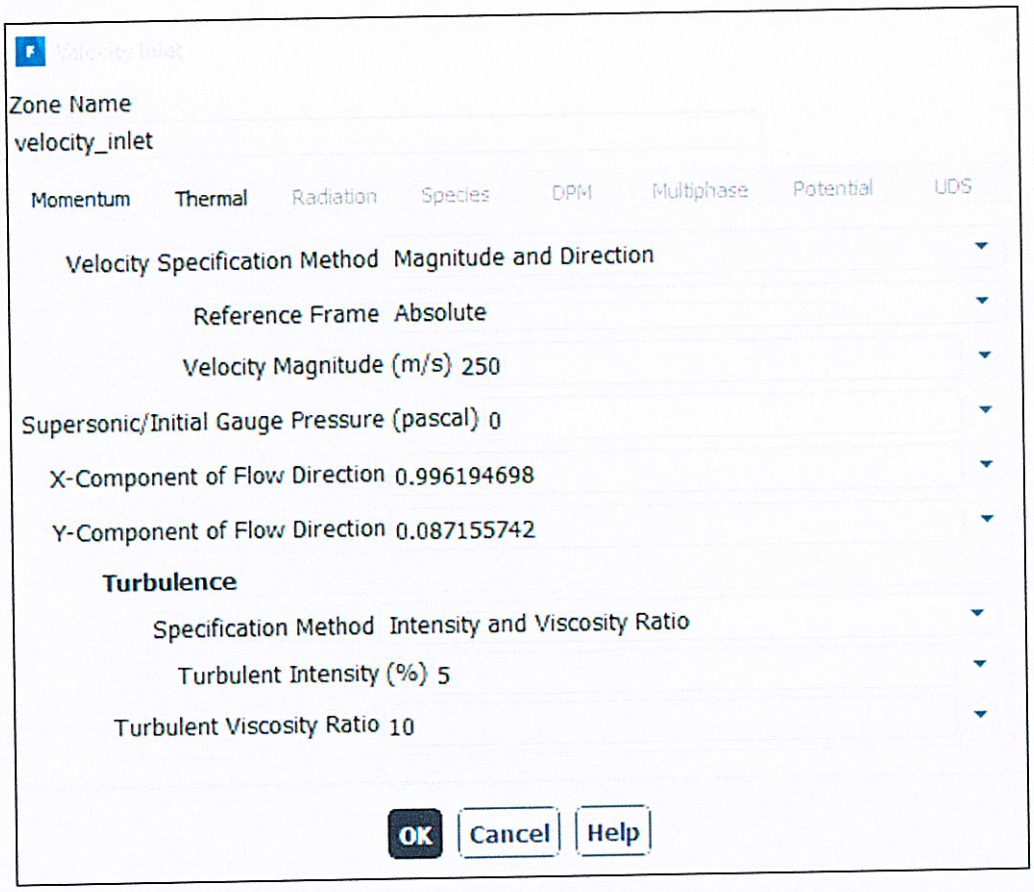


Figure (3.22): Velocity Inlet Boundary Conditions

We defined the pressure outlet on the opposite side of the surface's bounding box. We set the pressure gauge to the value of 0 pascals with activating the effect of the backflow and turbulence specifications. The purpose is to simulate the natural flow passing through the airfoil. Our methodology counts on applying all flow parameters of cruising altitude of 10,000m. This altitude changed the total pressure and temperature values to meet the natural conditions. Figure (3.23) exhibits Fluent's screenshot of pressure outlet options.

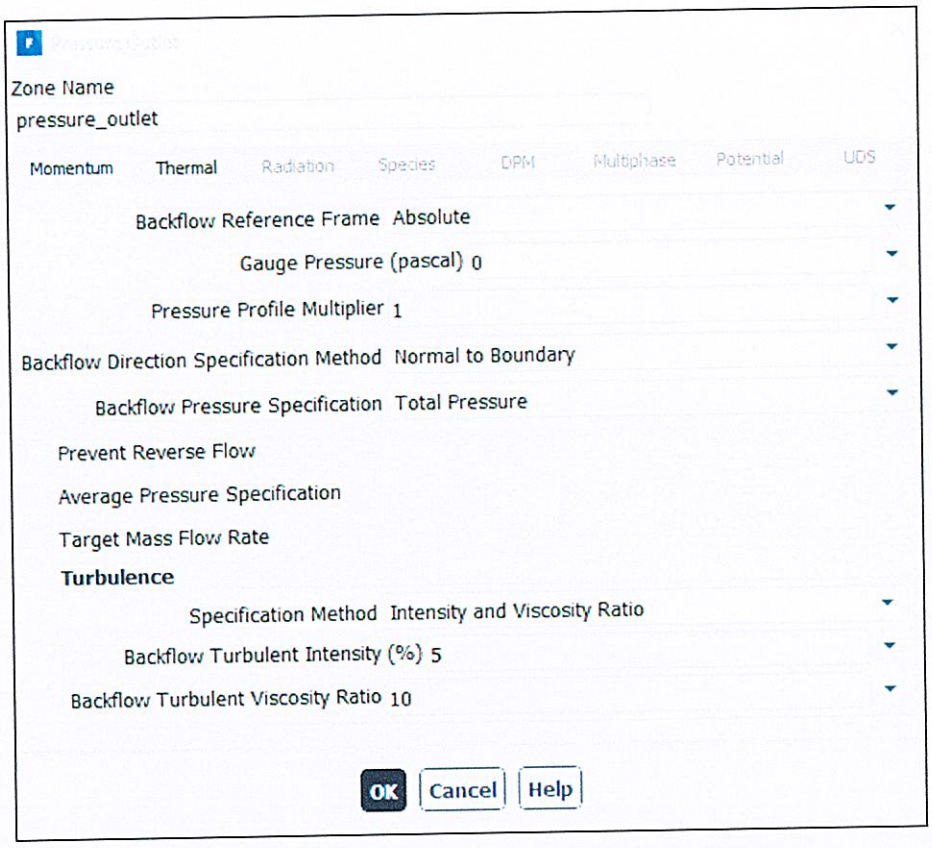


Figure (3.23): Pressure Outlet Options in Fluent

After that, we set the airfoil surface named wall. This part is critical in defining the correct expression for our project. A stationary wall with no slip and a smooth surface is an essential aspect of the flow model, as illustrated in Figure (3.24). As discussed earlier, turbulent flow and turbulent boundary layer feature options are mandatory for applying equations of energy, Euler, and Bernoulli to describe the flow passing over the airfoil precisely. Moreover, Ansys algorithms require proper selection of the boundary conditions to run the complicated equations to output converged numerical solutions.



Figure (3.24): Wall Boundary Conditions in Fluent

iii. Solution Setup

The Fluent algorithm couples' pressure and velocity in our setup with the best accuracy methods:

- Gradient: Least square cell-based.
- Pressure: Second order.
- Momentum: Second order upwind.
- Turbulent kinetic energy: Second order upwind.
- Specific dissipation rate: Second order upwind.
- Energy: Second order upwind.

Lift and drag forces are monitored, plotted, and reported in every iteration of this project. The direction of the forces changes as α changes to reconcile with the definition of the forces acting on the airfoil. Figure

(3.25) embellishes the lift and drag coefficients setup, which alters for every solution run as we change α and V per Ansys Fluent run.

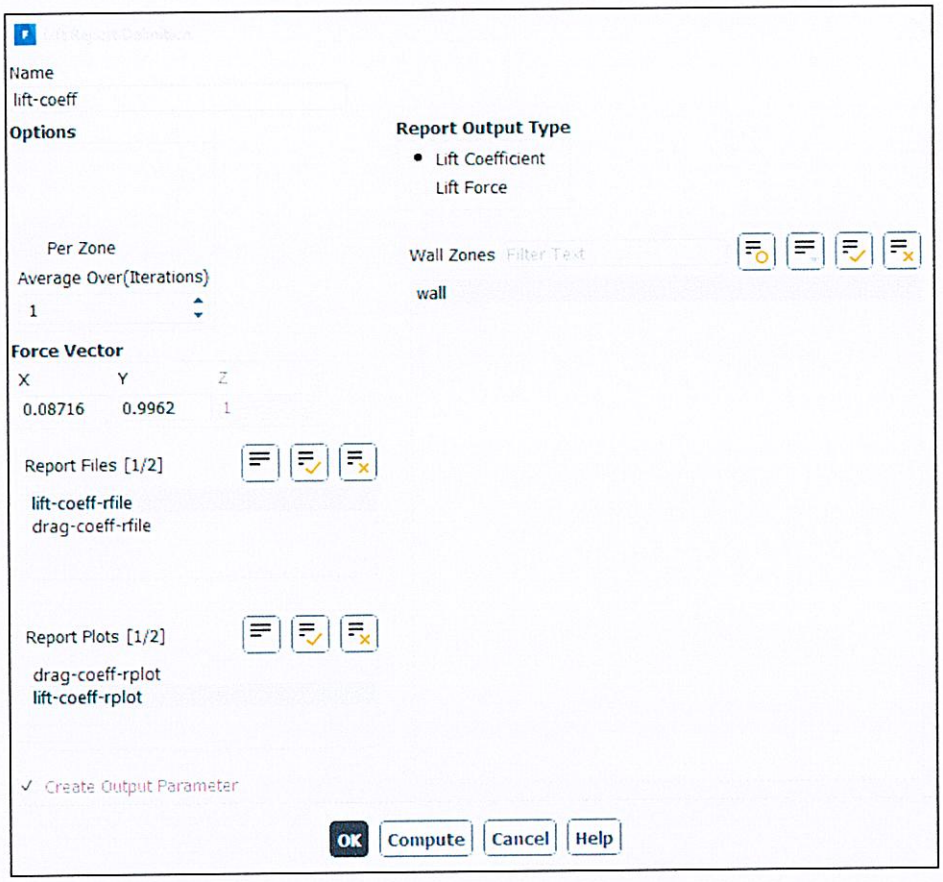


Figure (3.25): Lift and Drag Coefficients Setup in Fluent

One thousand iterations are with the assigned residual conditions every time until convergence. Figure (3.26) displays the convergence of solution accuracy.

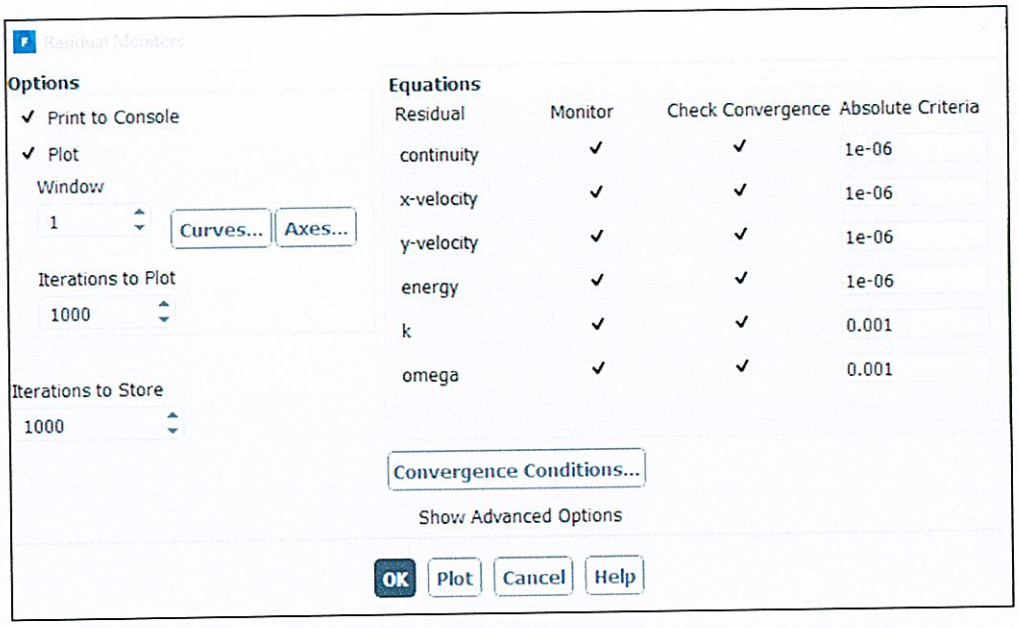


Figure (3.26): The Convergence of Solution Accuracy with the Assigned Residuals

3.6 Experimental Approach

The effect of the applied surface roughness will be verified experimentally, in addition to the previous numerical method. Many studies relied on different CFD programs or experiments in wind tunnels or by PIV screening technologies. However, only some of the studies verified both ways. The reason for that is the complexity of the setup and the difficulty of getting matched results precisely. Therefore, we decided to suffice with 2-D models in our project, which can sufficiently support our research hypothesis by utilizing the best available resources in the University of Bahrain computer laboratory, fluids mechanics laboratory and Applied Science University's 3-D printing facility.

The airfoil is positioned in a 2-D subsonic Wind Tunnel duct horizontally exposed to different angles of attack and various upstream air velocities. The Wind Tunnel maintained a fully developed

laminar/turbulent airflow during the test. The subsonic wind tunnel is connected to a computer control and analysis unit. We examined two types of models: smooth airfoil and roughened airfoil. Figure (3.27) illustrates the experiment process.

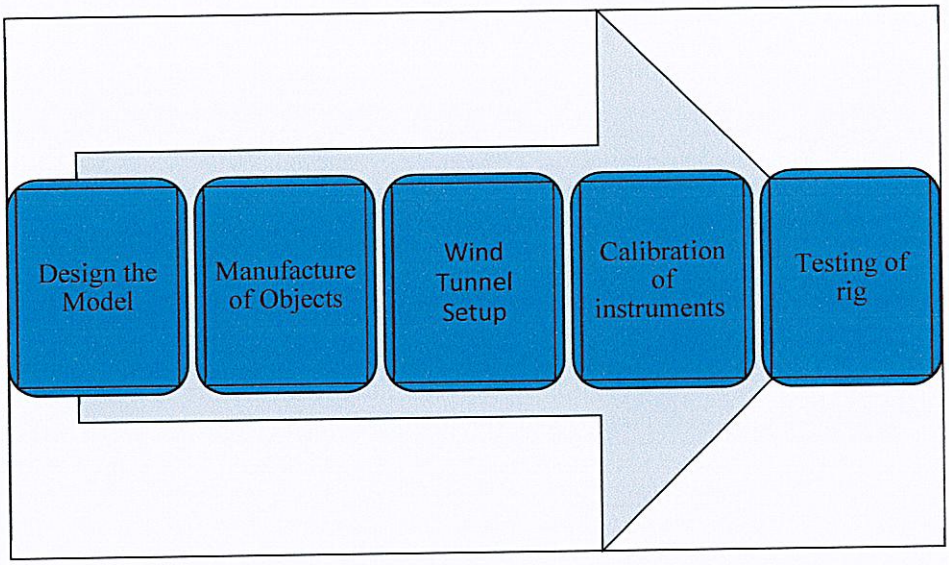


Figure (3.27): Experiment Process

3.6.1 Design of the Model

The model was designed identically to the testing specimen originally accompanied to UOB Fluid Mechanics laboratory 2-D Wind Tunnel: C-15. The model is 9.57 × 10 cm. Airfoil's points exported to Sloid Works 2012 drawing code. The foil was drawn and exported to the 3-D printer. Figure (3.28) displays the front and top views. We manufactured two copies of the model to test smooth surface (plain) airfoil and roughened airfoil.

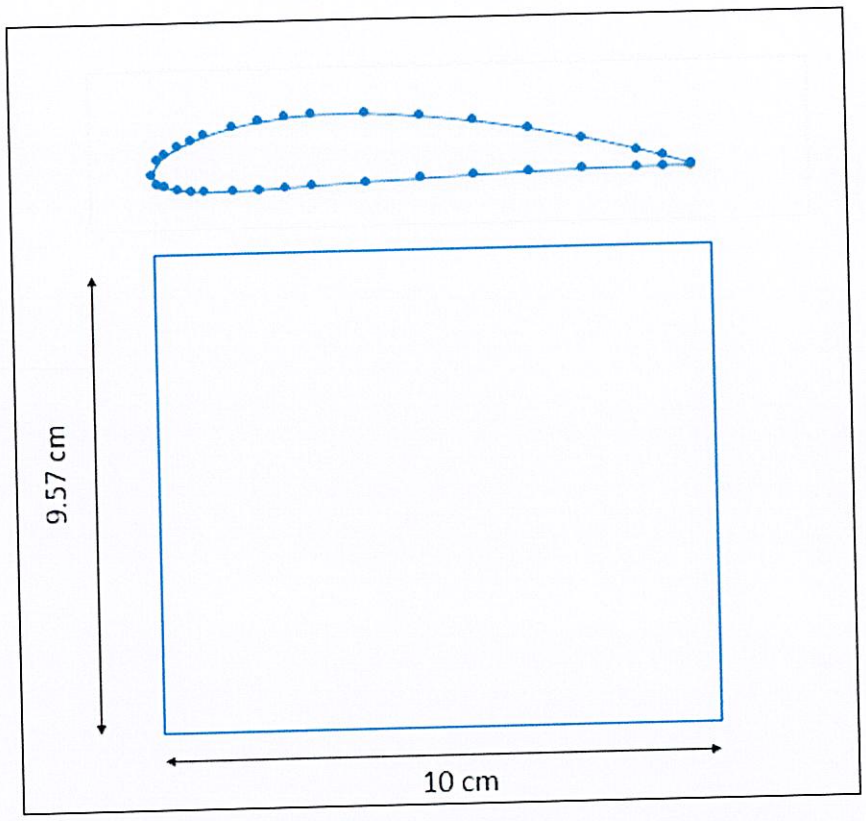


Figure (3.28): Front and Top View of the Model

3.6.2 Manufacture of Objects

The curved shape of the airfoil for the mentioned dimensions hindered our options in manufacturing the 3-D airfoil model in the project. Therefore, a 1:100 scale reduction was applied to the model to be positioned horizontally in the test section of the C-15 wind tunnel. High accuracy of model manufacturing is required to get the exact airfoil shape of the selected NACA 4412 model. Original design script files are prepared in the Solid Works program and then exported to the 3-D printer. The printer successfully printed two identical copies of the NACA 4412 airfoil with the required dimensions. The surface finish of 20 μm resulted after production. Appendix (D) documents the 3-D printer specifications.

3.6.3 Wind Tunnel Setup

Computer Controlled Subsonic Wind Tunnel - C15-20 is considered an experimental validation method. The C-15 Wind Tunnel shown in Figure (3.29) is a 2-D low-speed wind tunnel with a maximum speed of 35 m/s $\pm 2m/s$. Appendix (E) details the wind tunnel specifications. The testing facility consists of three sections:

a- The central duct: Transparent horizontal duct with convergent flow inlet and divergent outlet diffuser.

b- The practical accessories accompanying the wind tunnel: There is a direct connection between the software model and the electrical console (IFD 7), the electronic manometer bank, and the balancing fixture.

c- The central computer: This is attached to the main duct and preloaded with special software for processing the central duct of the wind tunnel input readings.

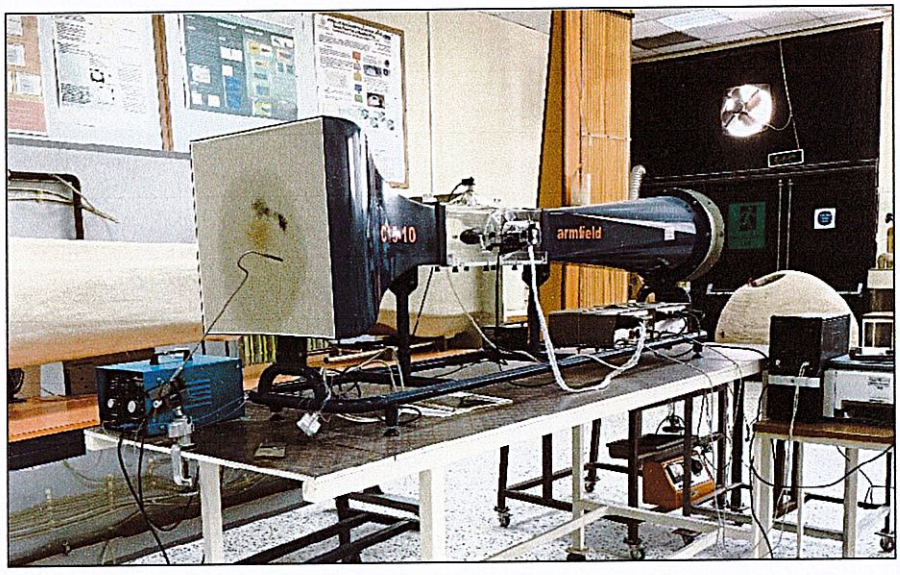


Figure (3.29): C15-20 Computer Controlled Subsonic Wind Tunnel

The main parts of the wind tunnel and their functions are listed below:

i. Wake Survey Rake

Ten tubes make up the rake, which is oriented toward the airflow and is arranged vertically in a row, as shown in Figure (3.30). The position of the rake is downstream of the testing model. There is a gap of 2.5mm between the rake and the assembly, allowing measurements at intervals of 2.5mm by interlacing two sets of readings. There is space between the tubes of 5mm and flexible tubing joints the tubes to establish a multi-way fast-release connection. These tubes are connected to (IDF7) and measure pressures behind the tested object inside the wind tunnel duct. (IDF7) receives the indicated measurements and converts them into data through the manometer bank, then to the main computer.

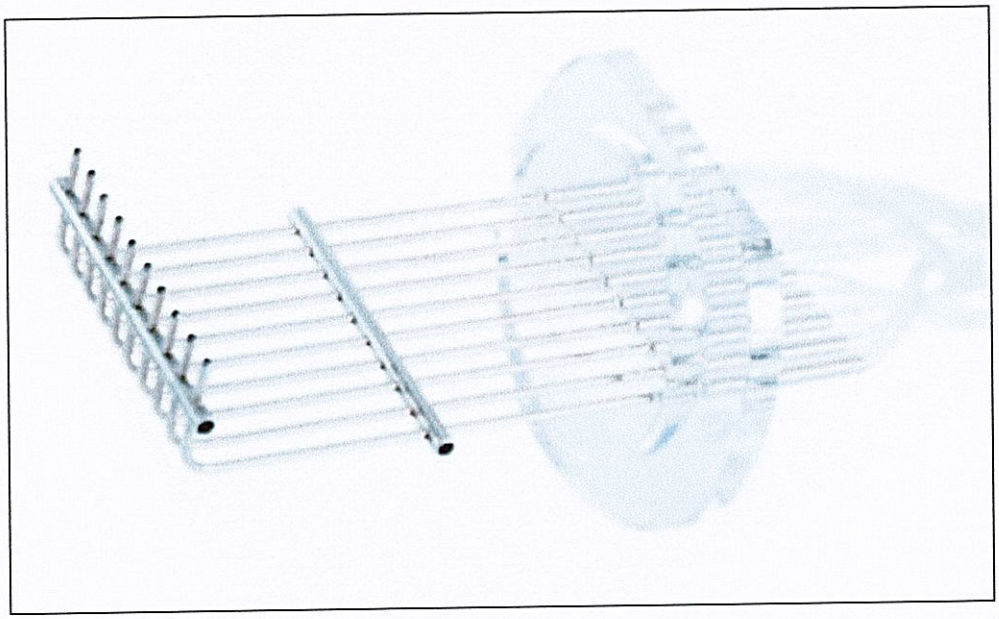


Figure (3.30): Stainless Steel Wake Rake Tubes Arrangement

ii. Electronic Manometer Bank

The Manometer Bank has sixteen (16) tubes, each with a range of 0 -178 mm H2O, incorporated into an electronic console. The software integrated the readings completely to manage the wind tunnel and utilizes a second USB connection to connect to the control PC. The reference to air pressure is made possible via ordinary tapping. Quick-release connections connect models and instruments d quickly, as Figure (3.31) reveals.

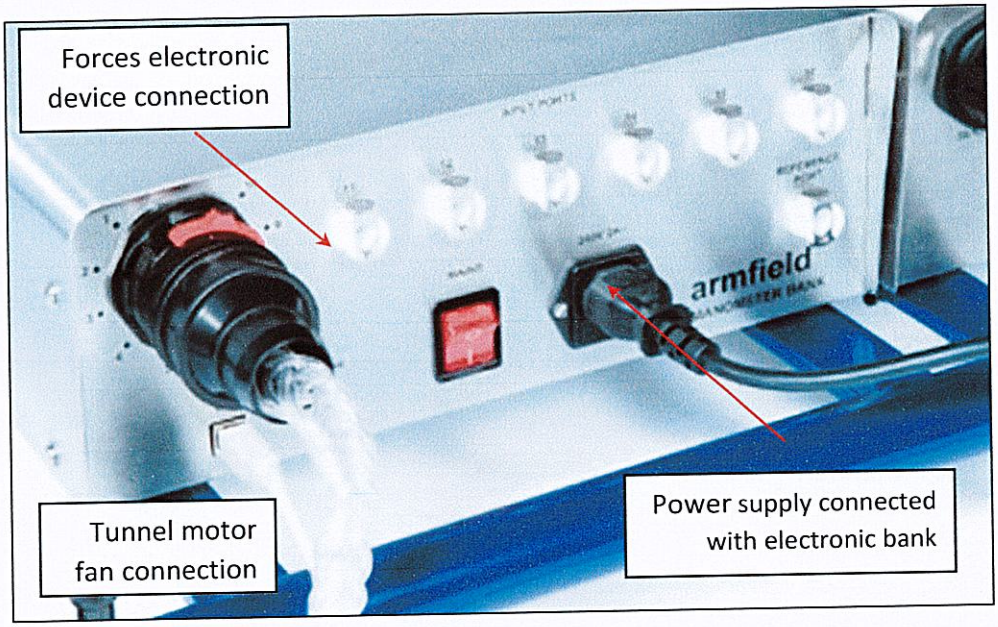


Figure (3.31): Electronic Manometer Bank

iii. Lift and Drag Electronic Balance Device

An electronic balance with two components that measure lift and drag on the tested models is placed inside the duct, as pictured in Figure (3.32). The lift and drag models are connected to the balance using a simple fixing that guarantees the model's proper orientation. The lift and drag forces are sensed and measured by electronic sensors and applied to a

reduction in the model weight. Additionally, a rotation could occur for the model while mounted to appraise the angle. On the control software screen running on the PC, the values from the lift, drag, and rotation sensors will be shown and are available for data logging.

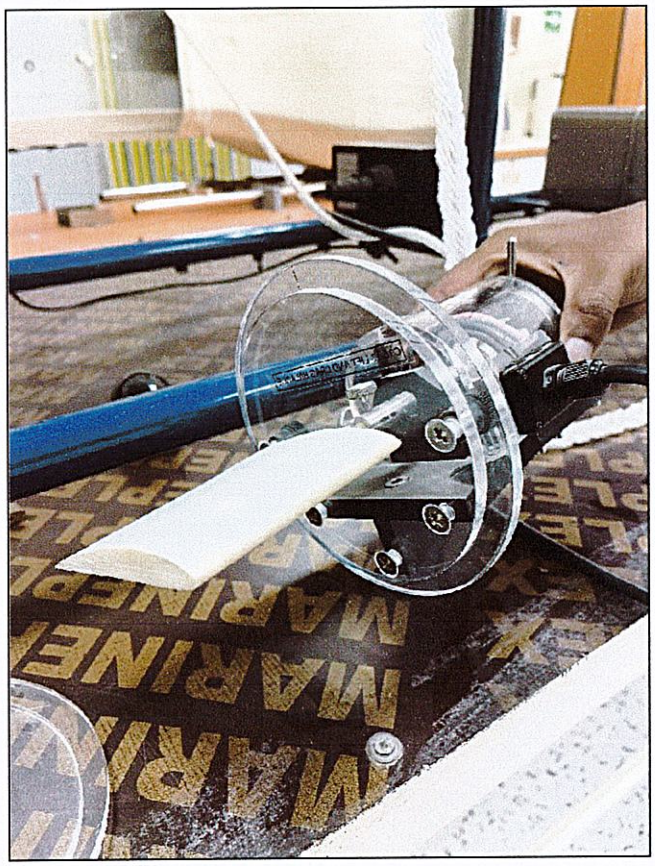


Figure (3.32) Lift and Drag Balance Device

iv. Calibrating the Models

After printing the two identical models, as stated previously, we set the surface roughness with sandpaper. We carried treatment at Royal Bahraini Airforce (RBAF) in Maintenance Support Shops. First, we applied ultra-fine aviation filler to smooth the 3-D printed curves, and we scrubbed the surface with fine sandpaper as follows:

a. Model 1: Upper and lower surfaces scrubbed with extra fine sandpaper ks= 0.0258 mm finish up.
b. Model 2: Upper surface with extra fine sandpaper, but fine sandpaper ks= 0.045 mm for the lower surface.
c. Model 3: Upper surface with extra fine sandpaper, but Fine sandpaper ks= 0.125 mm for the lower surface.
d. Mode 4: Upper surface with extra fine sandpaper, but medium (coarse) sandpaper ks= 0.19 mm for the lower surface.



Figure (3.33): Testing Models of 400 Grits Upper Surface and (400, 60 Grits) Lower Surfaces

Table (3.7) lists the types and sizes of sandpaper used to finish the models' surfaces and knows that we start from the roughest sandpaper to the finest ascendingly. Finally, Figure (3.32) exhibits our printed models after surface treatment.

Table (3.7) Sandpaper Sizes Used for the Models

Grade	Description	ISO/FEPA Grit designation	CAMI Grit designation	Average particle diameter (μm)
Medium	Medium to coarse surface texture after sanding	P60	60	190
		P80	80	265
Fine	Medium to fine surface texture after sanding	P100	100	125
		P240	240	45
Extra fine	It slightly wipes away patches/small inconsistencies but is not strong enough for removal	P400	320	25.8
		P500	350	35.0
		P600	360	36.0

Then, the four models' surface roughness was calibrated in RBAF Precision Measurement Equipment Laboratory (PMEL) using a dial gauge (depth gauge), and the average ks presented in Table (3.8).

Table (3.8): Average Surface Roughness Calibration

Model Number		Average depth
Model 1	Upper airfoil surface	0.5-1 Thou (0.0127-0.0258) mm
	Lower airfoil surface	0.5-1 Thou (0.0127-0.0258) mm
Model 2	Upper airfoil surface	0.5-1 Thou (0.0127-0.0258) mm
	Lower airfoil surface	1.5-2 Thou (0.0381-0.0508) mm
Model 3	Upper airfoil surface	0.5-1 Thou (0.0127-0.0258) mm
	Lower airfoil surface	4.0-5.5 Thou (0.102-0.14) mm
Model 4	Upper airfoil surface	0.5-1 Thou (0.0127-0.0258) mm
	Lower airfoil surface	5.0-5.15) Thou (0.127-0.131) mm

A total of ten measurements were taken for each model. Five measurements for the upper airfoil's surface and five for the lower airfoil's surface at the locations shown in Figure (3.34). Figure (3.35) shows the depth gauge used in the measurements.

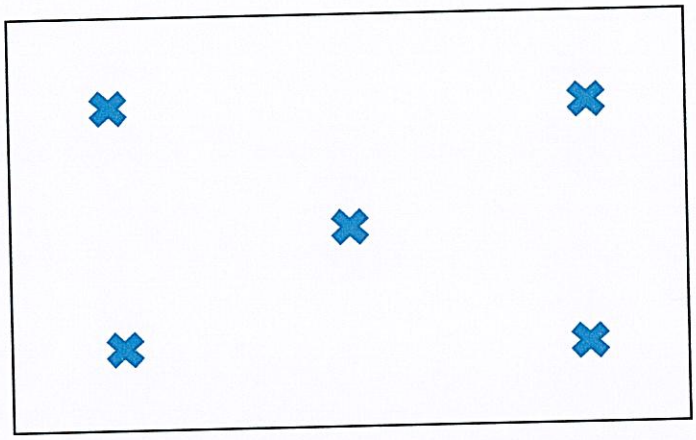


Figure (3.34): Surface Roughness measurement locations at lower and upper surfaces of NACA 4412 Airfoil

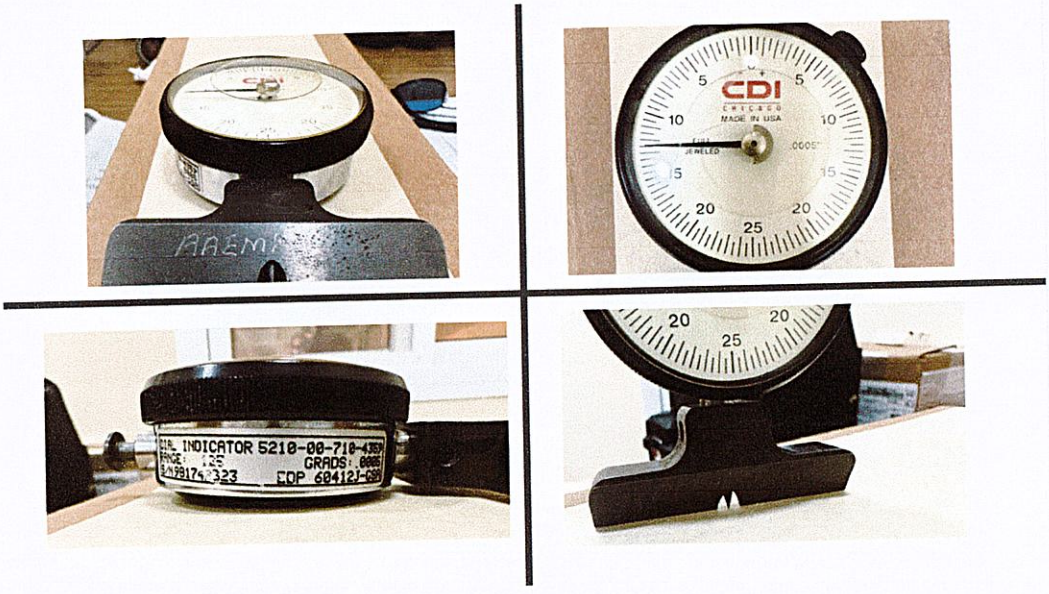


Figure (3.35): Depth Gauge Used to Measure Surface Smoothness

We calibrated the test models and the C-15 Wind as well. The wind tunnel has eight pre-installed different (drag–lift) and boundary layer models. Each model has a manual for performing the designated test in the Wind Tunnel. In addition, the computer has software to run every model under distinct operating conditions. All the expected results are obtainable in the software and the model's manual.

The C15-20: Lift & Drag Airfoil model is pictured in Figure (3.36). This model tests a plain symmetrical airfoil of NACA 0015. Including a mounting rod that enables installation on the Lift & Drag Balance, enabling the measurement of lift and drag with the airfoil at various angles of attack for a direct comparison of lift properties with pressure distribution. We operated the Wind Tunnel, followed all the steps, and got the identical results provided by the manufacturer. We considered this test a calibration test to ensure that the Wind Tunnel is operating and measuring precise outcomes. This model experiments with the identical parameters we need in our experimental verification, so we utilized the lift and drag model, the same operating software and exact airfoil dimensions mounted to the same balance device to ensure the quality of results.



Figure (3.36): C15-20: Lift and Drag Airfoil Model Calibration Test

v. Boundary Layer Measurements

The other testing experiment is the boundary layer thickness model. We observed the BL thickness and measured it from the surface of the designated models. Two models are tested in the wind tunnel, smooth and rough, as shown in Figure (3.37).

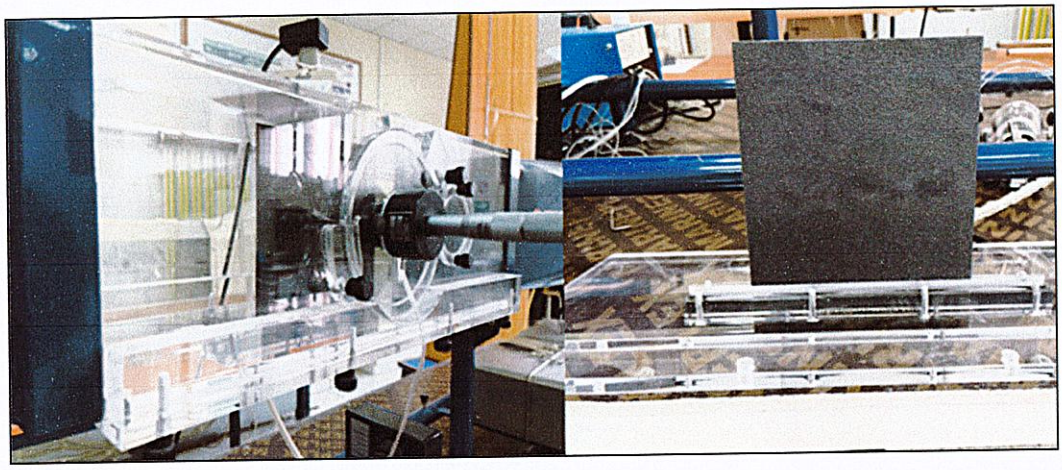


Figure (3.37): Boundary Layer Experiment Set

The concept of the experiment is measuring the velocity of adjacent flow to the pitot probe depicted in Figure (3.38). The velocity keeps rising when moving away from the adjacent surface until it becomes constant, indicating reaching the free air stream velocity.



Figure (3.38): Boundary Layer Probe Used in BL Experiments

The development of friction drag implies that there is a force exerted by the fluid on the body. In exerting this force, the fluid itself is slowed. The slower fluid particles at the body surface then exert a drag force on the faster fluid particles further away from the body. Although in theory the boundary layer is infinite, in practice the significance of the slowing of fluid particles (the effect of viscosity) reduces with distance from the boundary layer. It is usually assumed to be the region in which the flow velocityis less than 99% of the free stream velocity which is 35 m/s ±2 m/s. The thickness of the pitot tube is measured by Vernier Scale gauge shown in Figure (3.39) and found less than 1 mm thickness, so we considered the pitot thickness ≈ 0 mm.



Figure (3.38): Boundary Layer Probe Used in BL Experiments

Moving the probe tube away from the plate's surface increases the velocity of indicated air stream until it reaches free air stream velocity. This phenomenon is the main attribute of the boundary layer. The boundary

layer thickness δ is the distance travelled away by the pitot probe from the plate's surface. The thickness of the laminar boundary layer is proven to be smaller than the thickness of the turbulent boundary layer (Anderson J. D., 2017). A better understanding of the surface roughness impact on all aerodynamic characteristics will arise by measuring δ of the BL for our four models with different surface roughness values. The BL thickness will lead to anticipating the natural experimental effect of surface roughness on influencing the adjacent flow and developing the boundary layer from laminar to turbulent. Figure (3.39) depicts the effect of surface roughness on the moving transition region of BL upstream (Kadivar, Tormey, & McGranaghan, 2021). As we augment ks, the transition region from laminar to turbulent BL moves upstream with a certain amount, and we will verify that in the BL thickness experiment.

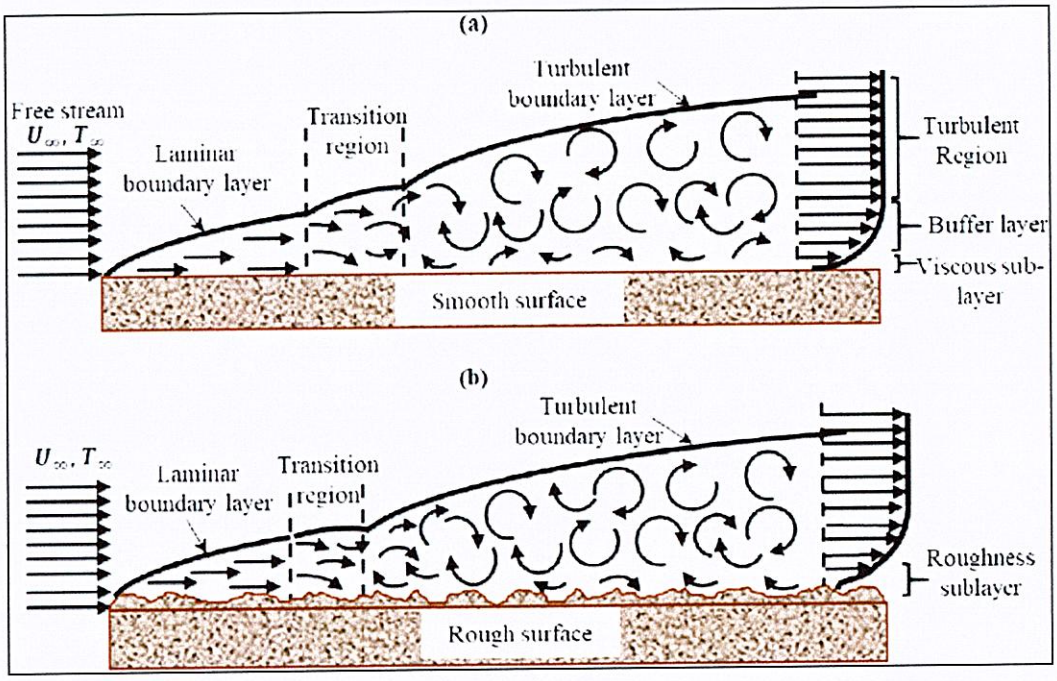


Figure (3.39): Surface Roughness Effect on Boundary Layer (Kadivar, Tormey, & McGranaghan, 2021)

We carried out two experiments to calibrate C-15 Wind Tunnel. Technical manual steps followed in each experiment. The results were identical to the per-calculated results for each standard model. Finally, we completed the calibration of that Wind Tunnel.

vi. Testing of the Rig

The wind tunnel operated for every model with fan speeds: 60%, 70%, 80%, 90%, and 100%. These fan speeds generate airflow speeds of 20, 23, 27, 30, and 35 m/s ±2 m/s, the maximum obtainable speed from the fan speed control unit, as presented in Table (3.9). We positioned the models at 0 degrees, 5 degrees, and 10 degrees angles of attack ±0.2 for every model per fan speed. The test is carried out twice for each of the four models to ensure the same output results. Figure (3.39) exhibits the tested model inside the wind tunnel's test section.

Table (3.9): C-15 Wind Tunnel Inlet Fan Speed Equivalent Inlet Velocities

Fan power percentage (%)	Inlet velocity (m/s) ±2 m/s
60	20
70	23
80	27
90	30
100	35

3.7 Experimental Procedures and Uncertainty

In our experiments, we maintained the same boundary conditions in testing every model: velocity, pressure, temperature, and Reynolds

number. However, despite that, some differences are noticed in each model's results. As a result, we computed the uncertainty percentage for our experiment.

The model shape, blockage area and the angles of attack impacted the maximum air speed inside the wind tunnel.

3.7.1 Experimental Procedures

i. Lift and Drag Experiment

1. All connections and preparations should be made at the beginning, as shown in Figure (3.39), including:
   a) The USB wire is linked to the (IFD 7), Electronic Manometer Bank, and (PC), as seen in Figure (3.31).
   b) All models: We connected all four different ks airfoil models pictured in Figure (3.34) to the fixing bar.
   c) We fixed the models without a gap between the model and the balance device.
2. The wind tunnel software program in the (PC) is switched on to running mode.
3. The (IFD 7) and Electronic Manometer Bank are switched ON.
4. Before beginning the experiment, the wind tunnel software application's drag and lift force parameters were set to zero.
5. The fan is turned on in standby mode at its lowest speed, progressively increasing until it reaches the required speed for each trail.

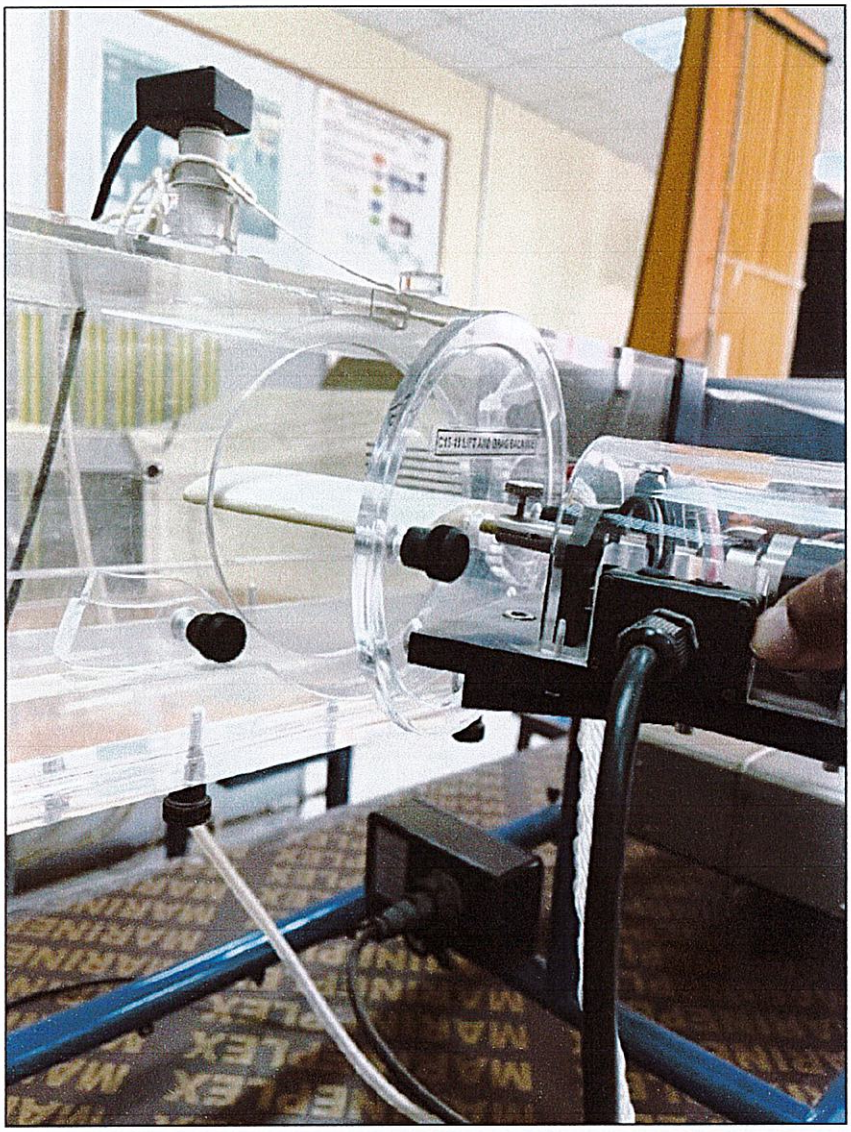


Figure (3.39): Airfoil inside Wind Tunnel's Duct

6. The inclination angle is changed after recording each data set for every speed.
7. The lab's air temperature indicator is set at 24 degrees Celsius to match the ambient temperature.
8. After every trial, the data is recorded.

ii. Boundary Layer Experiment

1. All connections are prepared as shown in Figure (3.40).

2. The boundary layer probe is adjecant to the airfoil lower surface and connected to the computer unit (IDF 7).
3.

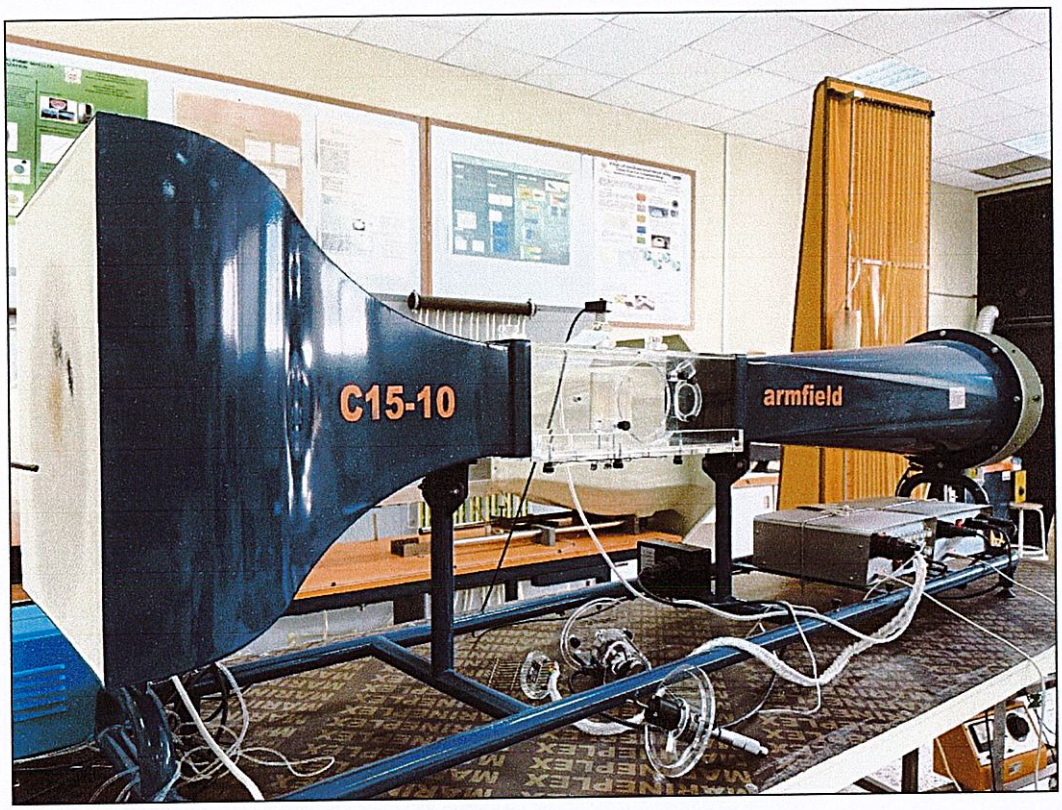


Figure (3.40): BL Experiment Setup

4. The lower surface of the test area is replaced by the BL setup mount, as seen in Figure (3.41).
5. The models are mounted with special rods to fit in the fixture, as illustrated in Figure (3.42).
6. The model is centered in the middle of the testing area, as shown in Figure (3.43).
7. The probe is fitted adjacent to the airfoil's lower surface initially. Then, the micrometer is turned counterclockwise on every trail (1 complete turn = 0.1mm).
8. Data was recorded every trial until velocity remained constant.

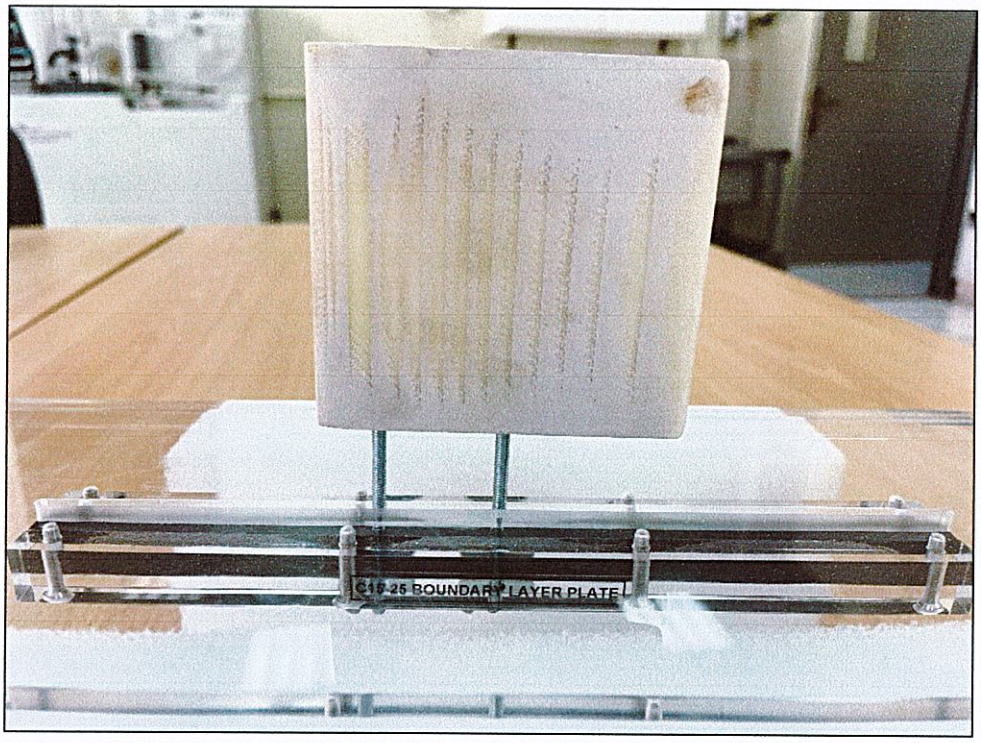


Figure (3.41): BL Experiment Fixture

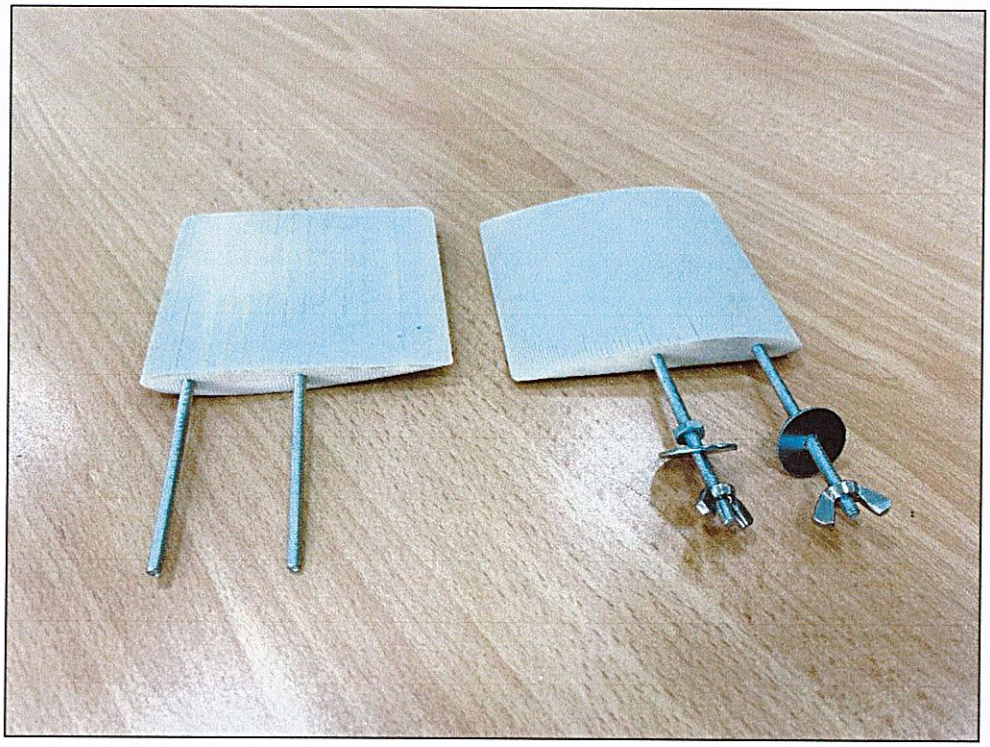


Figure (3.42): BL Experiment Model Setup

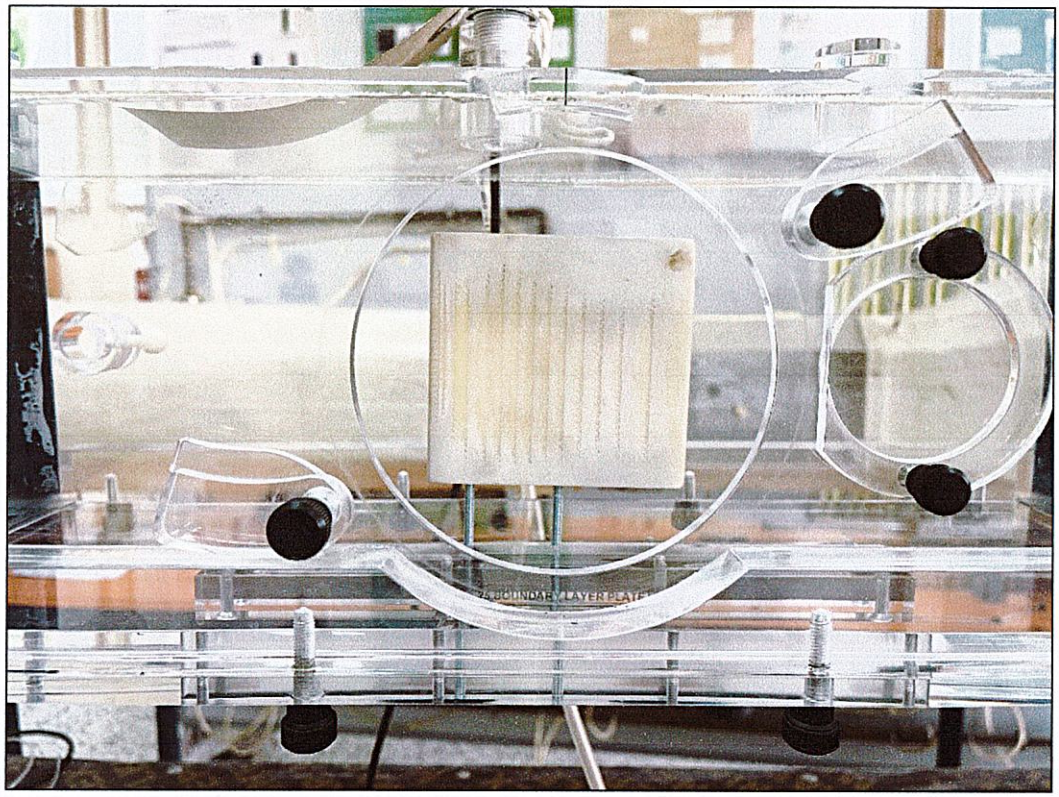


Figure (3.43): Model Placement in BL Experiment

3.7.2 Uncertainty Analysis

The same experiment is done twice for each trial to confirm the reliability of the data generated and to assess the precision and error % of our measurements. Additionally, the practical solution's uncertainty was analyzed about the numerical result using Fluent Ansys 2020 R1.

The free air velocity inside the wind tunnel oscillated $\pm 2\ m/s$. The model blockage area caused differences in the values of drag and lift coefficients ±3 %. Appendix (F) illustrates all experiments trail done in our investigations.

Appendix (E) also presents a detailed analysis of each measurement's standard uncertainty. The surface area is unclear by ±0.5026%. The estimated inlet velocity uncertainty measurement was ±0.1343%. For the smooth airfoil, the uncertainty of the drag coefficient measured at zero angles of attack was determined to be ±5.22%%. The

results on the lift coefficient revealed that the simple airfoil had a value of ±5.01%.

The total drag and lift coefficient calculations show uncertainty resulting from fluctuating errors. Beckwith derived these uncertainties from Beckwith's formula (Beckwith, Marangoni, & V, 2011).

$$U_R = \pm \sqrt{\sum_{i=1}^{n} \frac{\partial R}{\partial x_i} U_{x_i}} \quad (33)$$

U_R is the uncertainty of the measured value R, and U_{x_i} is the uncertainty of a given variable x_i based upon R.

3.8 Summary

Two sets prepared of models with applied roughness scripts for numerical calculations. One set consists of ten models with ks from 0.05 mm to 0.5 mm. The second set has four other models with ks from 1 mm to 4 mm. Carefully setting up all boundary conditions, and the turbulent model with SST K- ω adopted.

Two experiments conducted in this research: C_L and C_D experiment and BL thickness experiments in a two-dimensional horizontal wind tunnel with low subsonic speed. The Boundary conditions selected to be at sea level.

This chapter explains the work methodology and the results revealed in Chapter (4).

Chapter Four
Results, Discussions, Conclusions and Recommendations

4.1 Introduction

4.2 Results

4.3 Discussion

4.4 Conclusion

4.5 Recommendations

Chapter Four

Results, Discussions, Conclusions and Recommendations

4.1 Introduction

In this chapter, we will publish the results of our study, followed by a detailed discussion of different aspects of obtained results. Then we will demonstrate the study's conclusion and advise future suggested work.

4.2 Results

For discussion, we will prepare the results from Numerical and Experimental methods for our different ks models of the NACA 4412 airfoil. We used various velocities and various angles of attack α per testing trail. We tested a total of 244 unique setup models separately. The numerical results of 180 different setup models will focus on L (C_L), D (C_D) and L/D (C_L/ C_D). After that, we will view Another 60 experimental setups of four models' results for L (C_L), D (C_D) and L/D (C_L/ C_D). Finally, we will carry out four different setup models of experimental BL thickness measurements, and we will exhibit results and verified analytically by governing equations.

4.2.1 Numerical Results

After setting up 15 different ks models in Fluent Ansys 2020 R1, we will run each model 12 times. We will determine each model's L (C_L), D (C_D) and L/D (C_L/ C_D) for three different angles of attack α (0°, 5°, and 10°) and four different velocities (150 m/s, 200 m/s, 250 m/s, and 300 m/s). We performed 1000 iterations for every program simulation process as the

maximum iteration number for each trial. The turbulent flow model with $k-\omega$ is sensitive and challenging to control the residuals within $\mp 10^{-6}$ errors due to the nature of the model. The smooth airfoil is the only solution that converged with this accuracy, while other applied k models converged within $\mp 10^{-3}$ errors. However, we run all applied ks models until 1000 iterations with residuals accuracy $\mp 10^{-6}$ error. Appendix (C) lists Fluent Ansys 2020 R1 solution iterations for different airfoil models at V=300m/s and α=0°.

i. The Lift coefficient (C_L)

Lift Coefficient is obtained from Fluent Ansys 2020 R1 for a smooth surface and set 1 and 2 roughness heights. Figure (4.1) displays the change in C_L values with increasing the velocity from 150m/s, 200m/s, 250m/s and 300m/s for set 1 different surface roughness heights at α=0°. C_L was highest at ks = 0.15 mm for all test speeds.

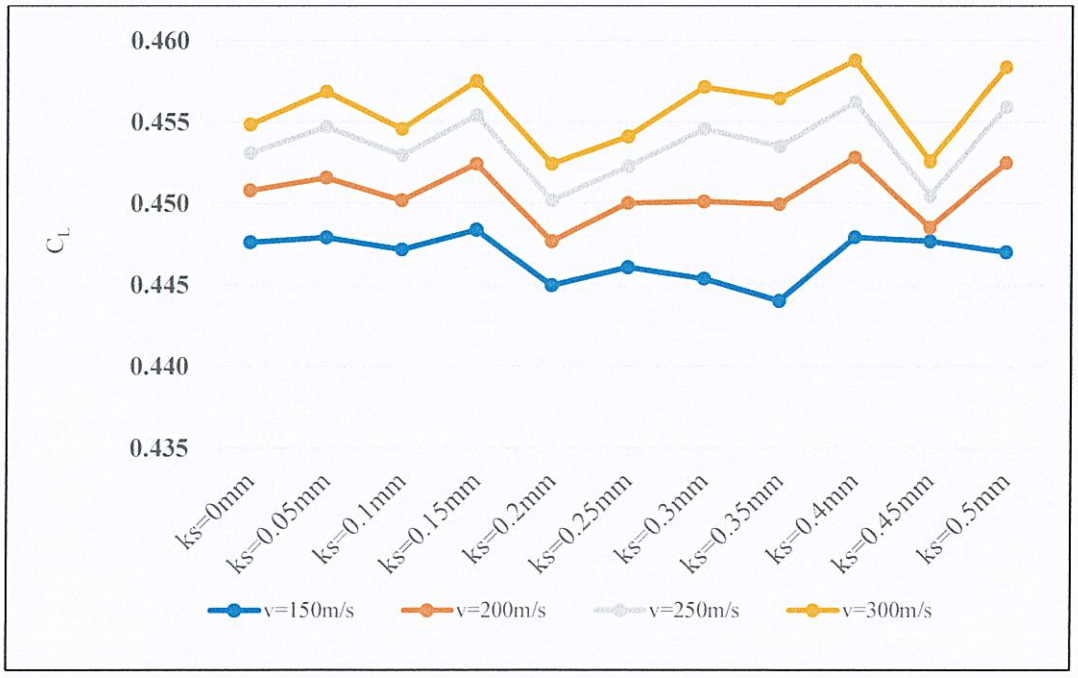


Figure (4.1): First Set Lift Coefficient C_L at α=0°

Figure (4.2), at $\alpha = 5^{o}$, shows a significant increase with values of C_L of approximately 50%. At this angle of attack, the highest C_L occurred for smooth airfoil at ks = 0 mm for all speeds.

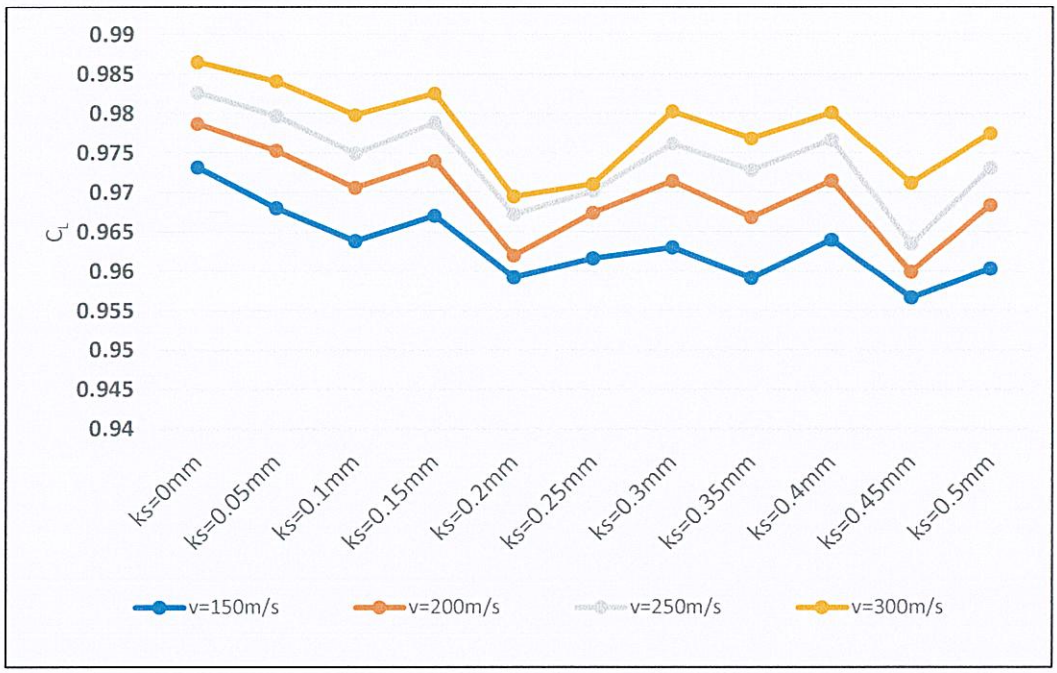


Figure (4.2): First Set Lift Coefficient C_L at $\alpha=5^{o}$

Moreover, at $\alpha = 10^{o}$ increment depicted in Figure (4.3) was enough to increase C_L by more than 50% compared to those at $\alpha = 5^{o}$. At this angle of attack, the highest C_L occurred for the airfoil at ks = 0.25 mm for all speeds.

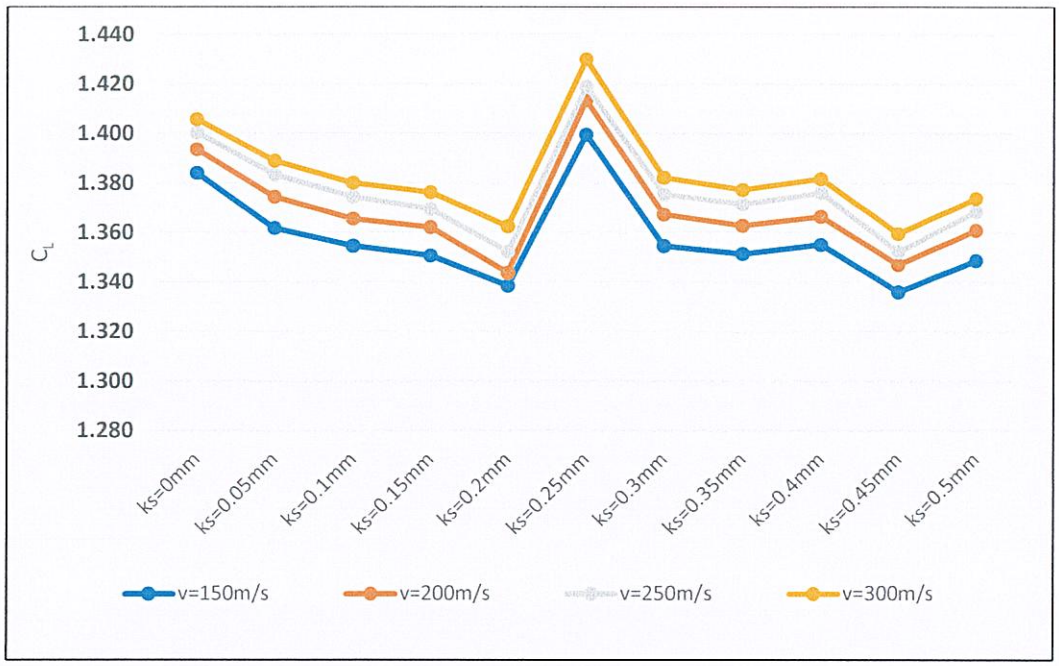


Figure (4.3): First Set Lift Coefficient C_L at α=10°

Figures (4.4), (4.5), and (4.6) illustrate the consequence of increasing α for 5° and 10° on set 2 of applied ks for the different velocities examined in the study. The C_L values at α = 0 are highest at ks = 3 mm and rise with advancing velocities. The C_L values rose by approximately twice their values at α = 5° at ks = 3 mm. However, at α = 10°, the highest CL values were again more considerable than those at α = 5°. We observed that the most elevated C_L was for the smooth plain foil at ks = 0. As ks values increased from 1 mm to 3 mm, C_L values remained almost constant and declined afterwards at ks = 4 mm for the different test velocity values.

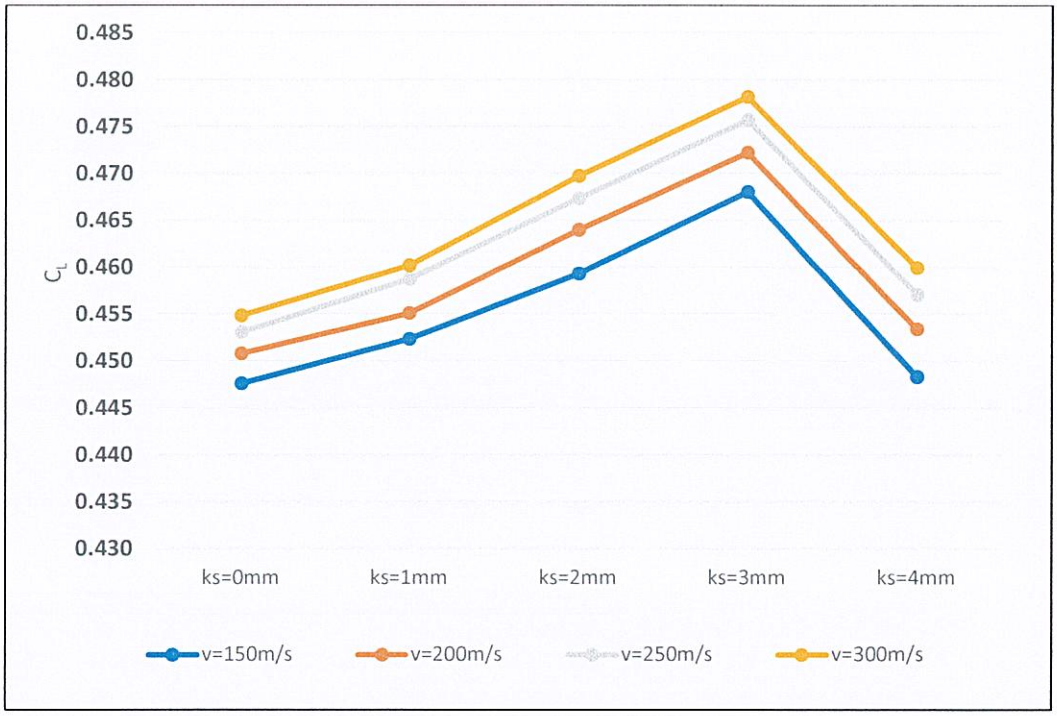


Figure (4.4): Second Set Lift Coefficient C_L at $\alpha=0^o$

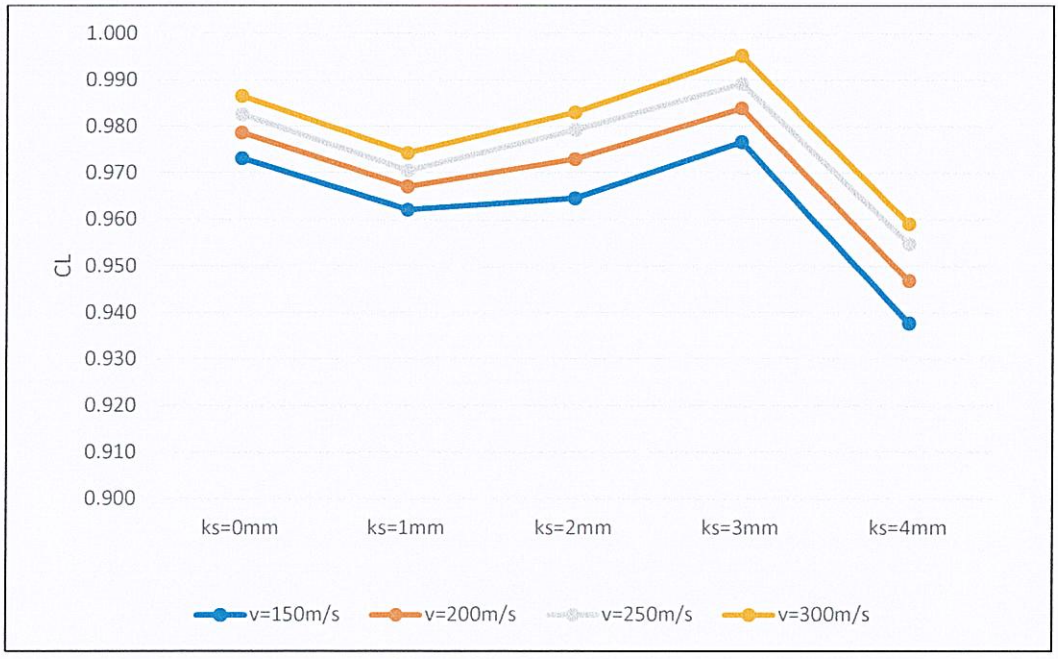


Figure (4.5): Second Set Lift Coefficient C_L at $\alpha=5^o$

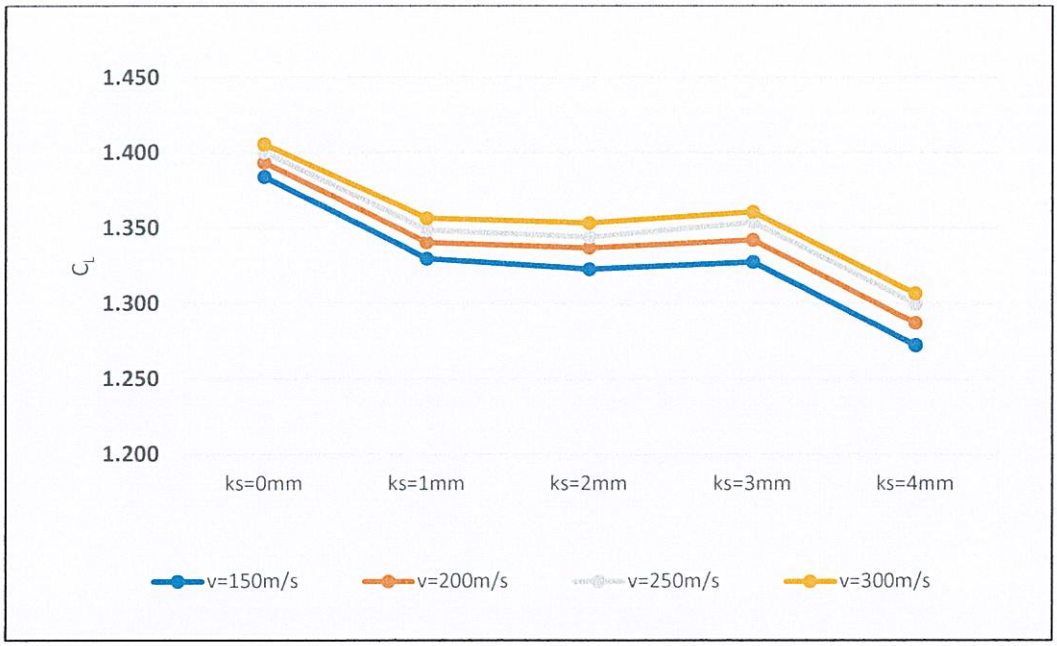


Figure (4.6): Second Set Lift Coefficient C_L at α=10°

Increasing applied ks in set 2 of applied k_s is more sensitive with the has shown immense values of C_L compared to set 1. We will discuss this in detail in the discussion section.

ii. Drag Coefficient (C_D)

The Drag Coefficient results from Fluent Ansys 2020 R1 for smooth surface, set 1 (ks = 0 to 0.5 mm) and set 2 (ks = 0 to 4 mm) roughness heights appear next. Figures (4.7), (4.8), and (4,9) demonstrate the change in C_D values with advancing the velocities from 150 m/s, 200 m/s, 250 m/s to 300 m/s for set 1 different ks at α = 0°, 5°, and 10°.

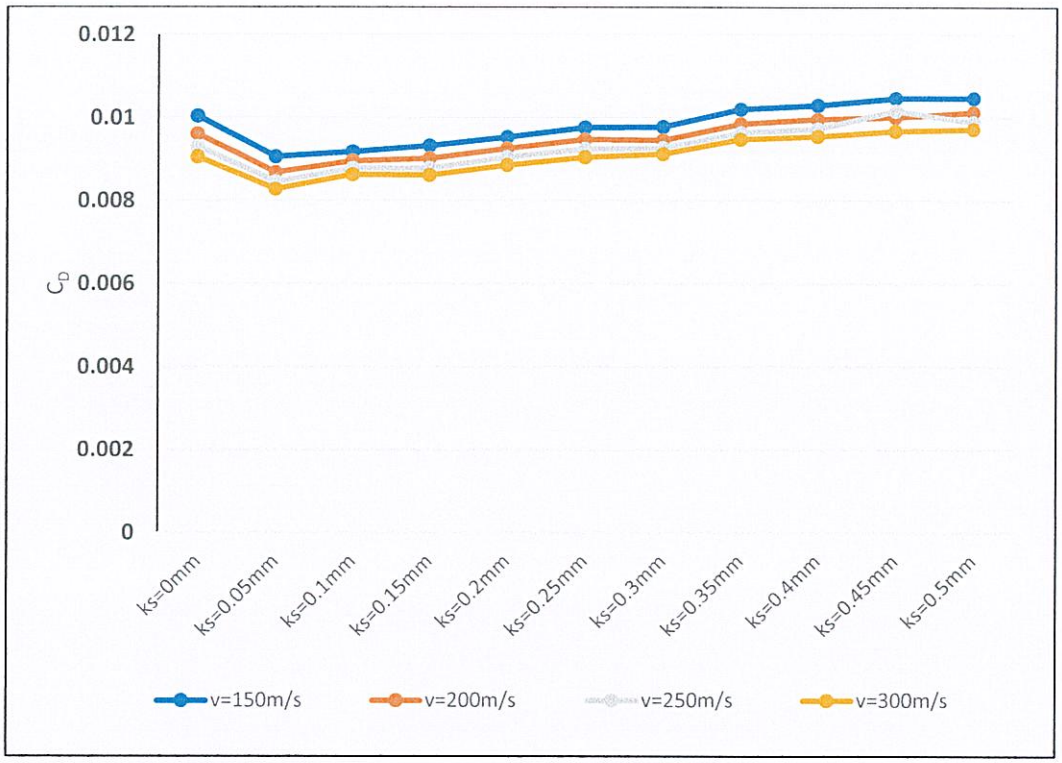


Figure (4.7): First Set Drag Coefficient C_D at $\alpha=0^o$

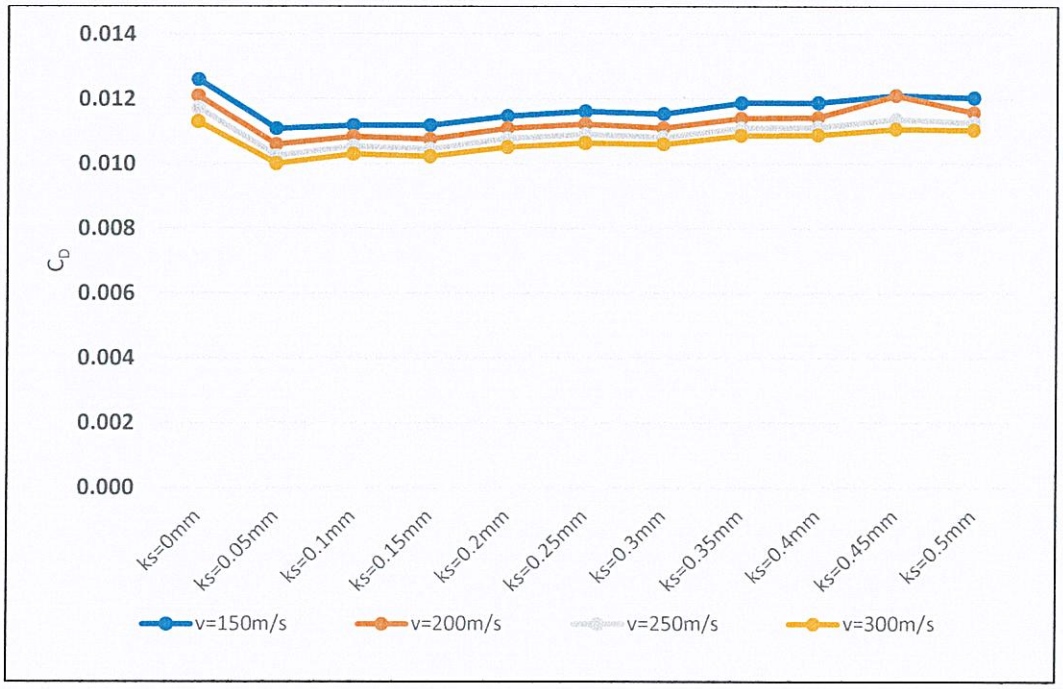


Figure (4.8): First Set Drag Coefficient C_D at $\alpha=5^o$

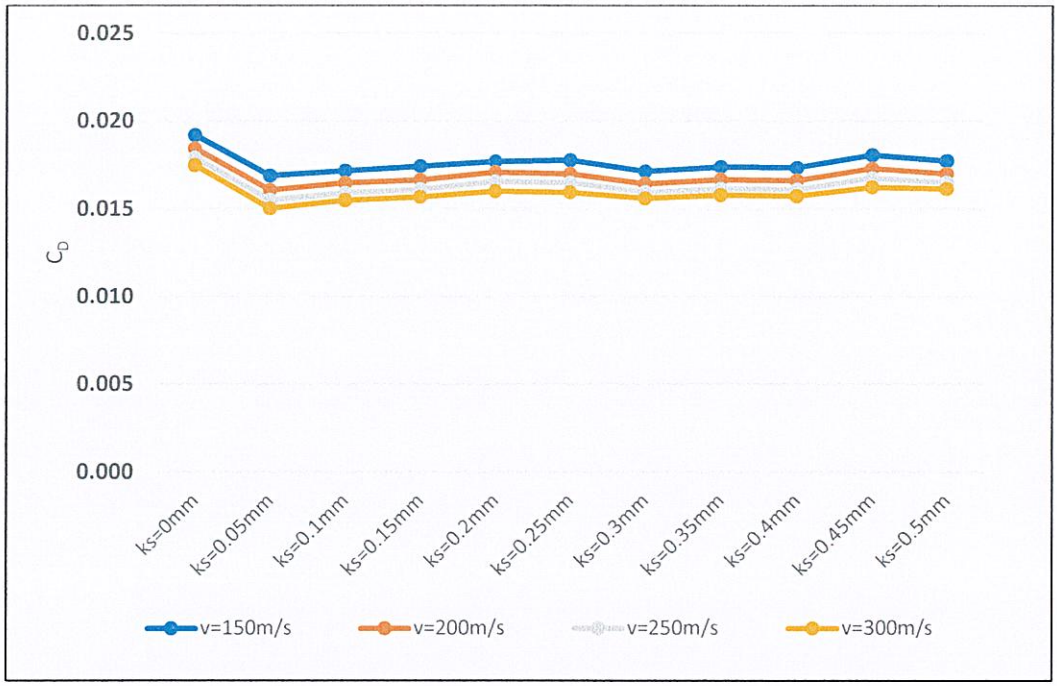


Figure (4.9): First Set Drag Coefficient C_D at $\alpha=10^o$

The results of C_D with raised ks are smooth and prominent. Set 1 of applied ks at different angles of attack shows a direct correlation between ks and C_D. We observed that C_D values dropped at higher velocity values. This drop will enforce our hypothesis and enrich the discussion in the following sections.

Set 2 of applied ks interaction with varying velocities. Figures (4.10), (4.11), and (4.12) exhibit velocities at various α. Vice versa is evident in the second set of applied ks. We noticed a significant increase in C_D values with all velocities and different α. In addition, we noted a progressive increment of C_D with larger applied ks.

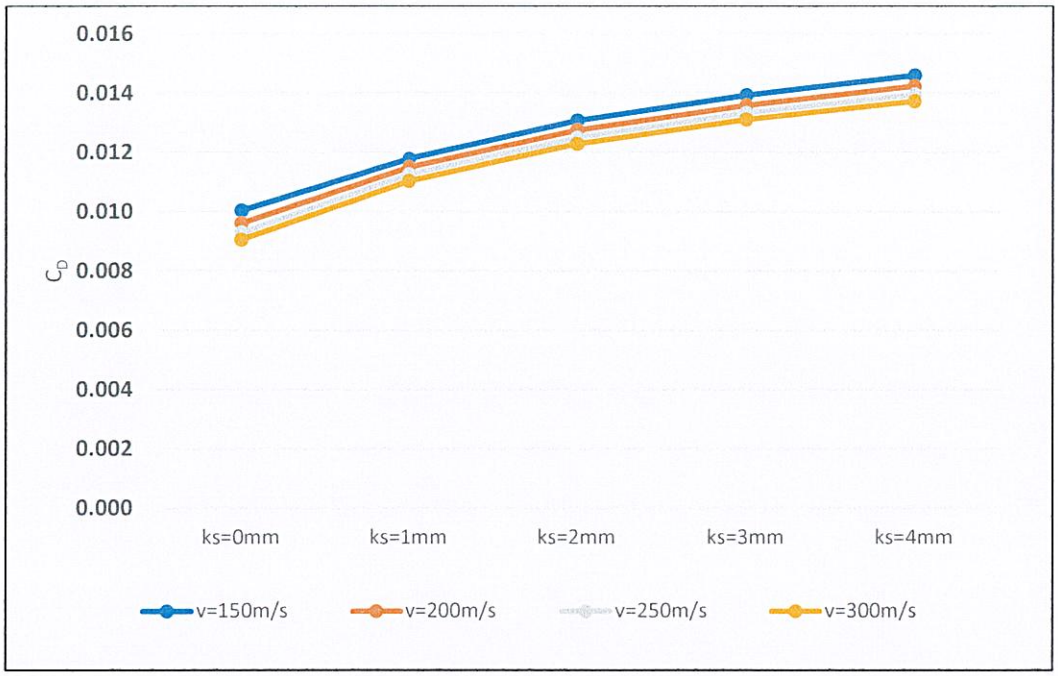


Figure (4.10): Second Set Drag Coefficient C_D at $\alpha=0^o$

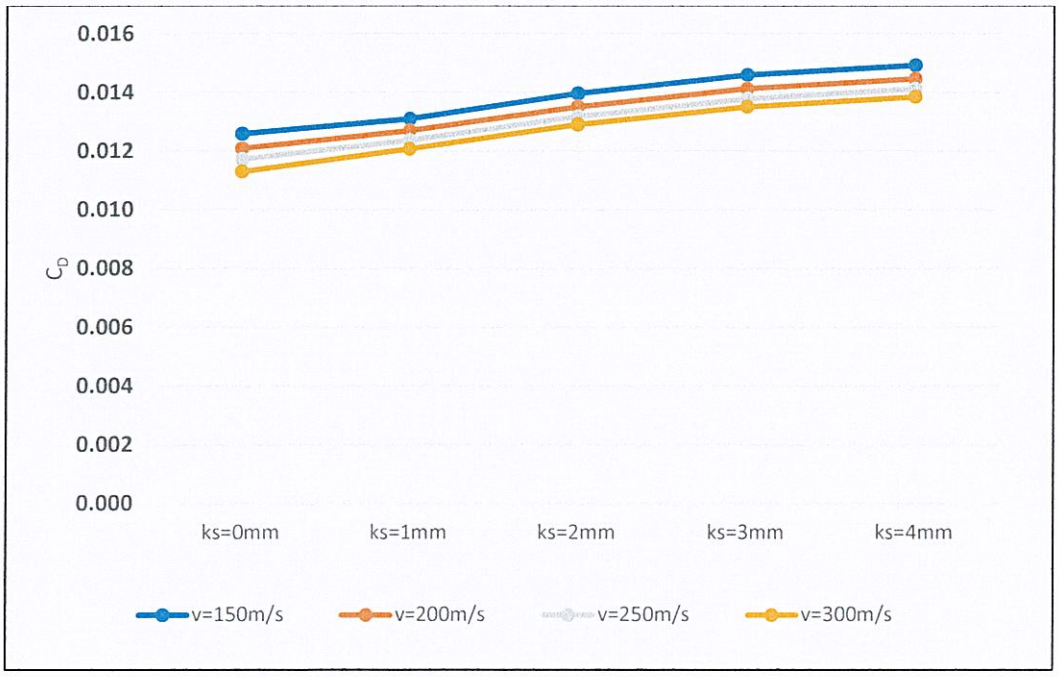


Figure (4.11): Second Set Drag Coefficient C_D at $\alpha=5^o$

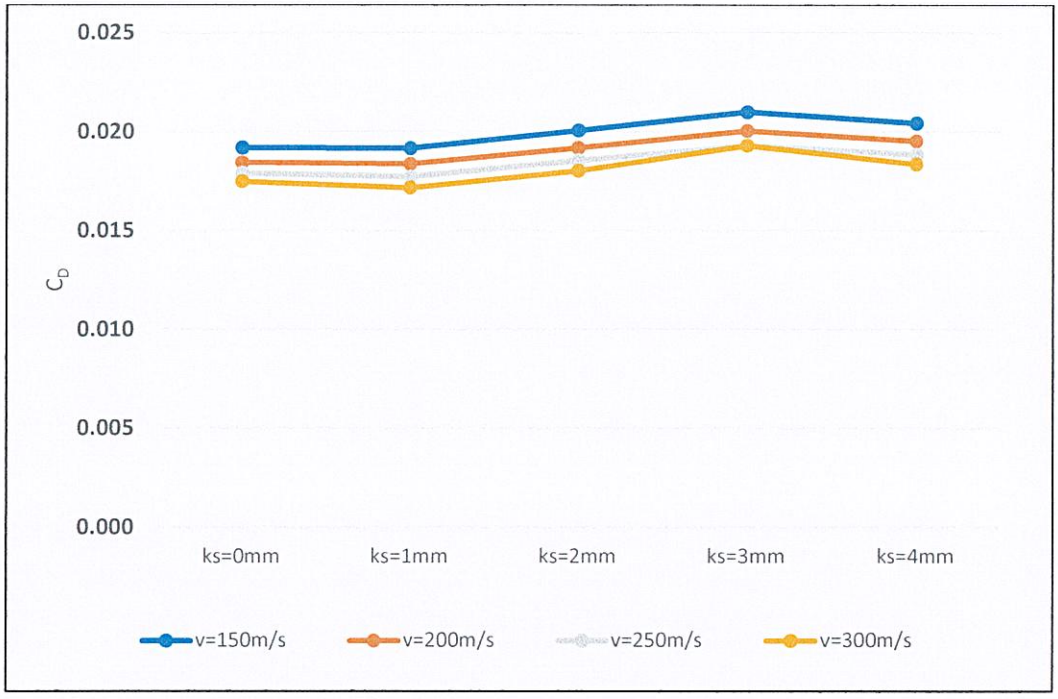


Figure (4.12): Second Drag Coefficient Set C_D at $\alpha=10^o$

iii. Lift to Drag Ratio (C_L/C_D)

The Lift to Drag Ratio (C_L/C_D) is the most critical indication of characteristic aerodynamic improvement acquired earlier in chapter (3) under our hypothesis. Set 1 of applied ks resulted in positive (C_L/C_D) values. Figures (4.13), (4.14), and (4.15) show that (C_L/C_D) values are sensitive to different applied ks values. It was obvious that (C_L/C_D) increased at ks = 0.05 mm for all velocities and angles of attack α. The ratio advanced from $\alpha = 0$ to 5^o and returned to its approximate values at $\alpha = 10^o$. We also recorded that the ratio is almost unchanged from ks = 0.1 mm to 0.5 mm. All C_L/C_D values for the roughened surfaces increased by approximately 14% over their smooth surfaces' counterparts.

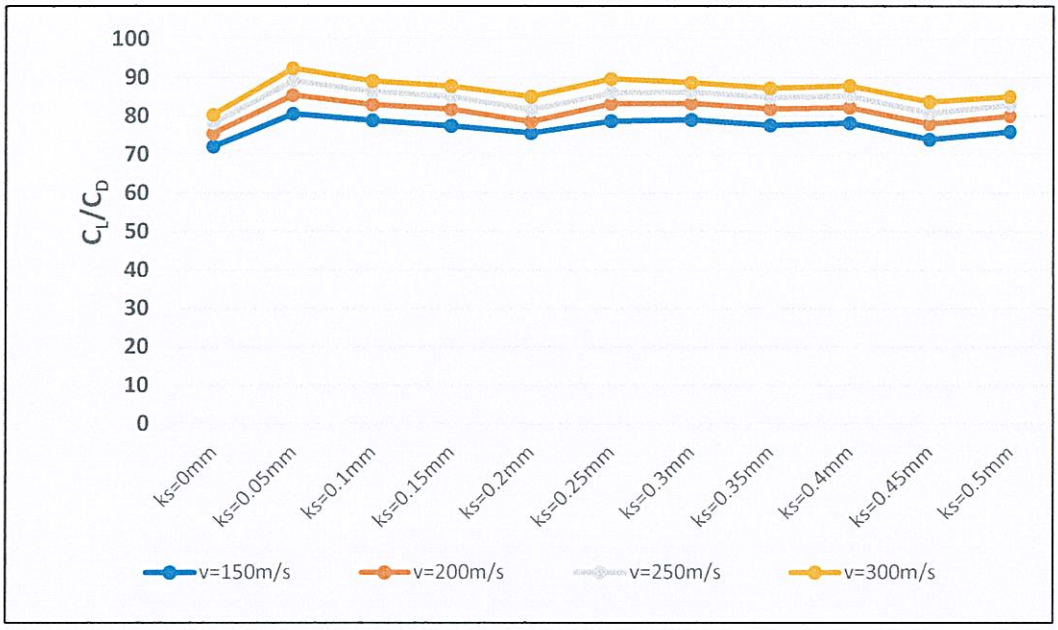


Figure (4.13): First Set Lift to Drag Ratio (C_L/C_D) at α=0°

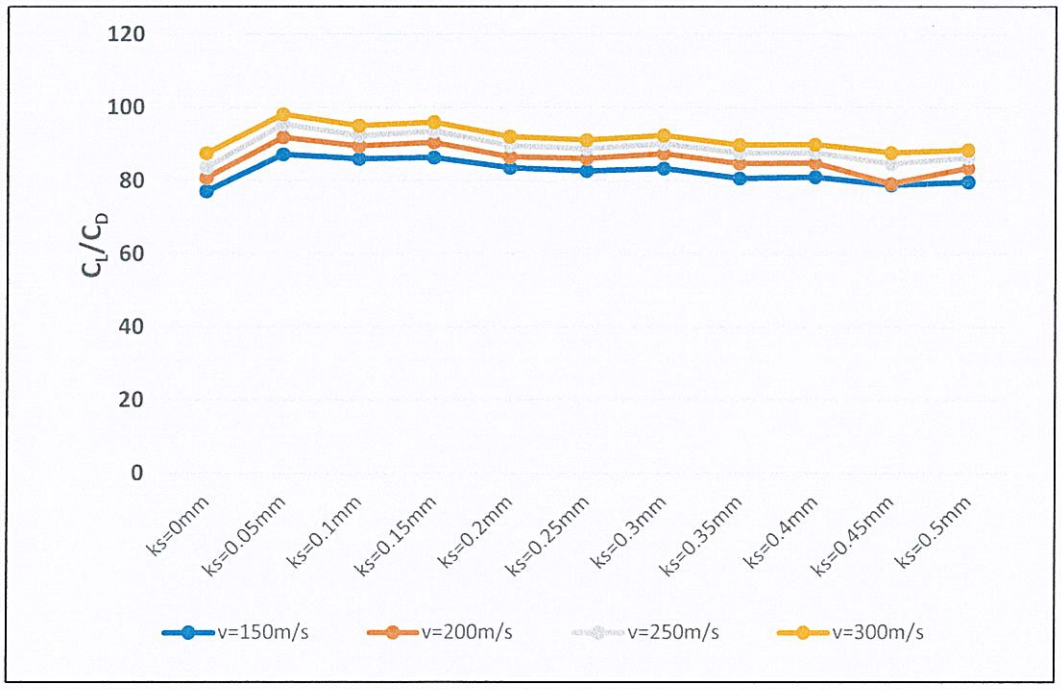


Figure (4.14): First Set Lift to Drag Ratio (C_L/C_D) at α=5°

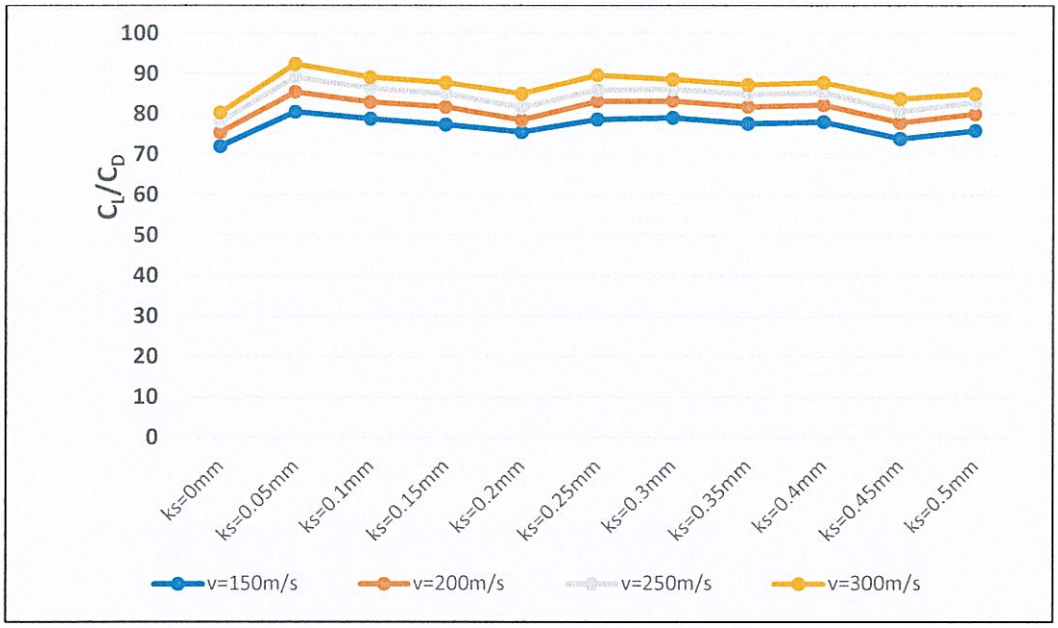


Figure (4.15): First Set Lift to Drag Ratio (C_L/C_D) at $\alpha=10^o$

The results of (C_L/C_D) for set 2 applied surface roughness ks are discouraging. We noticed a clear drop of (C_L/C_D) values with an increment of ks for all different velocities at all angles of attack α, as illustrated in Figures (4.16), (4.17), (4.18). The drop is noticeable in low velocities for all angles of attack. Furthermore, the roughened surfaces for set 2 have revealed a decreasing C_L/C_D value compared to the plain smooth surface counterpart for all velocities and angles of attack.

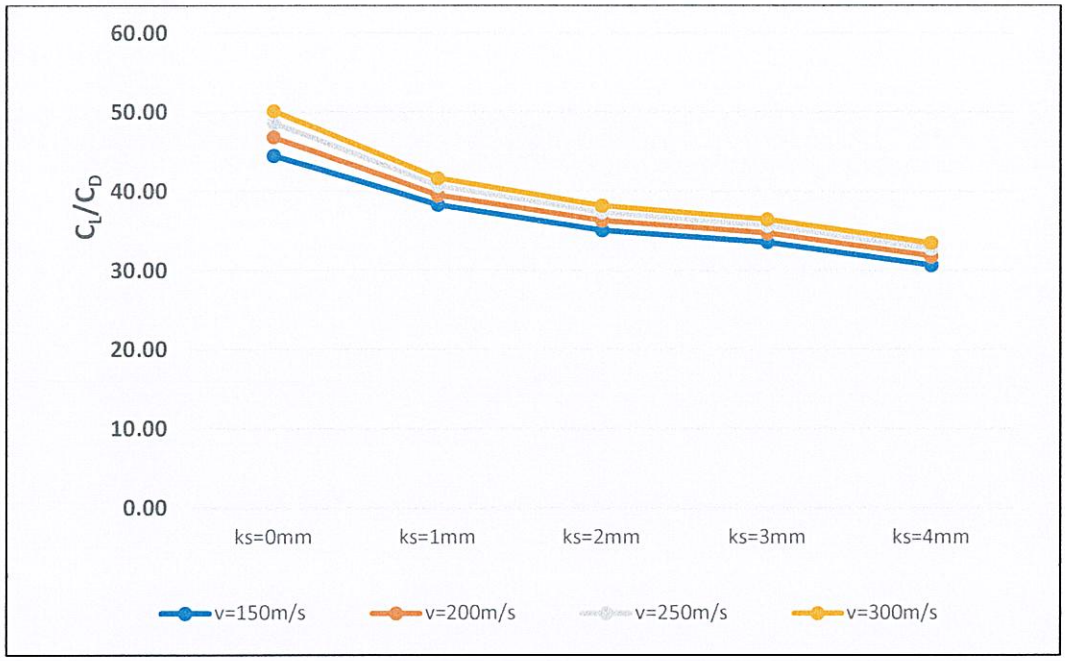


Figure (4.16): Second Set Lift to Drag Ratio (C_L/C_D) at α=0°

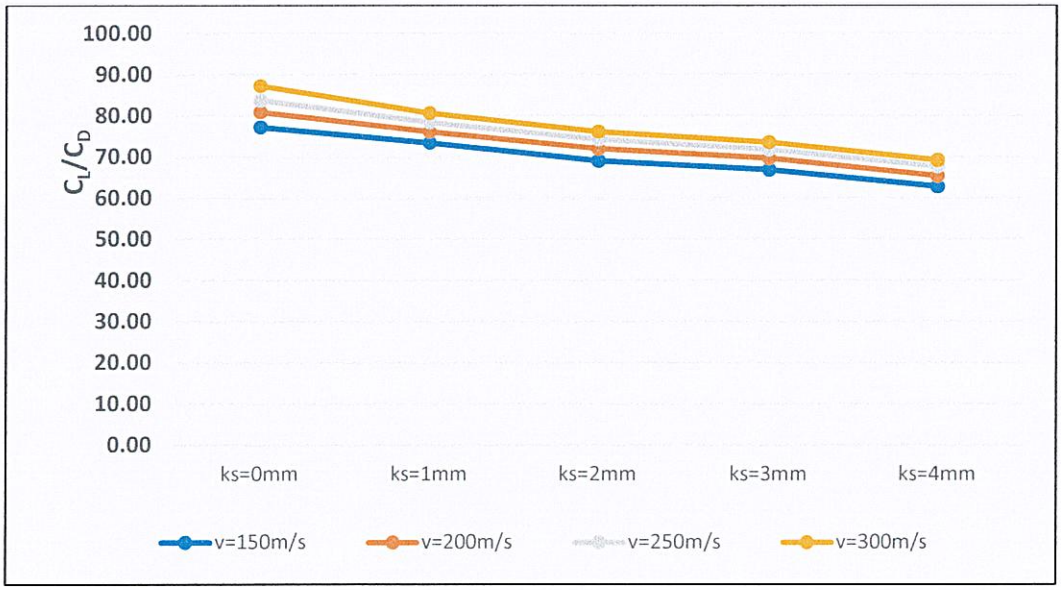


Figure (4.17): Second Set Lift to Drag Ratio (C_L/C_D) at α=5°

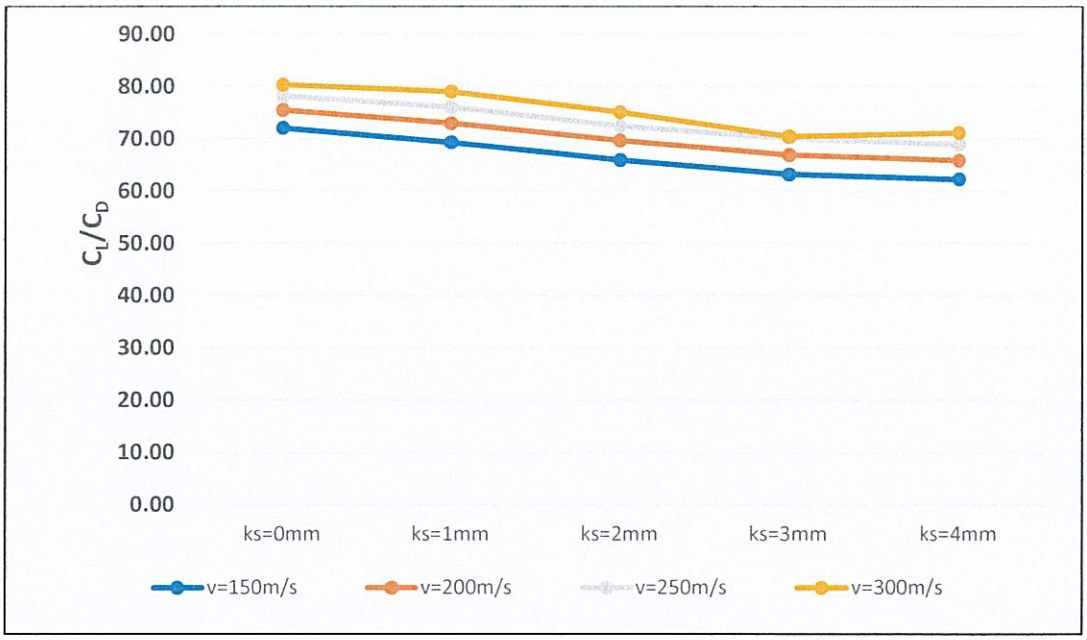


Figure (4.18): Second Set Lift to Drag Ratio (C_L/C_D) at $\alpha=10^o$

iv. Power Analysis

In level flight, we fulfil the following equation:

$$L = W = C_L \frac{1}{2} \rho V^2 A \tag{33}$$

If ρ, L, and A are constants, then $V \propto \frac{1}{\sqrt{C_L}}$ and the power required:

$$P = VD = C_D \frac{1}{2} \rho V^2 A \; V = C_D \frac{1}{2} \rho \frac{1}{C_L} A \frac{1}{\sqrt{C_L}} \tag{34}$$

$$P = \frac{C_D}{C_L^{3/2}} \tag{35}$$

Hence, the larger the value of $\frac{C_L^{3/2}}{C_D}$, the less power is required to operate the flight, which leads to energy conservation. For example, airfoil with ks=0.05mm had the best power conservation for all testing conditions

for set 1 of applied surface roughness ks as presented in Figures (4.19), (4.20), and (4.21).

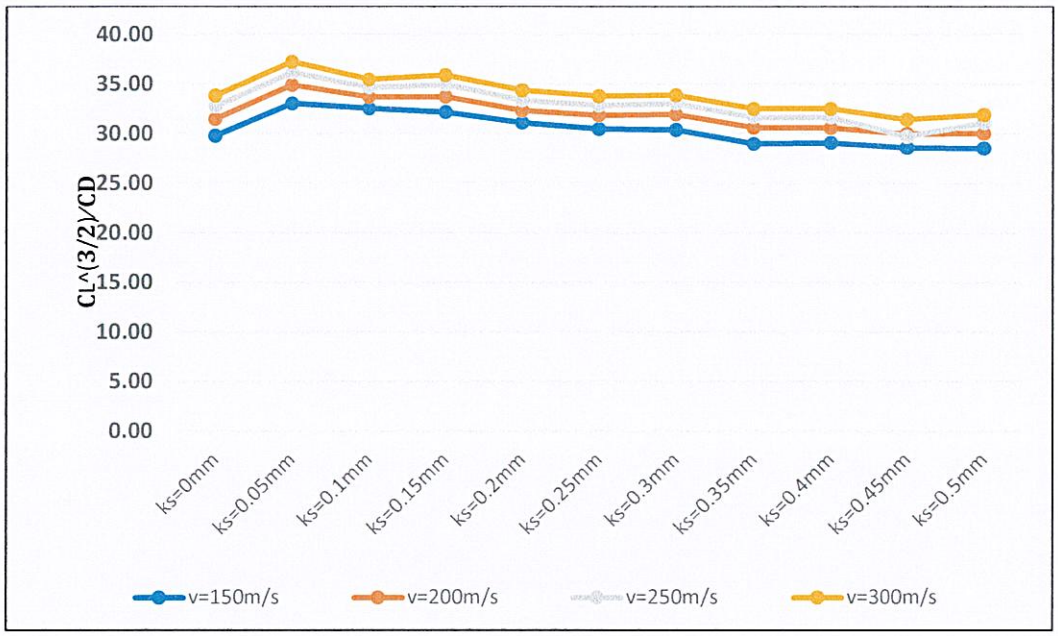


Figure (4.19): Power Analysis $C_L^{3/2}/C_D$ for First Set of ks at α=0°

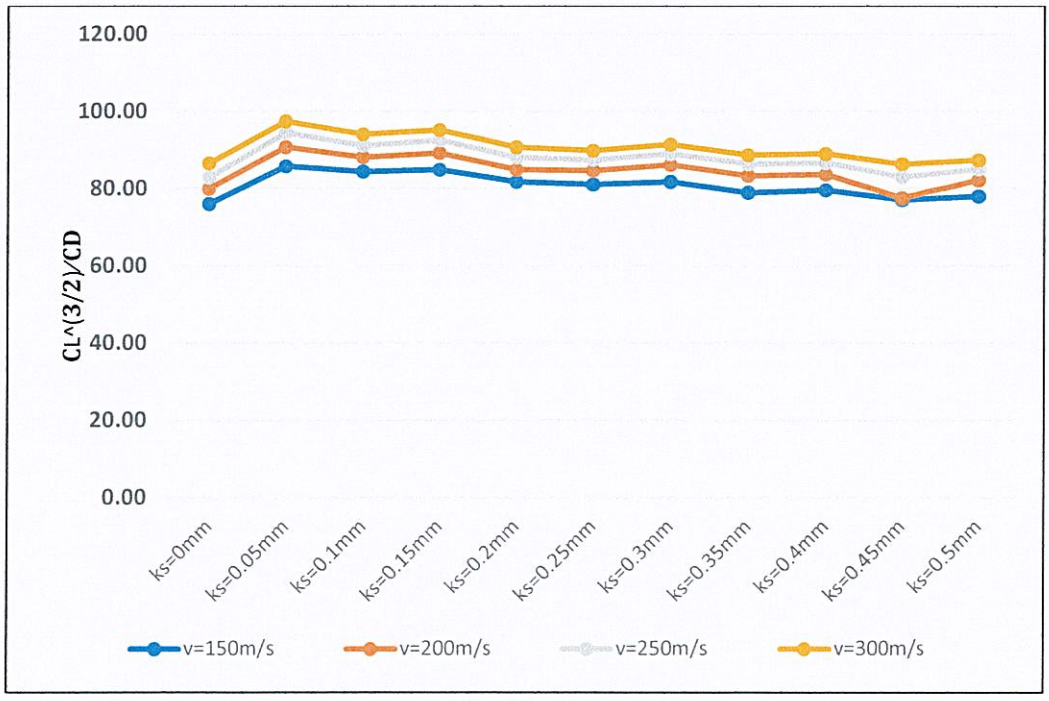


Figure (4.20): Power Analysis $C_L^{3/2}/C_D$ for First Set of ks at α=5°

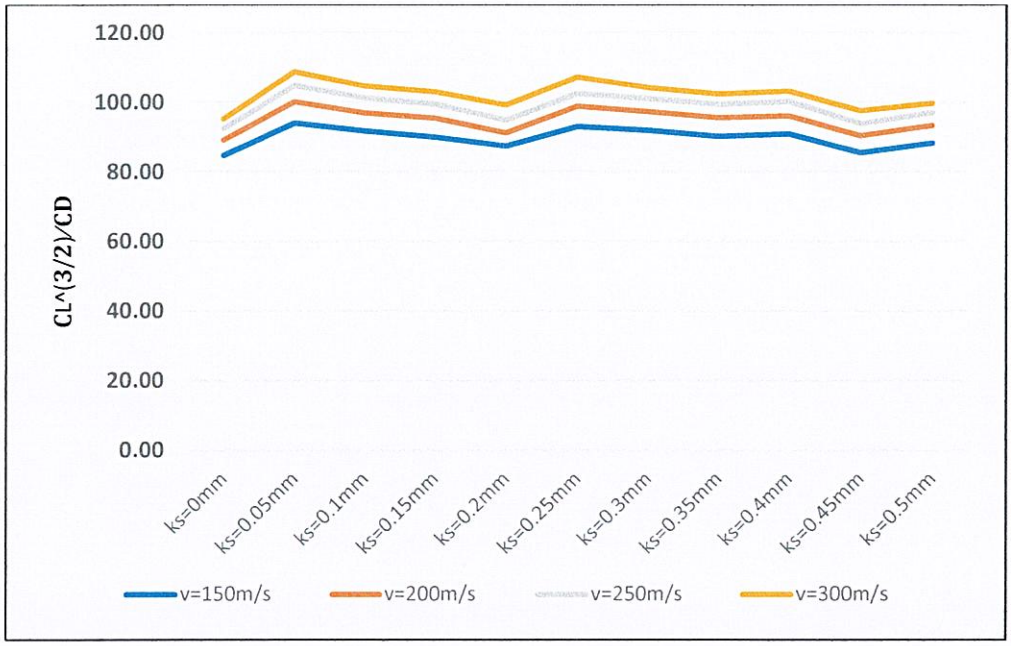


Figure (4.21): Power Analysis $C_L^{3/2}/C_D$ for First Set of ks at α=10°

For set 2 of applied surface roughness ks, the power demanded to run the aircraft will increase as ks increases. Figures (4.22), (4.23), and (4.24) depict these results.

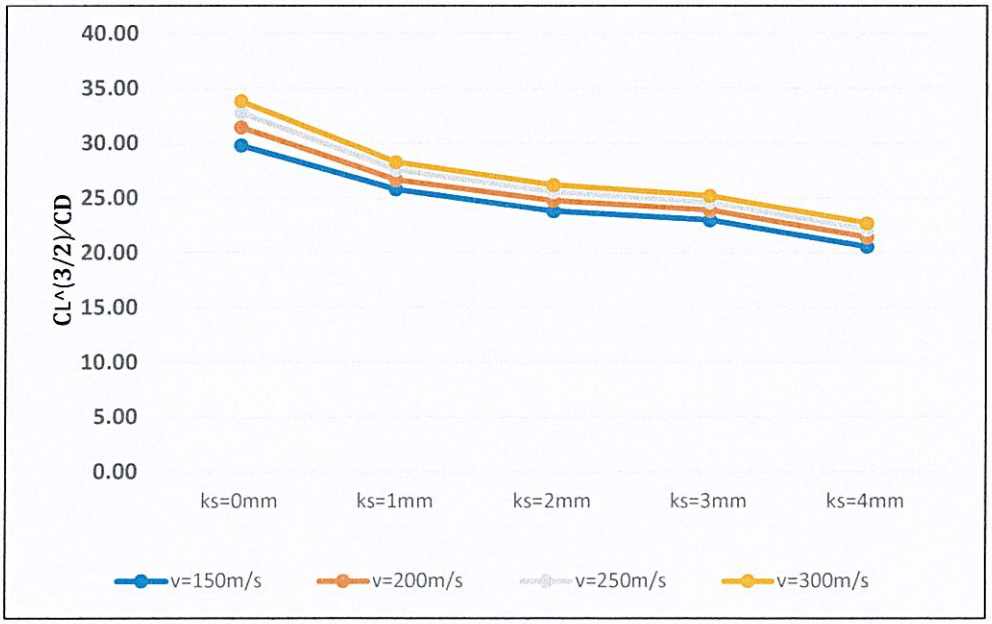


Figure (4.22): Power Analysis $C_L^{3/2}/C_D$ for Second Set of ks at α=0°

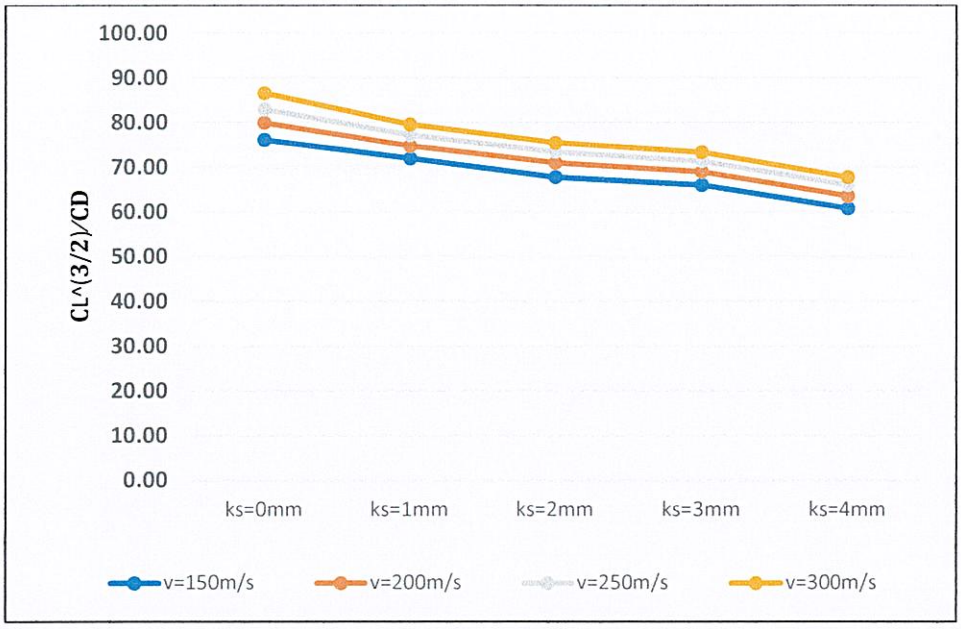


Figure (4.23): Power Analysis $C_L^{3/2}/C_D$ for Second Set of ks at α=5°

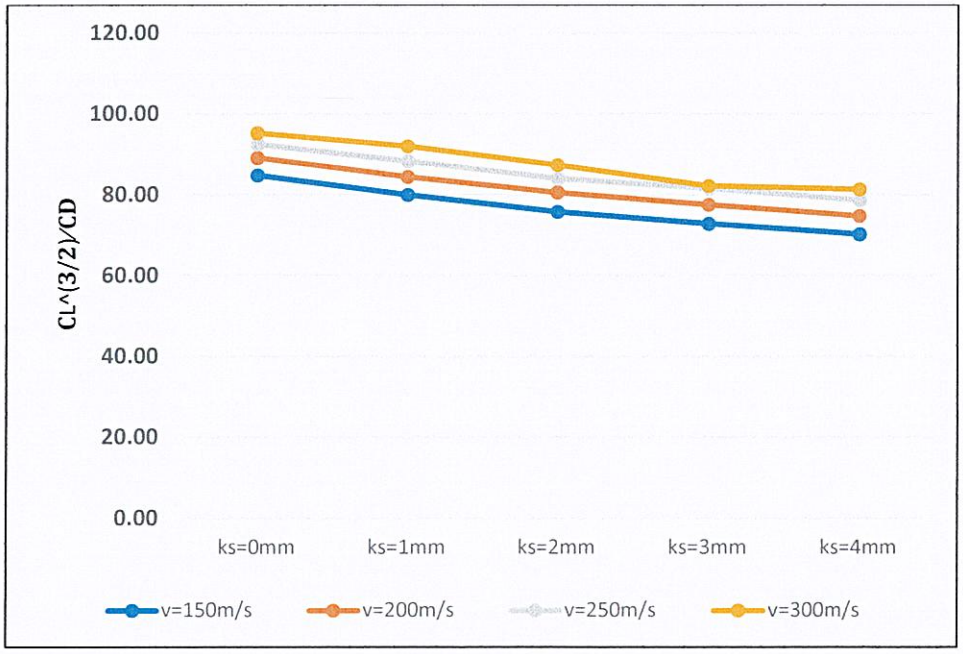


Figure (4.24): Power Analysis $C_L^{3/2}/C_D$ for Second Set of ks at α=10°

4.2.2 Experimental Results

C-15 Wind Tunnel operated in a closed room, a temperature of 24 C at sea level in the Fluid Mechanics Laboratory at the University of Bahrain (Isa Town Camp). We recorded all results twice to verify the accuracy of the data collected. Foremost, we performed two separate experiment setups, as elaborated in Chapter (3):

1- First, lift and Drag Forces Experiments.
2- Boundary Layer Experiments.

The output result's data focused on the following:

1- Lift Coefficient (C_L).
2- Drag Coefficient (C_D).
3- Lift to Drag Ratio (C_L/C_D)
4- Boundary Layer Thickness (BL thickness).

All four different lower surface roughness ks = 0.0258, 0.045, 0.125, and 0.19 mm were tested separately up to 100% fan speed, producing 35m/s $\pm$2m/s in the testing duct. In addition, we tested every model at different angles of attack; α= 0°, 5°, 10° $\pm 0.2^{o}$. Finally, we generated the results and will specify them in the following sections. Appendix (G) lists the full experimental results of the C-15 wind tunnel.

i. Lift Coefficient (C_L)

Under specified operating conditions, we measured C_L and revealed results in Figures (4.25), (4.26), and (4.27). The impact of surface roughness transition is evident despite of low speed of the wind tunnel. The boundary conditions of the wind tunnel simulate level flight at sea level. The tests revealed that C_L raised as α advanced from 0° to 10°. In addition, C_L increased with increasing tunnel test speeds. The most elevated C_L

values are observed at the lowest roughness of $k_s = 0.0258$ mm, at the angle of attack $\alpha = 5^o$ in the approximately cruising speed condition.

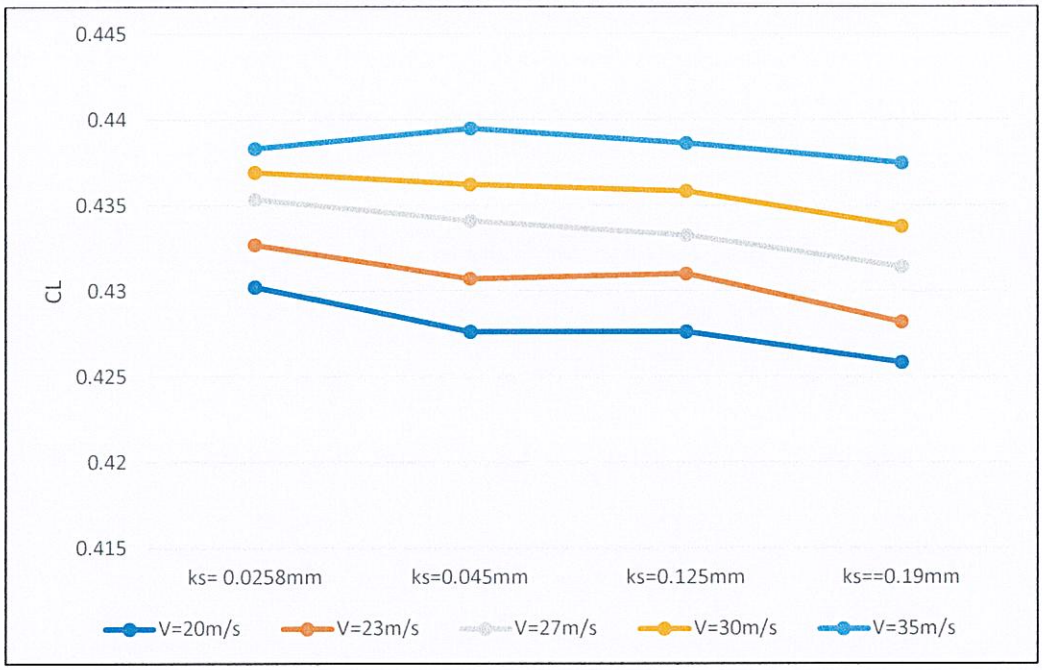


Figure (4.25): Experimental Lift Coefficient C_L at $\alpha=0^o$

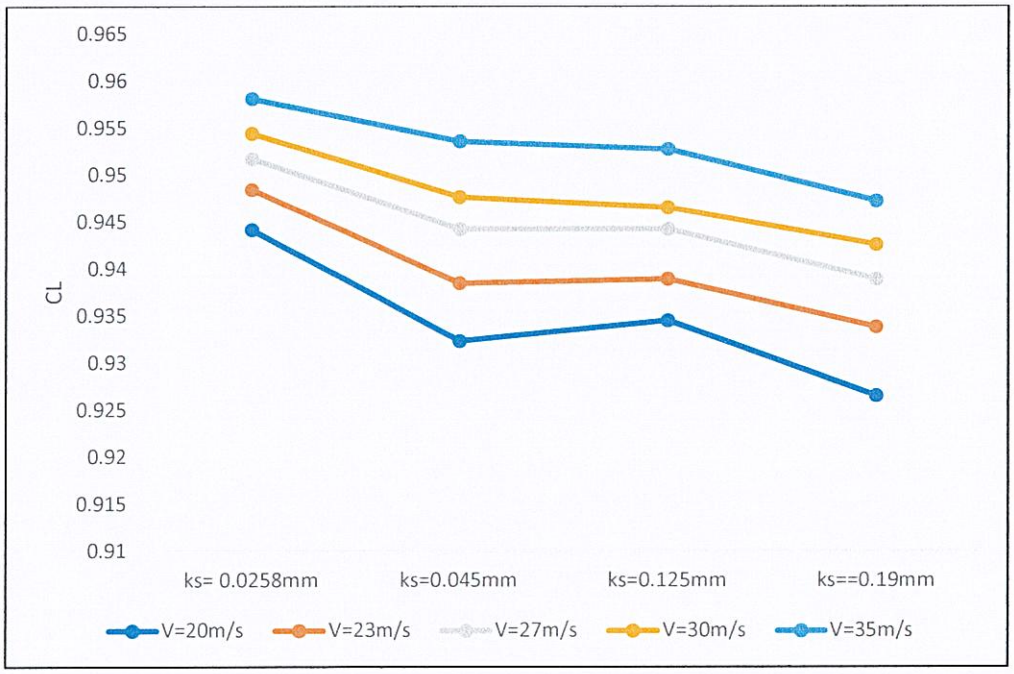


Figure (4.26): Experimental Lift Coefficient C_L at $\alpha=5^o$

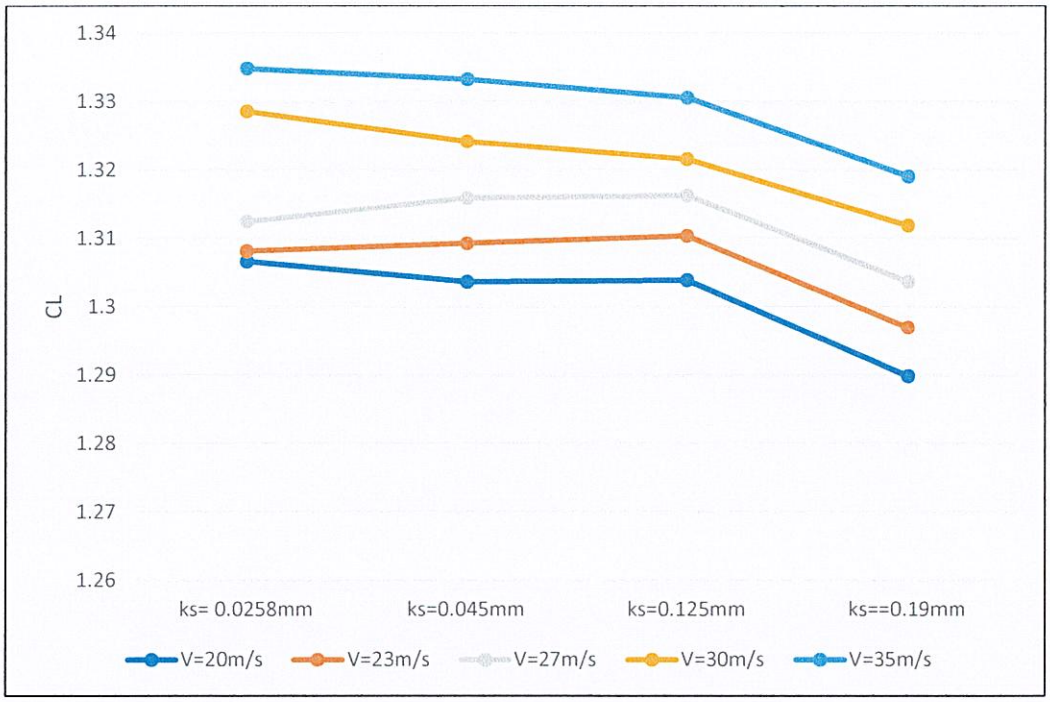


Figure (4.27): Experimental Lift Coefficient C_L at $\alpha=10^o$

ii. Drag Coefficient (C_D)

The same experiment and procedures of C_L measure the drag coefficient C_D. Due to low operating speed and air density, higher shear stress arises, which results in a slighter decrease in C_D values. These results, illustrated in Figures (4.28), (4.29), and (4.30), are realistic regarding the testing environment. At $\alpha = 0^o$, C_D decreased at higher test speeds and was observed to be most elevated at ks = 0.0258 mm and stayed almost constant between ks = 0.045 to 0.19 mm. At $\alpha = 5^o$ to 10^o, we noticed a similar C_D trend as above, with a minimal increase in C_D values.

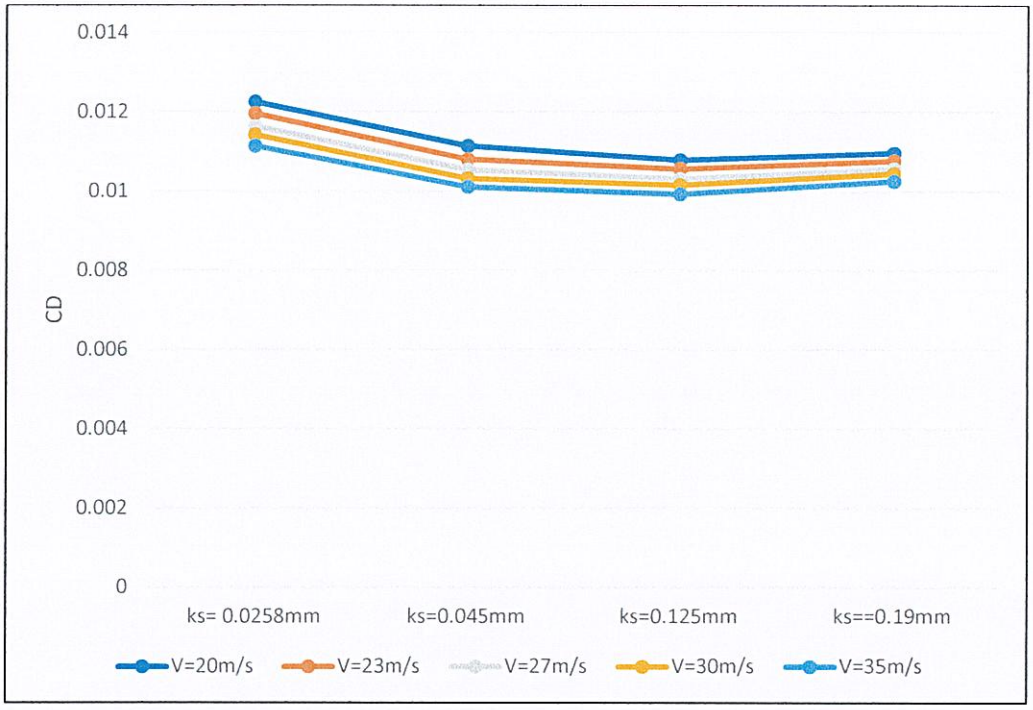


Figure (4.28): Experimental Drag Coefficient C_D at $\alpha=0^o$

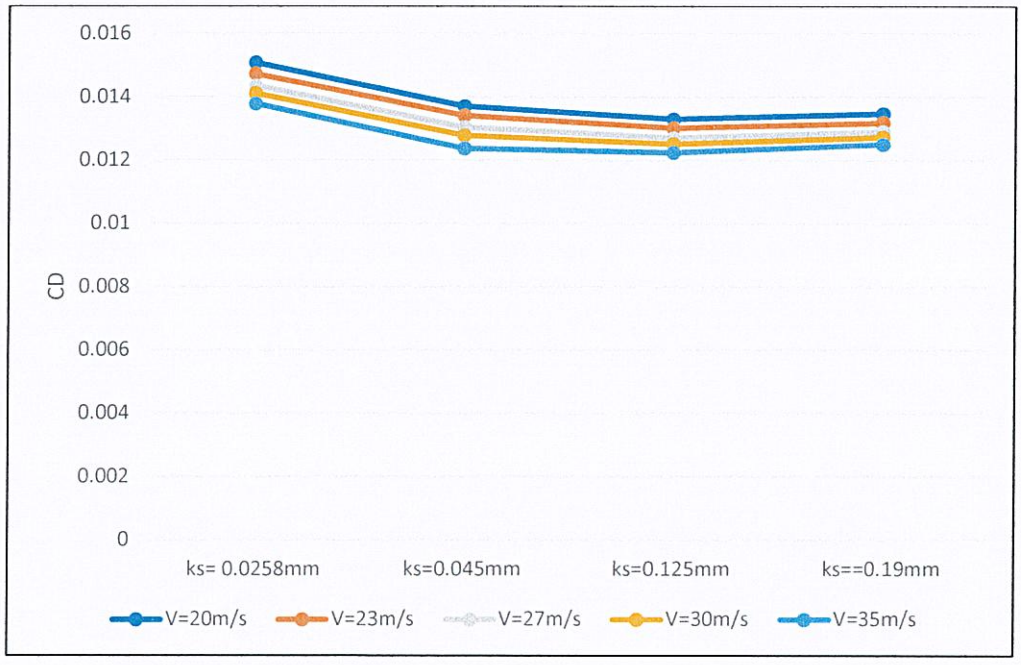


Figure (4.29): Experimental Drag Coefficient C_D at $\alpha=5^o$

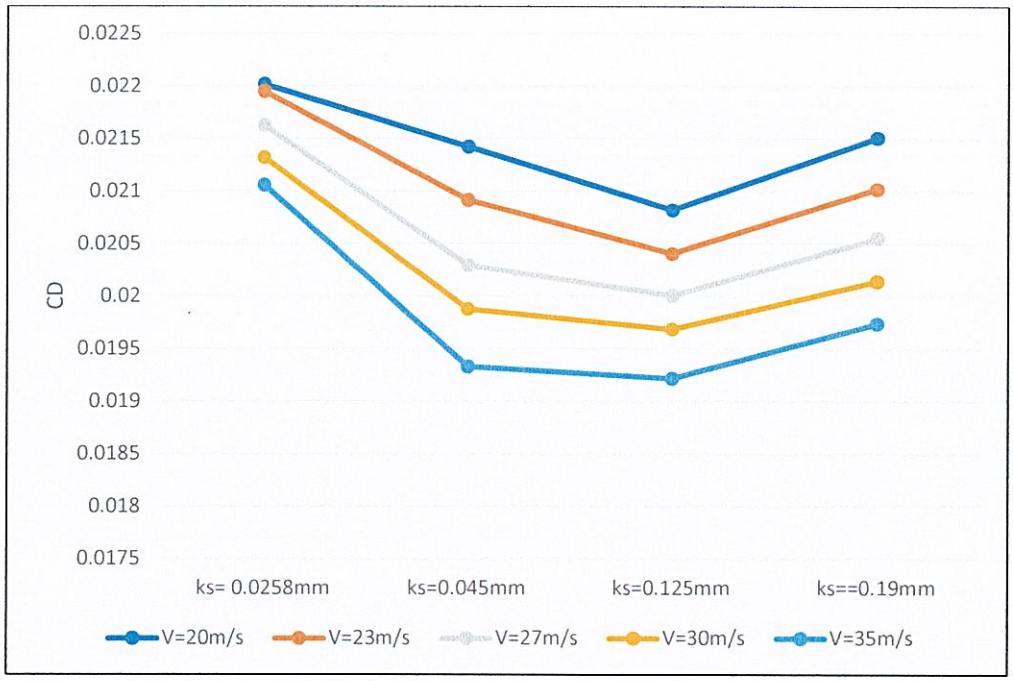


Figure (4.30): Experimental Drag Coefficient C_D at $\alpha=10^o$

iii. Lift to Drag Ratio (C_L/C_D)

Figures (4.31), (4.32), and (4.33) exhibit the results of the aerodynamic efficiency (C_L/C_D) ratio. The ratio enhanced by approximately 75% from $\alpha = 0^o$ to 5^o at the various test speeds. The highest growth is observed at ks = 0.125 mm. However, the ratio decreased at $\alpha = 10^o$, perhaps due to a pronounced increase in pressure drag at this angle of attack compared to that at $\alpha = 0^o$ - 5^o. Nevertheless, C_L/C_D remained highest at ks = 0.125 mm at $\alpha = 10^o$.

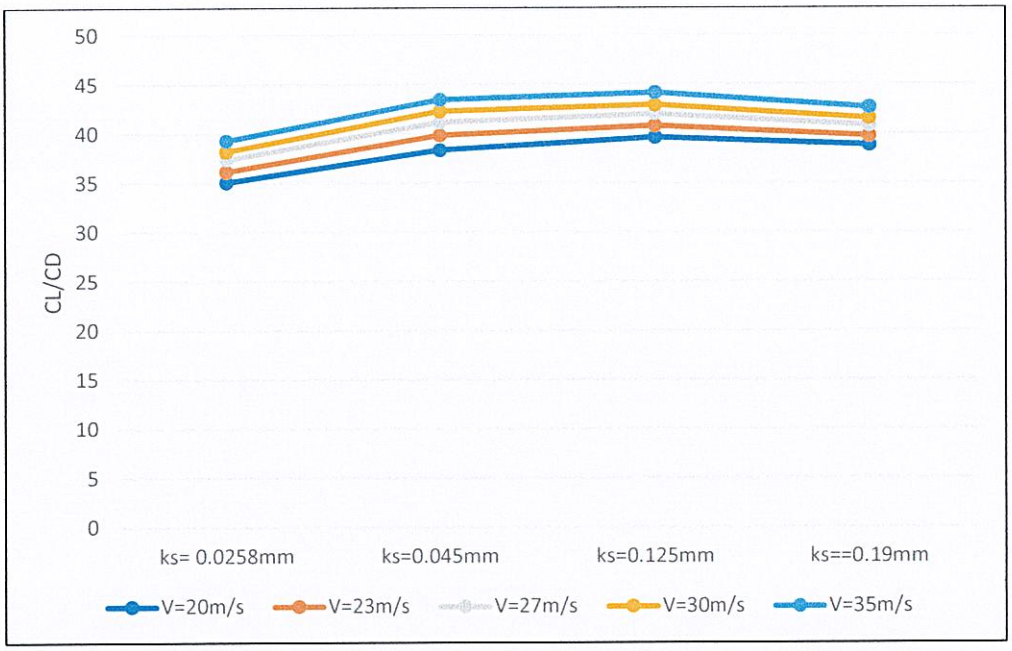


Figure (4.31): Experimental Lift to Drag Ratio (C_L/C_D) at $\alpha=0^o$

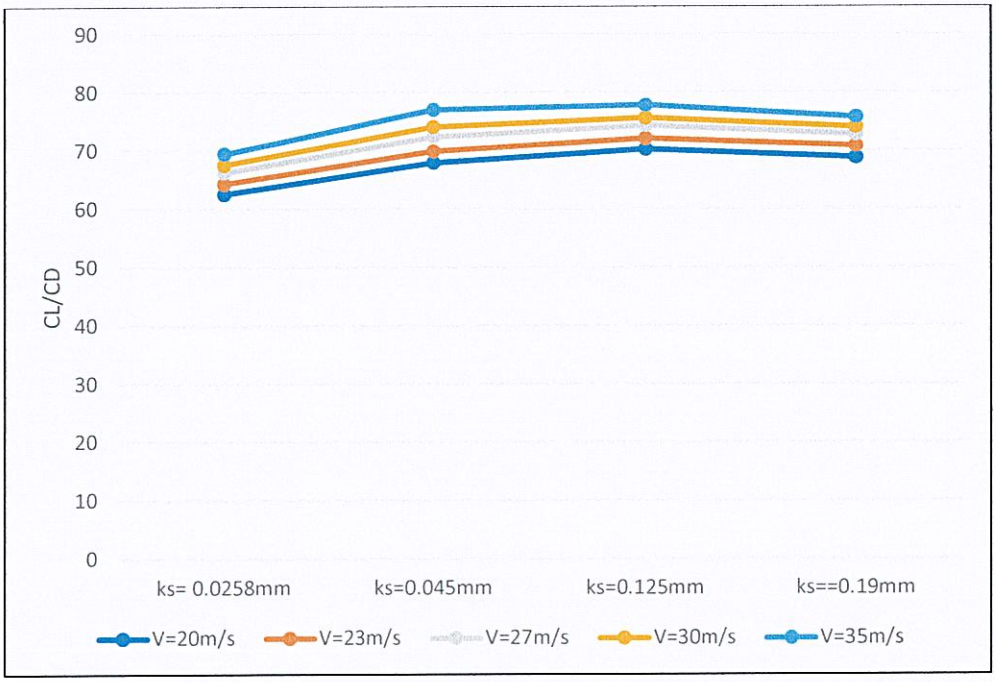


Figure (4.32): Experimental Lift to Drag Ratio (C_L/C_D) at $\alpha=5^o$

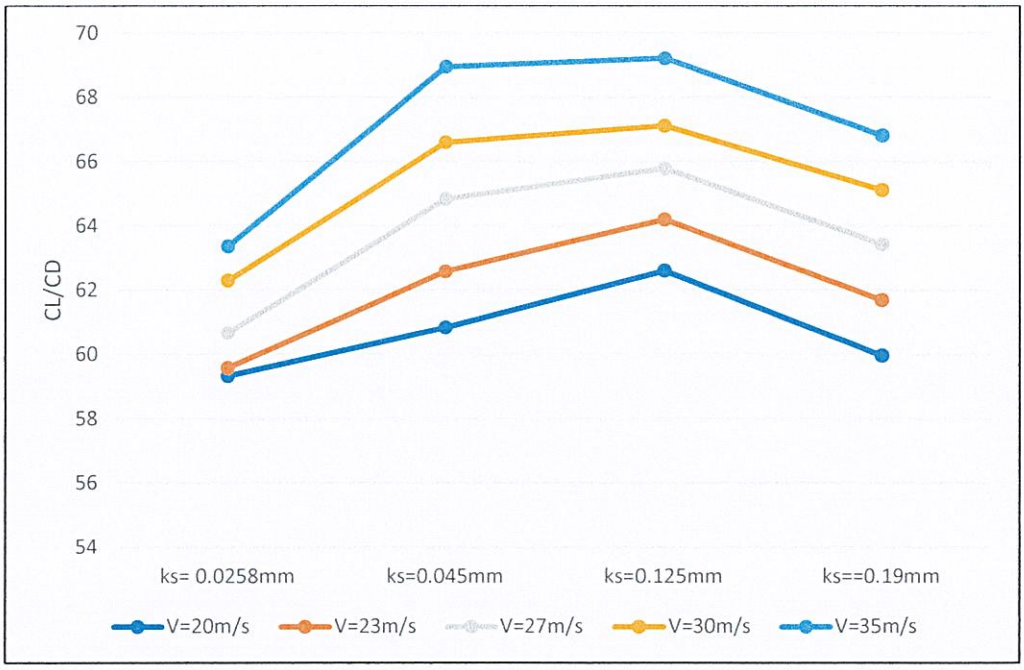


Figure (4.33): Experimental Lift to Drag Ratio (C_L/C_D) at $\alpha=10^o$

iv. Power Analysis

The power analysis conducted for experimental results outweighed airfoil with applied surface roughness ks= 0.125mm over other models (ks= 0.0258mm, ks= 0.045mm, ks= 0.125mm, and ks= 0.19mm). The best values of $C_L^{3/2}/C_D$ achieved in all angles of attack $\alpha= 0^o$, 5^o, 10^o and for the whole operating range speeds of 20m/s, 23m/s, 27m/s, 30 m/s, and 35 as displayed in Figures (4.34), (4.35), and (4.36).

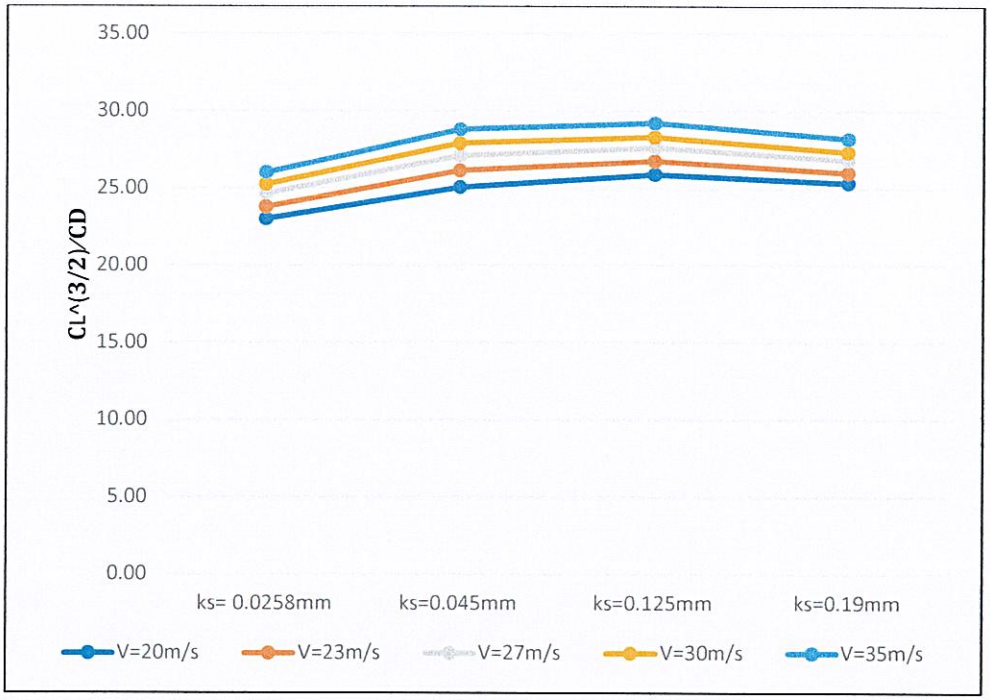


Figure (4.34): Power Analysis $C_L^{3/2}/C_D$ for Experimental Models of ks at $\alpha=0^o$

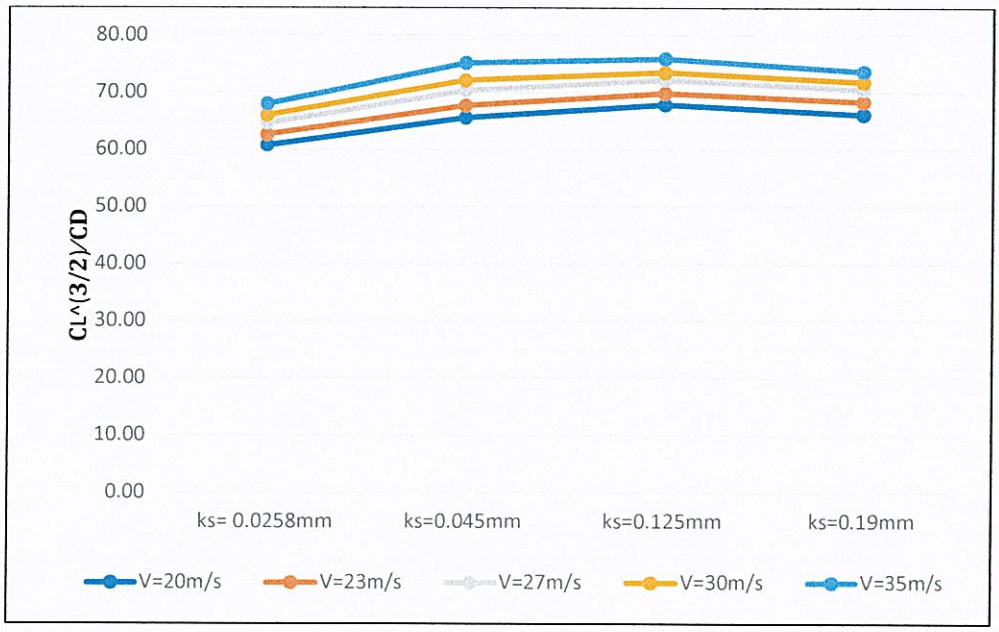


Figure (4.35): Power Analysis $C_L^{3/2}/C_D$ for Experimental Models of ks at $\alpha=5^o$

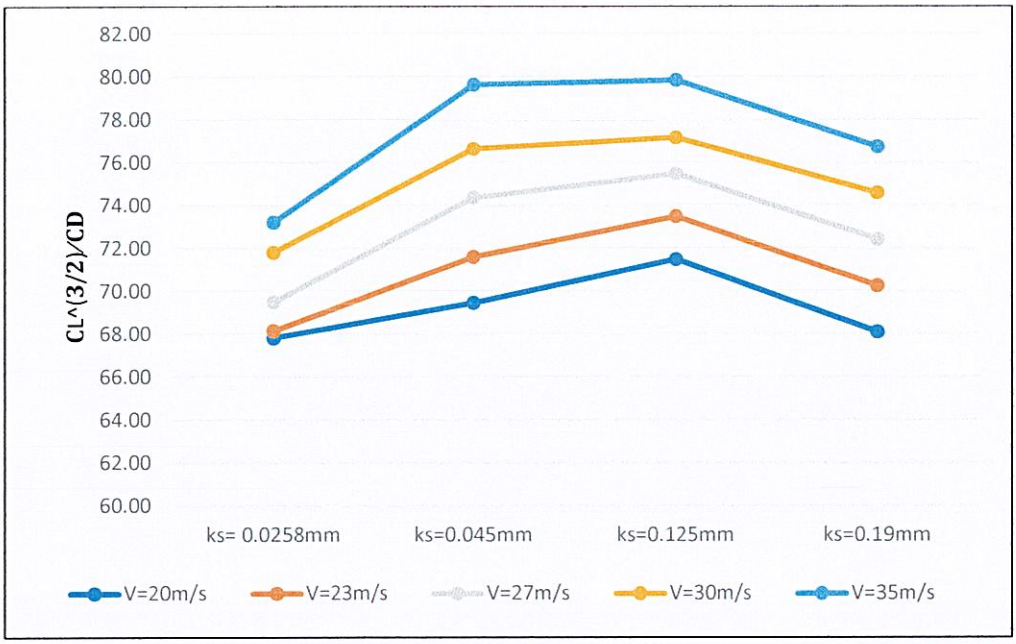


Figure (4.36): Power Analysis $C_L^{3/2}/C_D$ for Experimental Models of ks at α=10°

v. Results Verification

We operated Fluent Ansys 2020 R1 to verify experimental results, and we used the exact measurements stated in Figure (3.28) to draw and mesh a model identical to the experimental model. We used the aerodynamic model $k-\omega$ to simulate the flow with the same boundary conditions declared in the experiment in Chapter (3). The sand Grain equivalent surface roughness height option was selected to apply ks=0.0258 mm to the upper surface of all models and (ks= 0.045 mm, 0.125 mm, and 0.19 mm) to each model as we separated the surfaces in the options while we were selecting names of the edges in Meshing. The results comparison of lift coefficient C_L indicated a disparity in the results within the acceptable range at α=0° and α=5°, as Table (4.1) and Table (4.2)

deliver. Then we considered this method as verification for our experiments. Appendix (H) shows the iteration of the verification process.

Table (4.1): Experimental Results Verification at α=0°

V / ks	20m/s	23m/s	27m/s	30m/s	35m/s
ks= 0.0258mm	-1.22%	2.33%	1.75%	1.91%	1.88%
ks=0.045mm	3.32%	2.87%	2.97%	2.24%	1.77%
ks=0.125mm	3.71%	3.43%	3.31%	3.01%	2.77%
ks==0.19mm	4.59%	4.60%	4.26%	4.04%	3.62%

Table (4.2): Experimental Results Verification at α=5°

V / ks	20m/s	23m/s	27m/s	30m/s	35m/s
ks= 0.0258mm	3.75%	3.57%	3.29%	3.13%	2.93%
ks=0.045mm	5.09%	4.69%	4.11%	3.89%	3.42%
ks=0.125mm	4.74%	4.54%	4.21%	4.10%	3.62%
ks==0.19mm	5.73%	5.18%	4.87%	4.60%	4.29%

vi. Experimental Boundary Layer Thickness (BL Thickness)

measuring resulted in the expected behavior of airflow adjacent to the surface. Figures (4.37), (4.38), (4.39), and (4.40) reveal an increase in BL thickness with an increase in surface roughness. The boundary layer for rough surfaces is thicker than for a smooth surface. BL thickness is sensitive to the laminar/ turbulent adjacent flow and demonstrated dependency with ks. Discrete roughness on airfoil influences the boundary layer. As the roughness height grows, the transition point of the boundary

layer from laminar to turbulent shifts upstream. Controlling surface roughness leads to controlling boundary layer development and improving airfoil performance significantly. As stated by (Smith & Kaups, 1968), the flow field on a roughened surface without BL separation leads to a minor drag increase. Moreover, (Salzar & Barrientos, 2013) found that any increment in surface roughness will lead to an increase in parasite drag and loss of momentum of BL and can lead to BL separation.

The first result for each experiment is assumed to be at Y ≈0 mm, then the measured velocity assumed to be V ≈0 m/s.

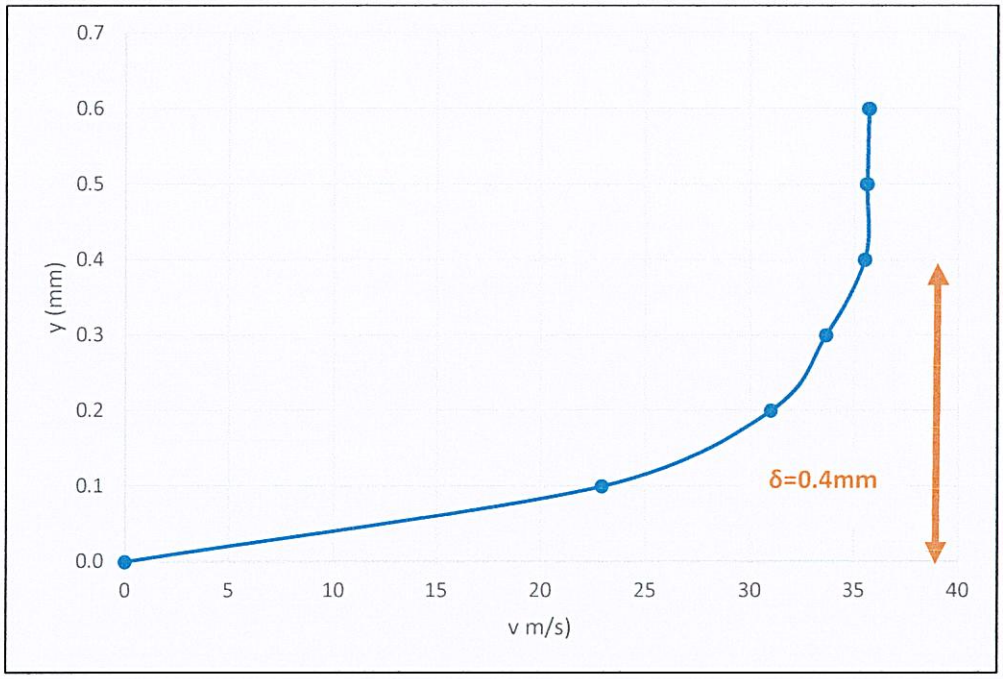


Figure (4.37): BL Thickness δ at 0.7C for ks =0.0258mm

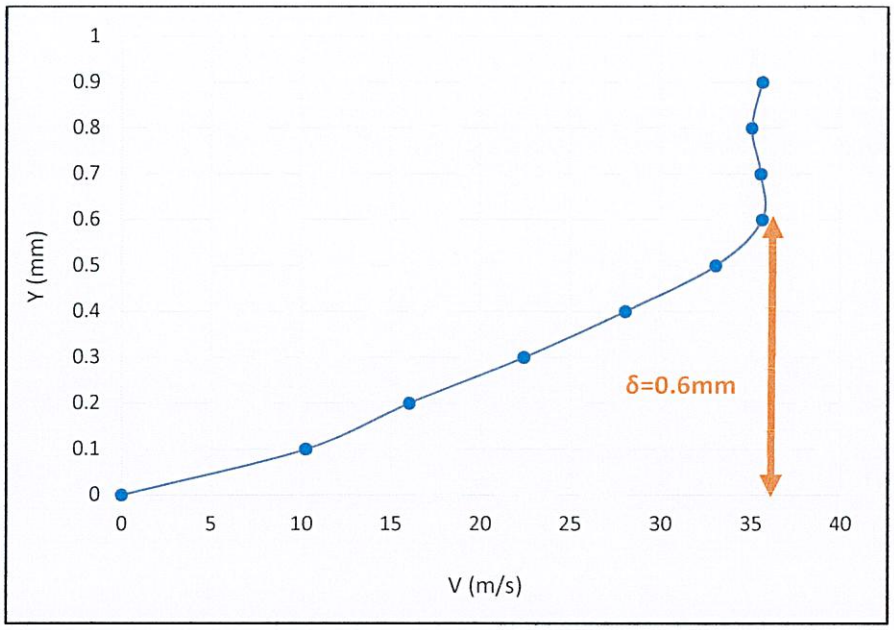


Figure (4.38): BL Thickness δ at 0.7C for ks =0.045mm

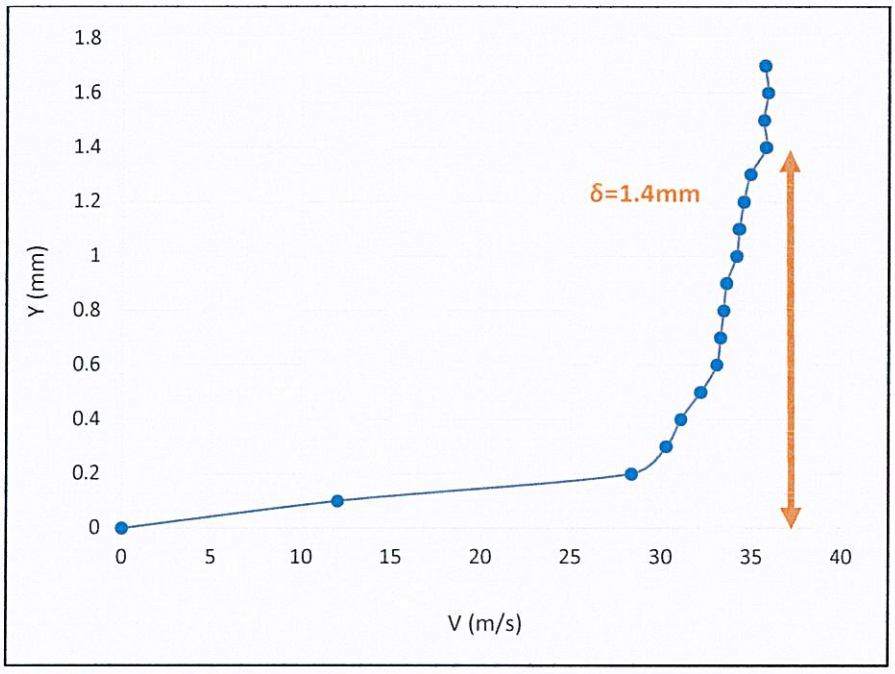


Figure (4.39): BL Thickness δ at 0.7C for ks =0.125mm

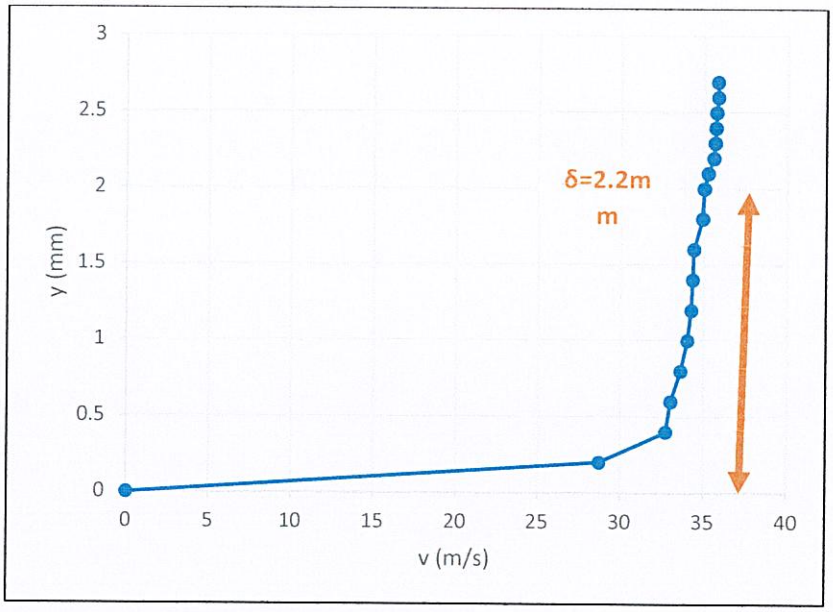


Figure (4.40): BL Thickness δ at 0.7C for ks =0.19mm

4.3 Discussions

We discussed Lift theory in Chapter (2) and the hypothesis adopted in Chapter (3) to utilize this theory in enhancing the Airfoil's aerodynamic characteristics.

4.3.1 Numerical Lift Coefficient Discussion

i. First Set of Applied Roughness C_L

In the beginning, we anticipated an increase in C_L for all angles of attack to NACA 4412 airfoil under different speeds, but unlikely C_L declined for all applied ks except: at ks =0.05mm (α= 0) and ks =0.25mm (α= 10°). Tables (4.3), (4.4), and (4.5) list the percentage difference in C_L between applied roughness patterns to the smooth surface airfoil.

For α= 0°, Airfoil with applied surface roughness k_s =0.05mm at lower surface resulted in the best C_L values. C_L increased by 0.06%, 0.17%, 0.35%, and 0.44% compared to smooth airfoil for velocities 150m/s, 200m/s, 250m/s, and 300m/s, respectively, as presented in Table (4.3).

Table (4.3): C_L Percentage Variation for Different Roughness of First Set models to the Smooth Airfoil at $\alpha = 0^o$

V / ks	150m/s	200m/s	250m/s	300m/s
ks= 0.05 mm	0.06%	0.17%	0.35%	0.44%
ks= 0.1 mm	-0.10%	-0.14%	-0.04%	-0.06%
ks = 0.15 mm	0.17%	0.36%	0.51%	0.58%
ks = 0.2 mm	-0.59%	-0.69%	-0.64%	-0.54%
ks = 0.25 mm	-0.35%	-0.18%	-0.18%	-0.16%
ks = 0.3 mm	-0.50%	-0.16%	0.32%	0.50%
ks = 0.35 mm	-0.81%	-0.19%	0.09%	0.35%
ks= 0.4 mm	0.06%	0.44%	0.69%	0.86%
ks = 0.45 mm	0.01%	-0.51%	-0.58%	-0.50%
ks = 0.5 mm	-0.14%	0.37%	0.62%	0.77%

When the inclination angle increased to $\alpha = 5^o$, Airfoil with applied surface roughness ks = 0.05mm at the lower surface reserved best results. At this roughness, C_L values decreased by 0.53%, 0.35%, 0.30%, and 0.25% compared to smooth Airfoil (Plain) for velocities 150 m/s, 200 m/s, 250 m/s, and 300 m/s, respectively. Table (4.4) exhibits the results of all models of applied roughness at $\alpha = 5^o$ and ks = 0.05 mm with the lowest CL decrease in all sets compared to smooth Airfoil.

Table (4.4): C_L Percentage Variation for Different Roughness of First Set models to the Smooth Airfoil at $\alpha = 5^o$

V / ks	150m/s	200m/s	250m/s	300m/s
ks= 0.05 mm	-0.53%	-0.35%	-0.30%	-0.25%
ks= 0.1 mm	-0.96%	-0.83%	-0.79%	-0.68%
ks = 0.15 mm	-0.63%	-0.49%	-0.38%	-0.41%
ks = 0.2 mm	-1.43%	-1.71%	-1.57%	-1.73%
ks = 0.25 mm	-1.18%	-1.15%	-1.27%	-1.57%
ks = 0.3 mm	-1.04%	-0.74%	-0.66%	-0.64%
ks = 0.35 mm	-1.44%	-1.21%	-1.00%	-0.98%
ks= 0.4 mm	-0.95%	-0.74%	-0.61%	-0.65%
ks = 0.45 mm	-1.70%	-1.92%	-1.95%	-1.55%
ks = 0.5 mm	-1.32%	-1.05%	-0.97%	-0.92%

When all models in the first set tested at $\alpha = 10^{o}$, only the model with ks =0.25mm at lower surface gained increment of C_L values. C_L reported increasing by 1.12%, 1.43%, 1.31%, and 1.72% at velocities of 150m/s, 200m/s, 250m/s, and 300m/s compared to smooth airfoil as shown in Table (4.5).

Note that all values of applied surface roughness heights ks of the first set are laying in the hydraulically smooth region as discussed in Chapter (3) and calculated in Table (3.1).

Table (4.5): C_L Percentage Variation for Different Roughness of First Set models to the Smooth Airfoil at $\alpha = 10^{o}$

V / k_s	150m/s	200m/s	250m/s	300m/s
ks= 0.05 mm	-1.61%	-1.38%	-1.23%	-1.20%
ks= 0.1 mm	-2.13%	-2.01%	-1.86%	-1.83%
ks = 0.15 mm	-2.41%	-2.26%	-2.21%	-2.10%
ks = 0.2 mm	-3.29%	-3.57%	-3.44%	-3.08%
ks = 0.25 mm	1.12%	1.43%	1.31%	1.72%
ks = 0.3 mm	-2.13%	-1.89%	-1.79%	-1.68%
ks = 0.35 mm	-2.36%	-2.21%	-2.08%	-2.03%
ks= 0.4 mm	-2.10%	-1.95%	-1.74%	-1.71%
ks = 0.45 mm	-3.47%	-3.35%	-3.45%	-3.29%
ks = 0.5 mm	-2.56%	-2.35%	-2.28%	-2.28%

These results can be understood better when we compare static pressure contours of NACA 4412 airfoil at $\alpha = 5^{o}$ and V = 250 m/s for smooth airfoil and Airfoil with applied k_s. Figure (4.41) displays that the Airfoil with ks = 0.05 mm lost 0.3% of C_L. This consequence is because of applied surface roughness to the lower surface. This roughness caused an increase of skin friction, as displayed in Figure (4.42), and then the pressure in the lower surface due to turbulent flow circulated along spherical applied roughness. This higher pressure affected the upper surface as well by

adding the amount of positive pressure to the surrounding streamlines around the Airfoil leading and trailing edges.

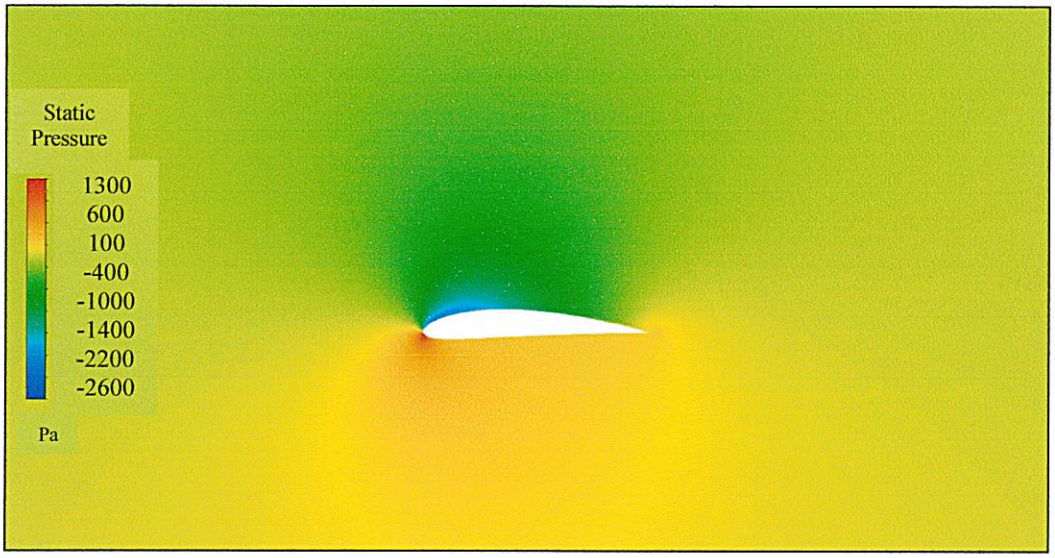


Figure (4.41): Static Pressure Contours of NACA 4412 at α= 5° and V=250m/s (ks =0.05mm)

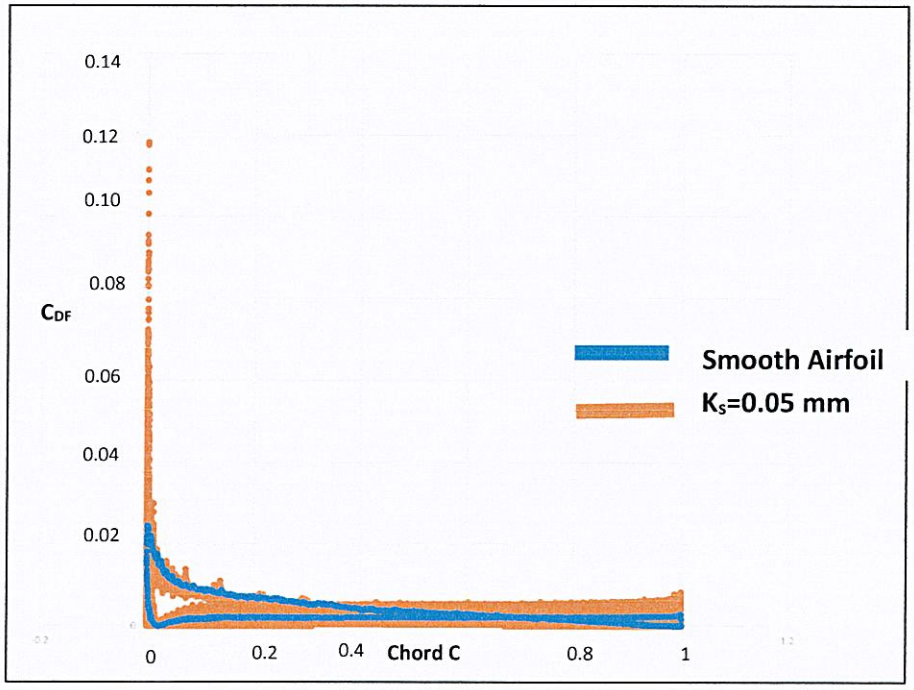


Figure (4.42): Skin Friction Comparison Between Smooth Airfoil and Airfoil with ks =0.05mm

The negative pressure of the upper surface decreased, as depicted in Figure (4.41) compared to the smooth airfoil in Figure (4.43). However, this effect also increased the pressure at the last 5% of the upper airfoil surface, as shown in Figure (4.41). This positive pressure sticks the flow downstream upper airfoil surface, so it delays the stall, controls the flow separation, and achieves better aerodynamic characteristics.

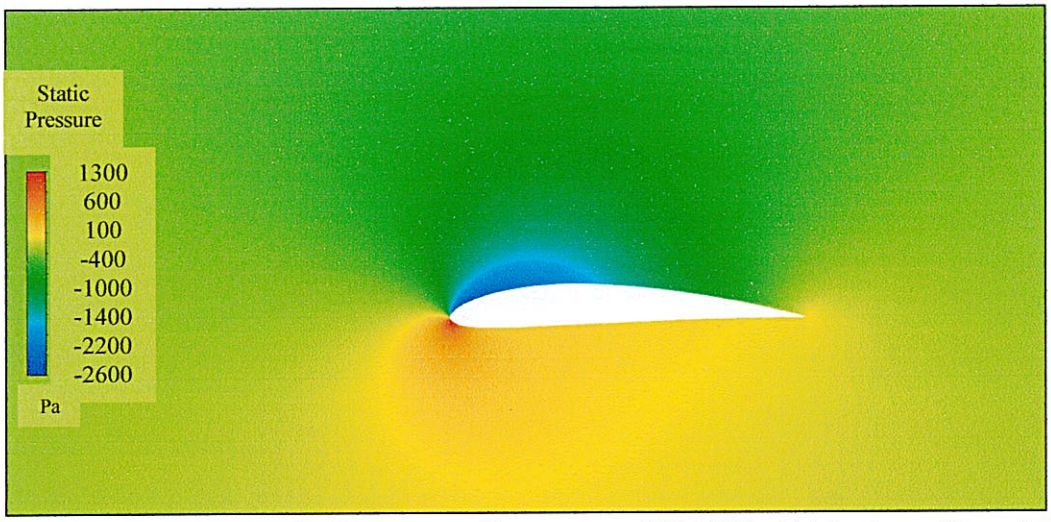


Figure (4.43): Static Pressure Contours of NACA 4412 at α= 5° and V=250m/s (Smooth Airfoil)

The total pressure was plotted for both the upper and lower Airfoil surfaces and verified that the total pressure of the lower surface in the Airfoil with ks = 0.05 mm is higher than plain surface airfoil. Also, the upper surface pressure of the Airfoil with ks = 0.05 mm is lower than the upper surface of the smooth Airfoil, as pictured in Figure (4.44). These observations supported our hypothesis.

B.4 Grid independency study for0.15mm roughness airfoil

Setup	Bounding box 90*50m/ Nodes 53069/ Elements 51480/High quality smoothing/smooth transition/ element size of face 1 =0.05 / v=250m/s	High quality/smooth transition/ element size of face 1 =0.05 /Nodes 427576/ Elements 796084/ element size of edge 0.00005/ Element size of face 0.01	Difference
LIFT COEFF	4.5113e-01	4.5542e-01	0.0095
DRAG COEFF	9.0951e-03	8.7960e-03	0.034

Lift and drag coeff for 0.15mm (150 m/s)

Angle of attack	Lift coeff	Drag coeff	l/d
0	4.4839e-01	9.3316e-03	48.05
5	9.6710e-01	1.1196e-02	86.38
10	1.3508e+00	1.7442e-02	77.45

Lift and drag coeff for 0.15mm (200 m/s)

Angle of attack	Lift coeff	Drag coeff	l/d
0	4.5245e-01	9.0208e-03	50.2
5	9.7399e-01	1.0766e-02	90.46
10	1.3622e+00	1.6650e-02	81.8

Lift and drag coeff for 0.15mm (250 m/s)

Angle of attack	Lift coeff	Drag coeff	l/d
0	4.5544e-01	8.7907e-03	51.81
5	9.7892e-01	1.0458e-02	93.6
10	1.3696e+00	1.6105e-02	85.04

Lift and drag coeff for 0.15mm (300 m/s)

Angle of attack	Lift coeff	Drag coeff	l/d
0	4.5754e-01	8.6141e-03	53.12
5	9.8256e-01	1.0223e-02	96.11
10	1.3764e+00	1.5675e-02	87.81

B.5 Grid independency study for airfoil with roughness 0.2mm

Setup	Bounding box 90*50m/ Nodes 53069/ Elements 51480/High quality smoothing/smooth transition/ element size of face 1 =0.05 / edge size 0.0001m/v=250m/s	High quality/smooth transition/nodes 1265829/ elements 2482903/ element size of face 1 =0.05 / edge size =0.00005	Difference
LIFT COEFF	4.4925e-01	4.5061e-01	0.03
DRAG COEFF	9.3032e-03	9.0482e-03	0.028

Lift and drag coeff for airfoil with roughness 0.2mm (150 m/s)

Angle of attack	Lift coeff	Drag coeff	l/d
0	4.4499e-01	9.5395e-03	47.16
5	9.5929e-01	1.1481e-02	83.55
10	1.3386e+00	1.7707e-02	75.6

Lift and drag coeff for airfoil with roughness 0.2mm (200 m/s)

Angle of attack	Lift coeff	Drag coeff	l/d
0	4.4770e-01	9.2673e-03	48.3
5	9.6202e-01	1.1106e-02	86.62
10	1.3439e+00	1.7086e-02	78.59

Lift and drag coeff for airfoil with roughness 0.2mm (250 m/s)

Angle of attack	Lift coeff	Drag coeff	l/d
0	4.5022e-01	9.0497e-03	49.75
5	9.6723e-01	1.0789e-02	89.65
10	1.3524e+00	1.6565e-02	81.642

Lift and drag coeff for airfoil with roughness 0.2mm (300 m/s)

Angle of attack	Lift coeff	Drag coeff	l/d
0	4.5244e-01	8.8550e-03	51.09
5	9.6953e-01	1.0518e-02	92.15
10	1.3626e+00	1.6013e-02	85.09

B.6 Grid independency study for airfoil with roughness 0.25mm

Setup	Bounding box 90*50m/ Nodes 53069/ Elements 51480/High quality smoothing/smooth transition/ element size of face 1 =0.05 / edge size 0.0001m/v=250m/s	High quality/smooth transition/ Nodes 927859/ Elements 1807423/element size of face 1 =0.05 / edge size 0.00005	Difference
LIFT COEFF	4.5086e-01	4.5229e-01	0.03
DRAG COEFF	9.3309e-03	9.2538e-03	0.005

Lift and drag coeff for airfoil with roughness 0.25mm (150 m/s)

Angle of attack	Lift coeff	Drag coeff	l/d
0	4.4610e-01	9.7727e-03	45.65
5	9.6170e-01	1.1623e-02	82.742
10	1.3997e+00	1.7778e-02	78.7

Lift and drag coeff for airfoil with roughness 0.25mm (200 m/s)

Angle of attack	Lift coeff	Drag coeff	l/d
0	4.5004e-01	9.4825e-03	47.46
5	9.6745e-01	1.1229e-02	86.16
10	1.4136e+00	1.6986e-02	83.22

Lift and drag coeff for airfoil with roughness 0.25mm (250 m/s)

Angle of attack	Lift coeff	Drag coeff	l/d
0	4.5229e-01	9.2538e-03	48.88
5	9.7022e-01	1.0918e-02	88.86
10	1.4190e+00	1.6482e-02	86.07

Lift and drag coeff for airfoil with roughness 0.25mm (300 m/s)

Angle of attack	Lift coeff	Drag coeff	l/d
0	4.5414e-01	9.0567e-03	50.14
5	9.7112e-01	1.0643e-02	91.24
10	1.4301e+00	1.5943e-02	89.7

B.7 Grid independency study for airfoil with roughness 0.3mm

Setup	Bounding box 90*50m/ Nodes 53069/ Elements 51480/High quality smoothing/smooth transition/ element size of face 1 =0.05 / refinement 2/v=250m/s (Quadrate elenments)	High quality/smooth transition/nodes 747935/ elements 736120/edge size 0.0004/ element size of face 1 =0.05 / refinement 3 (Quadrate elements)	Difference
LIFT COEFF	4.6517e-01	4.6111e-01	0.008 %
DRAG COEFF	1.0127e-02	9.8153e-03	0.03 %

Lift and drag coeff for airfoil with roughness 0.3mm (150 m/s)

Angle of attack	Lift coeff	Drag coeff	l/d
0	4.4540e-01	9.7852e-03	46.4
5	9.6307e-01	1.1551e-02	83.38
10	1.3547e+00	1.7136e-02	79.06

Lift and drag coeff for airfoil with roughness 0.3mm (200 m/s)

Angle of attack	Lift coeff	Drag coeff	l/d
0	4.5013e-01	9.4583e-03	47.59
5	9.7148e-01	1.1108e-02	87.45
10	1.3674e+00	1.6428e-02	83.24

Lift and drag coeff for airfoil with roughness 0.3mm (250 m/s)

Angle of attack	Lift coeff	Drag coeff	l/d
0	4.5459e-01	9.2758e-03	49.04
5	9.7619e-01	1.0824e-02	90.19
10	1.3755e+00	1.5953e-02	86.22

Lift and drag coeff for airfoil with roughness 0.3mm (300 m/s)

Angle of attack	Lift coeff	Drag coeff	l/d
0	4.5717e-01	9.1247e-03	50.1
5	9.8032e-01	1.0606e-02	92.43
10	1.3823e+00	1.5589e-02	88.67

B.8 Grid independency study for airfoil with roughness 0.35mm

Setup	Bounding box 90*50m/ Nodes 53069/ Elements 51480/High quality smoothing/smooth transition/ element size of face 1 =0.05 / refinement 2/v=250m/s (Quadrate)	High quality/smooth transition/ nodes 779582/ elements 767724/edge size .0004/element size of face 1 =0.05 / refinement 3 (Quadrate)	Difference
LIFT COEFF	4.5591e-01	4.5425e-01	0.004
DRAG COEFF	9.9152e-03	9.7622e-03	0.015

Lift and drag coeff for airfoil with roughness 0.35mm (150 m/s)

Angle of attack	Lift coeff	Drag coeff	l/d
0	4.4404e-01	1.0210e-02	43.49
5	9.5922e-01	1.1884e-02	80.72
10	1.3515e+00	1.7404e-02	77.65

Lift and drag coeff for airfoil with roughness 0.35mm (200 m/s)

Angle of attack	Lift coeff	Drag coeff	l/d
0	4.4997e-01	9.8621e-03	45.63
5	9.6688e-01	1.1407e-02	84.76
10	1.3629e+00	1.6653e-02	81.84

Lift and drag coeff for airfoil with roughness 0.35mm (250 m/s)

Angle of attack	Lift coeff	Drag coeff	l/d
0	4.5353e-01	9.6436e-03	47.03
5	9.7287e-01	1.1105e-02	87.61
10	1.3715e+00	1.6144e-02	84.95

Lift and drag coeff for airfoil with roughness 0.35mm (300 m/s)

Angle of attack	Lift coeff	Drag coeff	l/d
0	4.5647e-01	9.4853e-03	48.12
5	9.7689e-01	1.0876e-02	89.82
10	1.3774e+00	1.5784e-02	87.27

B.9 Grid independency study for airfoil with roughness 0.4mm

Setup	Bounding box 90*50m/ Nodes 53069/ Elements 51480/High quality smoothing/smooth transition/ element size of face 1 =0.05 / refinement 2/v=250m/s (Quadrate)	High quality/smooth transition/Nodes 755188/ Elements 742988/edge size 0.0004 element size of face 1 =0.05 / refinement 3 (Quadrate)	Difference
LIFT COEFF	4.6153e-01	4.5624e-01	0.005
DRAG COEFF	9.8558e-03	9.7375e-03	0.01

Lift and drag coeff for airfoil with roughness 0.4mm (150 m/s)

Angle of attack	Lift coeff	Drag coeff	l/d
0	4.4794e-01	1.0306e-02	43.46
5	9.6403e-01	1.1890e-02	81.08
10	1.3552e+00	1.7341e-02	78.15

Lift and drag coeff for airfoil with roughness 0.4mm (200 m/s)

Angle of attack	Lift coeff	Drag coeff	l/d
0	4.5283e-01	9.9709e-03	45.42
5	9.7153e-01	1.1440e-02	84.9
10	1.3665e+00	1.6607e-02	82.28

Lift and drag coeff for airfoil with roughness 0.4mm (250 m/s)

Angle of attack	Lift coeff	Drag coeff	l/d
0	4.5624e-01	9.7375e-03	46.85
5	9.7671e-01	1.1133e-02	87.73
10	1.3762e+00	1.6091e-02	85.26

Lift and drag coeff for airfoil with roughness 0.4mm (300 m/s)

Angle of attack	Lift coeff	Drag coeff	l/d
0	4.5880e-01	9.5566e-03	48
5	9.8016e-01	1.0893e-02	89.98
10	1.3818e+00	1.5728e-02	87.86

B.10 Grid independency study for airfoil with roughness 0.45mm

Setup	Bounding box 90*50m/ Nodes 53069/ Elements 51480/High quality smoothing/smooth transition/ element size of face 1 =0.01 /edge size 0.001 /v=250m/s	High quality/smooth transition/Nodes 926005/ elements 1804119 element size of face 1 =0.005 / edge size 0.0005	Difference
LIFT COEFF	4.5014e-01	4.5327e-01	0.006
DRAG COEFF	9.6274e-03	9.9205e-03	0.05

Lift and drag coeff for airfoil with roughness 0.45mm (150 m/s)

Angle of attack	Lift coeff	Drag coeff	l/d
0	4.4770e-01	1.0478e-02	42.73
5	9.5671e-01	1.2125e-02	78.9
10	1.3361e+00	1.8071e-02	73.94

Lift and drag coeff for airfoil with roughness 0.45mm (200 m/s)

Angle of attack	Lift coeff	Drag coeff	l/d
0	4.4852e-01	1.0019e-02	44.76
5	9.5996e-01	1.2115e-02	79.24
10	1.3470e+00	1.7289e-02	77.91

Lift and drag coeff for airfoil with roughness 0.45mm (250 m/s)

Angle of attack	Lift coeff	Drag coeff	l/d
0	4.5049e-01	1.0173e-02	44.28
5	9.6351e-01	1.1381e-02	84.66
10	1.3523e+00	1.6745e-02	80.76

Lift and drag coeff for airfoil with roughness 0.45mm (300 m/s)

Angle of attack	Lift coeff	Drag coeff	l/d
0	4.5259e-01	9.6878e-03	46.72
5	9.7126e-01	1.1079e-02	87.67
10	1.3596e+00	1.6230e-02	83.76

B.11 Grid independency study for airfoil with roughness 0.5mm

Setup	Bounding box 90*50m/ Nodes 53069/ Elements 51480/High quality smoothing/smooth transition/ element size of face 1 =0.05 / refinement 2/v=250m/s (Quadrate)	High quality/smooth transition/ Nodes 622976/ Elements 612393/edge size 0.0005element size of face 1 =0.05/refinement 3 (Quadrate)	Difference
LIFT COEFF	4.565e-01	4.5595e-01	0.002
DRAG COEFF	1.026e-02	9.8997e-03	0.02

Lift and drag coeff for airfoil with roughness 0.5mm (150 m/s)

Angle of attack	Lift coeff	Drag coeff	l/d
0	4.4703e-01	1.0479e-02	42.66
5	9.6040e-01	1.2053e-02	79.68
10	1.3487e+00	1.7751e-02	75.98

Lift and drag coeff for airfoil with roughness 0.5mm (200 m/s)

Angle of attack	Lift coeff	Drag coeff	l/d
0	4.5250e-01	1.0134e-02	44.65
5	9.6843e-01	1.1597e-02	83.51
10	1.3609e+00	1.7005e-02	80.03

Lift and drag coeff for airfoil with roughness 0.5mm (250 m/s)

Angle of attack	Lift coeff	Drag coeff	l/d
0	4.5595e-01	9.8997e-03	46.06
5	9.7318e-01	1.1278e-02	86.29
10	1.3686e+00	1.6507e-02	82.91

Lift and drag coeff for airfoil with roughness 0.5mm (300 m/s)

Angle of attack	Lift coeff	Drag coeff	l/d
0	4.5839e-01	9.7271e-03	47.125
5	9.7753e-01	1.1052e-02	88.45
10	1.3738e+00	1.6150e-02	85.08

B12 Grid independency study for1mm roughness airfoil

Setup	Bounding box 90*50m/ Nodes 317343/ Elements 610651/ High quality smoothing/smooth transition/ element size of face 1 =0.01 / edgesize 0.0001 /v=250m/s	High quality/smooth transition/ Nodes 478590/ Elements 909903/element size of face 1 =0.01 / edge sizing 0.00005	Difference
LIFT COEFF	4.5269e-01	4.5879e-01	0.013
DRAG COEFF	1.0672e-02	1.1258e-02	0.055

Lift and drag coeff for 1mm (150 m/s)

Angle of attack	Lift coeff	Drag coeff	l/d
0	4.5238e-01	1.1790e-02	38.36
5	9.6212e-01	1.3105e-02	73.42
10	1.3298e+00	1.9173e-02	69.35

Lift and drag coeff for 1 (200 m/s)

Angle of attack	Lift coeff	Drag coeff	l/d
0	4.5516e-01	1.1502e-02	39.57
5	9.6715e-01	1.2709e-02	76.1
10	1.3406e+00	1.8371e-02	72.97

Lift and drag coeff for 1 (250 m/s)

Angle of attack	Lift coeff	Drag coeff	l/d
0	4.5879e-01	1.1258e-02	40.75
5	9.7060e-01	1.2378e-02	78.41
10	1.3488e+00	1.7730e-02	76.07

Lift and drag coeff for 1 (300 m/s)

Angle of attack	Lift coeff	Drag coeff	l/d
0	4.6022e-01	1.1035e-02	41.7
5	9.7433e-01	1.2079e-02	80.66
10	1.3566e+00	1.7169e-02	79.01

B.13 Grid independency study for2mm roughness airfoil

Setup	Bounding box 90*50m/ Nodes / Elements High quality smoothing/smooth transition/ nodes 275294/ elements 531343/element size of face 1 =0.01 / edgesize 0.0001 /v=250m/s	High quality/smooth transition/ element size of face 1 =0.01 / nodes 376480/ elements 717521/edge sizing 0.00005	Difference
LIFT COEFF	4.6104e-01	4.6739e-01	0.013
DRAG COEFF	1.2035e-02	1.2502e-02	0.039

Lift and drag coeff for 2mm (150 m/s)

Angle of attack	Lift coeff	Drag coeff	l/d
0	4.5936e-01	1.3083e-02	35.11
5	9.6459e-01	1.3970e-02	69.05
10	1.3228e+00	2.0065e-02	65.93

Lift and drag coeff for 2 (200 m/s)

Angle of attack	Lift coeff	Drag coeff	l/d
0	4.6401e-01	1.2757e-02	36.37
5	9.7301e-01	1.3522e-02	71.96
10	1.3370e+00	1.9185e-02	69.69

Lift and drag coeff for 2 (250 m/s)

Angle of attack	Lift coeff	Drag coeff	l/d
0	4.6739e-01	1.2502e-02	37.38
5	9.7929e-01	1.3186e-02	74.27
10	1.3443e+00	1.8558e-02	72.4

Lift and drag coeff for2 (300 m/s)

Angle of attack	Lift coeff	Drag coeff	l/d
0	4.6978e-01	1.2291e-02	38.22
5	9.8305e-01	1.2914e-02	76.12
10	1.3535e+00	1.8020e-02	75.11

B.14 Grid independency study for3mm roughness airfoil

Setup	Bounding box 90*50m/ Nodes / Elements High quality smoothing/smooth transition/ element size of face 1 =0.01 / edgesize 0.0001 /v=250m/s	High quality/smooth transition/ nodes 377448/ elements 719525/element size of face 1 =0.01 / edge sizing 0.00005	Difference
LIFT COEFF	4.7266e-01	4.7573e-01	0.006
DRAG COEFF	1.2968e-02	1.3331e-02	0.027

Lift and drag coeff for 3mm (150 m/s)

Angle of attack	Lift coeff	Drag coeff	l/d
0	4.6807e-01	1.3933e-02	33.59
5	9.7671e-01	1.4608e-02	66.86
10	1.3276e+00	2.1003e-02	63.21

Lift and drag coeff for3 (200 m/s)

Angle of attack	Lift coeff	Drag coeff	l/d
0	4.7225e-01	1.3591e-02	34.75
5	9.8394e-01	1.4136e-02	69.6
10	1.3422e+00	2.0050e-02	66.94

Lift and drag coeff for 3 (250 m/s)

Angle of attack	Lift coeff	Drag coeff	l/d
0	4.7573e-01	1.3331e-02	35.69
5	9.8923e-01	1.3788e-02	71.74
10	1.3540e+00	1.9307e-02	70.13

Lift and drag coeff for3 (300 m/s)

Angle of attack	Lift coeff	Drag coeff	l/d
0	4.7820e-01	1.3113e-02	36.47
5	9.9529e-01	1.3522e-02	73.6
10	1.3609e+00	1.9307e-02	72.51

B.15 Grid independency study for4mm roughness airfoil

Setup	Bounding box 90*50m/ Nodes / Elements High quality smoothing/smooth transition/ element size of face 1 =0.01 / edgesize 0.0001 /v=250m/s	High quality/smooth transition/ element size/nodes 377578/ elements 719835/ face 1 =0.01 / edge sizing 0.00005	Difference
LIFT COEFF	4.5431e-01	4.5710e-01	0.006
DRAG COEFF	1.3680e-02	1.3959e-02	0.02

Lift and drag coeff for 4mm (150 m/s)

Angle of attack	Lift coeff	Drag coeff	l/d
0	4.4836e-01	1.4603e-02	30.7
5	9.3780e-01	1.4938e-02	62.78
10	1.2724e+00	2.0431e-02	62.28

Lift and drag coeff for4 (200 m/s)

Angle of attack	Lift coeff	Drag coeff	l/d
0	4.5344e-01	1.4236e-02	31.85
5	9.4686e-01	1.4477e-02	65.4
10	1.2872e+00	1.9535e-02	65.89

Lift and drag coeff for4 (250 m/s)

Angle of attack	Lift coeff	Drag coeff	l/d
0	4.5710e-01	1.3959e-02	32.75
5	9.5476e-01	1.4123e-02	67.6
10	1.2999e+00	1.8844e-02	68.98

Lift and drag coeff for4 (300 m/s)

Angle of attack	Lift coeff	Drag coeff	l/d
0	4.5997e-01	1.3732e-02	33.5
5	9.5912e-01	1.3858e-02	69.21
10	1.3068e+00	1.8361e-02	71.17

Appendix (C)

Fluent Ansys 2020 R1 Solution Iterations

C.1 Last 10 Iterations of Smooth Airfoil (300m/s) at $\alpha=0^{o}$

73631 mixed cells, zone 3, binary.

73631 cell partition ids, zone 3, 8 partitions, binary.

143549 2D interior faces, zone 1, binary.

1644 2D interior faces, zone 2, binary.

3495 2D wall faces, zone 6, binary.

138 2D velocity-inlet faces, zone 7, binary.

30 2D pressure-outlet faces, zone 8, binary.

75225 nodes, binary.

75225 node flags, binary.

Done.

iter continuity x-velocity y-velocity energy k omega lift-coeff drag-coeff time/iter

133 1.9152e-06 1.8586e-10 3.0835e-11 1.5278e-16 3.1476e-05 6.7876e-05 4.5488e-01 9.0614e-03 0:14:33 867

134 1.7663e-06 1.6981e-10 2.7832e-11 1.5131e-16 3.1188e-05 6.7133e-05 4.5488e-01 9.0614e-03 0:14:31 866

135 1.6337e-06 1.5535e-10 2.5387e-11 1.5054e-16 3.0906e-05 6.6403e-05 4.5488e-01 9.0614e-03 0:11:36 865

136 1.5208e-06 1.4238e-10 2.3405e-11 1.5182e-16 3.0627e-05 6.5685e-05 4.5488e-01 9.0614e-03 0:12:09 864

137 1.4225e-06 1.3062e-10 2.1761e-11 1.5449e-16 3.0354e-05 6.4979e-05 4.5488e-01 9.0614e-03 0:12:35 863

138 1.3368e-06 1.2088e-10 2.0836e-11 1.5263e-16 3.0084e-05 6.4285e-05 4.5488e-01 9.0614e-03 0:10:03 862

139 1.2554e-06 1.1222e-10 2.0399e-11 1.5461e-16 2.9820e-05 6.3603e-05 4.5488e-01 9.0614e-03 0:10:54 861

140 1.1821e-06 1.0494e-10 2.0068e-11 1.5134e-16 2.9559e-05 6.2932e-05 4.5488e-01 9.0614e-03 0:11:35 860

141 1.1112e-06 9.7994e-11 1.9618e-11 1.5351e-16 2.9303e-05 6.2272e-05 4.5488e-01 9.0614e-03 0:12:07 859

142 1.0476e-06 9.2205e-11 1.9242e-11 1.5072e-16 2.9050e-05 6.1623e-05 4.5488e-01 9.0614e-03 0:09:41 858

! 143 solution is converged

C.2 Last 10 Iterations of Airfoil with K=0.05 (300m/s) at $\alpha=0^{o}$

1980694 triangular cells, zone 3, binary.
Warning: reading 4 partition grid onto 8 compute node machine;
will auto partition.
1980694 cell partition ids, zone 3, 4 partitions, binary.
2890261 2D interior faces, zone 1, binary.
1440 2D interior faces, zone 2, binary.
158400 2D wall faces, zone 6, binary.
230 2D velocity-inlet faces, zone 7, binary.
50 2D pressure-outlet faces, zone 8, binary.
1069687 nodes, binary.
1069687 node flags, binary.

Done.

iter continuity x-velocity y-velocity energy k omega lift-coeff drag-coeff time/iter

123 4.1500e-04 7.6932e-08 1.1065e-08 1.6525e-16 1.5397e-04 5.3794e-05 4.5621e-01 8.2514e-03 2:38:11 877

124 3.9669e-04 7.3131e-08 1.0823e-08 1.6656e-16 1.5206e-04 5.2920e-05 4.5624e-01 8.2531e-03 2:32:41 876

125 3.8237e-04 6.9962e-08 1.0595e-08 1.6900e-16 1.5038e-04 5.2021e-05 4.5627e-01 8.2547e-03 2:34:05 875

126 3.6989e-04 6.7168e-08 1.0407e-08 1.6654e-16 1.4899e-04 5.1947e-05 4.5630e-01 8.2563e-03 2:35:10 874

127 3.7146e-04 6.6526e-08 1.0391e-08 1.6775e-16 1.4804e-04 5.1004e-05 4.5633e-01 8.2580e-03 2:30:11 873

128 3.6656e-04 6.5144e-08 1.0388e-08 1.6839e-16 1.4678e-04 4.9282e-05 4.5636e-01 8.2596e-03 2:31:59 872

129 3.4735e-04 6.1648e-08 1.0174e-08 1.6732e-16 1.4520e-04 4.8373e-05 4.5639e-01 8.2609e-03 2:30:29 871

130 3.3296e-04 5.8953e-08 9.9513e-09 1.6792e-16 1.4375e-04 4.7602e-05 4.5642e-01 8.2623e-03 2:32:09 870

131 3.2182e-04 5.6776e-08 9.7102e-09 1.6706e-16 1.4250e-04 4.6781e-05 4.5645e-01 8.2636e-03 2:30:33 869

132 3.1233e-04 5.4968e-08 9.4805e-09 1.6549e-16 1.4136e-04 4.5987e-05 4.5648e-01 8.2650e-03 2:32:07 868

iter continuity x-velocity y-velocity energy k omega lift-coeff drag-coeff time/iter

133 3.0402e-04 5.3387e-08 9.2287e-09 1.6624e-16 1.4031e-04 4.5183e-05 4.5651e-01 8.2662e-03 2:36:14 867

Done.

C.3 Last 10 Iterations of Airfoil with K=0.1 (300m/s) at $\alpha=0^{o}$

1795352 triangular cells, zone 3, binary.

1795352 cell partition ids, zone 3, 8 partitions, binary.

2664570 2D interior faces, zone 1, binary.

2789 2D interior faces, zone 2, binary.

51058 2D wall faces, zone 6, binary.

230 2D velocity-inlet faces, zone 7, binary.

50 2D pressure-outlet faces, zone 8, binary.

923345 nodes, binary.

923345 node flags, binary.

Done.

iter continuity x-velocity y-velocity energy k omega drag-coeff lift-coeff time/iter
637 1.1461e-05 3.3069e-10 2.0782e-10 1.7025e-16 4.1247e-05 2.6360e-05 1.0308e-02 9.7984e-01 0:41:05 363
638 1.0373e-05 3.2740e-10 2.0523e-10 1.6888e-16 4.1169e-05 2.6319e-05 1.0308e-02 9.7984e-01 0:41:13 362
639 1.1445e-05 3.2913e-10 2.0490e-10 1.6962e-16 4.1060e-05 2.6277e-05 1.0308e-02 9.7985e-01 0:41:19 361
640 1.0409e-05 3.2812e-10 2.0979e-10 1.7021e-16 4.0962e-05 2.6235e-05 1.0308e-02 9.7984e-01 0:41:21 360
641 1.1427e-05 3.2924e-10 2.0667e-10 1.7125e-16 4.0856e-05 2.6189e-05 1.0308e-02 9.7985e-01 0:41:22 359
642 1.0233e-05 3.2626e-10 2.0319e-10 1.7047e-16 4.0764e-05 2.6148e-05 1.0308e-02 9.7984e-01 0:40:10 358
643 1.1301e-05 3.2724e-10 2.0305e-10 1.6961e-16 4.0658e-05 2.6106e-05 1.0308e-02 9.7985e-01 0:40:22 357
644 1.0284e-05 3.2731e-10 2.0775e-10 1.6814e-16 4.0561e-05 2.6068e-05 1.0308e-02 9.7984e-01 0:40:31 356
645 1.1381e-05 3.2738e-10 2.0606e-10 1.6990e-16 4.0452e-05 2.6023e-05 1.0308e-02 9.7985e-01 0:40:36 355
646 1.0246e-05 3.2461e-10 2.0221e-10 1.6983e-16 4.0354e-05 2.5982e-05 1.0308e-02 9.7984e-01 0:41:50 354
Done.

C.4 Last 10 Iterations of Airfoil with K=0.15 (300m/s) at $\alpha=0^{o}$

796084 triangular cells, zone 3, binary.

796084 cell partition ids, zone 3, 8 partitions, binary.

1163137 2D interior faces, zone 1, binary.

1455 2D interior faces, zone 2, binary.

58788 2D wall faces, zone 6, binary.

230 2D velocity-inlet faces, zone 7, binary.

50 2D pressure-outlet faces, zone 8, binary.

427576 nodes, binary.

427576 node flags, binary.

Done.

iter continuity x-velocity y-velocity energy k omega lift-coeff drag-coeff time/iter

507 1.2983e-04 1.1561e-08 3.0846e-09 1.6735e-16 1.6986e-04 1.5479e-05 4.5751e-01 8.6188e-03 0:17:27 493

508 1.2965e-04 1.1501e-08 2.9857e-09 1.6635e-16 1.6979e-04 1.5414e-05 4.5751e-01 8.6189e-03 0:18:51 492

509 1.2866e-04 1.1419e-08 2.9754e-09 1.6705e-16 1.6977e-04 1.5473e-05 4.5751e-01 8.6189e-03 0:18:20 491

510 1.2915e-04 1.1362e-08 2.9924e-09 1.6710e-16 1.6963e-04 1.5421e-05 4.5751e-01 8.6189e-03 0:17:54 490

511 1.2876e-04 1.1351e-08 2.9549e-09 1.6700e-16 1.6962e-04 1.5465e-05 4.5751e-01 8.6189e-03 0:17:33 489

512 1.2917e-04 1.1452e-08 2.9711e-09 1.6711e-16 1.6948e-04 1.5449e-05 4.5751e-01 8.6189e-03 0:18:54 488

513 1.2908e-04 1.1537e-08 2.9879e-09 1.6747e-16 1.6949e-04 1.5456e-05 4.5751e-01 8.6188e-03 0:18:20 487

514 1.2937e-04 1.1538e-08 3.0594e-09 1.6532e-16 1.6934e-04 1.5469e-05 4.5751e-01 8.6188e-03 0:17:52 486

515 1.2720e-04 1.1400e-08 2.9764e-09 1.6769e-16 1.6934e-04 1.5449e-05 4.5751e-01 8.6187e-03 0:19:07 485

516 1.2510e-04 1.1284e-08 2.9089e-09 1.6628e-16 1.6917e-04 1.5458e-05 4.5751e-01 8.6187e-03 0:21:43 484

Done.

C.5 Last 10 Iterations of Airfoil with K=0.2 (300m/s) at $\alpha=0^{o}$

2482903 triangular cells, zone 3, binary.
2482903 cell partition ids, zone 3, 8 partitions, binary.
3696554 2D interior faces, zone 1, binary.
3423 2D interior faces, zone 2, binary.
48475 2D wall faces, zone 6, binary.
230 2D velocity-inlet faces, zone 7, binary.
50 2D pressure-outlet faces, zone 8, binary.
1265829 nodes, binary.
1265829 node flags, binary.

Done.

163 9.1137e-05 1.2770e-08 2.3673e-09 1.6996e-16 4.3290e-05 2.3825e-05 8.8576e-03 4.5224e-01 2:01:27 837

164 8.6852e-05 1.2205e-08 2.2322e-09 1.7077e-16 4.2942e-05 2.3437e-05 8.8576e-03 4.5225e-01 2:02:07 836

165 8.3671e-05 1.1735e-08 2.1155e-09 1.6952e-16 4.2627e-05 2.3086e-05 8.8575e-03 4.5226e-01 1:59:51 835

iter continuity x-velocity y-velocity energy k omega drag-coeff lift-coeff time/iter

166 8.1452e-05 1.1289e-08 2.1215e-09 1.7071e-16 4.2294e-05 2.2697e-05 8.8575e-03 4.5226e-01 1:58:00 834

167 7.5705e-05 1.0456e-08 1.9483e-09 1.7299e-16 4.1964e-05 2.2342e-05 8.8575e-03 4.5227e-01 1:56:30 833

168 7.1489e-05 9.8934e-09 1.8024e-09 1.7189e-16 4.1775e-05 2.2009e-05 8.8575e-03 4.5228e-01 1:55:17 832

169 6.9662e-05 9.7358e-09 1.7142e-09 1.7139e-16 4.1673e-05 2.1701e-05 8.8574e-03 4.5228e-01 1:57:02 831

170 6.8663e-05 9.5234e-09 1.7642e-09 1.7293e-16 4.1556e-05 2.1376e-05 8.8574e-03 4.5229e-01 1:55:39 830

171 6.4810e-05 8.9732e-09 1.6181e-09 1.7188e-16 4.1453e-05 2.1097e-05 8.8574e-03 4.5229e-01 1:54:31 829

172 6.3059e-05 8.8537e-09 1.5438e-09 1.7016e-16 4.1374e-05 2.0783e-05 8.8573e-03 4.5230e-01 1:56:21 828

173 6.1120e-05 8.6395e-09 1.4801e-09 1.6954e-16 4.1320e-05 2.0502e-05 8.8573e-03 4.5230e-01 1:57:46 827

174 6.1304e-05 8.5004e-09 1.5321e-09 1.6998e-16 4.1281e-05 2.0239e-05 8.8573e-03 4.5231e-01 1:58:53 826

Done.

C.6 Last 10 Iterations of Airfoil with K=0.25 (300m/s) at $\alpha=0^{o}$

1807423 triangular cells, zone 3, binary.

1807423 cell partition ids, zone 3, 8 partitions, binary.

2684168 2D interior faces, zone 1, binary.

2792 2D interior faces, zone 2, binary.

48015 2D wall faces, zone 6, binary.

27 2D wall faces, zone 7, binary.

27 2D wall faces, zone 5, binary.

230 2D velocity-inlet faces, zone 8, binary.

50 2D pressure-outlet faces, zone 9, binary.

27 shadow face pairs, binary.

927884 nodes, binary.

927884 node flags, binary.

Done.

240 1.0501e-05 1.0774e-09 2.4359e-10 1.6869e-16 3.0919e-05 1.0577e-05 4.5414e-01 9.0570e-03 1:11:05 760

241 1.0301e-05 1.0491e-09 2.3745e-10 1.7001e-16 3.0855e-05 1.0496e-05 4.5414e-01 9.0570e-03 1:11:58 759

242 1.0134e-05 1.0229e-09 2.3057e-10 1.6887e-16 3.0788e-05 1.0412e-05 4.5414e-01 9.0570e-03 1:12:40 758

iter continuity x-velocity y-velocity energy k omega lift-coeff drag-coeff time/iter

243 1.0025e-05 9.9472e-10 2.2848e-10 1.6675e-16 3.0715e-05 1.0331e-05 4.5414e-01 9.0570e-03 1:10:40 757

244 9.8695e-06 9.6958e-10 2.2137e-10 1.6709e-16 3.0636e-05 1.0248e-05 4.5414e-01 9.0570e-03 1:11:35 756

245 9.7530e-06 9.4365e-10 2.1924e-10 1.6931e-16 3.0550e-05 1.0168e-05 4.5414e-01 9.0570e-03 1:12:17 755

246 9.6511e-06 9.2023e-10 2.1487e-10 1.6725e-16 3.0462e-05 1.0086e-05 4.5414e-01 9.0570e-03 1:10:19 754

247 9.4773e-06 8.9544e-10 2.0925e-10 1.6611e-16 3.0375e-05 1.0014e-05 4.5414e-01 9.0570e-03 1:11:15 753

248 9.3721e-06 8.7429e-10 2.0553e-10 1.6805e-16 3.0288e-05 9.9411e-06 4.5414e-01 9.0570e-03 1:11:58 752

249 9.4192e-06 8.5315e-10 2.1209e-10 1.6690e-16 3.0199e-05 9.8657e-06 4.5414e-01 9.0570e-03 1:10:00 751

250 9.2881e-06 8.3256e-10 2.0534e-10 1.6908e-16 3.0117e-05 9.7895e-06 4.5414e-01 9.0570e-03 1:10:56 750

251 9.1203e-06 8.1075e-10 1.9986e-10 1.6662e-16 3.0027e-05 9.7181e-06 4.5414e-01 9.0570e-03 1:11:39 749

252 9.0260e-06 7.9245e-10 1.9663e-10 1.6771e-16 2.9930e-05 9.6495e-06 4.5414e-01 9.0570e-03 1:12:12 748

Done.

C.7 Last 10 Iterations of Airfoil with K=0.3 (300m/s) at $\alpha=0^{o}$

736120 mixed cells, zone 3, binary.

736120 cell partition ids, zone 3, 8 partitions, binary.

1457235 2D interior faces, zone 1, binary.

1468 2D interior faces, zone 2, binary.

25136 2D wall faces, zone 6, binary.

180 2D velocity-inlet faces, zone 7, binary.

36 2D pressure-outlet faces, zone 8, binary.

747935 nodes, binary.

747935 node flags, binary.

Done.

iter continuity x-velocity y-velocity energy k omega lift-coeff drag-coeff time/iter

342 1.8173e-04 2.6581e-09 2.3634e-09 1.5598e-16 3.9756e-06 1.3523e-05 4.5713e-01 9.1244e-03 0:29:41 658

343 1.9331e-04 3.0727e-09 2.5421e-09 1.5968e-16 3.9477e-06 1.3387e-05 4.5713e-01 9.1244e-03 0:30:17 657

344 1.8193e-04 2.5288e-09 2.2563e-09 1.5937e-16 3.8863e-06 1.3267e-05 4.5713e-01 9.1243e-03 0:30:45 656

345 1.7009e-04 2.5512e-09 2.1400e-09 1.6026e-16 3.8540e-06 1.3210e-05 4.5713e-01 9.1244e-03 0:31:06 655

346 1.7855e-04 2.7398e-09 2.4228e-09 1.5880e-16 3.8706e-06 1.3127e-05 4.5713e-01 9.1243e-03 0:29:12 654

347 1.8098e-04 2.6695e-09 2.4046e-09 1.5944e-16 3.8810e-06 1.3106e-05 4.5713e-01 9.1242e-03 0:29:52 653

348 1.7404e-04 2.6773e-09 2.3283e-09 1.6009e-16 3.8043e-06 1.2973e-05 4.5713e-01 9.1243e-03 0:30:22 652

349 1.8193e-04 2.6543e-09 2.3670e-09 1.5916e-16 3.8178e-06 1.2919e-05 4.5713e-01 9.1244e-03 0:30:46 651

350 1.7855e-04 2.6799e-09 2.4252e-09 1.5695e-16 3.8273e-06 1.2868e-05 4.5713e-01 9.1245e-03 0:28:55 650

351 1.7654e-04 2.7219e-09 2.3441e-09 1.5812e-16 3.7782e-06 1.2784e-05 4.5713e-01 9.1244e-03 0:29:35 649

352 1.8221e-04 2.7828e-09 2.3823e-09 1.5496e-16 3.7793e-06 1.2664e-05 4.5713e-01 9.1243e-03 0:30:07 648

iter continuity x-velocity y-velocity energy k omega lift-coeff drag-coeff time/iter

353 1.7023e-04 2.4481e-09 2.1660e-09 1.5907e-16 3.7450e-06 1.2572e-05 4.5713e-01 9.1242e-03 0:30:31 647

354 1.6618e-04 2.4510e-09 2.0388e-09 1.5846e-16 3.6844e-06 1.2486e-05 4.5713e-01 9.1243e-03 0:33:00 646

Done.

C.8 Last 10 Iterations of Airfoil with K=0.35 (300m/s) at $\alpha=0^{o}$

767724 mixed cells, zone 3, binary.

767724 cell partition ids, zone 3, 8 partitions, binary.

1520554 2D interior faces, zone 1, binary.

1468 2D interior faces, zone 2, binary.

25060 2D wall faces, zone 6, binary.

184 2D velocity-inlet faces, zone 7, binary.

40 2D pressure-outlet faces, zone 8, binary.

779582 nodes, binary.

779582 node flags, binary.

Done.

217 1.6054e-04 2.8231e-09 2.0768e-09 1.5959e-16 7.4782e-06 3.0981e-05 9.4807e-03 4.5637e-01 0:36:21 783
218 1.5892e-04 2.9775e-09 2.0850e-09 1.5939e-16 7.3892e-06 3.0737e-05 9.4807e-03 4.5637e-01 0:36:52 782
219 1.5827e-04 2.6217e-09 1.9756e-09 1.6094e-16 7.3612e-06 3.0475e-05 9.4808e-03 4.5637e-01 0:37:16 781
220 1.5630e-04 2.7728e-09 2.0047e-09 1.6256e-16 7.2854e-06 3.0232e-05 9.4808e-03 4.5637e-01 0:37:34 780

iter continuity x-velocity y-velocity energy k omega drag-coeff lift-coeff time/iter
221 1.5152e-04 2.5798e-09 1.9726e-09 1.6223e-16 7.2310e-06 2.9988e-05 9.4808e-03 4.5636e-01 0:37:48 779
222 1.4322e-04 2.5512e-09 1.8386e-09 1.6126e-16 7.1474e-06 2.9745e-05 9.4807e-03 4.5636e-01 0:37:59 778
223 1.4558e-04 2.5352e-09 1.8146e-09 1.6004e-16 7.0806e-06 2.9461e-05 9.4808e-03 4.5636e-01 0:38:07 777
224 1.3372e-04 2.2298e-09 1.5314e-09 1.6258e-16 7.0357e-06 2.9262e-05 9.4808e-03 4.5636e-01 0:38:13 776
225 1.5106e-04 2.5774e-09 1.9323e-09 1.6286e-16 7.0551e-06 2.9078e-05 9.4808e-03 4.5636e-01 0:38:17 775
226 1.5882e-04 2.7197e-09 2.1408e-09 1.6185e-16 7.0439e-06 2.8890e-05 9.4808e-03 4.5636e-01 0:38:20 774
Done.

C.9 Last 10 Iterations of Airfoil with K=0.4 (300m/s) at $\alpha=0^{o}$

742988 mixed cells, zone 3, binary.

742988 cell partition ids, zone 3, 8 partitions, binary.

1470636 2D interior faces, zone 1, binary.

1452 2D interior faces, zone 2, binary.

25864 2D wall faces, zone 6, binary.

40 2D pressure-outlet faces, zone 7, binary.

184 2D velocity-inlet faces, zone 8, binary.

755188 nodes, binary.

755188 node flags, binary.

Done.

172 5.1727e-05 3.4008e-09 9.0147e-10 1.6272e-16 1.0826e-05 4.5471e-05 4.5886e-01 9.5578e-03 0:38:33 828

173 4.6722e-05 3.2219e-09 7.6724e-10 1.6092e-16 1.0714e-05 4.5039e-05 4.5886e-01 9.5577e-03 0:39:04 827

174 5.0105e-05 3.0791e-09 7.3530e-10 1.6437e-16 1.0618e-05 4.4622e-05 4.5886e-01 9.5577e-03 0:39:29 826

175 4.8149e-05 2.9972e-09 6.7320e-10 1.6014e-16 1.0511e-05 4.4213e-05 4.5886e-01 9.5576e-03 0:39:48 825

176 5.6040e-05 3.0230e-09 8.6911e-10 1.6325e-16 1.0413e-05 4.3810e-05 4.5886e-01 9.5576e-03 0:40:02 824

iter continuity x-velocity y-velocity energy k omega lift-coeff drag-coeff time/iter

177 5.0981e-05 2.8566e-09 7.4571e-10 1.6033e-16 1.0313e-05 4.3421e-05 4.5886e-01 9.5574e-03 0:40:13 823

178 4.7898e-05 2.7961e-09 7.2595e-10 1.6062e-16 1.0221e-05 4.3045e-05 4.5886e-01 9.5574e-03 0:37:37 822

179 5.4926e-05 2.8016e-09 9.0146e-10 1.6393e-16 1.0121e-05 4.2633e-05 4.5886e-01 9.5574e-03 0:38:16 821

180 5.1332e-05 2.6667e-09 7.9582e-10 1.6041e-16 1.0009e-05 4.2247e-05 4.5886e-01 9.5574e-03 0:38:47 820

181 5.2166e-05 2.5845e-09 7.3827e-10 1.6310e-16 9.9406e-06 4.1876e-05 4.5885e-01 9.5574e-03 0:39:10 819

182 5.4435e-05 2.5998e-09 7.9593e-10 1.6197e-16 9.8690e-06 4.1514e-05 4.5885e-01 9.5573e-03 0:42:12 818

183 5.9202e-05 2.7671e-09 9.2057e-10 1.5921e-16 9.7812e-06 4.1132e-05 4.5885e-01 9.5572e-03 0:41:54 817

Done.

C.10 Last 10 Iterations of Airfoil with K=0.45 (300m/s) at $\alpha=0^{o}$

1804119 triangular cells, zone 3, binary.

1804119 cell partition ids, zone 3, 4 partitions, binary.

2679451 2D interior faces, zone 1, binary.

2782 2D interior faces, zone 2, binary.

232 2D velocity-inlet faces, zone 6, binary.

50 2D pressure-outlet faces, zone 7, binary.

47609 2D wall faces, zone 8, binary.

926005 nodes, binary.

926005 node flags, binary.

Done.

193 2.9252e-05 4.7643e-09 9.0317e-10 1.7275e-16 3.4700e-05 1.8113e-05 4.5506e-01 9.6981e-03 1:27:53 807

194 2.8871e-05 4.5995e-09 8.7646e-10 1.7288e-16 3.4486e-05 1.7922e-05 4.5507e-01 9.6981e-03 1:26:20 806

195 2.7724e-05 4.4353e-09 8.4273e-10 1.7246e-16 3.4279e-05 1.7709e-05 4.5507e-01 9.6981e-03 1:27:46 805

196 2.7035e-05 4.2773e-09 8.1572e-10 1.7185e-16 3.4085e-05 1.7524e-05 4.5507e-01 9.6980e-03 1:26:12 804

197 2.6253e-05 4.1263e-09 7.9007e-10 1.7288e-16 3.3883e-05 1.7314e-05 4.5508e-01 9.6980e-03 1:27:37 803

198 2.5029e-05 3.9758e-09 7.4793e-10 1.7348e-16 3.3677e-05 1.7123e-05 4.5508e-01 9.6980e-03 1:26:03 802

iter continuity x-velocity y-velocity energy k omega lift-coeff drag-coeff time/iter

199 2.4688e-05 3.7195e-09 7.3405e-10 1.7323e-16 3.3484e-05 1.6937e-05 4.5508e-01 9.6980e-03 1:22:06 801

200 2.3071e-05 3.5201e-09 6.8456e-10 1.7224e-16 3.3317e-05 1.6757e-05 4.5508e-01 9.6979e-03 1:21:36 800

201 2.2738e-05 3.3795e-09 6.6803e-10 1.7390e-16 3.3165e-05 1.6580e-05 4.5508e-01 9.6979e-03 1:23:50 799

202 2.2110e-05 3.3659e-09 6.3603e-10 1.7279e-16 3.3013e-05 1.6405e-05 4.5509e-01 9.6979e-03 1:22:57 798

203 2.1690e-05 3.3056e-09 6.2612e-10 1.7279e-16 3.2878e-05 1.6225e-05 4.5509e-01 9.6979e-03 1:24:52 797

204 2.1865e-05 3.2283e-09 6.2668e-10 1.7021e-16 3.2743e-05 1.6065e-05 4.5509e-01 9.6979e-03 1:23:44 796

205 2.0630e-05 3.0197e-09 5.9899e-10 1.7337e-16 3.2607e-05 1.5889e-05 4.5509e-01 9.6979e-03 1:22:48 795

Done.

C.11 Last 10 Iterations of Airfoil with K=0.5 (300m/s) at $\alpha=0^{o}$

612393 mixed cells, zone 3, binary.

612393 cell partition ids, zone 3, 8 partitions, binary.

1211549 2D interior faces, zone 1, binary.

1156 2D interior faces, zone 2, binary.

184 2D velocity-inlet faces, zone 6, binary.

40 2D pressure-outlet faces, zone 7, binary.

22440 2D wall faces, zone 8, binary.

622976 nodes, binary.

622976 node flags, binary.

Done.

190 4.8856e-05 2.3772e-09 7.3574e-10 1.5931e-16 9.4094e-06 3.8856e-05 9.7275e-03 4.5842e-01 0:31:19 810

191 4.0616e-05 2.1777e-09 6.2360e-10 1.5733e-16 9.3033e-06 3.8506e-05 9.7275e-03 4.5842e-01 0:30:25 809

192 4.5678e-05 2.1877e-09 6.3268e-10 1.6091e-16 9.2213e-06 3.8173e-05 9.7275e-03 4.5842e-01 0:32:23 808

193 4.6939e-05 2.1852e-09 6.8222e-10 1.5903e-16 9.1440e-06 3.7858e-05 9.7274e-03 4.5841e-01 0:31:15 807

194 4.5791e-05 2.0990e-09 6.6632e-10 1.5745e-16 9.0604e-06 3.7535e-05 9.7274e-03 4.5841e-01 0:30:21 806

195 4.4644e-05 2.0547e-09 6.4149e-10 1.6000e-16 8.9618e-06 3.7193e-05 9.7273e-03 4.5841e-01 0:32:18 805

196 4.0463e-05 1.9418e-09 5.8932e-10 1.5949e-16 8.8630e-06 3.6869e-05 9.7273e-03 4.5841e-01 0:31:10 804

197 3.7859e-05 1.8631e-09 5.7011e-10 1.6046e-16 8.7758e-06 3.6545e-05 9.7273e-03 4.5841e-01 0:30:15 803

198 3.9247e-05 1.7712e-09 5.3909e-10 1.5998e-16 8.7015e-06 3.6239e-05 9.7273e-03 4.5841e-01 0:29:31 802

iter continuity x-velocity y-velocity energy k omega drag-coeff lift-coeff time/iter

199 4.0042e-05 1.7603e-09 5.4533e-10 1.5947e-16 8.6292e-06 3.5933e-05 9.7273e-03 4.5841e-01 0:31:36 801

200 4.1261e-05 1.7033e-09 5.2994e-10 1.6206e-16 8.5648e-06 3.5635e-05 9.7273e-03 4.5841e-01 0:30:35 800

201 4.2660e-05 1.7325e-09 5.7924e-10 1.5931e-16 8.4938e-06 3.5342e-05 9.7273e-03 4.5841e-01 0:29:46 799

202 4.6015e-05 1.6936e-09 5.8403e-10 1.5802e-16 8.4331e-06 3.5049e-05 9.7273e-03 4.5841e-01 0:34:25 798

203 4.2636e-05 1.6353e-09 5.5579e-10 1.5674e-16 8.3529e-06 3.4756e-05 9.7273e-03 4.5841e-01 0:32:49 797

Done.

C.12 Last 10 Iterations of Airfoil with K=1mm (300m/s) at $\alpha=0^{o}$

909903 triangular cells, zone 3, binary.

Warning: reading 4 partition grid onto 8 compute node machine;

will auto partition.

909903 cell partition ids, zone 3, 4 partitions, binary.

1339775 2D interior faces, zone 1, binary.

1441 2D interior faces, zone 2, binary.

230 2D velocity-inlet faces, zone 6, binary.

50 2D pressure-outlet faces, zone 7, binary.

46997 2D wall faces, zone 8, binary.

478590 nodes, binary.

478590 node flags, binary.

Done.

216 2.0652e-05 4.6938e-09 9.0247e-10 1.6722e-16 2.9515e-05 1.3555e-05 4.6066e-01 1.1034e-02 0:36:10 784

217 1.9339e-05 4.2091e-09 8.5405e-10 1.6844e-16 2.9464e-05 1.3428e-05 4.6067e-01 1.1034e-02 0:36:44 783

218 1.8052e-05 3.7594e-09 8.0253e-10 1.6491e-16 2.9414e-05 1.3305e-05 4.6067e-01 1.1034e-02 0:37:10 782

219 1.6928e-05 3.3567e-09 7.5938e-10 1.6554e-16 2.9365e-05 1.3182e-05 4.6067e-01 1.1033e-02 0:37:30 781

220 1.5831e-05 2.9976e-09 7.1445e-10 1.6758e-16 2.9317e-05 1.3062e-05 4.6067e-01 1.1033e-02 0:35:10 780

iter continuity x-velocity y-velocity energy k omega lift-coeff drag-coeff time/iter

221 1.4759e-05 2.6356e-09 6.6432e-10 1.6380e-16 2.9266e-05 1.2943e-05 4.6067e-01 1.1033e-02 0:35:53 779

222 1.3690e-05 2.3335e-09 6.1582e-10 1.6575e-16 2.9220e-05 1.2828e-05 4.6067e-01 1.1033e-02 0:36:27 778

223 1.2842e-05 2.0873e-09 5.7289e-10 1.6667e-16 2.9175e-05 1.2715e-05 4.6067e-01 1.1033e-02 0:34:18 777

224 1.2083e-05 1.8814e-09 5.3488e-10 1.6765e-16 2.9134e-05 1.2607e-05 4.6067e-01 1.1033e-02 0:35:10 776

225 1.1594e-05 1.7549e-09 5.1383e-10 1.6592e-16 2.9096e-05 1.2499e-05 4.6067e-01 1.1033e-02 0:35:51 775

226 1.1071e-05 1.6234e-09 4.9022e-10 1.6593e-16 2.9062e-05 1.2395e-05 4.6067e-01 1.1033e-02 0:36:23 774

227 1.0601e-05 1.5045e-09 4.7017e-10 1.6546e-16 2.9026e-05 1.2291e-05 4.6067e-01 1.1033e-02 0:39:22 773

228 1.0150e-05 1.3942e-09 4.4848e-10 1.6683e-16 2.9024e-05 1.2190e-05 4.6067e-01 1.1033e-02 0:39:11 772

Done.

C.13 Last 10 Iterations of Airfoil with K=2mm (300m/s) at $\alpha=0^{o}$

717521 triangular cells, zone 3, binary.

717521 cell partition ids, zone 3, 8 partitions, binary.

1057121 2D interior faces, zone 1, binary.

1441 2D interior faces, zone 2, binary.

35159 2D wall faces, zone 6, binary.

230 2D velocity-inlet faces, zone 7, binary.

50 2D pressure-outlet faces, zone 8, binary.

376480 nodes, binary.

376480 node flags, binary.

Done

iter continuity x-velocity y-velocity energy k omega lift-coeff drag-coeff time/iter

235 8.2431e-06 9.6623e-10 3.1954e-10 1.6864e-16 5.7227e-05 1.2161e-05 4.6986e-01 1.2291e-02 0:28:03 765

236 8.2713e-06 9.6392e-10 3.1402e-10 1.6614e-16 5.7373e-05 1.2079e-05 4.6986e-01 1.2291e-02 0:30:03 764

237 8.2120e-06 9.5713e-10 3.1302e-10 1.6557e-16 5.7478e-05 1.1987e-05 4.6986e-01 1.2291e-02 0:29:06 763

238 8.1825e-06 9.6015e-10 3.1328e-10 1.6786e-16 5.7580e-05 1.1901e-05 4.6986e-01 1.2291e-02 0:28:20 762

239 8.1788e-06 9.7527e-10 3.1408e-10 1.6709e-16 5.7686e-05 1.1815e-05 4.6986e-01 1.2291e-02 0:27:42 761

240 8.1783e-06 9.8992e-10 3.1528e-10 1.6741e-16 5.7808e-05 1.1734e-05 4.6986e-01 1.2291e-02 0:29:44 760

241 8.1748e-06 1.0083e-09 3.1659e-10 1.6726e-16 5.7894e-05 1.1654e-05 4.6986e-01 1.2291e-02 0:28:49 759

242 8.2732e-06 1.0306e-09 3.1921e-10 1.6782e-16 5.8006e-05 1.1576e-05 4.6986e-01 1.2291e-02 0:30:36 758

iter continuity x-velocity y-velocity energy k omega lift-coeff drag-coeff time/iter

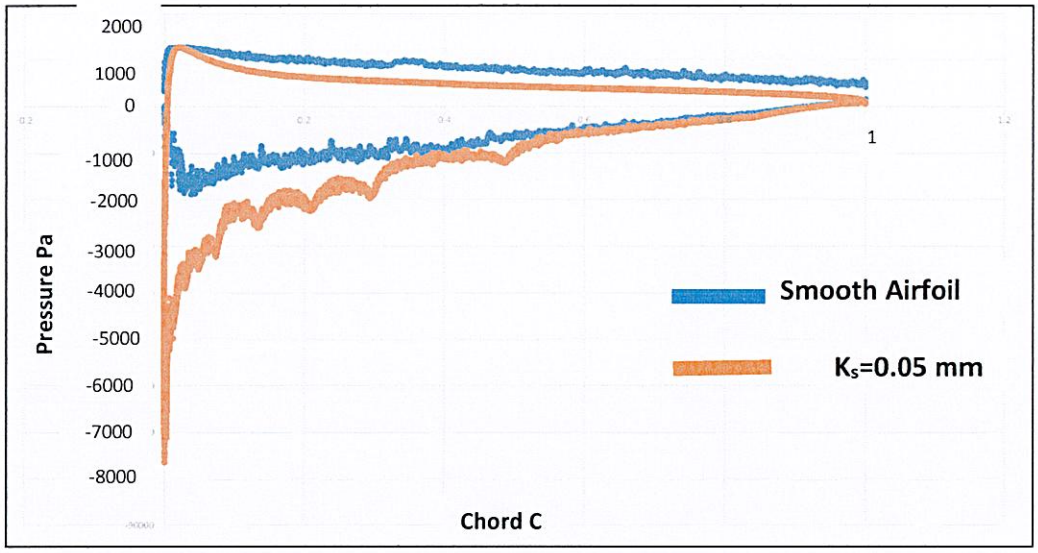


Figure (4.44): Total Pressure Comparison Between Smooth Airfoil and Airfoil with ks =0.05mm

ii. Second Set of Applied Roughness C_L

We considered the heights of applied surface roughness in this set to interfere with the boundary layer thickness. This ks stimulated the boundary layer to be rough, as indicated in Table (3.2). We detected an unexpected increase of C_L at $\alpha = 0^o$ and $\alpha = 5^o$ in all velocities for airfoil with ks=3mm. This increase is caused by the changed aerodynamic shape of the NACA 4412 airfoil due to the applied large diameter spherical surface roughness of ks =3mm. Future research can conduct more investigations into this part.

The second set of applied surface roughness to the lower surface of the NACA 4412 airfoil recorded the best results for ks =3mm. The values of C_L had percentages increase of 4.56%, 4.75%, 4.99%, and 5.13% compared to the smooth airfoil, as revealed in Table (4.6).

Table (4.6): C_L Percentage for Differences of Airfoils with Applied Roughness of Second Set of ks to the Smooth Airfoil $\alpha = 0^o$

V / ks	150m/s	200m/s	250m/s	300m/s
ks=1mm	1.06%	0.96%	1.25%	1.17%
ks=2mm	2.62%	2.92%	3.15%	3.28%
ks=3mm	4.56%	4.75%	4.99%	5.13%
ks=4mm	0.16%	0.58%	0.88%	1.12%

The second set of applied surface roughness to the lower surface had a drop in percentage values of C_L compared to smooth airfoil when α raised to 5^o for all ks except ks =3mm. The model with ks =3mm resulted in a slight growth of 0.36%, 0.53%, 0.66%, and 0.88% for velocities 150m/s, 200m/s, 250m/s, and 300m/s, respectively, as shown in Table (4.7).

Table (4.7): C_L of Percentage Differences of Airfoils with Applied Roughness of Second Set of k_s to the Smooth Airfoil $\alpha = 5^o$

V / ks	150m/s	200m/s	250m/s	300m/s
ks=1mm	-1.14%	-1.19%	-1.23%	-1.24%
ks=2mm	-0.89%	-0.59%	-0.35%	-0.36%
ks=3mm	0.36%	0.53%	0.66%	0.88%
ks=4mm	-3.64%	-3.26%	-2.84%	-2.79%

At a higher α of 10^o, all values of C_L dropped sharply because of a significant transformation in pressure distribution due formation of adverse pressure at the lower surface. NACA 4412 airfoil with a larger applied ks pattern at higher angles of attack α generated lower drag at the lower surface, decreasing lift force. The model with ks = 3 mm achieved the best result for applied surface roughness in this set. C_L had decreased to smooth airfoil by 4.09%, 3.7%, 3.33%, and 3.2% for velocities 150 m/s, 200 m/s, 250 m/s, and 300m/s, respectively, as presented in Table (4.8). Knowing

that the cruising α is usually between 4°-5° as elaborated in Chapter (3). In steady horizontal flight, we are mainly interested in aerodynamic performance in this region.

Table (4.8): C_L Percentage Differences of Airfoils with Applied Roughness of Second set of ks to the Smooth Airfoil α= 10°

V / ks	150m/s	200m/s	250m/s	300m/s
ks=1mm	-3.93%	-3.81%	-3.70%	-3.51%
ks=2mm	-4.44%	-4.07%	-4.02%	-3.73%
ks=3mm	-4.09%	-3.70%	-3.33%	-3.20%
ks=4mm	-8.08%	-7.64%	-7.19%	-7.05%

iii. Turbulent Flow Behavior

To verify our hypothesis, we examined turbulent energy contours for smooth airfoil in Figure (4.45), airfoil with applied roughness ks =0.05mm in Figure (4.46), and airfoil with applied roughness of ks =3mm in Figure (4.47). We simulated these airfoils in V=250m/s and α= 0°. In Figure (3.36), we noticed that the turbulent energy is very high especially downstream upper and lower airfoil surfaces. This energy decayed in Figures (4.46) and Figure (4.47), meaning the turbulences' severity decreased by increasing lower surface roughness. As a result, more regular flow is found downstream and smaller chances of flow separation or stability because of less severity of wake vortex at trailing edges.

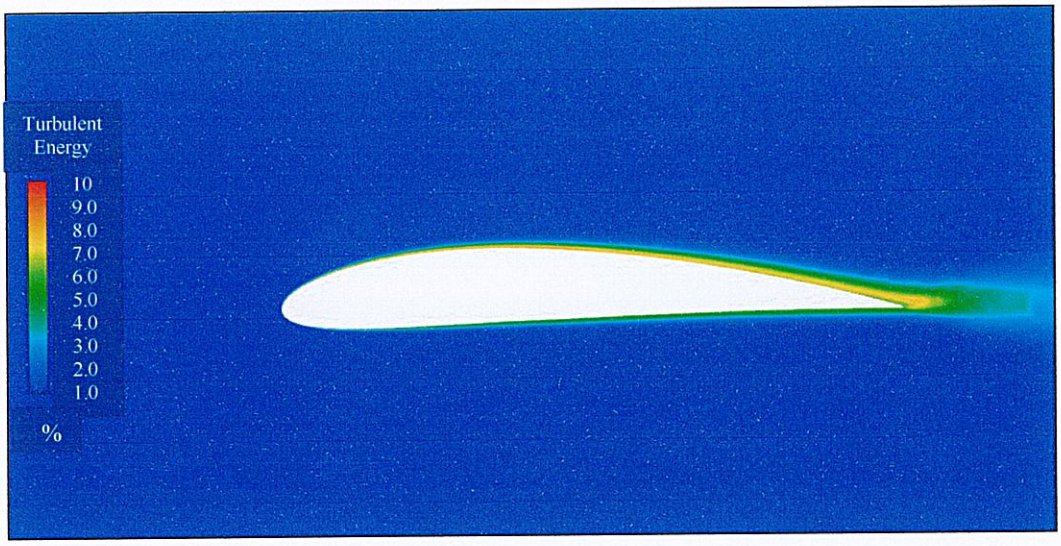


Figure (4.45): Turbulent Energy of NACA 4412 at α= 0° and V=250m/s (Smooth Airfoil)

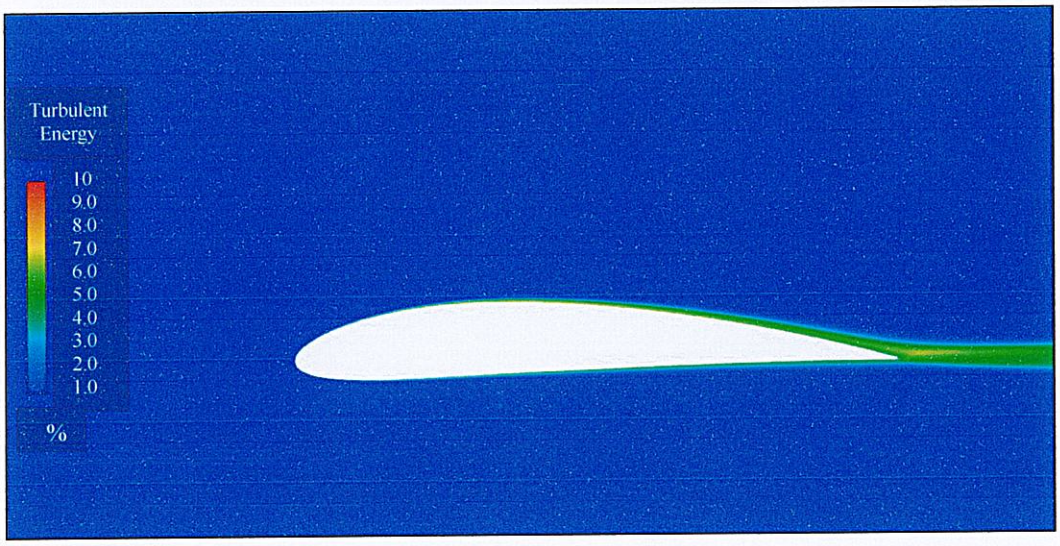


Figure (4.46): Turbulent Energy of NACA 4412 at α= 0° and V=250m/s (ks =0.05mm)

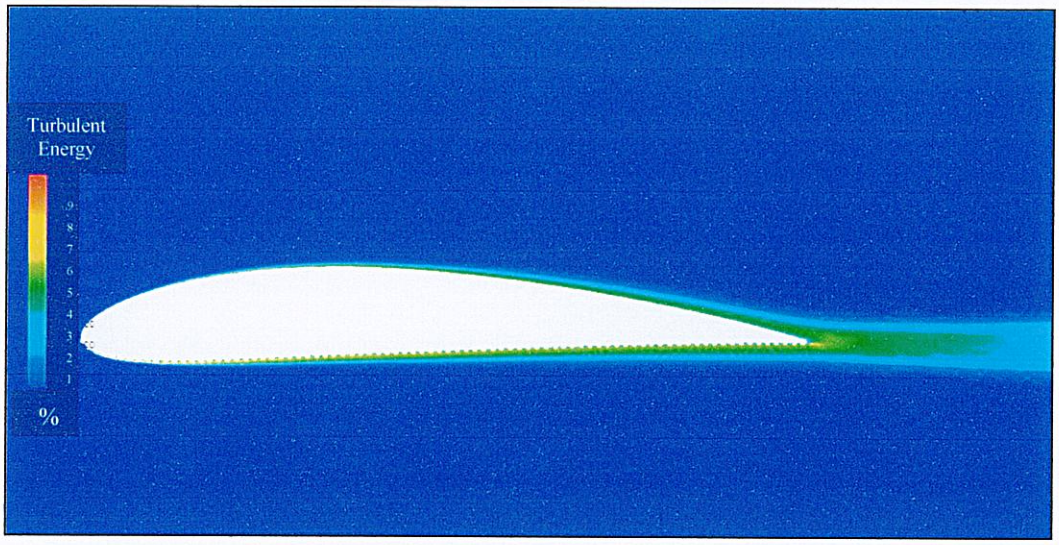


Figure (4.47): Turbulent Energy of NACA 4412 at α= 0° and V=250m/s (ks =3mm)

Figure (4.48) shows a plot for the turbulent intensity of the airflow. The fluctuating intensity of the lower surface is due to the spherical applied surface roughness to the lower surface. Despite both plain and airfoil with ks=0.05mm turbulent intensities being similar upstream, lower values observed downstream for airfoil with ks =0.05mm

This phenomenon caused a slight decrease of C_L at different operating conditions for airfoils with applied surface roughness ks. Our hypothesis suggested an increase of C_L with direct application of the Thin Airfoil Theory. However, other obstacles arose. The positive flow reaction around the airfoil and distributed pressure increase/ decrease enhanced the unexpected parameter, which is the drag coefficient C_D.

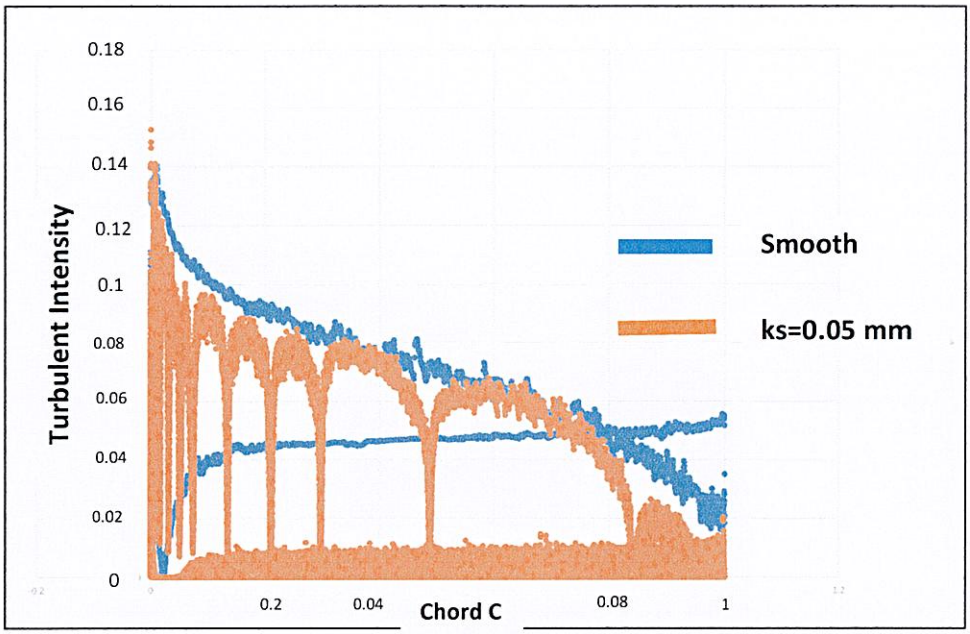


Figure (4.48): Turbulent Intensity comparison between Smooth Airfoil and Airfoil with ks =0.05mm

4.3.2 Numerical Drag Coefficient Discussion

i. First Set of Applied Roughness C_D

Although skin friction increased remarkably at the lower surface for airfoil with an applied surface roughness of ks =0.05mm, as shown in Figure (4.32), the complete C_D recorded decreased for most of the tested models in the first set of applied surface roughness.

All surface roughness heights from ks =0.05mm to ks=0.3mm recorded favorable C_D lowering at different testing velocities. Vise versa roughness heights from ks =0.35mm to ks =0.5mm. These observations could be related to boundary layer thickness interference for different heights. As indicated in Table (3.1), smaller ks values lay in the smooth hydraulically boundary layer. In comparison, more significant ks values

started to get in the transitional range of the boundary layer, where dependency in Re and other aerodynamic characteristics began to decay.

Applied surface roughness of ks =0.05mm resumed to record good results validating our hypothesis stated in Chapter (3) of sensitivity of aerodynamic characteristics to the surface roughness ks. C_D of airfoil with applied roughness ks =0.05mm was the best model, resulting in a decrease of total drag coefficient of the airfoil by 9.57%, 9.66%, 9.0%, and 8.57% for velocities: 150m/s, 200m/s, 250m/s, and 300m/s respectively as demonstrated in Table (4.8).

Otherwise, airfoil with applied roughness ks =0.5mm got the worst results.C_D increased compared to smooth airfoil by 4.31%, 5.37%, 6.39%, and 7.35% for velocities: 150m/s, 200m/s, 250m/s, and 300m/s. Table (4.9) presents these data.

Table (4.9): C_D Percentage Difference of Airfoils with Applied Roughness of First set of ks to the Smooth Airfoil $\alpha = 0^o$

V / ks	150m/s	200 m/s	250 m/s	300 m/s
ks= 0.05 mm	-9.75%	-9.66%	-9.00%	-8.57%
ks= 0.1 mm	-8.55%	-6.82%	-5.56%	-4.73%
ks = 0.15 mm	-7.11%	-6.21%	-5.53%	-4.94%
ks = 0.2 mm	-5.04%	-3.65%	-2.75%	-2.28%
ks = 0.25 mm	-2.72%	-1.41%	-0.55%	-0.05%
ks = 0.3 mm	-2.60%	-1.66%	-0.32%	0.70%
ks = 0.35 mm	1.63%	2.54%	3.64%	4.68%
ks= 0.4 mm	2.59%	3.67%	4.64%	5.46%
ks = 0.45 mm	4.30%	4.17%	9.32%	6.91%
ks = 0.5 mm	4.31%	5.37%	6.39%	7.35%

The increase of α to 5°, the standard cruising incident angle in aviation, greatly affected C_D values. All C_D results of applied surface

roughness on the lower surface of NACA 4412 airfoil models decreased. The model with ks =0.05mm continued to have the best results by decrement compared to smooth airfoil of 12.03%, 12.38%, 12.64%, and 11.44% for velocities: 150m/s, 200m/s, 250m/s, 300m/s respectively. Table (4.10) presents the results of the comparison between these airfoils.

Table (4.10): C_D Percentage Differences of Airfoils with Applied Roughness of First Set of ks to the Smooth Airfoil $\alpha = 5^o$

V / ks	150m/s	200 m/s	250 m/s	300 m/s
ks= 0.05 mm	-12.03%	-12.38%	-12.64%	-11.44%
ks= 0.1 mm	-11.16%	-10.44%	-10.05%	-8.90%
ks = 0.15 mm	-11.19%	-11.05%	-10.89%	-9.62%
ks = 0.2 mm	-8.92%	-8.24%	-8.07%	-7.01%
ks = 0.25 mm	-7.80%	-7.22%	-6.97%	-5.91%
ks = 0.3 mm	-8.37%	-8.22%	-7.77%	-6.23%
ks = 0.35 mm	-5.73%	-5.75%	-5.38%	-3.85%
ks= 0.4 mm	-5.68%	-5.48%	-5.14%	-3.70%
ks = 0.45 mm	-3.82%	0.10%	-3.02%	-2.05%
ks = 0.5 mm	-4.39%	-4.18%	-3.90%	-2.29%

We achieved another perfect result of C_D for a higher α of 10^o. C_D values keep decreasing for all applied roughness ks models but with a slight increase of rates more than $\alpha=5^o$. These promising results of C_D at all α, different velocities, and all first-set models are because of decreasing form drag despite increasing friction drag. The positive effect of increasing friction drag at the lower surface was decreasing negative pressure at the leading and trailing edges. This phenomenon led to better air flow movement adjacent to the surfaces and better application of turbulent flow characteristics.

NACA 4412 keeps performance in higher angles of attack as well concerning C_D. C_D decreased even higher at $\alpha = 10^o$. The applied surface roughness ks =0.05mm at the lower surface model preserved the lead with a percentage decrease compared to smooth airfoil by 12.02%, 12.85%, 13.40%, and 14.03% for velocities: 150m/s, 200m/s, 250m/s, and 300m/s as shown in Table (4.11).

Table (4.11): C_D Percentage Differences of Airfoils with Applied Roughness of First Set of ks to the Smooth Airfoil $\alpha = 10^o$

V / ks	150m/s	200 m/s	250 m/s	300 m/s
ks= 0.05 mm	-12.02%	-12.85%	-13.40%	-14.03%
ks= 0.1 mm	-10.59%	-10.75%	-11.15%	-11.46%
ks = 0.15 mm	-9.17%	-9.75%	-10.07%	-10.37%
ks = 0.2 mm	-7.79%	-7.39%	-7.50%	-8.44%
ks = 0.25 mm	-7.42%	-7.93%	-7.96%	-8.84%
ks = 0.3 mm	-10.76%	-10.95%	-10.92%	-10.86%
ks = 0.35 mm	-9.36%	-9.73%	-9.85%	-9.75%
ks= 0.4 mm	-9.69%	-9.98%	-10.15%	-10.07%
ks = 0.45 mm	-5.89%	-6.29%	-6.49%	-7.20%
ks = 0.5 mm	-7.56%	-7.83%	-7.82%	-7.66%

ii. Second Set of Applied Roughness C_D

The second set of applied surface roughness continued bad performance for different C_D values in all velocities and α. The reason for that is the exact reason for decreased C_L values discussed in the previous section. The changed aerodynamic shape of high ks airfoil models resisted the effect of applied surface roughness on the lower surface.

The airfoil model with ks = 1 mm represents the smallest value in this set. Because of that, we consider the boundary layer for this case in the transition region. That happened because the airflow moved in a non-

homogenous boundary layer state, where the dependency of Re and other flow parameters is minimal. Nevertheless, we consider higher ks values models in an entirely rough boundary layer region. At ks = 1 mm, C_D values increment compared to smooth airfoil is 17.36%, 19.59%, 20.98%, and 21.78% for velocities: 150 m/s, 200 m/s, 250 m/s and 300 m/s as shown in Table (4.12).

Table (4.12): C_D Percentage Differences of Airfoils with Applied Roughness of Second Set of ks to the Smooth Airfoil $\alpha = 0^o$

V / ks	150m/s	200m/s	250m/s	300m/s
ks=1mm	17.36%	19.59%	20.98%	21.78%
ks=2mm	30.23%	32.64%	34.35%	35.64%
ks=3mm	38.69%	41.31%	43.26%	44.71%
ks=4mm	45.36%	48.02%	50.01%	51.54%

The C_D values of applied roughness models shown in Table (4.13) slightly improved at $\alpha=5^o$ but with higher values than smooth airfoil. The airfoil model with ks =1mm continued to output the best results despite the increment compared to the smooth airfoil model. C_D increased by 3.96%, 5.01%, 5.47%, and 6.79% for velocities: 150m/s, 200m/s, 250m/s, and 300m/s respectively.

Table (4.13): C_D Percentage Differences of Airfoils with Applied Roughness of Second Set of ks to the Smooth Airfoil $\alpha = 5^o$

V / ks	150m/s	200m/s	250m/s	300m/s
ks=1mm	3.96%	5.01%	5.47%	6.79%
ks=2mm	10.82%	11.72%	12.36%	14.17%
ks=3mm	15.88%	16.80%	17.48%	19.55%
ks=4mm	18.50%	19.61%	20.34%	22.52%

The only decrease in the C_D at $\alpha=10^o$ for the second set compared to smooth airfoil was the model with ks =1mm again. C_D values of ks =1mm compared to smooth airfoil decreased by 0.15%, 0.42%, 0.99%, and 1.83% for velocities: 150m/s, 200m/s, 250m/s, and 300m/s respectively, as exhibited in Table (4.14).

Table (4.14): C_D Percentage Differences of Airfoils with Applied Roughness of Second Set of ks to the Smooth Airfoil $\alpha= 10^o$

V / ks	150m/s	200m/s	250m/s	300m/s
ks=1mm	-0.15%	-0.42%	-0.99%	-1.83%
ks=2mm	4.49%	3.99%	3.63%	3.04%
ks=3mm	9.38%	8.68%	7.81%	10.40%
ks=4mm	6.40%	5.89%	5.23%	4.99%

4.3.3 Numerical Lift-to-Drag Coefficient Discussion

i. First Set of Applied Roughness C_L/ C_D

Lift to drag ratio is presumed to be the principal indication of good aerodynamic design. In the first set of different applied surface roughness, the model with ks=0.05mm at the lower surface demonstrated the best results of C_L and C_D compared to smooth airfoil. Other different k_s models also revealed good improvement in C_L and C_D values. C_L/ C_D for ks=0.05mm model results show a gain of C_L/ C_D at $\alpha= 0^o$ compared to the smooth airfoil model as follows: 10.88%, 10.90%, 10.27%, and 9.86% for velocities: 150m/s, 200m/s, 250m/s, and 300m/s respectively. While other values recorded advancements for ks =0.1mm to ks =0.3mm, a decrease in C_L/ C_D values for ks =0.35mm to ks =0.5mm are noted due to high C_D values at $\alpha=0^o$. Table (4.15) lists the results of the comparison for NACA

4412 airfoil between C_L/ C_D values for the first set of applied surface roughness to smooth airfoil.

Table (4.15): C_L/ C_D Percentage Differences of Airfoils with Applied Roughness of First Set of ks to the Smooth Airfoil $\alpha= 0^o$

V / ks	150m/s	200m/s	250m/s	300m/s
ks= 0.05 mm	10.88%	10.90%	10.27%	9.86%
ks= 0.1 mm	9.25%	7.19%	5.85%	4.90%
ks = 0.15 mm	7.83%	7.10%	6.39%	5.82%
ks = 0.2 mm	5.83%	3.05%	2.16%	1.77%
ks = 0.25 mm	4.69%	1.26%	0.37%	-0.12%
ks = 0.3 mm	4.13%	1.54%	0.70%	-0.20%
ks = 0.35 mm	-2.40%	-2.65%	-3.43%	-4.14%
ks= 0.4 mm	-2.47%	-3.09%	-3.80%	-4.38%
ks = 0.45 mm	-4.11%	-4.50%	-9.08%	-6.93%
ks = 0.5 mm	-4.26%	-4.74%	-5.42%	-6.13%

As α increased to 5°, C_L/ C_D values rose for all models, as shown in Table (4.16). Applied surface roughness of ks =0.05mm at the lower surface of the model continued growth of C_L/ C_D values at α=5°. It also gained an additional increment in percentage difference compared to smooth airfoil this time. C_L/ C_D resulted in an advantage over the plain model by 13.08%, 13.73%, 14.13%, and 12.20% for velocities: 150m/s, 200m/s, 250m/s, and 300m/s, respectively. This angle of incident is the joint setting angle for many airplanes, primarily commercial. We noted that ks $\geq$0.3mm models have the least aerodynamic characteristics compared to ks $\leq$0.3mm models.

Table (4.16): C_L/ C_D Percentage Differences of Airfoils with Applied Roughness of First Set of ks to the Smooth Airfoil α= 5°

V / ks	150m/s	200m/s	250m/s	300m/s
ks= 0.05 mm	13.08%	13.73%	14.13%	12.20%
ks= 0.1 mm	11.48%	10.73%	10.29%	8.59%
ks = 0.15 mm	11.89%	11.86%	11.79%	9.75%
ks = 0.2 mm	8.23%	7.11%	7.07%	5.23%
ks = 0.25 mm	7.18%	6.54%	6.13%	4.19%
ks = 0.3 mm	8.01%	8.14%	7.72%	5.55%
ks = 0.35 mm	4.56%	4.81%	4.63%	2.57%
ks= 0.4 mm	5.03%	4.98%	4.78%	2.75%
ks = 0.45 mm	2.20%	-2.02%	1.11%	0.11%
ks = 0.5 mm	3.21%	3.26%	3.06%	1.00%

The model with ks =0.05mm continued to be distinguished from other models at $\alpha=10^0$. Values of C_L/ C_D recorded a slight decrease to values of $\alpha=5^0$. C_L/ C_D percentage increments between the model with ks =0.05mm to smooth airfoil are 11.83%, 13.7%, 14.06%, and 14.92% for velocities: 150m/s, 200m/s, 250m/s, and 300m/s respectively as shown in Table (4.17).

Table (4.17): C_L/ C_D Percentage Differences of Airfoils with Applied Roughness of First Set of ks to the Smooth Airfoil α= 10°

V / ks	150m/s	200m/s	250m/s	300m/s
ks= 0.05 mm	11.83%	13.17%	14.06%	14.92%
ks= 0.1 mm	9.46%	9.80%	10.45%	10.88%
ks = 0.15 mm	7.43%	8.30%	8.73%	9.23%
ks = 0.2 mm	4.87%	4.12%	4.39%	5.85%
ks = 0.25 mm	9.22%	10.16%	10.08%	11.59%
ks = 0.3 mm	9.67%	10.18%	10.24%	10.30%
ks = 0.35 mm	7.72%	8.34%	8.62%	8.56%
ks= 0.4 mm	8.41%	8.92%	9.35%	9.29%
ks = 0.45 mm	2.57%	3.13%	3.26%	4.21%
ks = 0.5 mm	5.40%	5.94%	6.01%	5.82%

ii. Second Set of Applied Roughness C_L/ C_D

The second set of applied roughness obtained the worst performance in C_L/ C_D values compared to smooth airfoil. This low performance is because drag force increment at high α values dominates the roughened lower surfaces dominates. The model with ks =1mm, which is the smallest value of ks in the models in this set, recorded the lowest loss of C_L/ C_D values compared to the plain wing. As explained earlier, this is because of the large diameter spherical applied surface roughness pattern to the lower surface of the airfoil. The aerodynamic shape of the NACA 4412 airfoil changes progressively as we increase the diameter of the applied spherical surface roughness. This change led to advancing C_D and declined C_L.

Values of C_L/ C_D for the best model of the second set (ks =1mm) compared to smooth airfoil decreased at $\alpha=0^o$ by: 13.89%, 15.58%, 16.31%, and 16.92% for velocities: 150m/s, 200m/s, 250m/s, and 300m/s respectively as shown in Table (4.18)

Table (4.18): C_L/ C_D Percentage Differences of Airfoils with Applied Roughness of Second set of ks to the Smooth Airfoil $\alpha= 0^o$

V / ks	150m/s	200m/s	250m/s	300m/s
ks=1mm	-13.89%	-15.58%	-16.31%	-16.92%
ks=2mm	-21.20%	-22.40%	-23.23%	-23.86%
ks=3mm	-24.61%	-25.87%	-26.72%	-27.35%
ks=4mm	-31.10%	-32.05%	-32.75%	-33.27%

The severity of C_L/ C_D decrements reduced when α increased to 5°. Moreover, the model with ks =1mm still recorded the best performance compared with other models. For example, the percentage decrement for C_L/ C_D values for the model with ks =1mm compared to smooth airfoil at $\alpha=5^o$ are 4.91%, 5.9%, 6.35%, 7.52% for velocities: 150m/s, 200m/s, 250m/s, 300m/s respectively as listed in Table (4.19).

Table (4.19): C_L/ C_D Percentage Differences of Airfoils with Applied Roughness of Second Set of ks to the Smooth Airfoil $\alpha= 5^o$

V / ks	150m/s	200m/s	250m/s	300m/s
ks=1mm	-4.91%	-5.90%	-6.35%	-7.52%
ks=2mm	-10.56%	-11.02%	-11.31%	-12.73%
ks=3mm	-13.40%	-13.93%	-14.32%	-15.61%
ks=4mm	-18.68%	-19.12%	-19.26%	-20.65%

The model with ks =1mm recorded the lowest decrement of values of C_L/ C_D compared to the smooth airfoil model at $\alpha=10^0$. The percentage decrement in C_L/ C_D values between the model with ks =1mm to smooth airfoil model is 3.78%, 3.40%, 2.73%, and 1.71% for velocities: 150m/s, 200m/s, 250m/s, 300m/s respectively as shown in Table (4.20).

Table (4.20): C_L/ C_D Percentage Differences of Airfoils with Applied Roughness of Second set of ks to the Smooth Airfoil $\alpha= 10^o$

V / ks	150m/s	200m/s	250m/s	300m/s
ks=1mm	-3.78%	-3.40%	-2.73%	-1.71%
ks=2mm	-8.55%	-7.75%	-7.38%	-6.56%
ks=3mm	-12.31%	-11.39%	-10.33%	-12.32%
ks=4mm	-13.61%	-12.78%	-11.80%	-11.46%

4.3.4 Numerical Power Analysis Discussion

Airfoil with the applied surface roughness of ks=0.05mm had minimized power needed to produce the required Lift by 10.91%, 10.98%, 10.48%, and 10.10% better than smooth airfoil with ks $\cong$ 0. That recorded at the angle of attack $\alpha=0^o$ for velocities: 150 m/s, 200 m/s, 250 m/s, and 300 m/s, respectively, as recorded in Table (4.21).

Table (4.21): Power Analysis $C_L^{3/2}/C_D$ Percentage Variation for Different Roughness of First Set models to Smooth Airfoil at α= 0°

V / ks	150m/s	200m/s	250m/s	300m/s
ks= 0.05 mm	10.91%	10.98%	10.48%	10.10%
ks= 0.1 mm	9.18%	7.11%	5.83%	4.86%
ks = 0.15 mm	7.92%	7.19%	6.67%	6.12%
ks = 0.2 mm	4.37%	2.70%	1.84%	1.51%
ks = 0.25 mm	2.26%	1.16%	0.28%	-0.19%
ks = 0.3 mm	1.89%	1.45%	0.81%	0.06%
ks = 0.35 mm	-2.79%	-2.76%	-3.38%	-3.97%
ks= 0.4 mm	-2.43%	-2.90%	-3.45%	-3.95%
ks = 0.45 mm	-4.11%	-4.74%	-9.32%	-7.17%
ks = 0.5 mm	-4.33%	-4.56%	-5.12%	-5.76%

At an angle of attack α=5°, $C_L^{3/2}/C_D$ further increased, with the best results compared to the smooth airfoil model. The model also achieved that with ks= 0.05mm. As a result, we understood the improvement of required power to operate the aircraft to decrease by 12.78%, 13.53%, 13.95%, and 12.50% for velocities: 150 m/s, 200 m/s, 250 m/s, and 300 m/s, respectively as presented in Table (4.22).

Table (4.22): Power Analysis $C_L^{3/2}/C_D$ Percentage Variation for Different Roughness of First Set models to Smooth Airfoil at α= 5°

V / ks	150m/s	200m/s	250m/s	300m/s
ks= 0.05 mm	12.78%	13.53%	13.95%	12.50%
ks= 0.1 mm	10.94%	10.28%	9.86%	8.65%
ks = 0.15 mm	11.53%	11.60%	11.57%	9.96%
ks = 0.2 mm	7.45%	6.19%	6.22%	4.76%
ks = 0.25 mm	6.54%	5.92%	5.45%	3.79%
ks = 0.3 mm	7.43%	7.75%	7.35%	5.63%
ks = 0.35 mm	3.79%	4.18%	4.10%	2.47%
ks= 0.4 mm	4.52%	4.63%	4.45%	2.82%
ks = 0.45 mm	1.33%	-2.96%	0.11%	-0.28%
ks = 0.5 mm	2.53%	2.72%	2.55%	0.94%

At an angle of attack α=10°, the power needed to operate the aircraft is lower than the smooth airfoil model ks ≅ 0 mm. The airfoil model with applied surface roughness ks=0.05 mm had the best results for set 1 of applied surface roughness ks, as presented in Table (4.23).

Table (4.23): Power Analysis $C_L^{3/2}/C_D$ Percentage Variation for Different Roughness of First Set models to Smooth Airfoil at α= 10°

V / ks	150m/s	200m/s	250m/s	300m/s
ks= 0.05 mm	10.93%	12.38%	13.36%	14.23%
ks= 0.1 mm	8.28%	8.69%	9.42%	9.87%
ks = 0.15 mm	6.13%	7.07%	7.52%	8.08%
ks = 0.2 mm	3.13%	2.24%	2.58%	4.21%
ks = 0.25 mm	9.83%	10.95%	10.80%	12.54%
ks = 0.3 mm	8.49%	9.14%	9.25%	9.38%
ks = 0.35 mm	6.44%	7.13%	7.49%	7.45%
ks= 0.4 mm	7.27%	7.86%	8.40%	8.35%
ks = 0.45 mm	0.77%	1.39%	1.46%	2.48%
ks = 0.5 mm	4.04%	4.68%	4.79%	4.60%

For the second set, we observed an increase of the power in all applied surface heights ks= 1-4 mm compared to smooth airfoil. Hence, we proved the negative effect for more considerable surface roughness heights ks applied to the lower surface of the NACA 4412 airfoil. Comparison for $C_L^{3/2}/C_D$ for set 2 of ks at different angles of attack α= 0°, 5°, and 10° for velocities: 150m/s, 200m/s, 250m/s, and 300m/s, are presented in Tables (4.24), (4.25), (4.26).

Table (4.24): Power Analysis $C_L^{3/2}/C_D$ Percentage Difference of Airfoils with Applied Roughness of Second set of ks to the Smooth Airfoil α= 0°

V / ks	150m/s	200m/s	250m/s	300m/s
ks=1mm	-13.44%	-15.17%	-15.79%	-16.43%
ks=2mm	-20.18%	-21.28%	-22.03%	-22.62%
ks=3mm	-22.91%	-24.13%	-24.91%	-25.52%
ks=4mm	-31.04%	-31.85%	-32.46%	-32.90%

Table (4.25): Power Analysis $C_L^{3/2}/C_D$ Percentage Difference of Airfoils with Applied Roughness of Second set of k_s to the Smooth Airfoil α= 5°

V / ks	150m/s	200m/s	250m/s	300m/s
ks=1mm	-5.45%	-6.46%	-6.93%	-8.10%
ks=2mm	-10.96%	-11.28%	-11.46%	-12.89%
ks=3mm	-13.24%	-13.70%	-14.03%	-15.24%
ks=4mm	-20.18%	-20.45%	-20.42%	-21.77%

Table (4.26): Power Analysis $C_L^{3/2}/C_D$ Percentage Difference of Airfoils with Applied Roughness of Second set of ks to the Smooth Airfoil α= 10°

V / ks	150m/s	200m/s	250m/s	300m/s
ks=1mm	-5.69%	-5.26%	-4.55%	-3.45%
ks=2mm	-10.60%	-9.64%	-9.26%	-8.32%
ks=3mm	-14.12%	-13.04%	-11.84%	-13.73%
ks=4mm	-17.17%	-16.17%	-15.03%	-14.64%

4.3.5 Experimental Lift Coefficient Discussion

Different operating conditions rule the lift coefficient results obtained experimentally. For instance, using a 2-D wind tunnel at sea level with $\rho = 1.185\ \frac{kg}{m^3}$, $T_\infty = 24.0C$, and a shallow maximum velocity of

35m/s has influenced the expected results. However, we obtained the results from Fluent Ansys 2020 R1 in cruising velocity and 10,000m altitude. So, it cannot be directly compared with experimental results.

However, the results obtained from experiments in the Fluid mechanics lab are still helpful and reflect another operating condition for flying at sea level flights. The consequences of applied surface roughness to the lower surface of testing models in the wind tunnel are tested and evaluated in our research. A broader vision of observations is carried out and analyzed. That contributed to understanding the phenomenon of the effect of surface roughness on aerodynamic characteristics generally, which is crucial to the research field.

The best operating condition that serves our research is at high altitudes, low temperatures, low density, low pressure, and low viscosity generate a suitable environment for airflow movement. At these altitudes, it examined the availability of circulating the flow around the airfoil and the applied surface roughness. Also, we control the pressure distribution better than the sea level atmosphere.

Another consideration is the smooth airfoil model in our experiment. We could not manufacture a surface with ks =0mm when we compared numerical work to the experimental work. The finest surface finish obtained was ks =0.0258mm. Moreover, all comparisons referred to this surface finish by smooth airfoil or $k_s \cong 0$mm and affected the data collected experimentally.

Model of NACA 4412 airfoil with applied surface roughness ks =0.045mm had the best results of C_L compared to smooth airfoil at $\alpha = 0^o$. with this model, and C_L decreased by 0.61%, 0.46%, 0.29%, 0.16%, and

0.27% for velocities 20m/s, 23m/s, 27m/s, 30m/s, and 35m/s as shown in Table (4.27).

Table (4.27): C_L Percentage Difference of Airfoils with Applied Roughness of k_s to the Smooth Airfoil at $\alpha = 0^o$

V / ks	20m/s	23m/s	27m/s	30m/s	35m/s
ks=0.045mm	-0.61%	-0.46%	-0.29%	-0.16%	0.27%
ks=0.125mm	-0.61%	-0.40%	-0.48%	-0.25%	0.07%
ks=0.19mm	-1.03%	-1.04%	-0.91%	-0.72%	-0.20%

At a higher angle of attack of 5°, airfoil with ks =0.045mm generated a higher Lift than other airfoil models compared to $k_s \cong 0mm$. As a result, the decrement of C_L recorded is 1.26%, 1.05%, 0.78%, 0.71% and 0.47% at velocities of 20m/s, 23m/s, 27m/s, 30m/s, and 35m/s, respectively, as indicated in Table (4.28).

Table (4.28): C_L Percentage Difference of Airfoils with Applied Roughness of ks to the Smooth Airfoil at $\alpha = 5^o$

V / ks	20m/s	23m/s	27m/s	30m/s	35m/s
ks=0.045mm	-1.26%	-1.05%	-0.78%	-0.71%	-0.47%
ks=0.125mm	-1.03%	-1.00%	-0.78%	-0.83%	-0.56%
ks=0.19mm	-1.87%	-1.54%	-1.35%	-1.24%	-1.14%

At $\alpha = 10^o$, C_L values degraded in all models compared to the smooth airfoil model with a slighter level. The best model was ks =0.19mm compared to the airfoil model $k_s \cong 0mm$, which recorded C_L decrement of 0.23%, 0.08%, 0.26%, 0.33%, and 0.12% for velocities: 20m/s, 23m/s, 27m/s, 30m/s, and 35m/s as exhibited in Table (4.29).

Table (4.29): C_L Percentage Difference of Airfoils with Applied Roughness of k_s to the Smooth Airfoil at $\alpha = 10^o$

V / ks	20m/s	23m/s	27m/s	30m/s	35m/s
ks=0.045mm	-0.23%	0.08%	0.26%	-0.33%	-0.12%
ks=0.125mm	-0.21%	0.17%	0.29%	-0.53%	-0.32%
ks=0.19mm	-1.29%	-0.86%	-0.67%	-1.26%	-1.18%

4.3.6 Experimental Drag Coefficient Discussion

The experimental C_D results were the most unpredictable in this research. The reason is the operating conditions, which synchronized enormously with roughened surfaces phenomenon. Nevertheless, there are good improvements at lower α and support our hypothesis at sea level low subsonic speeds.

C_D at $\alpha = 0^o$ comparison with the model of ks =0.0258mm ($k_s \cong 0mm$) resulted in some encouraging results for the model of ks =0.125mm applied at a lower surface of NACA 4412 airfoil as follows: We observed improvements for velocities V=20m/s and V=23m/s, V=27m/s, V=30m/s, and V=35m/s with values of C_D by 11.95%, 11.67%, 11.39%, 11.18%, and 10.88%. Table (4.30) shows C_D values compared to smooth airfoil.

Table (4.30): C_D Percentage Difference of Airfoils with Applied Roughness of ks to the Smooth Airfoil at $\alpha = 0^o$

V / ks	20m/s	23m/s	27m/s	30m/s	35m/s
ks=0.045mm	-9.03%	-9.64%	-9.43%	-9.79%	-9.29%
ks=0.125mm	-11.95%	-11.67%	-11.39%	-11.18%	-10.88%
ks=0.19mm	-10.54%	-9.98%	-9.23%	-8.70%	-7.99%

The airfoil model at α= 5° with ks =0.125mm continued the best results for C_D over other applied roughness models compared to the $k_s \cong 0mm$ model. C_D values had the following advantages: 11.83%, 11.66%, 11.50%, 11.33%, and 11.18% for velocities: 20m/s, 23m/s, 27m/s, 30m/s, and 35m/s respectively as shown in Table (4.31).

Table (4.31): C_D Percentage Difference of Airfoils with Applied Roughness of ks to the Smooth Airfoil at α= 5°

V / ks	20m/s	23m/s	27m/s	30m/s	35m/s
ks=0.045mm	-9.10%	-8.95%	-9.15%	-9.45%	-10.23%
ks=0.125mm	-11.83%	-11.66%	-11.50%	-11.33%	-11.18%
ks=0.19mm	-10.70%	-10.53%	-10.12%	-9.86%	-9.32%

All models at α= 10° had good results of C_D values compared to airfoil with $k_s \cong 0mm$, as presented in Figure (4.24). However, overall, airfoil model NACA 4412 with an applied surface roughness of ks=0.125mm was performing the best regarding C_D results with 5.43%, 7.03%, 7.50%, 7.67%, and 8.75% for velocities: 20m/s, 23m/s, 27m/s, 30m/s, and 35m/s respectively as shown in Table (4.32).

Table (4.32): C_D Percentage Difference of Airfoils with Applied Roughness of k_s to the Smooth Airfoil at α= 10°

V / ks	20m/s	23m/s	27m/s	30m/s	35m/s
ks=0.045mm	-2.69%	-4.71%	-6.17%	-6.77%	-8.21%
ks=0.125mm	-5.43%	-7.03%	-7.50%	-7.67%	-8.75%
ks=0.19mm	-2.32%	-4.24%	-4.98%	-5.53%	-6.28%

4.3.7 Experimental Lift-to-Drag Coefficient Discussion

Finally, C_L/C_D experimental results indicated that NACA 4412 airfoil model tested in the wind tunnel had the best results when we applied roughness of ks =0.125mm. Furthermore, the results discovered that setting angles between 0° and 5° achieved the best performance of the model. Another reason for making differences between Numerical and Experimental solutions is the replacement of spherical roughness with sand-grains equivalent, although it was proven similar (Adams & Grant, 2012).

In Table (4.33), the airfoil model with ks =0.125mm resulted in C_L/C_D enhancement over the airfoil model with ks ≅ 0mm at α= 0°. C_L/C_D recorded: 12.88%, 12.76%, 12.31%, 12.30%, and 12.29% for velocities: V=20m/s, 23m/s, 27m/s, 30m/s and 35m/s respectively.

Table (4.33): C_L/C_D Percentage Difference of Airfoils with Applied Roughness of ks to the Smooth Airfoil at α= 0°

V / ks	20m/s	23m/s	27m/s	30m/s	35m/s
ks=0.045mm	9.25%	10.16%	10.09%	10.66%	10.54%
ks=0.125mm	12.88%	12.76%	12.31%	12.30%	12.29%
ks=0.19mm	10.63%	9.93%	9.17%	8.74%	8.47%

The airfoil model with ks =0.125mm continued positive results over the smooth airfoil model. We found that the C_L/C_D percentage difference of airfoils with K=0.045m to the smooth airfoil at α= 5° is 12.25%, 12.07%, 12.11%, 11.84%, and 11.96% for velocities: V=20m/s, 23m/s, 27m/s, 30m/s and 35m/s respectively as shown in Table (4.34).

Table (4.34): C_L/C_D Percentage Difference of Airfoils with Applied Roughness of ks to the Smooth Airfoil at α= 5°

V / ks	20m/s	23m/s	27m/s	30m/s	35m/s
ks=0.045mm	8.63%	8.67%	9.21%	9.65%	10.87%
ks=0.125mm	12.25%	12.07%	12.11%	11.84%	11.96%
ks=0.19mm	9.88%	10.04%	9.76%	9.57%	9.02%

We observed fluctuating improved results for the C_L/C_D percentage difference of airfoil with applied roughness of ks=0.125mm compared to the smooth airfoil at α= 10°. Nevertheless, C_L/C_D results are still best achieved by the airfoil model with ks=0.125mm compared to $k_s \cong 0mm$ as follows: 5.52%, 7.75%, 8.42%, 7.74%, and 9.23% for velocities: V=20m/s, 23m/s, 27m/s, 30m/s and 35m/s respectively as shown in Table (4.35).

Table (4.35): C_L/C_D Percentage Difference of Airfoils with Applied Roughness of ks to the Smooth Airfoil at α= 10°

V / ks	20m/s	23m/s	27m/s	30m/s	35m/s
ks=0.045mm	2.53%	5.03%	6.85%	6.90%	8.82%
ks=0.125mm	5.52%	7.75%	8.42%	7.74%	9.23%
ks=0.19mm	1.06%	3.53%	4.53%	4.53%	5.43%

4.3.8 Boundary Layer Thickness Measurement Discussion

The turbulent and laminar BL properties reviewed in Chapter (2). Chapter (3) discusses BL thickness differences between laminar and turbulent. The main differences between them are the thickness and the location. As illustrated in Figure (3.37), the location of the transition

region, or the transition point X_{cr}, depends on Re and the roughness of the surface. X_{cr} shifts toward upstream when Re or k_s increases (Kadivar, Tormey, & McGranaghan, 2021).

The first model of the NACA 4412 airfoil had the following experimental results obtained from Figures (4.28), (4.29), (4.30), and (4.31):

For k_s =0.0258mm, δ=0.4 mm, at X= 0.7C

For k_s =0.045mm, δ=0.6 mm, at X= 0.7C

For k_s =0.125mm, δ=1.4 mm, at X= 0.7C

For k_s =0.19mm, δ=2.2 mm, at X= 0.7C

Equations (16, 18) of laminar and turbulent boundary layer thickness at X= 0.7C used to calculate BL thickness δ for the same Re yields theoretically:

$\delta_{laminar} = 1.03mm$, $\delta_{turbulent} = 2.51mm$

With these results, an explanation for the experimental results was explained: A theoretical formula did not include parameters to the surface roughness values, and a standard theoretical solution comes from this formula.

For ks =0.0258mm, δ=0.4 mm, at X= 0.7C, the boundary layer is considered laminar and compares $\delta_{laminar}$ to the result. For ks =0.045mm, δ=0.6 mm, at X= 0.7C, $\delta_{laminar}$ should also be compared to the result. Nevertheless, for ks =0.125mm, δ=1.4 mm, at X= 0.7C, the result showed that the surface had entered the transition region of BL at X=0.7C, so the result lies between $\delta_{turbulent}$ and $\delta_{laminar}$. Finally, for ks =0.19mm, δ=2.2 mm, at X= 0.7C, BL is thoroughly turbulent and thicker than laminar BL, so $\delta_{turbulent}$ is better described as the result.

4.3.9 Experimental Power Analysis Discussion

We observed minimization in power in the experimental study for all applied surface roughness heights ks in all conditions, Sea level flight and low subsonic speeds. These results supported our hypothesis of adding surface roughness ks to the bottom surface of the NACA 4412 airfoil. For small values, as explained in Chapter (3), smaller values of ks lie in the hydraulically smooth and beginning transition regions of BL. In these regions, ks enhanced the values of most aerodynamic parameters. For example, an experimental model with surface roughness height ks= 0.125mm had the highest $C_L^{3/2}/C_D$ values, which means the lowest energy required to generate the same thrust T and lift L.

Compared to plain NACA 4412 airfoil, and Airfoil with applied surface roughness to the bottom surface ks= 0.125 mm recorded at $\alpha = 0^o$ percentage increments of 12.53%, 12.54%, 12.04%, 12.16%, and 12.32% for velocities of 20 m/s, 23 m/s, 27 m/s, 30 m/s, and 35 m/s respectively. These data are presented in Tables (4.36), (4.37), and (4.38), where the comparison is at angles of attack $\alpha = 0^o$, 5°, and 10°.

Table (4.36): Power Analysis $C_L^{3/2}/C_D$ Percentage Difference of Airfoils with Applied Roughness of ks to the Smooth Airfoil at $\alpha = 0^o$

V / ks	20m/s	23m/s	27m/s	30m/s	35m/s
ks=0.045mm	8.92%	9.90%	9.93%	10.57%	10.69%
ks=0.125mm	12.53%	12.54%	12.04%	12.16%	12.32%
ks=0.19mm	10.06%	9.35%	8.67%	8.34%	8.37%

Table (4.37): Power Analysis $C_L^{3/2}/C_D$Percentage Difference of Airfoils with Applied Roughness of ks to the Smooth Airfoil at α= 5°

V / ks	20m/s	23m/s	27m/s	30m/s	35m/s
ks=0.045mm	7.95%	8.10%	8.78%	9.25%	10.61%
ks=0.125mm	11.68%	11.50%	11.67%	11.38%	11.65%
ks=0.19mm	8.85%	9.19%	9.02%	8.88%	8.40%

Table (4.38): Power Analysis $C_L^{3/2}/C_D$Percentage Difference of Airfoils with Applied Roughness of ks to the Smooth Airfoil at α= 10°

V / ks	20m/s	23m/s	27m/s	30m/s	35m/s
ks=0.045mm	2.41%	5.07%	6.99%	6.73%	8.75%
ks=0.125mm	5.40%	7.84%	8.58%	7.45%	9.05%
ks=0.19mm	0.41%	3.09%	4.18%	3.87%	4.81%

4.4 Conclusions

Investigation of the potential benefits of drag reduction studies oriented us towards the expectations of applying various new technologies.

The study carried out Numerical and Experimental work to study the impact of applying different surface roughness amplitudes to the lower surface of the NACA 4412 airfoil in aerodynamic characteristics.

The study simulated turbulent flow past airfoil Numerically to focus on the drag coefficient, lift coefficient, and lift-to-drag ratio at different high subsonic speeds and angles of attack. The study concluded that a reduction in the total drag at low angles of attack in level flight when the airfoil's lower surface is roughened, and Lift has increased to a small

extent. The form drag decreases, the flow separation is delayed, and the pressure gradient is avoided, despite increased skin friction drag. The adaptations in aerodynamic characteristics have been attained by changing the roughened surface. The model with an applied surface roughness of ks =0.05mm is the best compared to the smooth airfoil. Large values of ks resulted in degraded values of all aerodynamic characteristics.

Low subsonic speeds tested experimentally showed that more significant values of applied surface roughness heights produce the best aerodynamic results. Furthermore, airfoil with ks=0.125mm resulted in the best aerodynamic characteristics for low subsonic speeds.

BL thickness is sensitive to surface roughness change. By increasing ks, the transition from laminar to turbulent BL shifts upstream.

Finally, small surface roughness values enhance the aerodynamic characteristics, namely, Lift to drag ratio and Minimum power required at high and low subsonic speeds.

4.1 Recommendations

1- Applying low-cost film with rounded roughness pattern to the lower surface of NACA 4412 airfoil for commercial aircraft already using it.

2- Continue the research into different airfoils and flight regimes.

3- Study the surface roughness effect for other parts of the aircraft.

References

Abdel-Rahman, A., & Chakroun, W. (1997). Surface roughness effects on flow over airfoils. *Wind Engineering*, 125-137.

Achenbach, E. (1971). Influence of surface roughness on the cross-flow around a circular cylinder. *Journal of fluid mechanics, 46*(2), 321–335.

Achenbach, E. (1974). The effects of surface roughness and tunnel blockage on the flow past spheres. *Journal of fluid mechanics, 65*(1), 113-125.

Adams, T., & Grant, C. (2012). A Simple Algorithm to Relate Measured Surface Roughness to Equivalent Sand-grain Roughness. *International Journal of Mechanical Engineering and Mechatronics, 1*(1), 66-71. doi:10.11159/ijmem.2012.008

Anderson, J. D. (2005). *Introduction to Flight* (Third ed.). Mcgra Hill.

Anderson, J. D. (2017). *Fundamentals of Aerodynamics* (Sixth ed.). Mcgraw. Hill.

Bahr, D., Bullock, S., Cumpsty, N., W. Dodds, D. D., Epstein, A., Ferguson, W., . . . Renger, K. (n.d.). Aviation and the Global Atmosphere. In J. E. Penner, D. H. Lister, D. J. Griggs, M. McFarland, D. J. Dokken, & M. Wright (Ed.), *Aircraft Technology and Its Relation to Emissions.* Intergovernmental panel on climate change. Retrieved from https://www.grida.no/climate/ipcc/aviation/088.htm

Beam, R. M., & Warming, R. (1978). An implicit factored scheme for the compressible navier-stokes equations. *AIAA journal, 16*(4), 93–402.

Beckwith, T. G., Marangoni, R. D., & V, J. H. (2011). *Mechanical Meassurements* (sixth ed.). Pearson Learning Solutions.

Bimbato, A., Alcântara Pereira, L., & Hirata, M. (2019). Development of a new Lagrangian vortex method for evaluating effects of surfaces roughness. *European Journal of Mechanics - B/Fluids, 74*. doi:10.1016/j.euromechflu.2018.09.001

Bloch, D., & Mueller, T. (1986). Effects of distributed grit roughness on separation and transition on an airfoil at low reynolds numbers. *in 4th Applied Aerodynamics Conference*, (p. 1788).

Boccard, N. (2009). Capacity factor of wind power realized value vs. estimates. *Energy Policy, 37*(7), 2679-2688.

BRAGG, M., & GREGOREK, G. (1989). Environmentally induced surface roughness effects on laminar flow airfoils-implications for flight safety. *Aircraft Design and Operations Meeting*, 2049.

Bragg, M., Heinrich, D., Valarezo, W., McGhee, & McGhee, R. (1994). Effect of underwing frost on a transport aircraft airfoil at flight reynolds number. *Journal of Aircraft, 31*(6), 1372–1379.

Brumby, R. (1991). The effect of wing ice contamination on essential flight characteristics. *in AGARD Conference Proceedings*(496).

Cao, Y., Ma, C., Zhang, Q., & Sheridan, J. (2012, December). Numerical simulation of ice accretions on an aircraft wing. *Aerospace Science and Technology, 23*(1), 296-304. doi:10.1016/j.ast.2011.08.004

Cayiroglua, I., & Kilicb, R. (2017). Wing Aerodynamic Optimization by Using Genetic Algoritm and Ansys. *ACTA PHYSICA POLONICA A, 132*(3-II). doi:10.12693/APhysPolA.132.981

Chakroun, W., Al-Mesri, I., & Al-Fahad, S. (2004). Effect of surface roughness on the aerodynamic characteristics of a symmetrical airfoil. *Wind Engineering, 28*(5), 547-564.

Colebrook, C. F., Blench, T., Chatley, H., Essex, E., Finniecome, J., Lacey, G., . . . Macdonald, G. (1939). Correspondence. turbulent flow in pipes, with particular reference to the transition region between the smooth and rough pipe laws.(includes plates). *Journal of the Institution of Civil engineers, 12*(8), 393–422.

Costes, M., & Moens, F. (2019). Advanced numerical prediction of iced airfoil aerodynamics. *Aerospace Science and Technology, 91*, 186–207. doi:10.1016/j.ast.2019.05.010

Darcy, H. (1857). Recherches expe´rimentales relatives au mouvement de l'eau dans. *1*.

Dietenberger, M. (1983). A proposed simple and safe aircraft take-off or landing procedure with wing roughness or protuberances., (p. 604).

FINLAY, M. (2022). Flying High: The Reasons Why Aircraft Cruise At Such Considerable Altitudes. *Simple Flying*. Retrieved from https://simpleflying.com/reasons-why-aircraft-fly-so-high-in-cruise/

Finnigan, J., & Gersten. (2000). Turbulence in Plant Canopies. *Anual Review of Fluid Mechanics, 32*, 519-571.

Flack, K. A., Schultz, M. P., & Volino, R. J. (2020). The effect of a systematic change in surface roughness skewness on turbulence

and drag. *International Journal of Heat and Fluid Flow, 85*, 108669.

Gowda, A. S. (2019, April). Comparison of Aerodynamic Performance of NACA 4412 and 2412 using Computational Approach. *International Journal of Engineering Trends and Technology (IJETT), 67*(4), 73-75. Retrieved from http://www.ijettjournal.org

Gülcan, O., Günaydın, K., & Çelik, A. (2022). Investigation on Surface Roughness of PolyJet-Printed Airfoil Geometries for Small UAV Applications. (C. Bisagni, Ed.) *9(2)*(82). doi:10.3390/aerospace9020082

Hagen, G. H. (1854). *U¨ ber den einfluss der temperatur auf die bewegung des wassers in ro¨hren.* (akademie der wissenschaften, Ed.) Druckerei der Ko¨nigl.

Haosheng, C., Darong, C., & Yongjian, L. (2006). *Investigation on effect of surface roughness pattern to drag force reduction using rotary rheometer.*

Hengst, J. V., & Boer, J. (1991). The effect of hoar-frosted wings on the fokker 50 take-off characteristics. *AGARD CP, 496*, 292.

Hood, M. J. (1939). Surface roughness and wing drag: An american opinion upon a problem becoming of ever-increasing importance. *Aircraft Engineering and Aerospace Technology.*

Houghton, E. L., Carpenter, P. W., Collicott, S. H., & Valentine, D. T. (2013). *Aerodynamics for Engineering Students* (sixth ed.). Waltham: Butterworth-Heinemann.

Hövelmann, A., Knoth1, F., & Breitsamter, C. (2016, 1 7). AVT-183 diamond wing flow field characteristics Part 1: Varying leading-

edge roughness and the effects on flow separation onset. *Aerospace Science and Technology*(75), 18-30. Retrieved from www.elsevier.com/locate/aescte

Jime´nez, J. (2004). Turbulent flows over rough wall. *Annu. Rev. Fluid Mech., 36*, 173–196,.

Kadivar, M., Tormey, D., & McGranaghan, G. (2021). A review on turbulent flow over rough surfaces: Fundamentals and theories. *International Journal of Thermofluids, 10*. Retrieved from http://www.elsevier.com/locate/ijtf

Kadivar, M., Tormey, D., & McGranaghan, G. (2021). A review on turbulent flow over rough surfaces: Fundamentals and theories. *International Journal of Thermofluids, 10*(100077). Retrieved February March, 2021, from www.esilver.com/locate/ijitf

Kazimieras. (2017). Basic Aerodynamics. In C. B.-6. 1, *Module 8 Basic Aerodynamics* (pp. 1-74). Vilnius: Kazimieras University. Retrieved 2017, from https://www.ksu.lt/wp-content/uploads/2017/06/M8-Selected-pages-Basic-Aerodynamics.pdf

Khatir, T., Djillali, B., Khatir, S., Abdelkader, L., & Wahab, M. A. (2017). Experimental and numerical investigation of flutter phenomenon of an aitcraft wing (NACA 0012). *MECHANIKA, 23(4)*(1392-1207), 562-566. doi:10.5755/j01.mech.23.4.15175

Kurz, B., H., & Kloker, M. J. (2015). Discrete-roughness Effects in a Three-dimensional Boundary Layer on an Airfoil by Means of DNS. *Procedia IUTAM, 14*, 163–172. doi:10.1016/j.piutam.2015.03.037

Latin, R. M., & Bowersox, R. D. (2002). Temporal turbulent flow structure for supersonic rough-wall boundary layers. *AIAA journal, 40*(5), 832–841.

Liu, Y., Zhang, K., Tian, W., & Hu, H. (2020). An experimental investigation on the dynamic ice accretion and unsteady heat transfer over an airfoil surface with embedded initial ice roughness. *International Journal of Heat and Mass Transfer, 146*(118900).

Ljungstroem, B. L. (1972). Wind tunnel investigation of simulated hoar frost on a 2-dimensional wing section with and without high lift devices. *tech. rep.*

McCormick, B. W. (1995). *Aerodynamics Aeronautics and Flight Mechanics* (second ed.). John Wiley & sons inc.

Megson, T. (2022). *Aircraft Structures for Engineering Students* (Seventh ed.). (E. Ltd., Ed.) Butterworth-Heinemann. doi:10.1016/C2019-0-03113-5

Menter, F. R. (1992, October). Improved two-equation k–ω turbulence models for aerodynamic flows. *NASA technical memorandum 103975*(94035-1000), 1-38.

Moody, L. F. (1944). Friction factors for pipe flow. *Trans. Asme, 66*, 671–684.

Moran, J. (2003). *An introduction to theoretical and computational aerodynamics.* Courier corporation.

NACA 4412 (naca4412-il). (2022). Retrieved from Airfoil Tools: http://airfoiltools.com/airfoil/details?airfoil=naca4412-il

NASA. (n.d.). *Similarity Parameters*. Retrieved from National Aeronautics and Aerospace Administration: https://www.grc.nasa.gov/www/k-12/airplane/airsim.html

Nikradze, J. (1950). vDI Forschungsheft. *Technical Memorandum 1292.*

Nikuradse, J. (1950). *Laws of flow in rough pipe.*

Ockfen, A. E., & Matveev, K. I. (2009). Aerodynamic characteristics of NACA 4412 airfoil section with flap in extreme ground effect. *International Journal of Naval Architecture and Ocean Engineering, 1*(1), 1-12. doi:10.2478/IJNAOE-2013-000

Özçakmak, Ö., Madsen, H., Sørensen, N., Sørensen, J., Fischer, A., & Bak, C. (2018). Inflow Turbulence and Leading Edge Roughness Effects on Laminar-Turbelent Transition on NACA 63-418 Airfoil. *Journal of Physics: Conference Series 1037, 2*(022005). doi:10.1088/1742-6596/1037/2/022005

P.Sanjay, T.N, S., & Bharadwaj, P. (2016). Grid Independence Study for Convergent and Convergent-Divergent Nozzles used for Spray Atomization Process using CFD Techniques (Fluent). *International Journal for Scientific Research & Development|, 4*(006). Retrieved from http://www.ijsrd.com

Raupach, M. R., Antonia, R. A., & Rajagopalan, S. (1991). Rough-wall turbulent boundary layers.

Rauparch, M., & Thom, A. S. (1981). Turbelnce in and above plant canopies. *Anual Review of Fluid Mechanics, 13*(1), 97-129.

Roe, P. L. (1981). Approximate riemann solvers, parameter vectors, and difference schemes. *Journal of computational physics, 43*(2), 357–372.

Salazar, F., & Barrientos, A. (2013). Surface Roughness Measurement on a Wing Aircraft by Speckle Correlation. *Sensors, 13*, 11772-11781. doi:10.3390/s130911772

Schlichting, H., & Gersten, K. (2016). *Boundary-Layer Theory.* Springer.

Sheldahl, R. E., & CKlimas, P. (1981). *Aerodynamic characteristics of seven symmetrical airfoil sections through 180-degree angle of attack for use in aerodynamic analysis of vertical axis wind turbines.* Albuquerque, NM (USA).

Singirsu, S. R. (2018). *The Finite Element Method in Engineering* (sixth ed.). Butterwoth Heineman. doi:doi.org/10.1016/B978-0-12-811768-2.00017-1

Smith, A., & Kaups, K. (1968). Aerodynamics of surface roughness and imperfections. *SAE Transactions*, 668–688.

Sun, Y., Wang, Z. J., & Liu, Y. (2006). High-order multidomain spectral difference method for the navier-stokes equations. *in 44th AIAA Aerospace Sciences Meeting and Exhibit*, (p. 301).

Talay, T. A. (1975). *Introduction to the Aerodynamics of Flight* (Vol. 367). (S. a. Office, Ed.) National Aeronautics and space.

Toth, A., & Bobok, E. (2017). *Chapter 10 - Gathering System of Geothermal Fluids.* (A. Toth, & E. Bobok, Eds.) Flow and Heat Transfer in Geothermal Systems, Esilver. doi:10.1016/B978-0-12-800277-3.00010-4

Valarezo, W. O., Lynch, F. T., & McGhee, R. J. (1993). Aerodynamic performance effects due to small leading-edge ice (roughness) on wings and tails. *Journal of aircraft, 30*(6), 807–812.

Wang, M., Lu, X., Yang, C., Zhao, S., & Zhang, Y. (2021). Numerical investigation of distributed roughness effects on separated flow transition over a highly loaded compressor blade. *Physics of Fluids, 33*(114104). Retrieved from https://doi.org/10.1063/5.0066615

White, E., Kutz, D., Freels, J., Monschke, J., Grife, R., Sun, Y., & Chao, D. (2011). Leading edge roughness effects on 63(3)-418 airfoil performance. *49th ALAA Aerospace Sciences Meeting including the New Horizons Forum and Aerospace Expostion*, 352.

Zarketa-Astigarraga, A., Penalba, M., Martin-Mayor, A., & Martinez-Agirre, M. (2022). Experimental assessment of scale-effects on the aerodynamic characterization of a transitionally-operating airfoil working under clean flow conditions. *Measurement, 188*(110414). doi:10.1016/j.measurement.2021.110414

Zhang, X., Wang, G., Zhang, M., Liu, H. &., & W. (2017). Numerical study of the aerodynamic performance of blunt trailing-edge airfoil considering the sensitive roughness height. International Journal of Hydrogen Energy. *International Journal of Hydrogen Energy, 42*(29), 18252–18262. doi:10.1016/j.ijhydene.2017.04.158

Zhang, Y. (2018). Effects of distributed leading-edge roughness on aerodynamic performance of a low-Reynolds-number airfoil: an experimental study. *Theoretical & Applied Mechanics Letters*(letter 8), 201-207. Retrieved from www.elsevier.com/locate/taml

Zhou, Y., & Wang, Z. (2011). Effect of surface roughness on laminar separation bubble over a wing at a low-reynolds number. *in 49th*

AIAA Aerospace Sciences Meeting including the New Horizons Forum and Aerospace Exposition, (p. 736).

Zhou, Y., & Wang, Z. (2012). Effects of surface roughness on separated and transitional flows over a wing. *AIAA journal, 50*(3), 593–609.

APPENDIX (A)

Meshing Properties for the Models

A.1 Smooth Airfoil's Meshing properties

Properties	smooth airfoil NACA 44121
Element order	Linear
Element size	Standard (5.1478 m)
Growth rate	1.2
Mesh defeaturing	$2.5739 \times 10^{-2} m$
Capture curvature	5.1478×10^{-2}
Boundary box diagonal	102.96m
Average surface area	$2250\ m^2$
Minimum edge length	1.0105 m
Mesh quality	High smoothing
Inflation option	Smooth transition
Nodes	75225
Elements	73631
Meshing method	Quadrilateral dominant
Free face mesh type	Quad/Tri
Airfoil edges Sizing	2 edges divided to 2000 with minimum size 5.1478×10^{-2} and bias factor 1.2
Elliptic face sizing	1 face with element size 4×10^{-2} and 1.2 growth rate
Refinement	Elliptic face (2)

A.2 0.05mm applied Surface Roughness Airfoil's properties

Properties	$ks = 0.05mm$ NACA 4412
Growth rate	1.2
Minimum edge length	5.040510^{-5}m
Mesh quality	High smoothing
Inflation option	Smooth transition
Nodes	106987
Elements	1980694
Meshing method	All Triangles Method with triangles for free face
Airfoil edges Sizing	10052 edges with element size $1 \times 10^{-5}m$ with same proximity size and bias factor 1.2
face sizing	Elliptic face with element size 1×10^{-2}m and 1.2 growth rate. The box with element size 1.0m
Refinement	null

A.3 0.1mm applied Surface Roughness Airfoil's properties

Properties	$ks = 0.1mm$ NACA 4412
Growth rate	1.2
Minimum edge length	1.2543×10^{-5}m
Mesh quality	Medium smoothing
Inflation option	Smooth transition
Nodes	923345
Elements	1795352
Meshing method	All Triangles Method with triangles for free face
Airfoil edges Sizing	5120 edges with element size $5 \times 10^{-5}m$ with same proximity size and bias factor 1.2
face sizing	Elliptic face with element size 5×10^{-3}m and 1.2 growth rate. The box with element size 1.0m
Refinement	null

A.4 0.15mm applied Surface Roughness Airfoil's properties

Properties	$ks = 0.15mm$ NACA 4412
Growth rate	1.2
Minimum edge length	7.9808×10^{-6}m
Mesh quality	Medium smoothing
Inflation option	Smooth transition
Nodes	427576
Elements	796084
Meshing method	All Triangles Method with triangles for free face
Airfoil edges Sizing	3379 edges with element size $4 \times 10^{-5}m$ with same proximity size and bias factor 1.2
face sizing	Elliptic face with element size 1×10^{-2}m and 1.2 growth rate. The box with element size 1.0m
Refinement	null

A.5 0.2mm applied Surface Roughness Airfoil's properties

Properties	$ks = 0.2mm$ NACA 4412
Growth rate	1.2
Minimum edge length	1.4646×10^{-6}m
Mesh quality	Medium smoothing
Inflation option	Smooth transition
Nodes	12658292482903
Elements	796084
Meshing method	All Triangles Method with triangles for free face
Airfoil edges Sizing	2597 edges with element size $5 \times 10^{-5}m$ with same proximity size and bias factor 1.2
face sizing	Elliptic face with element size 4×10^{-3}m and 1.2 growth rate. The box with element size 1.0m
Refinement	null

A.6 0.25mm applied Surface Roughness Airfoil's properties

Properties	$ks = 0.25mm$ NACA 4412
Growth rate	1.2
Minimum edge length	3.0515×10^{-5}m
Mesh quality	High smoothing
Inflation option	Smooth transition
Nodes	927859
Elements	1807423
Meshing method	All Triangles Method with triangles for free face
Airfoil edges Sizing	2098 edges with element size $5 \times 10^{-5}m$ with same proximity size and bias factor 1.2
face sizing	Elliptic face with element size 5×10^{-3}m and 1.2 growth rate. The box with element size 1.0m
Refinement	null

A.7 0.3mm applied Surface Roughness Airfoil's properties

Properties	$ks = 0.3mm$ NACA 4412
Growth rate	1.2
Minimum edge length	1.9035×10^{-4}m
Mesh quality	High smoothing
Inflation option	Smooth transition
Nodes	747935
Elements	736120
Meshing method	Quadrilateral dominant with Quad/Tri for free face
Airfoil edges Sizing	1703 edges with element size $4 \times 10^{-4}m$ with same proximity size and bias factor 1.2
face sizing	Elliptic face with element size 4×10^{-2}m and 1.2 growth rate.
Refinement	3 for 2 faces

A.8 0.35mm applied Surface Roughness Airfoil's properties

Properties	$ks = 0.35mm$ NACA 4412
Growth rate	1.2
Minimum edge length	3.8308×10^{-5}m
Mesh quality	High smoothing
Inflation option	Smooth transition
Nodes	779582
Elements	767724
Meshing method	Quadrilateral dominant with Quad/Tri for free face
Airfoil edges Sizing	1525 edges with element size $4 \times 10^{-4}m$ with same proximity size and bias factor 1.2
face sizing	Elliptic face with element size 4×10^{-2}m and 1.2 growth rate.
Refinement	3 for 2 faces

A.9 0.4mm applied Surface Roughness Airfoil's properties

Properties	$ks = 0.4mm$ NACA 4412
Growth rate	1.2
Minimum edge length	2.403×10^{-4}m
Mesh quality	High smoothing
Inflation option	Smooth transition
Nodes	755188
Elements	742988
Meshing method	Quadrilateral dominant with Quad/Tri for free face
Airfoil edges Sizing	1243 edges with element size $4 \times 10^{-4}m$ with same proximity size and bias factor 1.2
face sizing	Elliptic face with element size 4×10^{-2}m and 1.2 growth rate.
Refinement	3 for 2 faces

A.10 0.45mm applied Surface Roughness Airfoil's properties

Properties	$ks = 0.45mm$ NACA 4412
Growth rate	1.2
Minimum edge length	5.4572×10^{-7}m
Mesh quality	High smoothing
Inflation option	Smooth transition
Nodes	926005
Elements	1804119
Meshing method	All Triangles Method with triangles for free face
Airfoil edges Sizing	1199 edges with element size $5 \times 10^{-3}m$ with same proximity size and bias factor 1.2
face sizing	Elliptic face with element size 4×10^{-2}m and 1.2 growth rate. The box with element size 1.0m.
Refinement	null

A.11 0.5mm applied Surface Roughness Airfoil's properties

Properties	$ks = 0.5mm$ NACA 4412
Growth rate	1.2
Minimum edge length	1.7079×10^{-5}m
Mesh quality	High smoothing
Inflation option	Smooth transition
Nodes	622976
Elements	612393
Meshing method	Quadrilateral dominant with Quad/Tri for free face
Airfoil edges Sizing	1703 edges with element size $5 \times 10^{-4}m$ with same proximity size and bias factor 1.2
face sizing	Elliptic face with element size 5×10^{-2}m and 1.2 growth rate.
Refinement	3 for 2 faces

A.12 1mm applied Surface Roughness Airfoil's properties

Properties	$ks = 1mm$ NACA 4412
Growth rate	1.2
Minimum edge length	4.7948×10^{-6}m
Mesh quality	High smoothing
Inflation option	Smooth transition
Nodes	478590
Elements	909903
Meshing method	All Triangles Method with triangles for free face
Airfoil edges Sizing	601 edges with element size $5 \times 10^{-5}m$ with same proximity size and bias factor 1.2
face sizing	Elliptic face with element size 1×10^{-2}m and 1.2 growth rate. The box with element size 1.0m.
Refinement	null

A.13 2mm applied Surface Roughness Airfoil's properties

Properties	$ks = 2mm$ NACA 4412
Growth rate	1.2
Minimum edge length	1.907×10^{-3}m
Mesh quality	High smoothing
Inflation option	Smooth transition
Nodes	376480
Elements	717521
Meshing method	All Triangles Method with triangles for free face
Airfoil edges Sizing	252 edges with element size $5 \times 10^{-5}m$ with same proximity size and bias factor 1.2
face sizing	Elliptic face with element size 1×10^{-2}m and 1.2 growth rate. The box with element size 1.0m.
Refinement	null

A.14 3mm applied Surface Roughness Airfoil's properties

Properties	$ks = 3mm$ NACA 4412
Growth rate	1.2
Minimum edge length	1.542×10^{-3}m
Mesh quality	High smoothing
Inflation option	Smooth transition
Nodes	3374489
Elements	719525
Meshing method	All Triangles Method with triangles for free face
Airfoil edges Sizing	168 edges with element size $5 \times 10^{-5}m$ with same proximity size and bias factor 1.2
face sizing	Elliptic face with element size 1×10^{-2}m and 1.2 growth rate. The box with element size 1.0m.
Refinement	null

A.15 4mm applied Surface Roughness Airfoil's properties

Properties	$ks = 4mm$ NACA 4412
Growth rate	1.2
Minimum edge length	2.6229×10^{-2}m
Mesh quality	High smoothing
Inflation option	Smooth transition
Nodes	377578
Elements	719835
Meshing method	All Triangles Method with triangles for free face
Airfoil edges Sizing	126 edges with element size $5 \times 10^{-5}m$ with same proximity size and bias factor 1.2
face sizing	Elliptic face with element size 1×10^{-2}m and 1.2 growth rate. The box with element size 1.0m.
Refinement	null

APPENDIX (B)

Grid Independency Study

B.1 Grid independency study for smooth airfoil

Setup	Bounding box 90*50m/ Nodes 53069/ Elements 51480/High quality smoothing/smooth transition/ element size of face 1 =0.05 / refinement 0 /v=250m/s	High quality/smooth transition/ element size of face 1 =0.05 / refinement 1	Difference
LIFT COEFF	4.5556e-01	4.5555e-01	0.000002 %
DRAG COEFF	9.2872e-03	9.3317e-03	0.004 %

Lift and drag coeff for plain wing (150 m/s)

Angle of attack	Lift coeff	Drag coeff
0	1.6194e-01	3.6287e-03
5	3.5523e-01	-2.6476e-02
10	5.2276e-01	-8.5049e-02

Lift and drag coeff for plain wing (200 m/s)

Angle of attack	Lift coeff	Drag coeff
0	2.9002e-01	6.1747e-03
5	6.3514e-01	-4.7713e-02
10	9.3585e-01	-1.5284e-01

Lift and drag coeff for plain wing (250 m/s)

Angle of attack	Lift coeff	Drag coeff
0	4.5555e-01	9.3317e-03
5	9.9652e-01	-7.5290e-02
10	1.4695e+00	-2.4063e-01

Lift and drag coeff for plain wing (300 m/s)

Angle of attack	Lift coeff	Drag coeff
0	6.5865e-01	1.3080e-02
5	1.4395e+00	-1.0924e-01
10	2.1241e+00	-3.4854e-01

B.2 Grid independency study for airfoil with roughness 0.05mm

Setup	Bounding box 90*50m/ Nodes 53069/ Elements 51480/High quality smoothing/smooth transition/ element size of face 1 =0.05 / v=250m/s	High quality/smooth transition/nodes 1069687/ elements 1980694/edge size 0.00001/ element size of face 1 =0.05 /	Difference
LIFT COEFF	4.5213e-1	4.5472e-01	0.006
DRAG COEFF	8.6003e-1	8.4674e-03	0.016

Lift and drag coeff for airfoil with roughness 0.05mm (150 m/s)

Angle of attack	Lift coeff	Drag coeff	l/d
0	4.4793e-01	9.0665e-03	49.409
5	9.6809e-01	1.1089e-02	87.3
10	1.3619e+00	1.6894e-02	80.62

Lift and drag coeff for airfoil with roughness 0.05mm (200 m/s)

Angle of attack	Lift coeff	Drag coeff	l/d
0	4.5160e-01	8.6884e-03	51.98
5	9.7533e-01	1.0605e-02	91.97
10	1.3745e+00	1.6078e-02	85.49

Lift and drag coeff for airfoil with roughness 0.05mm (250 m/s)

Angle of attack	Lift coeff	Drag coeff	l/d
0	4.5472e-01	8.4674e-03	53.702
5	9.7973e-01	1.0253e-02	95.56
10	1.3834e+00	1.5508e-02	89.2

Lift and drag coeff for airfoil with roughness 0.05mm (300 m/s)

Angle of attack	Lift coeff	Drag coeff	l/d
0	4.5688e-01	8.2847e-03	55.15
5	9.8415e-01	1.0017e-02	98.25
10	1.3890e+00	1.5035e-02	92.46

B.3 Grid independency study for0.1mm roughness airfoil

Setup	Bounding box 90*50m/ Nodes 53069/ Elements 51480/High quality smoothing/smooth transition/ element size of face 1 =0.05 /edge size 0.0001 /v=250m/s	High quality/smooth transition/Nodes 923345/elements 1795352/ element size of face 1 =0.05 / edge size= 0.00005	Difference
LIFT COEFF	4.5093e-01	4.5330e-01	0.005
DRAG COEFF	9.0056e-03	8.7861e-03	0.024

Lift and drag coeff 0.1mm (150 m/s)

Angle of attack	Lift coeff	Drag coeff	l/d
0	4.4720e-01	9.1873e-03	48.676
5	9.6387e-01	1.1199e-02	86.06
10	1.3547e+00	1.7169e-02	78.9

Lift and drag coeff for plain wing (200 m/s)

Angle of attack	Lift coeff	Drag coeff	l/d
0	4.5022e-01	8.9615e-03	50.24
5	9.7064e-01	1.0839e-02	89.55
10	1.3657e+00	1.6465e-02	82.95

Lift and drag coeff for plain wing (250 m/s)

Angle of attack	Lift coeff	Drag coeff	l/d
0	4.5296e-01	8.7877e-03	51.545
5	9.7496e-01	1.0557e-02	92.35
10	1.3745e+00	1.5911e-02	86.39

Lift and drag coeff for plain wing (300 m/s)

Angle of attack	Lift coeff	Drag coeff	l/d
0	4.5459e-01	8.6332e-03	52.66
5	9.7985e-01	1.0304e-02	95.09
10	1.3802e+00	1.5484e-02	89.14

243 8.3389e-06 1.0499e-09 3.2554e-10 1.6883e-16 5.8093e-05 1.1501e-05 4.6986e-01 1.2291e-02 0:29:30 757

244 8.4295e-06 1.0681e-09 3.2639e-10 1.6681e-16 5.8195e-05 1.1425e-05 4.6986e-01 1.2291e-02 0:28:36 756

245 8.4617e-06 1.0801e-09 3.2862e-10 1.6518e-16 5.8270e-05 1.1354e-05 4.6986e-01 1.2291e-02 0:30:24 755

246 8.4696e-06 1.0906e-09 3.2846e-10 1.6573e-16 5.8349e-05 1.1279e-05 4.6986e-01 1.2291e-02 0:29:19 754

Done..

C.14 Last 10 Iterations of Airfoil with K=3mm (300m/s) at $\alpha=0^{o}$

719525 triangular cells, zone 3, binary.

719525 cell partition ids, zone 3, 8 partitions, binary.

1060161 2D interior faces, zone 1, binary.

1441 2D interior faces, zone 2, binary.

35091 2D wall faces, zone 6, binary.

230 2D velocity-inlet faces, zone 7, binary.

50 2D pressure-outlet faces, zone 8, binary.

377448 nodes, binary.

377448 node flags, binary.

324 9.3872e-06 9.7114e-10 3.6156e-10 1.6938e-16 5.8339e-05 9.4037e-06 1.3112e-02 4.7824e-01 0:25:10 676

325 8.9816e-06 9.3661e-10 3.5877e-10 1.6939e-16 5.8241e-05 9.3805e-06 1.3112e-02 4.7824e-01 0:24:36 675

326 8.7579e-06 8.8712e-10 3.4226e-10 1.7027e-16 5.8155e-05 9.3537e-06 1.3112e-02 4.7824e-01 0:26:24 674

327 8.6558e-06 8.6908e-10 3.5298e-10 1.6812e-16 5.8046e-05 9.3281e-06 1.3112e-02 4.7824e-01 0:25:34 673

328 8.2182e-06 8.1597e-10 3.3242e-10 1.6925e-16 5.7946e-05 9.3008e-06 1.3112e-02 4.7824e-01 0:24:54 672

329 8.0694e-06 7.6942e-10 3.1815e-10 1.6826e-16 5.7827e-05 9.2797e-06 1.3112e-02 4.7824e-01 0:24:22 671

330 8.0274e-06 7.5645e-10 3.3151e-10 1.6783e-16 5.7724e-05 9.2611e-06 1.3112e-02 4.7824e-01 0:26:10 670

iter continuity x-velocity y-velocity energy k omega drag-coeff lift-coeff time/iter

331 7.7109e-06 7.1523e-10 3.2120e-10 1.7022e-16 5.7604e-05 9.2458e-06 1.3112e-02 4.7824e-01 0:25:22 669

332 7.6592e-06 6.9163e-10 3.2687e-10 1.6908e-16 5.7507e-05 9.2282e-06 1.3112e-02 4.7824e-01 0:24:43 668

333 7.7221e-06 6.7688e-10 3.3819e-10 1.6922e-16 5.7389e-05 9.2011e-06 1.3112e-02 4.7824e-01 0:26:25 667

334 7.3431e-06 6.3015e-10 3.1864e-10 1.7017e-16 5.7285e-05 9.1745e-06 1.3112e-02 4.7824e-01 0:25:32 666

335 7.2497e-06 5.9260e-10 3.0100e-10 1.6903e-16 5.7164e-05 9.1537e-06 1.3112e-02 4.7824e-01 0:27:03 665

336 7.3132e-06 5.9211e-10 3.1522e-10 1.6851e-16 5.7065e-05 9.1340e-06 1.3112e-02 4.7824e-01 0:26:02 664

337 7.0771e-06 5.5818e-10 3.0175e-10 1.7079e-16 5.6947e-05 9.1144e-06 1.3112e-02 4.7824e-01 0:25:13 663

338 7.0203e-06 5.3095e-10 2.9311e-10 1.7046e-16 5.6849e-05 9.0949e-06 1.3112e-02 4.7824e-01 0:26:46 662

Done.

C.15 Last 10 Iterations of Airfoil with K=4mm (300m/s) at $\alpha=0^{o}$

719835 triangular cells, zone 3, binary.

719835 cell partition ids, zone 3, 8 partitions, binary.

1060651 2D interior faces, zone 1, binary.

1441 2D interior faces, zone 2, binary.

35041 2D wall faces, zone 6, binary.

230 2D velocity-inlet faces, zone 7, binary.

50 2D pressure-outlet faces, zone 8, binary.

377578 nodes, binary.

377578 node flags, binary.

iter continuity x-velocity y-velocity energy k omega drag-coeff lift-coeff time/iter

986 7.6127e-06 6.4611e-10 3.0358e-10 1.6718e-16 5.6748e-05 7.4677e-06 1.3732e-02 4.6001e-01 0:00:32 14

987 7.5883e-06 6.5350e-10 3.0265e-10 1.6966e-16 5.6762e-05 7.4679e-06 1.3732e-02 4.6001e-01 0:00:29 13

988 7.6173e-06 6.6057e-10 3.0132e-10 1.7168e-16 5.6810e-05 7.4684e-06 1.3732e-02 4.6001e-01 0:00:26 12

989 7.6805e-06 6.7312e-10 3.0292e-10 1.6640e-16 5.7093e-05 7.4703e-06 1.3732e-02 4.6001e-01 0:00:26 11

990 7.7350e-06 6.8334e-10 3.0168e-10 1.6943e-16 5.7266e-05 7.4700e-06 1.3732e-02 4.6001e-01 0:00:23 10

iter continuity x-velocity y-velocity energy k omega drag-coeff lift-coeff time/iter

991 7.7642e-06 6.9525e-10 3.0290e-10 1.6815e-16 5.7136e-05 7.4711e-06 1.3732e-02 4.6001e-01 0:00:20 9

992 7.7884e-06 7.0269e-10 3.0046e-10 1.6824e-16 5.7101e-05 7.4713e-06 1.3732e-02 4.6001e-01 0:00:17 8

993 7.7675e-06 7.0808e-10 3.0004e-10 1.6816e-16 5.7370e-05 7.4719e-06 1.3732e-02 4.6001e-01 0:00:16 7

994 7.7376e-06 7.0733e-10 2.9706e-10 1.6878e-16 5.7600e-05 7.4737e-06 1.3732e-02 4.6001e-01 0:00:14 6

995 7.7274e-06 7.0958e-10 3.2105e-10 1.6753e-16 5.7513e-05 7.4760e-06 1.3732e-02 4.6001e-01 0:00:11 5

996 7.7396e-06 6.9851e-10 3.0334e-10 1.6694e-16 5.7449e-05 7.4782e-06 1.3732e-02 4.6001e-01 0:00:09 4

997 7.5476e-06 6.8641e-10 2.9523e-10 1.6734e-16 5.7647e-05 7.4776e-06 1.3732e-02 4.6001e-01 0:00:06 3

998 7.4330e-06 6.7487e-10 2.8992e-10 1.6700e-16 5.7763e-05 7.4788e-06 1.3732e-02 4.6001e-01 0:00:05 2

999 7.3719e-06 6.6257e-10 2.8589e-10 1.6753e-16 5.7560e-05 7.4796e-06 1.3732e-02 4.6001e-01 0:00:02 1

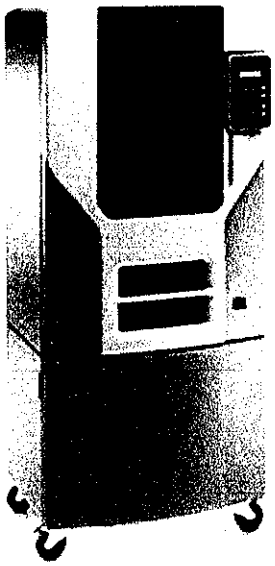
1000 7.3433e-06 6.5402e-10 2.8656e-10 1.6801e-16 5.7407e-05 7.4810e-06 1.3732e-02 4.6001e-01 0:00:00 0

Appendix (D)

Dimension 1200es 3-D Printer Specifications

Print out substantial, robust 3-D models at your office. With the Dimension SST 1200esTM and BST 1200es 3D Printers, see your creations come to life. They convert 3-D CAD files into realistic, useable 3D models that you can both debate and test. The Dimension 1200es 3D Printers' huge build volume provides you the space to produce models at the required size. Additionally, they are easy to use: Simply select "print" to prepare the CAD file and print the model. Once the support material has been removed, your design will be visible in three dimensions. combine and save When you purchase the Dimension 3-D Print Pack, you'll instantly have everything you need to start printing 3-D models at a low cost. You obtain a:

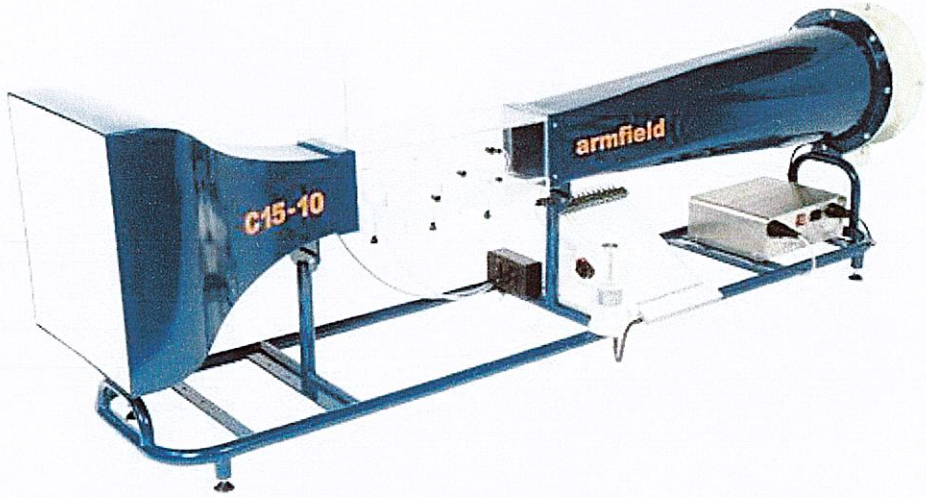
- Dimension 1200es SST 3D Printer
- SCA-1200 support removal system
- Startup supply of materials.



- Support material: Soluble Support Technology (SST) or Breakaway Support Technology (BST)
- Build size: 254 x 254 x 305 mm (10 x 10 x 12 in)
- Layer thickness: 0.254 mm (.010 in) or .330 mm (.013 in) of precisely deposited ABSplus model and support material
- Workstation compatibility: Windows XP/Windows 7
- Network connectivity: Ethernet TCP/IP 10/100Base-T
- Size and weight: 838 x 737 x 1143 mm (33 x 29 x 45 in) 148 kg (326 lbs)
- Power requirements: 110–120 VAC, 60 Hz, minimum 15A dedicated circuit; or 220–240 VAC 50/60 Hz, minimum 7A dedicated circuit
- Regulatory compliance: CE/ETL
- Special facility requirements: None

Appendix (E)

C15-20 Computer Controlled Subsonic Wind Tunnel



Specifications of C15-10 Computer Controlled Subsonic Wind Tunnel:

- Small computer-controlled wind tunnel.
- Clear acrylic working section (150mm x 150mm x 455mm) for excellent visibility
- AC fan with inverter control for precise speed adjustment up to 34 m/s air velocity
- A variety of optional instruments and models

- Quick-release connections with multiple or single lanes for models and manometers
- Models affixed to the working section's side wall include fast release catches.
- Complete with data logging and educational software
- A base that may be removed from the working part to provide room for big or intricate models.
- Flow visualization facility included
- Bernoulli equipment and other options for air flow experiments are available.

Appendix (F)

Uncertainty Analysis

F.1 Uncertainty Associated with the airfoil's Surface Area

The drag and lift coefficients are determined using the projected top area of the airfoil. The wings area formula is shown in the following equation. S stands for span, and C for chord in a simple wing.

$$A = S \times C \tag{E.1}$$

The calculation for the uncertainty in A is as follows.

$$U_A = \sqrt{(\frac{\partial A}{\partial S} U_S)^2 + (\frac{\partial A}{\partial C} U_C)^2} \tag{E.2}$$

$$\frac{\partial A}{\partial C} = 1 \ , \frac{\partial A}{\partial S} = 9.57 \, , \quad \text{and } U_S, \ U_C = \pm 0.5 \, mm$$

Thus $U_A = \pm 4.81 \, mm^2$

The total uncertainty in the airfoil's surface for the smooth airfoil is:

$$\frac{U_A}{A} \times 100 = \pm 0.5026 \, \%$$

F.2 Uncertainty Associated with the Air flow Velocity at the Inlet of the Wind Tunnel

The following formula, which is based on air density, relates the free stream air flow velocity at the wind tunnel's intake to the static pressure within the wind tunnel. The speed indicated by:

$$V_\infty = \sqrt{\frac{2\Delta P_s}{\rho}} \tag{E.3}$$

For ρ = 1.18546 kg/m^3, P_s = 374.74 Pa, the uncertainty was calculated as:

$$U_{V_\infty} = \sqrt{(\frac{\partial V_\infty}{\partial P_S} U_{P_S})^2 + (\frac{\partial V_\infty}{\partial \rho} U_P)^2} \qquad \text{(E.4)}$$

Where

$\frac{\partial V_\infty}{\partial P_S} = \frac{1}{\sqrt{2P_S\rho}}$, and $U_{P_S} = \pm 0.981\ Pa$, and

$\frac{\partial V_\infty}{\partial \rho} = -\sqrt{\frac{P_S}{2\rho^3}}$, and $U_\rho = \pm 4.2 \times 10^{-4}\ kg/m^3$

Thus $U_{V_\infty} = \pm 0.047\ m/s$

The total uncertainty in the inlet velocity, for $V_\infty = 35\ m/s$ is

$\frac{U_{V_\infty}}{V_\infty} \times 100 = \pm 0.1343\ \%$

F.3 Uncertainty Associated with the Drag Coefficient of the Airfoil

The following formula was used to calculate the drag coefficient at zero angle of attack α=0°:

$$C_D = \frac{2F_D}{\rho V_\infty^2 A \cos\cos\alpha}$$

(E.5)

For α = 0° , ρ = 1.18546 kg/m^3 and for $V_\infty = 35\ m/s$, the drag force was F_D = 0.242 N for the smooth airfoil. The uncertainty in C_D is given by:

$$U_{C_D} = \sqrt{(\frac{\partial C_D}{\partial F_D} U_{F_D})^2 + (\frac{\partial C_D}{\partial \rho} U_\rho)^2 + (\frac{\partial C_D}{\partial V_\infty} U_{V_\infty})^2 + (\frac{\partial C_D}{\partial A} U_A)^2} \qquad \text{(E.6)}$$

Were

$\frac{\partial C_D}{\partial F_D} = \frac{2}{\rho V_\infty^2 A \cos\cos\alpha'}$ and $U_{F_D} = \pm 0.0031\ N$,

$\frac{\partial C_D}{\partial \rho} = -\frac{2F_D}{\rho^2 V_\infty^2 A \cos\cos\alpha'}$ and $U_\rho = \pm 4.2 \times 10^{-4}\ kg/m^3$,

$\frac{\partial C_D}{\partial V_\infty} = -\frac{4F_D}{\rho V_\infty^3 A \cos\cos\alpha'}$ and $U_{V_\infty} = \pm 0.047\ m/s$,

$$\frac{\partial C_D}{\partial A} = \frac{2F_D}{\rho V_\infty^2 A^2 coscos\,\alpha'} \qquad \text{and } U_A = \pm 5.22 \times 10^{-5}\ m^2$$

Thus, $U_{C_D} = \pm 0.047$

The total uncertainty in the drag coefficient, for the smooth airfoil at $V_\infty = 35\ m/s$ is : $\frac{U_{C_D}}{C_D} \times 100 = \pm 5.22\ \%$

F.4 Uncertainty Associated with the Lift Coefficient of the Airfoil

The lift coefficient at angle of attack of zero $\alpha = 0^o$ was obtained from the next formula:

$$C_L = \frac{2F_L}{\rho V_\infty^2 A coscos\,\alpha} \qquad \text{(E.7)}$$

For $\alpha = 0^o$, $\rho = 1.18546$ kg/m^3 and for $V_\infty = 35\ m/s$, the lift force was $F_L = 0.047\ N$ for the smooth airfoil. The uncertainty in C_L was calculated as:

$$U_{C_L} = \sqrt{(\frac{\partial C_L}{\partial F_L} U_{F_L})^2 + (\frac{\partial C_L}{\partial \rho} U_\rho)^2 + (\frac{\partial C_L}{\partial V_\infty} U_{V_\infty})^2 + (\frac{\partial C_L}{\partial A} U_A)^2} \qquad \text{(E.8)}$$

Where

$$\frac{\partial C_L}{\partial F_L} = \frac{2}{\rho V_\infty^2 A coscos\,\alpha'} \qquad \text{and } U_{F_L} = \pm 0.0035\ N\ ,$$

$$\frac{\partial C_L}{\partial \rho} = -\frac{2F_L}{\rho^2 V_\infty^2 A coscos\,\alpha'} \qquad \text{and } U_\rho = \pm 4.2 \times 10^{-4}\ kg/m^3\ ,$$

$$\frac{\partial C_L}{\partial V_\infty} = -\frac{4F_L}{\rho V_\infty^3 A coscos\,\alpha'} \qquad \text{and } U_{V_\infty} = \pm 0.047\ m/s\ ,$$

$$\frac{\partial C_L}{\partial A} = \frac{2F_L}{\rho V_\infty^2 A^2 coscos\,\alpha'} \qquad \text{and } U_A = \pm 5.22 \times 10^{-5}\ m^2$$

Thus, $U_{C_L} = \pm 0.0047$

The total uncertainty in the drag coefficient, for the plain wing at $V_\infty = 35\ m/s$ is : $\frac{U_{C_L}}{C_L} \times 100 = \pm 5.01\ \%$

Appendix (G)

Wind Tunnel Results

Force and Drag Experimental results

G.1 Wind Tunnel (C-15) Test 1: Airfoil K=0.0258 mm

Test 1:	Fan Speed [%]	Rotation r [°]	Ambient Temperature T [°C]	Density of Air [kg/m³]	Air Velocity v [m/s]	Reynolds Number Re	C_L	C_D
1	60	0.0	24.00	1.185460	20.259339	85773	0.43026	0.01226
2	70	0.0	24.00	1.185460	23.039446	99511	0.43272	0.011963
3	80	0.1	24.00	1.185460	26.598795	115416	0.43537	0.011639
4	90	0.0	24.00	1.185460	29.767721	133896	0.43695	0.011435
5	100	0.0	24.00	1.185460	32.867474	156643	0.43834	0.011148
6	60	5.2	24.00	1.185460	20.497524	85781	0.94419	0.015091
7	70	5.2	24.00	1.185460	23.948483	99523	0.94846	0.014741
8	80	5.2	24.00	1.185460	27.496078	115422	0.95173	0.014357
9	90	5.2	24.00	1.185460	31.786405	133901	0.95445	0.014121
10	100	5.2	24.00	1.185460	34.538095	156649	0.95812	0.013789
11	60	10.1	24.00	1.185460	20.639116	85790	1.3067	0.022021
12	70	10.1	24.00	1.185460	24.069783	99580	1.3082	0.021953
13	80	10.1	24.00	1.185460	27.812014	115464	1.3125	0.02163
14	90	10.1	24.00	1.185460	31.355925	133933	1.3286	0.021325
15	100	10.1	24.00	1.185460	34.957160	156658	1.3349	0.021063

Force and Drag Experimental results

G.2 Wind Tunnel (C-15) Test2: Airfoil K=0.045 mm

Test 1:	Fan Speed [%]	Rotation r [°]	Ambient Temperature T [°C]	Density of Air [kg/m³]	Air Velocity v [m/s]	Reynolds Number Re	C_L	C_D
1	60	0.0	24.00	1.185460	20.307199	85976	0.42763	0.011153
2	70	0.0	24.00	1.185460	22.398505	100592	0.43073	0.01081
3	80	0.1	24.00	1.185460	26.925261	117693	0.43411	0.010542
4	90	0.0	24.00	1.185460	30.793610	137700	0.43623	0.010316
5	100	0.1	24.00	1.185460	34.509976	161109	0.43951	0.010112
6	60	5.0	24.00	1.185460	20.592026	85979	0.93233	0.013717
7	70	5.0	24.00	1.185460	23.988985	100599	0.93848	0.013422
8	80	5.0	24.00	1.185460	28.124401	117740	0.94426	0.013043
9	90	5.0	24.00	1.185460	31.847427	137704	0.94765	0.012787
10	100	5.0	24.00	1.185460	35.671879	161185	0.95357	0.012378
11	60	10.1	24.00	1.185460	21.012029	85988	1.3037	0.021428
12	70	10.1	24.00	1.185460	24.230572	100608	1.3093	0.02092
13	80	10.1	24.00	1.185460	28.330746	117860	1.3159	0.020295
14	90	10.1	24.00	1.185460	32.180981	137786	1.3242	0.019882
15	100	10.1	24.00	1.185460	35.590144	161206	1.3333	0.019333

Force and Drag Experimental results

G.3 Wind Tunnel (C-15) Test 3: Airfoil with K= 0.125 mm

Test 3:	Fan Speed [%]	Rotation r [°]	Ambient Temperature T [°C]	Density of Air [kg/m³]	Air Velocity v [m/s]	Reynolds Number Re	C_L	C_D
1	60	0.0	24.00	1.185460	20.16327670	85366	0.42763	0.010795
2	70	0.0	24.00	1.185460	22.52815175	99878	0.43101	0.010567
3	80	0.0	24.00	1.185460	26.59879458	116856	0.43327	0.010313
4	90	0.1	24.00	1.185460	30.05979128	136723	0.43585	0.010157
5	100	0.1	24.00	1.185460	33.88546357	159966	0.43864	0.009935
6	60	5.0	24.00	1.185460	20.01831956	85401	0.93451	0.013306
7	70	5.1	24.00	1.185460	23.70402162	99894	0.93895	0.013022
8	80	5.0	24.00	1.185460	27.49607760	116897	0.94427	0.012706
9	90	5.1	24.00	1.185460	31.41778347	136844	0.94652	0.012521
10	100	5.1	24.00	1.185460	35.59014419	159621	0.95275	0.012247
11	60	10.1	24.00	1.185460	20.63911557	85472	1.3039	0.020825
12	70	10.1	24.00	1.185460	23.62197215	99902	1.3104	0.020409
13	80	10.1	24.00	1.185460	27.70710202	116917	1.3163	0.020008
14	90	10.1	24.00	1.185460	31.75585015	136895	1.3216	0.019689
15	100	10.1	24.00	1.185460	35.23376775	159680	1.3306	0.019221

Force and Drag Experimental results

G.4 Wind Tunnel (C-15) Test 4: Airfoil with K=0.19 mm

Test 3:	Fan Speed [%]	Rotation r [°]	Ambient Temperature T [°C]	Density of Air [kg/m³]	Air Velocity v [m/s]	Reynolds Number Re	C_L	C_D
1	60	0.0	24.00	1.185460	19.42767822	82252	0.42584	0.010968
2	70	0.0	24.00	1.185460	22.65705697	96234	0.4282	0.010769
3	80	0.0	24.00	1.185460	26.67168810	112594	0.43142	0.010565
4	90	0.1	24.00	1.185460	29.89788236	131735	0.43379	0.01044
5	100	0.0	24.00	1.185460	33.53991956	155131	0.43748	0.010257
6	60	5.3	24.00	1.185460	20.45010870	85294	0.92653	0.013477
7	70	5.3	24.00	1.185460	23.70402162	98139	0.93383	0.013189
8	80	5.3	24.00	1.185460	27.31897878	113259	0.93891	0.012904
9	90	5.3	24.00	1.185460	31.23184112	134166	0.9426	0.012728
10	100	5.3	24.00	1.185460	32.57077681	156899	0.94723	0.012504
11	60	10.3	24.00	1.185460	20.49752381	85311	1.2899	0.02151
12	70	10.3	24.00	1.185460	23.53963669	98527	1.297	0.021022
13	80	10.3	24.00	1.185460	27.21216625	114015	1.3037	0.020553
14	90	10.3	24.00	1.185460	31.90833278	135740	1.3119	0.020145
15	100	10.3	24.00	1.185460	34.67834571	157100	1.3191	0.019741

Boundary Layer Experiment

G.5 Wind Tunnel (C-15) Test 5: Airfoil 0.5C K=0.0258 mm

Ambient Temperature T [°C]	Density of Air [kg/m³]	Tunnel Air Velocity [m/s]	Pitot Position y [mm]	Pitot Air Velocity [m/s]
24.0	1.185	35.9	0.0	0
24.0	1.185	35.7	0.1	22.92001
24.0	1.185	36.2	0.2	30.99469
24.0	1.185	35.7	0.3	33.65136
24.0	1.185	36.0	0.4	35.51751
24.0	1.185	35.8	0.5	35.62251
24.0	1.185	36.2	0.6	35.70254

Boundary Layer Experiment

G.6 Wind Tunnel (C-15) Test 5: Airfoil 0.5C Boundary Layer K=0.045 mm

Ambient Temperature T [°C]	Density of Air [kg/m³]	Tunnel Air Velocity [m/s]	Pitot Position y [mm]	Pitot Air Velocity [m/s]
24.0	1.185	35.7	0.0	0.0
24.0	1.185	35.5	0.1	10.221165
24.0	1.185	35.5	0.2	16.0258
24.0	1.185	35.7	0.3	22.39842
24.0	1.185	35.6	0.4	28.0225
24.0	1.185	35.9	0.5	33.0258
24.0	1.185	35.5	0.6	35.60259
24.0	1.185	36.1	0.7	35.52544
24.0	1.185	35.2	0.8	35.02546
24.0	1.185	35.9	0.9	35.62002

Boundary Layer Experiment

G.7 Wind Tunnel (C-15) Test 6: Airfoil 0.5C Boundary Layer

K=0.125 mm

Ambient Temperature T [°C]	Density of Air [kg/m³]	Tunnel Air Velocity [m/s]	Pitot Position y [mm]	Pitot Air Velocity [m/s]
24.0	1.185	36.0	0.0	0
24.0	1.185	36.1	0.1	12.03255
24.0	1.185	36.0	0.2	28.36012
24.0	1.185	35.8	0.3	30.2588
24.0	1.185	35.8	0.4	31.06885
24.0	1.185	35.7	0.5	32.15441
24.0	1.185	35.6	0.6	33.02998
24.0	1.185	35.9	0.7	33.236641
24.0	1.185	35.5	0.8	33.415998
24.0	1.185	35.9	0.9	33.58201
24.0	1.185	35.9	1.0	34.12022
24.0	1.185	35.7	1.1	34.26902
24.0	1.185	36.2	1.2	34.52201
24.0	1.185	35.7	1.3	34.87751
24.0	1.185	36.0	1.4	35.758918
24.0	1.185	35.8	1.5	35.633327
24.0	1.185	36.2	1.6	35.866302
24.0	1.185	36.0	1.7	35.710225

Boundary Layer Experiment

G.8 Wind Tunnel (C-15) Test 5: Airfoil 0.5C Boundary Layer K=0.19 mm

Ambient Temperature T [°C]	Density of Air [kg/m³]	Tunnel Air Velocity [m/s]	Pitot Position y [mm]	Pitot Air Velocity [m/s]
24.0	1.185	34.6	0	0
24.0	1.185	35.2	0.2	28.72102
24.0	1.185	35.9	0.4	32.73921
24.0	1.185	35.8	0.6	33.02696
24.0	1.185	35.9	0.8	33.62023
24.0	1.185	35.1	1	34.0265
24.0	1.185	35.2	1.2	34.25511
24.0	1.185	36.1	1.4	34.33617
24.0	1.185	35.4	1.6	34.40019
24.0	1.185	35.9	1.8	34.92223
24.0	1.185	35.4	2	35.00036
24.0	1.185	35.6	2.1	35.22241
24.0	1.185	35.9	2.2	35.55102
24.0	1.185	35.9	2.3	35.6222
24.0	1.185	36.1	2.4	35.66202
24.0	1.185	35.8	2.5	35.70026
24.0	1.185	35.4	2.6	35.82225
24.0	1.185	35.8	2.7	35.78885

Appendix (H)

Experimental Results Verification

H-1: At α=0°

Upper ks=0.0258 mm, Lower ks=0.0258 mm at V=20 m/s

iter continuity x-velocity y-velocity energy k omega lift-coeff drag-coeff time/iter

56 1.8890e-03 1.6819e-07 2.2731e-08 1.6337e-16 3.3938e-04 3.1395e-04 4.4239e-01 1.2532e-02 0:04:09 944

57 1.8310e-03 1.5882e-07 2.1200e-08 1.5957e-16 3.2653e-04 3.0437e-04 4.4241e-01 1.2531e-02 0:06:27 943

58 1.6627e-03 1.4708e-07 1.9381e-08 1.5947e-16 3.1557e-04 2.9641e-04 4.4242e-01 1.2530e-02 0:05:10 942

59 1.6331e-03 1.4063e-07 1.8232e-08 1.5956e-16 3.0384e-04 2.8726e-04 4.4243e-01 1.2529e-02 0:04:07 941

60 1.4639e-03 1.3077e-07 1.6563e-08 1.6027e-16 2.9422e-04 2.7919e-04 4.4244e-01 1.2528e-02 0:06:26 940

61 1.4511e-03 1.2599e-07 1.5584e-08 1.6275e-16 2.8405e-04 2.7179e-04 4.4244e-01 1.2527e-02 0:05:08 939

62 1.3161e-03 1.1743e-07 1.4240e-08 1.6510e-16 2.7564e-04 2.6629e-04 4.4245e-01 1.2525e-02 0:04:06 938

63 1.3074e-03 1.1266e-07 1.3558e-08 1.6342e-16 2.6636e-04 2.5900e-04 4.4245e-01 1.2524e-02 0:06:24 937

64 1.1502e-03 1.0347e-07 1.2361e-08 1.6159e-16 2.5876e-04 2.5333e-04 4.4246e-01 1.2523e-02 0:05:07 936

65 1.1513e-03 9.8964e-08 1.1852e-08 1.6146e-16 2.5030e-04 2.4756e-04 4.4246e-01 1.2523e-02 0:07:12 935

66 1.0306e-03 9.1095e-08 1.0943e-08 1.6255e-16 2.4359e-04 2.4346e-04 4.4247e-01 1.2522e-02 0:05:46 934

iter continuity x-velocity y-velocity energy k omega lift-coeff drag-coeff time/iter

67 1.0414e-03 8.7457e-08 1.0718e-08 1.6280e-16 2.3602e-04 2.3767e-04 4.4248e-01 1.2521e-02 0:04:36 933

! 68 solution is converged

68 9.0237e-04 7.9670e-08 9.9309e-09 1.6024e-16 2.3003e-04 2.3342e-04 4.4249e-01 1.2520e-02 0:06:47 932

Upper ks=0.0258 mm, Lower ks=0.0258 mm at V=23 m/s

iter continuity x-velocity y-velocity energy k omega lift-coeff drag-coeff time/iter

56 1.7754e-03 1.6332e-07 2.2291e-08 1.5973e-16 3.2381e-04 2.9669e-04 4.4281e-01 1.2222e-02 0:05:10 944

57 1.6435e-03 1.5116e-07 2.0438e-08 1.5902e-16 3.1160e-04 2.8783e-04 4.4283e-01 1.2221e-02 0:04:08 943

58 1.5250e-03 1.4046e-07 1.8718e-08 1.6077e-16 3.0045e-04 2.7919e-04 4.4284e-01 1.2220e-02 0:06:27 942

59 1.4193e-03 1.3119e-07 1.7110e-08 1.5638e-16 2.9032e-04 2.7163e-04 4.4284e-01 1.2218e-02 0:05:09 941

60 1.3218e-03 1.2341e-07 1.5572e-08 1.5928e-16 2.8063e-04 2.6418e-04 4.4284e-01 1.2217e-02 0:04:07 940

61 1.2337e-03 1.1642e-07 1.4186e-08 1.5780e-16 2.7158e-04 2.5755e-04
4.4284e-01 1.2216e-02 0:06:25 939
62 1.1580e-03 1.0992e-07 1.3003e-08 1.5718e-16 2.6318e-04 2.5137e-04
4.4284e-01 1.2215e-02 0:05:08 938
63 1.1013e-03 1.0351e-07 1.2270e-08 1.5866e-16 2.5535e-04 2.4553e-04
4.4284e-01 1.2214e-02 0:04:06 937
64 1.0324e-03 9.7068e-08 1.1438e-08 1.5746e-16 2.4752e-04 2.3994e-04
4.4284e-01 1.2213e-02 0:06:24 936
! 65 solution is converged
65 9.6691e-04 9.0874e-08 1.0713e-08 1.5841e-16 2.4027e-04 2.3484e-04
4.4284e-01 1.2213e-02 0:05:07 935

Upper ks=0.0258 mm, Lower ks=0.0258 mm at V=27 m/s

iter continuity x-velocity y-velocity energy k omega lift-coeff drag-coeff
time/iter
56 1.7591e-03 1.5864e-07 2.1542e-08 1.6283e-16 3.0635e-04 2.7795e-04
4.4429e-01 1.1903e-02 0:04:10 944
57 1.6583e-03 1.4692e-07 1.9934e-08 1.5971e-16 2.9443e-04 2.6950e-04
4.4430e-01 1.1902e-02 0:06:28 943
58 1.5177e-03 1.3590e-07 1.8169e-08 1.5774e-16 2.8352e-04 2.6133e-04
4.4431e-01 1.1900e-02 0:05:10 942
59 1.4231e-03 1.2708e-07 1.6732e-08 1.5617e-16 2.7338e-04 2.5417e-04
4.4432e-01 1.1899e-02 0:07:16 941
60 1.3080e-03 1.1887e-07 1.5086e-08 1.5934e-16 2.6439e-04 2.4740e-04
4.4432e-01 1.1898e-02 0:05:49 940

61 1.2428e-03 1.1218e-07 1.3936e-08 1.5926e-16 2.5616e-04 2.4123e-04
4.4431e-01 1.1897e-02 0:04:39 939
62 1.1488e-03 1.0515e-07 1.2763e-08 1.5726e-16 2.4828e-04 2.3531e-04
4.4431e-01 1.1896e-02 0:06:50 938
63 1.0704e-03 9.8571e-08 1.1891e-08 1.5695e-16 2.4082e-04 2.2990e-04
4.4430e-01 1.1895e-02 0:05:28 937
! 64 solution is converged
64 9.9860e-04 9.2410e-08 1.1245e-08 1.6008e-16 2.3398e-04 2.2501e-04
4.4430e-01 1.1894e-02 0:07:29 936

Upper ks=0.0258 mm, Lower ks=0.0258 mm at V=30 m/s

iter continuity x-velocity y-velocity energy k omega lift-coeff drag-coeff
time/iter
56 1.7244e-03 1.5809e-07 2.1657e-08 1.6832e-16 2.9390e-04 2.6518e-04
4.4531e-01 1.1716e-02 0:04:11 944
57 1.5893e-03 1.4538e-07 1.9898e-08 1.6142e-16 2.8254e-04 2.5684e-04
4.4532e-01 1.1714e-02 0:06:29 943
58 1.4647e-03 1.3422e-07 1.8227e-08 1.6186e-16 2.7182e-04 2.4957e-04
4.4533e-01 1.1713e-02 0:05:11 942
59 1.3568e-03 1.2457e-07 1.6649e-08 1.6379e-16 2.6203e-04 2.4239e-04
4.4534e-01 1.1712e-02 0:04:09 941
60 1.2627e-03 1.1665e-07 1.5170e-08 1.5984e-16 2.5298e-04 2.3604e-04
4.4534e-01 1.1710e-02 0:06:27 940
61 1.1764e-03 1.0959e-07 1.3798e-08 1.6480e-16 2.4481e-04 2.3004e-04
4.4534e-01 1.1709e-02 0:05:09 939
62 1.0971e-03 1.0281e-07 1.2602e-08 1.6242e-16 2.3742e-04 2.2454e-04
4.4534e-01 1.1708e-02 0:04:07 938

63 1.0242e-03 9.6274e-08 1.1625e-08 1.6550e-16 2.3040e-04 2.1937e-04
4.4533e-01 1.1707e-02 0:06:25 937
! 64 solution is converged
64 9.5809e-04 9.0235e-08 1.0869e-08 1.6405e-16 2.2375e-04 2.1456e-04
4.4532e-01 1.1707e-02 0:05:07 936

Upper ks=0.0258 mm, Lower ks=0.0258 mm at V=35 m/s

iter continuity x-velocity y-velocity energy k omega lift-coeff drag-coeff
time/iter
56 1.6824e-03 1.5577e-07 2.1186e-08 1.7031e-16 2.7876e-04 2.4682e-04
4.4662e-01 1.1474e-02 0:04:39 944
57 1.5439e-03 1.4286e-07 1.9272e-08 1.6599e-16 2.6777e-04 2.3963e-04
4.4663e-01 1.1473e-02 0:06:52 943
58 1.4228e-03 1.3153e-07 1.7566e-08 1.6634e-16 2.5775e-04 2.3255e-04
4.4663e-01 1.1472e-02 0:05:29 942
59 1.3174e-03 1.2162e-07 1.6051e-08 1.6784e-16 2.4809e-04 2.2624e-04
4.4664e-01 1.1470e-02 0:04:23 941
60 1.2261e-03 1.1336e-07 1.4664e-08 1.6860e-16 2.3939e-04 2.2005e-04
4.4664e-01 1.1469e-02 0:06:38 940
61 1.1414e-03 1.0612e-07 1.3413e-08 1.6682e-16 2.3120e-04 2.1461e-04
4.4664e-01 1.1468e-02 0:05:18 939
62 1.0635e-03 9.9269e-08 1.2342e-08 1.6520e-16 2.2384e-04 2.0928e-04
4.4663e-01 1.1467e-02 0:04:14 938
! 63 solution is converged
63 9.9107e-04 9.2871e-08 1.1468e-08 1.6847e-16 2.1708e-04 2.0454e-04
4.4662e-01 1.1466e-02 0:06:31 937

Upper ks=0.0258 mm, Lower ks=0.045 mm at V=20 m/s

iter continuity x-velocity y-velocity energy k omega lift-coeff drag-coeff time/iter

45 4.4801e-03 3.9776e-07 6.1161e-08 1.6377e-16 5.5400e-04 4.8729e-04 4.4141e-01 1.2583e-02 0:06:58 955

46 4.2195e-03 3.6809e-07 5.4539e-08 1.6144e-16 5.2905e-04 4.6605e-04 4.4137e-01 1.2582e-02 0:05:34 954

47 3.7412e-03 3.3918e-07 4.8802e-08 1.6371e-16 5.0456e-04 4.4660e-04 4.4140e-01 1.2582e-02 0:04:27 953

48 3.5365e-03 3.1306e-07 4.3354e-08 1.6441e-16 4.8176e-04 4.2748e-04 4.4149e-01 1.2581e-02 0:06:44 952

49 3.2757e-03 2.9079e-07 4.2268e-08 1.6059e-16 4.5911e-04 4.0934e-04 4.4156e-01 1.2579e-02 0:05:23 951

50 2.9881e-03 2.6737e-07 3.9407e-08 1.6370e-16 4.3842e-04 3.9194e-04 4.4157e-01 1.2576e-02 0:04:18 950

51 2.7093e-03 2.4514e-07 3.4109e-08 1.6363e-16 4.1897e-04 3.7741e-04 4.4155e-01 1.2573e-02 0:06:36 949

52 2.6415e-03 2.2760e-07 2.9668e-08 1.6164e-16 4.0090e-04 3.6223e-04 4.4152e-01 1.2572e-02 0:05:16 948

53 2.3423e-03 2.0974e-07 2.6953e-08 1.6369e-16 3.8393e-04 3.4962e-04 4.4157e-01 1.2572e-02 0:07:22 947

54 2.1635e-03 1.9422e-07 2.5787e-08 1.6511e-16 3.6822e-04 3.3700e-04 4.4169e-01 1.2572e-02 0:05:53 946

55 2.1901e-03 1.8501e-07 2.9855e-08 1.6405e-16 3.5333e-04 3.2565e-04 4.4180e-01 1.2571e-02 0:04:42 945

iter continuity x-velocity y-velocity energy k omega lift-coeff drag-coeff time/iter

56 2.0139e-03 1.7483e-07 3.0988e-08 1.6463e-16 3.3945e-04 3.1450e-04 4.4186e-01 1.2569e-02 0:06:54 944

57 1.8202e-03 1.6211e-07 2.8315e-08 1.6516e-16 3.2702e-04 3.0479e-04 4.4187e-01 1.2566e-02 0:05:31 943

58 1.6615e-03 1.4892e-07 2.3363e-08 1.6287e-16 3.1561e-04 2.9571e-04 4.4182e-01 1.2564e-02 0:04:25 942

59 1.7119e-03 1.4090e-07 2.0059e-08 1.6349e-16 3.0480e-04 2.8783e-04 4.4176e-01 1.2562e-02 0:06:40 941

60 1.5340e-03 1.3499e-07 1.9559e-08 1.6517e-16 2.9454e-04 2.8063e-04 4.4176e-01 1.2563e-02 0:05:19 940

61 1.4886e-03 1.2585e-07 1.6469e-08 1.6340e-16 2.8452e-04 2.7264e-04 4.4182e-01 1.2563e-02 0:04:15 939

62 1.3282e-03 1.1763e-07 1.5574e-08 1.6735e-16 2.7526e-04 2.6550e-04 4.4185e-01 1.2561e-02 0:06:32 938

63 1.1991e-03 1.0987e-07 1.4764e-08 1.6460e-16 2.6665e-04 2.5888e-04 4.4182e-01 1.2559e-02 0:05:13 937

64 1.1134e-03 1.0315e-07 1.2728e-08 1.6470e-16 2.5858e-04 2.5355e-04 4.4175e-01 1.2557e-02 0:04:10 936

65 1.2734e-03 1.0295e-07 1.5744e-08 1.6814e-16 2.5063e-04 2.4803e-04 4.4169e-01 1.2556e-02 0:06:27 935

66 1.1264e-03 9.7682e-08 1.6551e-08 1.6462e-16 2.4306e-04 2.4365e-04 4.4172e-01 1.2557e-02 0:05:09 934

iter continuity x-velocity y-velocity energy k omega lift-coeff drag-coeff time/iter

67 1.0927e-03 8.7105e-08 1.2679e-08 1.6461e-16 2.3614e-04 2.3860e-04
4.4179e-01 1.2557e-02 0:07:14 933
! 68 solution is converged
68 9.8481e-04 8.2567e-08 1.3745e-08 1.6285e-16 2.2946e-04 2.3345e-04
4.4184e-01 1.2556e-02 0:05:47 932

Upper ks=0.0258 mm, Lower ks=0.045 mm at V=23 m/s

iter continuity x-velocity y-velocity energy k omega lift-coeff drag-coeff
time/iter
56 1.7838e-03 1.6381e-07 2.2552e-08 1.5722e-16 3.2539e-04 2.9700e-04
4.4310e-01 1.2283e-02 0:06:40 944
57 1.6510e-03 1.5168e-07 2.0647e-08 1.5794e-16 3.1303e-04 2.8813e-04
4.4311e-01 1.2281e-02 0:05:20 943
58 1.5321e-03 1.4100e-07 1.8884e-08 1.5655e-16 3.0171e-04 2.7943e-04
4.4312e-01 1.2280e-02 0:04:16 942
59 1.4231e-03 1.3174e-07 1.7229e-08 1.5805e-16 2.9149e-04 2.7178e-04
4.4313e-01 1.2279e-02 0:06:33 941
60 1.3260e-03 1.2401e-07 1.5636e-08 1.6018e-16 2.8169e-04 2.6425e-04
4.4313e-01 1.2278e-02 0:05:14 940
61 1.2365e-03 1.1689e-07 1.4223e-08 1.6101e-16 2.7254e-04 2.5755e-04
4.4313e-01 1.2276e-02 0:04:11 939
62 1.1583e-03 1.1020e-07 1.3069e-08 1.6160e-16 2.6393e-04 2.5109e-04
4.4313e-01 1.2275e-02 0:06:28 938
63 1.0875e-03 1.0345e-07 1.2166e-08 1.6151e-16 2.5590e-04 2.4524e-04
4.4312e-01 1.2274e-02 0:05:10 937
64 1.0200e-03 9.7078e-08 1.1435e-08 1.5890e-16 2.4803e-04 2.3960e-04
4.4312e-01 1.2274e-02 0:04:08 936

! 65 solution is converged

65 9.5443e-04 9.0786e-08 1.0841e-08 1.5819e-16 2.4063e-04 2.3434e-04 4.4312e-01 1.2273e-02 0:06:25 935

Upper ks=0.0258 mm, Lower ks=0.045 mm at V=27 m/s

iter continuity x-velocity y-velocity energy k omega lift-coeff drag-coeff time/iter

56 1.7573e-03 1.5955e-07 2.2056e-08 1.6071e-16 3.0769e-04 2.7759e-04 4.4463e-01 1.1998e-02 0:05:20 944

57 1.6195e-03 1.4714e-07 2.0226e-08 1.5973e-16 2.9563e-04 2.6960e-04 4.4465e-01 1.1997e-02 0:04:16 943

58 1.4939e-03 1.3630e-07 1.8509e-08 1.6045e-16 2.8454e-04 2.6108e-04 4.4466e-01 1.1995e-02 0:06:33 942

59 1.3825e-03 1.2702e-07 1.6910e-08 1.5615e-16 2.7437e-04 2.5423e-04 4.4466e-01 1.1994e-02 0:05:14 941

60 1.2864e-03 1.1921e-07 1.5383e-08 1.5795e-16 2.6519e-04 2.4705e-04 4.4466e-01 1.1993e-02 0:07:19 940

61 1.1995e-03 1.1206e-07 1.3987e-08 1.6045e-16 2.5690e-04 2.4110e-04 4.4466e-01 1.1992e-02 0:05:51 939

62 1.1221e-03 1.0531e-07 1.2813e-08 1.5873e-16 2.4889e-04 2.3501e-04 4.4466e-01 1.1991e-02 0:04:40 938

63 1.0485e-03 9.8768e-08 1.1885e-08 1.5639e-16 2.4144e-04 2.2972e-04 4.4465e-01 1.1990e-02 0:06:51 937

! 64 solution is converged

64 9.8141e-04 9.2569e-08 1.1147e-08 1.5852e-16 2.3439e-04 2.2441e-04 4.4465e-01 1.1990e-02 0:05:29 936

Upper ks=0.0258 mm, Lower ks=0.045 mm at V=30 m/s

iter continuity x-velocity y-velocity energy k omega lift-coeff drag-coeff time/iter

56 1.7328e-03 1.5839e-07 2.1889e-08 1.6371e-16 2.9507e-04 2.6528e-04 4.4576e-01 1.1837e-02 0:05:20 944

57 1.5953e-03 1.4570e-07 2.0140e-08 1.6393e-16 2.8368e-04 2.5679e-04 4.4578e-01 1.1835e-02 0:07:24 943

58 1.4707e-03 1.3451e-07 1.8449e-08 1.6310e-16 2.7282e-04 2.4963e-04 4.4579e-01 1.1834e-02 0:05:55 942

59 1.3595e-03 1.2494e-07 1.6900e-08 1.6608e-16 2.6301e-04 2.4231e-04 4.4579e-01 1.1833e-02 0:04:44 941

60 1.2632e-03 1.1693e-07 1.5409e-08 1.6276e-16 2.5391e-04 2.3605e-04 4.4579e-01 1.1831e-02 0:06:55 940

61 1.1761e-03 1.0975e-07 1.4008e-08 1.6245e-16 2.4556e-04 2.2989e-04 4.4579e-01 1.1830e-02 0:05:31 939

62 1.0966e-03 1.0298e-07 1.2756e-08 1.6461e-16 2.3812e-04 2.2449e-04 4.4579e-01 1.1829e-02 0:04:25 938

63 1.0232e-03 9.6434e-08 1.1748e-08 1.6620e-16 2.3100e-04 2.1916e-04 4.4579e-01 1.1828e-02 0:06:39 937

! 64 solution is converged

64 9.5639e-04 9.0315e-08 1.0958e-08 1.6479e-16 2.2430e-04 2.1442e-04 4.4578e-01 1.1828e-02 0:05:19 936

Upper ks=0.0258 mm, Lower ks=0.045 mm at V=35 m/s

iter continuity x-velocity y-velocity energy k omega lift-coeff drag-coeff time/iter

56 1.6929e-03 1.5608e-07 2.1447e-08 1.6600e-16 2.7937e-04 2.4685e-04 4.4726e-01 1.1634e-02 0:05:20 944

57 1.5536e-03 1.4326e-07 1.9603e-08 1.6567e-16 2.6851e-04 2.3943e-04 4.4727e-01 1.1632e-02 0:04:16 943

58 1.4293e-03 1.3189e-07 1.7913e-08 1.6662e-16 2.5828e-04 2.3256e-04 4.4727e-01 1.1631e-02 0:06:33 942

59 1.3208e-03 1.2194e-07 1.6358e-08 1.6584e-16 2.4861e-04 2.2604e-04 4.4728e-01 1.1630e-02 0:05:14 941

60 1.2271e-03 1.1371e-07 1.4932e-08 1.6625e-16 2.3973e-04 2.1999e-04 4.4728e-01 1.1629e-02 0:07:19 940

61 1.1415e-03 1.0646e-07 1.3606e-08 1.6771e-16 2.3163e-04 2.1438e-04 4.4728e-01 1.1628e-02 0:05:51 939

62 1.0633e-03 9.9625e-08 1.2454e-08 1.6628e-16 2.2420e-04 2.0914e-04 4.4728e-01 1.1627e-02 0:07:48 938

! 63 solution is converged

63 9.9137e-04 9.3168e-08 1.1532e-08 1.6389e-16 2.1735e-04 2.0428e-04 4.4727e-01 1.1626e-02 0:06:14 937

Upper ks=0.0258 mm, Lower ks=0.125 mm at V=20 m/s

iter continuity x-velocity y-velocity energy k omega lift-coeff drag-coeff time/iter

56 1.8695e-03 1.7324e-07 2.3335e-08 1.6587e-16 3.4224e-04 3.1275e-04 4.4345e-01 1.3099e-02 0:06:30 944

57 1.7337e-03 1.6105e-07 2.1337e-08 1.6235e-16 3.2921e-04 3.0263e-04 4.4346e-01 1.3098e-02 0:05:12 943

58 1.6130e-03 1.5026e-07 1.9546e-08 1.6002e-16 3.1751e-04 2.9335e-04 4.4347e-01 1.3097e-02 0:04:09 942

59 1.5025e-03 1.4112e-07 1.7909e-08 1.6467e-16 3.0629e-04 2.8447e-04
4.4348e-01 1.3096e-02 0:06:27 941
60 1.4037e-03 1.3312e-07 1.6321e-08 1.6617e-16 2.9593e-04 2.7644e-04
4.4348e-01 1.3095e-02 0:05:10 940
61 1.3135e-03 1.2552e-07 1.4949e-08 1.6342e-16 2.8589e-04 2.6886e-04
4.4348e-01 1.3094e-02 0:04:07 939
62 1.2256e-03 1.1803e-07 1.3830e-08 1.6656e-16 2.7630e-04 2.6212e-04
4.4348e-01 1.3093e-02 0:06:25 938
63 1.1489e-03 1.1062e-07 1.2882e-08 1.6164e-16 2.6703e-04 2.5559e-04
4.4348e-01 1.3091e-02 0:05:08 937
64 1.0766e-03 1.0314e-07 1.2062e-08 1.6237e-16 2.5827e-04 2.4982e-04
4.4347e-01 1.3090e-02 0:04:06 936
65 1.0100e-03 9.6043e-08 1.1263e-08 1.6460e-16 2.4987e-04 2.4418e-04
4.4347e-01 1.3089e-02 0:06:24 935
! 66 solution is converged
66 9.4492e-04 8.9521e-08 1.0498e-08 1.6102e-16 2.4207e-04 2.3921e-04
4.4348e-01 1.3088e-02 0:05:07 934

Upper ks=0.0258 mm, Lower ks=0.125 mm at V=23m/s

iter continuity x-velocity y-velocity energy k omega lift-coeff drag-coeff
time/iter
56 1.8572e-03 1.7063e-07 2.3484e-08 1.6009e-16 3.2737e-04 2.9619e-04
4.4574e-01 1.2884e-02 0:06:30 944
57 1.7167e-03 1.5801e-07 2.1521e-08 1.5443e-16 3.1481e-04 2.8731e-04
4.4576e-01 1.2883e-02 0:05:11 943
58 1.5884e-03 1.4664e-07 1.9677e-08 1.6086e-16 3.0319e-04 2.7817e-04
4.4577e-01 1.2882e-02 0:07:17 942

59 1.4757e-03 1.3704e-07 1.7928e-08 1.6111e-16 2.9245e-04 2.7042e-04
4.4577e-01 1.2881e-02 0:05:49 941
60 1.3695e-03 1.2852e-07 1.6271e-08 1.5948e-16 2.8268e-04 2.6256e-04
4.4577e-01 1.2880e-02 0:04:39 940
61 1.2738e-03 1.2083e-07 1.4780e-08 1.5624e-16 2.7354e-04 2.5573e-04
4.4577e-01 1.2879e-02 0:06:51 939
62 1.1874e-03 1.1360e-07 1.3578e-08 1.5682e-16 2.6481e-04 2.4903e-04
4.4577e-01 1.2878e-02 0:05:28 938
63 1.1108e-03 1.0651e-07 1.2619e-08 1.5842e-16 2.5658e-04 2.4313e-04
4.4576e-01 1.2877e-02 0:04:22 937
64 1.0396e-03 9.9858e-08 1.1860e-08 1.6103e-16 2.4844e-04 2.3736e-04
4.4576e-01 1.2877e-02 0:06:37 936
! 65 solution is converged
65 9.7688e-04 9.3394e-08 1.1288e-08 1.5796e-16 2.4065e-04 2.3212e-04
4.4575e-01 1.2876e-02 0:05:17 935

Upper ks=0.0258 mm, Lower ks=0.125 mm at V=27 m/s

iter continuity x-velocity y-velocity energy k omega lift-coeff drag-coeff
time/iter
56 1.8275e-03 1.6665e-07 2.3141e-08 1.5887e-16 3.0949e-04 2.7692e-04
4.4758e-01 1.2677e-02 0:05:10 944
57 1.6869e-03 1.5390e-07 2.1196e-08 1.5852e-16 2.9719e-04 2.6881e-04
4.4759e-01 1.2676e-02 0:04:08 943
58 1.5581e-03 1.4255e-07 1.9373e-08 1.5731e-16 2.8586e-04 2.6008e-04
4.4760e-01 1.2675e-02 0:06:27 942
59 1.4459e-03 1.3253e-07 1.7695e-08 1.5770e-16 2.7560e-04 2.5313e-04
4.4761e-01 1.2674e-02 0:05:09 941

60 1.3446e-03 1.2415e-07 1.6088e-08 1.5846e-16 2.6610e-04 2.4572e-04
4.4761e-01 1.2674e-02 0:04:07 940
61 1.2488e-03 1.1620e-07 1.4600e-08 1.5585e-16 2.5738e-04 2.3961e-04
4.4761e-01 1.2673e-02 0:06:25 939
62 1.1597e-03 1.0871e-07 1.3367e-08 1.5791e-16 2.4919e-04 2.3334e-04
4.4761e-01 1.2672e-02 0:05:08 938
63 1.0770e-03 1.0169e-07 1.2377e-08 1.5918e-16 2.4163e-04 2.2789e-04
4.4760e-01 1.2672e-02 0:04:06 937
64 1.0046e-03 9.5129e-08 1.1598e-08 1.5833e-16 2.3451e-04 2.2246e-04
4.4759e-01 1.2671e-02 0:06:24 936
! 65 solution is converged
65 9.3812e-04 8.8988e-08 1.1048e-08 1.5980e-16 2.2765e-04 2.1761e-04
4.4759e-01 1.2670e-02 0:05:07 935

Upper ks=0.0258 mm, Lower ks=0.125 mm at V=30 m/s

iter continuity x-velocity y-velocity energy k omega lift-coeff drag-coeff
time/iter
56 1.8042e-03 1.6494e-07 2.2998e-08 1.6867e-16 2.9766e-04 2.6470e-04
4.4895e-01 1.2564e-02 0:06:53 944
57 1.6583e-03 1.5203e-07 2.1105e-08 1.6623e-16 2.8605e-04 2.5615e-04
4.4896e-01 1.2563e-02 0:05:30 943
58 1.5315e-03 1.4074e-07 1.9301e-08 1.6425e-16 2.7502e-04 2.4885e-04
4.4897e-01 1.2562e-02 0:04:23 942
59 1.4210e-03 1.3068e-07 1.7654e-08 1.6643e-16 2.6493e-04 2.4146e-04
4.4898e-01 1.2562e-02 0:06:39 941
60 1.3221e-03 1.2206e-07 1.6069e-08 1.6588e-16 2.5559e-04 2.3501e-04
4.4898e-01 1.2561e-02 0:05:19 940

61 1.2262e-03 1.1403e-07 1.4591e-08 1.6246e-16 2.4698e-04 2.2868e-04
4.4898e-01 1.2560e-02 0:04:15 939
62 1.1361e-03 1.0648e-07 1.3311e-08 1.6374e-16 2.3911e-04 2.2310e-04
4.4898e-01 1.2560e-02 0:06:31 938
63 1.0546e-03 9.9412e-08 1.2267e-08 1.6328e-16 2.3174e-04 2.1764e-04
4.4897e-01 1.2559e-02 0:05:13 937
! 64 solution is converged
64 9.8004e-04 9.2861e-08 1.1436e-08 1.6283e-16 2.2491e-04 2.1272e-04
4.4896e-01 1.2559e-02 0:04:10 936

Upper ks=0.0258 mm, Lower ks=0.125 mm at V=35 m/s

iter continuity x-velocity y-velocity energy k omega lift-coeff drag-coeff
time/iter
56 1.7762e-03 1.6175e-07 2.2587e-08 1.6268e-16 2.8158e-04 2.4615e-04
4.5078e-01 1.2431e-02 0:05:13 944
57 1.6335e-03 1.4869e-07 2.0757e-08 1.6508e-16 2.7048e-04 2.3888e-04
4.5080e-01 1.2430e-02 0:04:10 943
58 1.5000e-03 1.3713e-07 1.9039e-08 1.6610e-16 2.6019e-04 2.3162e-04
4.5081e-01 1.2430e-02 0:06:28 942
59 1.3814e-03 1.2721e-07 1.7484e-08 1.6514e-16 2.5036e-04 2.2534e-04
4.5081e-01 1.2429e-02 0:05:10 941
60 1.2806e-03 1.1864e-07 1.5963e-08 1.6586e-16 2.4134e-04 2.1900e-04
4.5082e-01 1.2428e-02 0:04:08 940
61 1.1888e-03 1.1067e-07 1.4493e-08 1.6983e-16 2.3299e-04 2.1348e-04
4.5082e-01 1.2428e-02 0:06:26 939
62 1.1014e-03 1.0304e-07 1.3154e-08 1.6691e-16 2.2528e-04 2.0799e-04
4.5081e-01 1.2428e-02 0:05:08 938

63 1.0187e-03 9.5874e-08 1.2077e-08 1.6585e-16 2.1815e-04 2.0308e-04
4.5081e-01 1.2427e-02 0:04:07 937
! 64 solution is converged
64 9.4319e-04 8.9375e-08 1.1184e-08 1.6563e-16 2.1172e-04 1.9847e-04
4.5080e-01 1.2427e-02 0:06:24 936

Upper ks=0.0258 mm, Lower ks=0.19 mm at V=20 m/s

iter continuity x-velocity y-velocity energy k omega lift-coeff drag-coeff
time/iter
56 1.9003e-03 1.7788e-07 2.3785e-08 1.6292e-16 3.4202e-04 3.1118e-04
4.4543e-01 1.3549e-02 0:04:12 944
57 1.7626e-03 1.6496e-07 2.1692e-08 1.6142e-16 3.2927e-04 3.0099e-04
4.4545e-01 1.3548e-02 0:06:30 943
58 1.6337e-03 1.5392e-07 1.9860e-08 1.5981e-16 3.1738e-04 2.9163e-04
4.4546e-01 1.3547e-02 0:05:12 942
59 1.5216e-03 1.4481e-07 1.8198e-08 1.6172e-16 3.0601e-04 2.8275e-04
4.4546e-01 1.3546e-02 0:04:09 941
60 1.4203e-03 1.3636e-07 1.6625e-08 1.6191e-16 2.9573e-04 2.7468e-04
4.4546e-01 1.3545e-02 0:06:27 940
61 1.3264e-03 1.2819e-07 1.5289e-08 1.6263e-16 2.8564e-04 2.6707e-04
4.4546e-01 1.3544e-02 0:05:09 939
62 1.2390e-03 1.2042e-07 1.4231e-08 1.6334e-16 2.7598e-04 2.6031e-04
4.4545e-01 1.3543e-02 0:04:07 938
63 1.1602e-03 1.1266e-07 1.3343e-08 1.6356e-16 2.6663e-04 2.5378e-04
4.4545e-01 1.3541e-02 0:06:25 937
64 1.0859e-03 1.0497e-07 1.2591e-08 1.6616e-16 2.5771e-04 2.4800e-04
4.4544e-01 1.3540e-02 0:05:08 936

65 1.0187e-03 9.7589e-08 1.1900e-08 1.6803e-16 2.4923e-04 2.4244e-04
4.4544e-01 1.3539e-02 0:04:06 935
! 66 solution is converged
66 9.5233e-04 9.0525e-08 1.1136e-08 1.6375e-16 2.4135e-04 2.3740e-04
4.4544e-01 1.3538e-02 0:06:23 934

Upper ks=0.0258 mm, Lower ks=0.19 mm at V=23 m/s

iter continuity x-velocity y-velocity energy k omega lift-coeff drag-coeff
time/iter
56 1.8848e-03 1.7541e-07 2.3782e-08 1.5556e-16 3.2673e-04 2.9483e-04
4.4785e-01 1.3359e-02 0:04:29 944
57 1.7449e-03 1.6223e-07 2.1742e-08 1.5957e-16 3.1425e-04 2.8580e-04
4.4786e-01 1.3359e-02 0:06:44 943
58 1.6082e-03 1.5041e-07 1.9854e-08 1.5525e-16 3.0266e-04 2.7669e-04
4.4787e-01 1.3358e-02 0:05:23 942
59 1.4859e-03 1.4041e-07 1.8116e-08 1.5815e-16 2.9213e-04 2.6887e-04
4.4788e-01 1.3357e-02 0:04:18 941
60 1.3771e-03 1.3160e-07 1.6452e-08 1.5918e-16 2.8215e-04 2.6099e-04
4.4788e-01 1.3357e-02 0:06:34 940
61 1.2791e-03 1.2341e-07 1.4980e-08 1.5719e-16 2.7275e-04 2.5409e-04
4.4788e-01 1.3356e-02 0:05:15 939
62 1.1914e-03 1.1566e-07 1.3820e-08 1.5704e-16 2.6413e-04 2.4738e-04
4.4788e-01 1.3355e-02 0:04:12 938
63 1.1160e-03 1.0834e-07 1.2953e-08 1.5746e-16 2.5588e-04 2.4141e-04
4.4787e-01 1.3354e-02 0:06:29 937
64 1.0456e-03 1.0163e-07 1.2301e-08 1.5765e-16 2.4774e-04 2.3567e-04
4.4786e-01 1.3353e-02 0:05:10 936

! 65 solution is converged

65 9.8202e-04 9.5172e-08 1.1815e-08 1.5697e-16 2.3992e-04 2.3042e-04 4.4785e-01 1.3352e-02 0:04:08 935

Upper ks=0.0258 mm, Lower ks=0.19 mm at V=27 m/s

iter continuity x-velocity y-velocity energy k omega lift-coeff drag-coeff time/iter

56 1.8528e-03 1.7089e-07 2.3350e-08 1.5416e-16 3.0845e-04 2.7563e-04 4.4984e-01 1.3180e-02 0:05:10 944

57 1.7047e-03 1.5778e-07 2.1322e-08 1.5777e-16 2.9635e-04 2.6734e-04 4.4985e-01 1.3180e-02 0:04:07 943

58 1.5710e-03 1.4608e-07 1.9474e-08 1.5951e-16 2.8512e-04 2.5870e-04 4.4986e-01 1.3180e-02 0:06:26 942

59 1.4503e-03 1.3598e-07 1.7756e-08 1.5633e-16 2.7489e-04 2.5159e-04 4.4987e-01 1.3179e-02 0:05:09 941

60 1.3422e-03 1.2706e-07 1.6151e-08 1.6076e-16 2.6537e-04 2.4420e-04 4.4987e-01 1.3179e-02 0:07:15 940

61 1.2433e-03 1.1865e-07 1.4701e-08 1.6075e-16 2.5680e-04 2.3804e-04 4.4987e-01 1.3178e-02 0:05:47 939

62 1.1556e-03 1.1084e-07 1.3518e-08 1.5910e-16 2.4865e-04 2.3178e-04 4.4987e-01 1.3178e-02 0:04:38 938

63 1.0769e-03 1.0355e-07 1.2624e-08 1.5791e-16 2.4091e-04 2.2636e-04 4.4986e-01 1.3177e-02 0:06:49 937

64 1.0081e-03 9.6937e-08 1.1924e-08 1.5842e-16 2.3370e-04 2.2092e-04 4.4985e-01 1.3177e-02 0:05:27 936

! 65 solution is converged

65 9.4735e-04 9.0857e-08 1.1430e-08 1.5684e-16 2.2683e-04 2.1612e-04
4.4984e-01 1.3176e-02 0:04:21 935

Upper ks=0.0258 mm, Lower ks=0.19 mm at V=3 m/s

iter continuity x-velocity y-velocity energy k omega lift-coeff drag-coeff
time/iter
56 1.8429e-03 1.6947e-07 2.3319e-08 1.6213e-16 2.9689e-04 2.6323e-04
4.5130e-01 1.3084e-02 0:04:12 944
57 1.6944e-03 1.5609e-07 2.1352e-08 1.6613e-16 2.8529e-04 2.5516e-04
4.5131e-01 1.3084e-02 0:06:30 943
58 1.5813e-03 1.4455e-07 1.9703e-08 1.6367e-16 2.7445e-04 2.4741e-04
4.5132e-01 1.3083e-02 0:05:12 942
59 1.4525e-03 1.3422e-07 1.7926e-08 1.6632e-16 2.6452e-04 2.4037e-04
4.5133e-01 1.3083e-02 0:04:09 941
60 1.3378e-03 1.2525e-07 1.6213e-08 1.6650e-16 2.5514e-04 2.3367e-04
4.5133e-01 1.3083e-02 0:06:27 940
61 1.2367e-03 1.1678e-07 1.4693e-08 1.6425e-16 2.4656e-04 2.2759e-04
4.5133e-01 1.3083e-02 0:05:09 939
62 1.1546e-03 1.0887e-07 1.3633e-08 1.6727e-16 2.3870e-04 2.2176e-04
4.5132e-01 1.3082e-02 0:07:15 938
63 1.0721e-03 1.0131e-07 1.2608e-08 1.6527e-16 2.3140e-04 2.1642e-04
4.5132e-01 1.3082e-02 0:05:47 937
64 1.0005e-03 9.4598e-08 1.1779e-08 1.6491e-16 2.2439e-04 2.1135e-04
4.5131e-01 1.3081e-02 0:04:38 936
! 65 solution is converged
65 9.3474e-04 8.8555e-08 1.1209e-08 1.6270e-16 2.1789e-04 2.0662e-04
4.5130e-01 1.3081e-02 0:06:49 935

Upper ks=0.0258 mm, Lower ks=0.19 mm at V=35 m/s

iter continuity x-velocity y-velocity energy k omega lift-coeff drag-coeff time/iter

56 1.8175e-03 1.6595e-07 2.3093e-08 1.6523e-16 2.8006e-04 2.4513e-04 4.5325e-01 1.2972e-02 0:06:29 944

57 1.6690e-03 1.5278e-07 2.1100e-08 1.6679e-16 2.6895e-04 2.3777e-04 4.5327e-01 1.2972e-02 0:05:11 943

58 1.5331e-03 1.4102e-07 1.9268e-08 1.6829e-16 2.5870e-04 2.3060e-04 4.5328e-01 1.2972e-02 0:04:08 942

59 1.4115e-03 1.3066e-07 1.7626e-08 1.6879e-16 2.4876e-04 2.2422e-04 4.5328e-01 1.2972e-02 0:06:27 941

60 1.3000e-03 1.2192e-07 1.6077e-08 1.6698e-16 2.3994e-04 2.1785e-04 4.5329e-01 1.2972e-02 0:05:09 940

61 1.1902e-03 1.1342e-07 1.4642e-08 1.6237e-16 2.3163e-04 2.1235e-04 4.5329e-01 1.2971e-02 0:04:07 939

62 1.0936e-03 1.0544e-07 1.3310e-08 1.6492e-16 2.2398e-04 2.0680e-04 4.5329e-01 1.2971e-02 0:06:25 938

63 1.0100e-03 9.7959e-08 1.2212e-08 1.6736e-16 2.1682e-04 2.0196e-04 4.5328e-01 1.2971e-02 0:05:08 937

! 64 solution is converged

64 9.3595e-04 9.0927e-08 1.1322e-08 1.6441e-16 2.1039e-04 1.9725e-04 4.5328e-01 1.2971e-02 0:07:13 936

H-2: At α=5°

Upper ks=0.0258 mm, Lower ks=0.0258 mm at V=20 m/s

iter continuity x-velocity y-velocity energy k omega lift-force drag-coeff time/iter

408 7.8151e-06 1.9204e-10 1.0359e-10 1.5981e-16 1.9418e-05 9.6006e-06 9.7960e-01 1.3392e-02 0:03:14 592

409 1.5815e-05 5.0830e-10 5.1307e-10 1.6182e-16 1.9352e-05 9.5920e-06 9.7960e-01 1.3392e-02 0:04:33 591

410 1.4413e-05 3.6975e-10 3.3536e-10 1.6314e-16 1.9273e-05 9.5345e-06 9.7960e-01 1.3392e-02 0:03:38 590

411 1.5602e-05 5.1184e-10 5.1411e-10 1.6272e-16 1.9202e-05 9.5146e-06 9.7960e-01 1.3392e-02 0:02:54 589

412 9.2229e-06 3.1171e-10 2.6562e-10 1.6037e-16 1.9112e-05 9.4493e-06 9.7960e-01 1.3392e-02 0:04:17 588

413 8.1492e-06 2.2886e-10 1.5801e-10 1.6318e-16 1.9031e-05 9.4205e-06 9.7960e-01 1.3392e-02 0:03:25 587

414 7.3097e-06 1.8559e-10 1.0176e-10 1.6145e-16 1.8951e-05 9.3677e-06 9.7960e-01 1.3392e-02 0:02:44 586

415 6.2173e-06 1.6016e-10 7.1867e-11 1.6361e-16 1.8876e-05 9.3416e-06 9.7960e-01 1.3392e-02 0:04:08 585

416 1.5741e-05 4.9708e-10 5.1486e-10 1.6320e-16 1.8811e-05 9.3140e-06 9.7960e-01 1.3392e-02 0:03:18 584

417 1.1616e-05 3.9054e-10 3.9397e-10 1.5738e-16 1.8737e-05 9.2692e-06 9.7960e-01 1.3392e-02 0:04:35 583

Done.

Upper ks=0.0258 mm, Lower ks=0.0258 mm at V=23 m/s

269 2.1368e-06 2.1414e-10 5.7291e-11 1.5948e-16 3.5806e-05 1.8273e-05 9.8232e-01 1.3120e-02 0:05:00 731

270 2.0951e-06 2.1192e-10 5.7704e-11 1.5386e-16 3.5616e-05 1.8155e-05 9.8232e-01 1.3120e-02 0:04:00 730

271 2.0458e-06 2.0859e-10 5.6034e-11 1.5709e-16 3.5429e-05 1.8078e-05 9.8232e-01 1.3120e-02 0:05:37 729

272 2.0096e-06 2.0635e-10 5.6509e-11 1.5610e-16 3.5241e-05 1.7962e-05 9.8232e-01 1.3120e-02 0:04:29 728

273 1.9659e-06 2.0301e-10 5.4890e-11 1.5533e-16 3.5057e-05 1.7886e-05 9.8232e-01 1.3120e-02 0:03:35 727

274 1.9341e-06 2.0078e-10 5.5430e-11 1.5548e-16 3.4872e-05 1.7772e-05 9.8232e-01 1.3120e-02 0:05:17 726

275 1.8952e-06 1.9744e-10 5.3850e-11 1.5686e-16 3.4691e-05 1.7698e-05 9.8232e-01 1.3120e-02 0:04:13 725

iter continuity x-velocity y-velocity energy k omega lift-force drag-coeff time/iter

276 1.8655e-06 1.9522e-10 5.4455e-11 1.5984e-16 3.4509e-05 1.7585e-05 9.8232e-01 1.3120e-02 0:03:22 724

277 1.8291e-06 1.9194e-10 5.2901e-11 1.5661e-16 3.4331e-05 1.7512e-05 9.8232e-01 1.3120e-02 0:05:06 723

278 1.8015e-06 1.8978e-10 5.3561e-11 1.5695e-16 3.4152e-05 1.7401e-05 9.8232e-01 1.3120e-02 0:04:05 722

279 1.7681e-06 1.8657e-10 5.2032e-11 1.5824e-16 3.3976e-05 1.7330e-05 9.8232e-01 1.3120e-02 0:03:15 721

Done.

Upper ks=0.0258 mm, Lower ks=0.0258 mm at V=27 m/s

iter continuity x-velocity y-velocity energy k omega lift-force drag-coeff time/iter
283 2.4487e-05 3.6710e-10 1.5017e-10 1.5656e-16 3.1768e-05 1.6579e-05 9.8299e-01 1.2819e-02 0:03:57 717
284 1.9478e-05 3.1061e-10 1.4964e-10 1.6292e-16 3.1618e-05 1.6541e-05 9.8299e-01 1.2819e-02 0:03:09 716
285 2.5521e-05 5.2867e-10 2.5701e-10 1.5952e-16 3.1476e-05 1.6415e-05 9.8299e-01 1.2819e-02 0:04:54 715

286 2.7531e-05 3.9287e-10 1.8591e-10 1.6210e-16 3.1353e-05 1.6390e-05 9.8299e-01 1.2819e-02 0:03:55 714

iter continuity x-velocity y-velocity energy k omega lift-force drag-coeff time/iter
287 2.8880e-05 5.6220e-10 2.5337e-10 1.6304e-16 3.1149e-05 1.6250e-05 9.8299e-01 1.2819e-02 0:05:30 713
288 1.6790e-05 3.4176e-10 1.4791e-10 1.6219e-16 3.0986e-05 1.6180e-05 9.8299e-01 1.2819e-02 0:04:24 712
289 2.2702e-05 3.1398e-10 1.4268e-10 1.6161e-16 3.0857e-05 1.6129e-05 9.8299e-01 1.2819e-02 0:03:31 711
290 2.9471e-05 5.2980e-10 2.5385e-10 1.6067e-16 3.0718e-05 1.6023e-05 9.8299e-01 1.2819e-02 0:05:10 710
291 1.9771e-05 3.7182e-10 1.7850e-10 1.6026e-16 3.0590e-05 1.5966e-05 9.8299e-01 1.2819e-02 0:04:08 709
292 3.2051e-05 5.6188e-10 2.4445e-10 1.6216e-16 3.0405e-05 1.5882e-05 9.8299e-01 1.2819e-02 0:03:18 708
Done.

Upper ks=0.0258 mm, Lower ks=0.0258 mm at V=30 m/s

iter continuity x-velocity y-velocity energy k omega lift-force drag-coeff time/iter
276 1.3311e-06 1.4730e-10 4.1322e-11 1.6540e-16 3.1586e-05 1.6777e-05 9.8433e-01 1.2646e-02 0:03:14 724
277 1.3136e-06 1.4435e-10 4.0475e-11 1.6019e-16 3.1429e-05 1.6708e-05 9.8433e-01 1.2646e-02 0:05:00 723
278 1.3068e-06 1.4392e-10 4.0509e-11 1.6407e-16 3.1272e-05 1.6607e-05 9.8433e-01 1.2646e-02 0:03:59 722
279 1.2917e-06 1.4160e-10 3.9803e-11 1.6416e-16 3.1117e-05 1.6539e-05 9.8433e-01 1.2646e-02 0:05:35 721
280 1.2864e-06 1.4156e-10 3.9882e-11 1.6621e-16 3.0963e-05 1.6440e-05 9.8433e-01 1.2646e-02 0:04:28 720
281 1.2722e-06 1.3940e-10 3.9198e-11 1.6474e-16 3.0811e-05 1.6374e-05 9.8433e-01 1.2646e-02 0:05:58 719
282 1.2862e-06 1.4215e-10 3.9921e-11 1.6435e-16 3.0659e-05 1.6276e-05 9.8433e-01 1.2646e-02 0:04:46 718
283 1.2691e-06 1.3931e-10 3.9100e-11 1.6282e-16 3.0509e-05 1.6211e-05 9.8433e-01 1.2646e-02 0:06:12 717
284 1.2627e-06 1.3899e-10 3.9175e-11 1.6475e-16 3.0359e-05 1.6115e-05 9.8433e-01 1.2646e-02 0:04:57 716

285 1.2488e-06 1.3677e-10 3.8509e-11 1.6162e-16 3.0212e-05 1.6050e-05 9.8433e-01 1.2646e-02 0:03:57 715
286 1.2614e-06 1.3933e-10 3.9199e-11 1.6709e-16 3.0065e-05 1.5956e-05 9.8433e-01 1.2646e-02 0:05:32 714
Done.

Upper ks=0.0258 mm, Lower ks=0.0258 mm at V=35 m/s

iter continuity x-velocity y-velocity energy k omega lift-force drag-coeff time/iter
210 1.9447e-06 2.0983e-10 5.7596e-11 1.6666e-16 4.2932e-05 2.3384e-05 9.8616e-01 1.2419e-02 0:03:52 790
211 1.9069e-06 2.0586e-10 5.7034e-11 1.6090e-16 4.2665e-05 2.3219e-05 9.8616e-01 1.2419e-02 0:05:43 789
212 1.8832e-06 2.0317e-10 5.6333e-11 1.6456e-16 4.2403e-05 2.3092e-05 9.8616e-01 1.2419e-02 0:04:34 788
213 1.8478e-06 1.9950e-10 5.5869e-11 1.6288e-16 4.2141e-05 2.2931e-05 9.8616e-01 1.2419e-02 0:03:39 787
214 1.8264e-06 1.9709e-10 5.5235e-11 1.6199e-16 4.1884e-05 2.2807e-05 9.8616e-01 1.2419e-02 0:05:32 786
215 1.7930e-06 1.9376e-10 5.4854e-11 1.6621e-16 4.1628e-05 2.2649e-05 9.8616e-01 1.2419e-02 0:04:26 785
216 1.7746e-06 1.9168e-10 5.4285e-11 1.6289e-16 4.1376e-05 2.2528e-05 9.8616e-01 1.2419e-02 0:06:09 784
217 1.7443e-06 1.8867e-10 5.3971e-11 1.6263e-16 4.1125e-05 2.2373e-05 9.8616e-01 1.2419e-02 0:04:55 783
218 1.7292e-06 1.8697e-10 5.3454e-11 1.6580e-16 4.0878e-05 2.2254e-05 9.8616e-01 1.2419e-02 0:03:56 782
219 1.7017e-06 1.8440e-10 5.3189e-11 1.6161e-16 4.0632e-05 2.2102e-05 9.8616e-01 1.2418e-02 0:05:44 781
Done.

Upper ks=0.0258 mm, Lower ks=0.045 mm at V=20 m/s

iter continuity x-velocity y-velocity energy k omega lift-force drag-coeff time/iter
276 2.2795e-06 2.4024e-10 6.4005e-11 1.6150e-16 3.5821e-05 1.7771e-05 9.7976e-01 1.3402e-02 0:03:10 724
277 2.2461e-06 2.3755e-10 6.2459e-11 1.6404e-16 3.5632e-05 1.7701e-05 9.7976e-01 1.3402e-02 0:04:56 723

278 2.2246e-06 2.3365e-10 6.2220e-11 1.6196e-16 3.5440e-05 1.7581e-05 9.7976e-01 1.3402e-02 0:03:57 722
279 2.2097e-06 2.3061e-10 6.0830e-11 1.6092e-16 3.5254e-05 1.7511e-05 9.7976e-01 1.3402e-02 0:05:33 721
280 2.2040e-06 2.2663e-10 6.0928e-11 1.6253e-16 3.5065e-05 1.7394e-05 9.7976e-01 1.3402e-02 0:04:26 720
281 2.1973e-06 2.2422e-10 5.9913e-11 1.6140e-16 3.4882e-05 1.7325e-05 9.7976e-01 1.3402e-02 0:03:33 719
282 2.1971e-06 2.2113e-10 6.0332e-11 1.6117e-16 3.4696e-05 1.7209e-05 9.7976e-01 1.3402e-02 0:05:14 718
Done.

Upper ks=0.0258 mm, Lower ks=0.045 mm at V=23 m/s

iter continuity x-velocity y-velocity energy k omega lift-force drag-coeff time/iter
272 1.7884e-06 1.9240e-10 5.6492e-11 1.5563e-16 3.5358e-05 1.8004e-05 9.8250e-01 1.3132e-02 0:04:58 728
273 1.7771e-06 1.9117e-10 5.7223e-11 1.5478e-16 3.5172e-05 1.7885e-05 9.8250e-01 1.3132e-02 0:03:58 727
274 1.7535e-06 1.8959e-10 5.5625e-11 1.5563e-16 3.4990e-05 1.7814e-05 9.8250e-01 1.3132e-02 0:05:36 726
275 1.7435e-06 1.8831e-10 5.6401e-11 1.5376e-16 3.4807e-05 1.7697e-05 9.8250e-01 1.3132e-02 0:04:28 725

iter continuity x-velocity y-velocity energy k omega lift-force drag-coeff time/iter
276 1.7208e-06 1.8658e-10 5.4808e-11 1.5653e-16 3.4628e-05 1.7627e-05 9.8250e-01 1.3132e-02 0:05:59 724
277 1.7278e-06 1.8834e-10 5.6322e-11 1.5475e-16 3.4448e-05 1.7512e-05 9.8250e-01 1.3132e-02 0:04:47 723
278 1.7037e-06 1.8541e-10 5.4418e-11 1.5871e-16 3.4271e-05 1.7443e-05 9.8250e-01 1.3132e-02 0:03:49 722
279 1.7098e-06 1.8663e-10 5.5947e-11 1.5452e-16 3.4094e-05 1.7330e-05 9.8250e-01 1.3132e-02 0:05:27 721
280 1.6842e-06 1.8329e-10 5.4008e-11 1.5465e-16 3.3920e-05 1.7262e-05 9.8250e-01 1.3132e-02 0:04:21 720
281 1.6732e-06 1.8110e-10 5.4791e-11 1.5707e-16 3.3746e-05 1.7151e-05 9.8250e-01 1.3132e-02 0:03:29 719
Done.

Upper ks=0.0258 mm, Lower ks=0.045 mm at V=27 m/s

iter continuity x-velocity y-velocity energy k omega lift-force drag-coeff time/iter
203 5.9371e-06 3.3968e-10 8.9048e-11 1.5969e-16 4.9893e-05 2.6208e-05 9.8313e-01 1.2839e-02 0:05:27 797
204 5.1769e-06 3.2905e-10 8.5992e-11 1.5951e-16 4.9569e-05 2.6060e-05 9.8313e-01 1.2839e-02 0:04:21 796
205 4.5894e-06 3.2053e-10 8.2569e-11 1.5900e-16 4.9244e-05 2.5864e-05 9.8313e-01 1.2839e-02 0:03:29 795
206 4.1464e-06 3.1164e-10 7.9981e-11 1.5870e-16 4.8926e-05 2.5720e-05 9.8313e-01 1.2839e-02 0:05:26 794
207 3.7848e-06 3.0416e-10 7.7256e-11 1.6104e-16 4.8609e-05 2.5527e-05 9.8313e-01 1.2838e-02 0:04:20 793
208 3.4960e-06 2.9629e-10 7.5395e-11 1.6025e-16 4.8298e-05 2.5386e-05 9.8313e-01 1.2838e-02 0:06:06 792
209 3.2637e-06 2.8993e-10 7.3455e-11 1.6063e-16 4.7987e-05 2.5197e-05 9.8313e-01 1.2838e-02 0:04:53 791

iter continuity x-velocity y-velocity energy k omega lift-force drag-coeff time/iter
210 3.0684e-06 2.8333e-10 7.2284e-11 1.5908e-16 4.7683e-05 2.5060e-05 9.8313e-01 1.2838e-02 0:03:54 790
211 2.9075e-06 2.7793e-10 7.0881e-11 1.6090e-16 4.7378e-05 2.4875e-05 9.8313e-01 1.2838e-02 0:05:45 789
212 2.7701e-06 2.7202e-10 7.0152e-11 1.5919e-16 4.7080e-05 2.4740e-05 9.8313e-01 1.2838e-02 0:04:35 788
Done.

Upper ks=0.0258 mm, Lower ks=0.045 mm at V=30 m/s

iter continuity x-velocity y-velocity energy k omega lift-force drag-coeff
237 1.6537e-06 1.8643e-10 5.1328e-11 1.6525e-16 3.8839e-05 2.0724e-05 9.8449e-01 1.2673e-02 0:04:15 763
238 1.6409e-06 1.8502e-10 5.0864e-11 1.6468e-16 3.8617e-05 2.0585e-05 9.8449e-01 1.2673e-02 0:03:24 762
239 1.6149e-06 1.8190e-10 5.0084e-11 1.6410e-16 3.8401e-05 2.0488e-05 9.8449e-01 1.2673e-02 0:05:15 761
240 1.6279e-06 1.8435e-10 5.0495e-11 1.6182e-16 3.8184e-05 2.0351e-05 9.8449e-01 1.2673e-02 0:06:44 760
241 1.5995e-06 1.8052e-10 4.9572e-11 1.6339e-16 3.7970e-05 2.0255e-05 9.8449e-01 1.2673e-02 0:05:23 759

242 1.5889e-06 1.7936e-10 4.9186e-11 1.6485e-16 3.7757e-05 2.0121e-05 9.8449e-01 1.2673e-02 0:04:18 758

iter continuity x-velocity y-velocity energy k omega lift-force drag-coeff time/iter
243 1.5644e-06 1.7632e-10 4.8461e-11 1.6435e-16 3.7548e-05 2.0027e-05 9.8449e-01 1.2673e-02 0:05:57 757
244 1.5793e-06 1.7887e-10 4.8932e-11 1.6637e-16 3.7339e-05 1.9895e-05 9.8449e-01 1.2673e-02 0:04:46 756
245 1.5520e-06 1.7513e-10 4.8077e-11 1.6403e-16 3.7133e-05 1.9803e-05 9.8449e-01 1.2673e-02 0:03:48 755
246 1.5427e-06 1.7408e-10 4.7751e-11 1.6463e-16 3.6928e-05 1.9673e-05 9.8449e-01 1.2673e-02 0:05:33 754
Done.

Upper ks=0.0258 mm, Lower ks=0.045 mm at V=35 m/s

iter continuity x-velocity y-velocity energy k omega lift-force drag-coeff time/iter
181 3.3957e-06 3.5514e-10 7.7871e-11 1.6582e-16 5.2000e-05 2.8373e-05 9.8626e-01 1.2460e-02 0:05:51 819
182 3.2910e-06 3.4356e-10 7.6852e-11 1.6395e-16 5.1632e-05 2.8195e-05 9.8626e-01 1.2460e-02 0:04:40 818
183 3.1753e-06 3.3093e-10 7.6048e-11 1.5978e-16 5.1267e-05 2.7971e-05 9.8626e-01 1.2460e-02 0:03:44 817
184 3.0876e-06 3.2118e-10 7.5623e-11 1.6614e-16 5.0908e-05 2.7798e-05 9.8626e-01 1.2460e-02 0:05:42 816
185 2.9891e-06 3.1054e-10 7.5249e-11 1.6607e-16 5.0552e-05 2.7580e-05 9.8626e-01 1.2460e-02 0:04:33 815
186 2.9133e-06 3.0263e-10 7.5034e-11 1.6415e-16 5.0202e-05 2.7411e-05 9.8626e-01 1.2460e-02 0:03:38 814
187 2.8263e-06 2.9388e-10 7.4858e-11 1.6161e-16 4.9855e-05 2.7197e-05 9.8626e-01 1.2460e-02 0:05:37 813

iter continuity x-velocity y-velocity energy k omega lift-force drag-coeff time/iter
188 2.7629e-06 2.8840e-10 7.4912e-11 1.6354e-16 4.9518e-05 2.7039e-05 9.8626e-01 1.2460e-02 0:04:29 812
189 5.8675e-06 4.1520e-10 3.5450e-10 1.6629e-16 4.9193e-05 2.6828e-05 9.8626e-01 1.2460e-02 0:03:35 811
190 9.7869e-06 3.6462e-10 3.9865e-10 1.6406e-16 4.8856e-05 2.6667e-05 9.8626e-01 1.2460e-02 0:05:34 810

Done.

Upper ks=0.0258 mm, Lower ks=0.125 mm at V=20 m/s

iter continuity x-velocity y-velocity energy k omega lift-force drag-coeff
182 4.0168e-06 4.3907e-10 1.1423e-10 1.5915e-16 6.4452e-05 3.2095e-05 9.7875e-01 1.3590e-02 0:05:03 818
183 3.9347e-06 4.3136e-10 1.1321e-10 1.6046e-16 6.3972e-05 3.1811e-05 9.7875e-01 1.3590e-02 0:06:45 817
184 3.8573e-06 4.2446e-10 1.1280e-10 1.6111e-16 6.3505e-05 3.1619e-05 9.7875e-01 1.3590e-02 0:05:24 816
185 3.7944e-06 4.1791e-10 1.1171e-10 1.6356e-16 6.3038e-05 3.1342e-05 9.7875e-01 1.3590e-02 0:04:19 815
186 3.7282e-06 4.1215e-10 1.1120e-10 1.6345e-16 6.2581e-05 3.1155e-05 9.7875e-01 1.3590e-02 0:06:10 814
187 3.6723e-06 4.0639e-10 1.1000e-10 1.6156e-16 6.2123e-05 3.0884e-05 9.7875e-01 1.3590e-02 0:04:55 813

iter continuity x-velocity y-velocity energy k omega lift-force drag-coeff time/iter
188 3.6139e-06 4.0106e-10 1.0936e-10 1.6414e-16 6.1679e-05 3.0701e-05 9.7875e-01 1.3590e-02 0:03:56 812
189 3.5650e-06 3.9535e-10 1.0806e-10 1.6160e-16 6.1232e-05 3.0436e-05 9.7875e-01 1.3590e-02 0:05:51 811
190 3.5092e-06 3.9003e-10 1.0732e-10 1.6386e-16 6.0796e-05 3.0257e-05 9.7875e-01 1.3590e-02 0:04:40 810
191 3.4603e-06 3.8451e-10 1.0595e-10 1.6056e-16 6.0360e-05 2.9998e-05 9.7875e-01 1.3590e-02 0:03:44 809
Done.

Upper ks=0.0258 mm, Lower ks=0.125 mm at V=23 m/s

iter continuity x-velocity y-velocity energy k omega lift-force drag-coeff time/iter
259 1.7266e-06 1.9409e-10 5.5580e-11 1.5916e-16 3.7590e-05 1.9214e-05 9.8164e-01 1.3355e-02 0:03:19 741
260 1.7449e-06 1.9638e-10 5.6008e-11 1.5846e-16 3.7383e-05 1.9085e-05 9.8164e-01 1.3355e-02 0:05:07 740
261 1.7062e-06 1.9177e-10 5.4954e-11 1.5899e-16 3.7182e-05 1.9003e-05 9.8164e-01 1.3355e-02 0:04:05 739

262 1.7245e-06 1.9406e-10 5.5377e-11 1.6106e-16 3.6979e-05 1.8876e-05 9.8164e-01 1.3355e-02 0:05:44 738
263 1.6861e-06 1.8950e-10 5.4334e-11 1.5706e-16 3.6781e-05 1.8795e-05 9.8164e-01 1.3355e-02 0:04:35 737
264 1.7042e-06 1.9177e-10 5.4751e-11 1.5575e-16 3.6581e-05 1.8670e-05 9.8164e-01 1.3355e-02 0:03:39 736

iter continuity x-velocity y-velocity energy k omega lift-force drag-coeff time/iter
265 1.6662e-06 1.8725e-10 5.3717e-11 1.5717e-16 3.6387e-05 1.8591e-05 9.8164e-01 1.3355e-02 0:05:22 735
266 1.6842e-06 1.8952e-10 5.4131e-11 1.5715e-16 3.6190e-05 1.8468e-05 9.8164e-01 1.3355e-02 0:04:17 734
267 1.6463e-06 1.8503e-10 5.3105e-11 1.5901e-16 3.5999e-05 1.8390e-05 9.8164e-01 1.3355e-02 0:05:52 733
268 1.6643e-06 1.8729e-10 5.3516e-11 1.5599e-16 3.5806e-05 1.8269e-05 9.8164e-01 1.3355e-02 0:04:41 732
Done.

Upper ks=0.0258 mm, Lower ks=0.125 mm at V=27 m/s

iter continuity x-velocity y-velocity energy k omega lift-force drag-coeff time/iter
397 1.7138e-06 9.0429e-11 2.8819e-11 1.6251e-16 1.9140e-05 9.9530e-06 9.8398e-01 1.3107e-02 0:04:15 603
398 1.5191e-06 9.1048e-11 2.8631e-11 1.5690e-16 1.9065e-05 9.9013e-06 9.8398e-01 1.3107e-02 0:03:24 602
399 1.3447e-06 8.9804e-11 2.8049e-11 1.6311e-16 1.8992e-05 9.8741e-06 9.8398e-01 1.3107e-02 0:04:43 601
400 1.2210e-06 9.0476e-11 2.8050e-11 1.6555e-16 1.8917e-05 9.8217e-06 9.8398e-01 1.3107e-02 0:03:46 600
401 1.1023e-06 8.9495e-11 2.7636e-11 1.6043e-16 1.8845e-05 9.7956e-06 9.8398e-01 1.3107e-02 0:03:00 599
402 1.0482e-06 9.0221e-11 2.7678e-11 1.5725e-16 1.8772e-05 9.7436e-06 9.8398e-01 1.3107e-02 0:04:24 598
! 403 solution is converged
403 9.8319e-07 8.9235e-11 2.7251e-11 1.5918e-16 1.8701e-05 9.7182e-06 9.8398e-01 1.3107e-02 0:03:31 597

Upper ks=0.0258 mm, Lower ks=0.125 mm at V=30m/s

iter continuity x-velocity y-velocity energy k omega lift-force drag-coeff time/iter
254 1.4889e-06 1.6909e-10 4.7090e-11 1.6324e-16 3.5105e-05 1.8761e-05 9.8533e-01 1.2966e-02 0:04:38 746
255 1.4532e-06 1.6471e-10 4.6115e-11 1.5926e-16 3.4919e-05 1.8678e-05 9.8533e-01 1.2966e-02 0:06:11 745
256 1.4716e-06 1.6709e-10 4.6598e-11 1.6764e-16 3.4731e-05 1.8558e-05 9.8533e-01 1.2966e-02 0:04:57 744
257 1.4363e-06 1.6277e-10 4.5634e-11 1.6432e-16 3.4548e-05 1.8477e-05 9.8533e-01 1.2966e-02 0:03:57 743
258 1.4547e-06 1.6515e-10 4.6113e-11 1.6259e-16 3.4364e-05 1.8359e-05 9.8533e-01 1.2966e-02 0:05:38 742
259 1.4198e-06 1.6089e-10 4.5160e-11 1.6409e-16 3.4184e-05 1.8279e-05 9.8533e-01 1.2966e-02 0:04:30 741
Done.

Upper ks=0.0258 mm, Lower ks=0.125 mm at V=35 m/s

iter continuity x-velocity y-velocity energy k omega lift-force drag-coeff time/iter
309 1.0290e-06 1.1513e-10 3.2796e-11 1.6170e-16 2.5331e-05 1.3746e-05 9.8718e-01 1.2789e-02 0:03:47 691
310 1.0492e-06 1.1696e-10 3.3015e-11 1.6470e-16 2.5218e-05 1.3694e-05 9.8718e-01 1.2789e-02 0:05:19 690
311 1.0203e-06 1.1409e-10 3.2358e-11 1.6284e-16 2.5105e-05 1.3621e-05 9.8718e-01 1.2789e-02 0:04:15 689
312 1.0392e-06 1.1585e-10 3.2583e-11 1.6577e-16 2.4993e-05 1.3570e-05 9.8718e-01 1.2789e-02 0:03:24 688
313 1.0104e-06 1.1303e-10 3.1928e-11 1.6242e-16 2.4882e-05 1.3498e-05 9.8718e-01 1.2789e-02 0:05:00 687
314 1.0279e-06 1.1470e-10 3.2161e-11 1.6517e-16 2.4772e-05 1.3447e-05 9.8718e-01 1.2789e-02 0:04:00 686
! 315 solution is converged
315 9.9988e-07 1.1190e-10 3.1512e-11 1.6241e-16 2.4663e-05 1.3377e-05 9.8718e-01 1.2789e-02 0:03:12 685

Upper ks=0.0258 mm, Lower ks=0.19 mm at V=20 m/s

iter continuity x-velocity y-velocity energy k omega lift-force drag-coeff time/iter
390 1.0488e-06 1.1513e-10 3.5127e-11 1.6302e-16 2.0982e-05 1.0319e-05 9.7960e-01 1.3795e-02 0:03:20 610
391 1.0330e-06 1.1327e-10 3.4744e-11 1.6165e-16 2.0896e-05 1.0285e-05 9.7960e-01 1.3795e-02 0:02:40 609
392 1.0349e-06 1.1358e-10 3.4688e-11 1.6041e-16 2.0809e-05 1.0232e-05 9.7960e-01 1.3795e-02 0:04:09 608
393 1.0195e-06 1.1181e-10 3.4336e-11 1.6234e-16 2.0725e-05 1.0200e-05 9.7960e-01 1.3795e-02 0:03:19 607
394 1.0378e-06 1.1432e-10 3.4761e-11 1.6169e-16 2.0639e-05 1.0145e-05 9.7960e-01 1.3795e-02 0:04:40 606
395 1.0209e-06 1.1208e-10 3.4373e-11 1.6251e-16 2.0556e-05 1.0115e-05 9.7960e-01 1.3795e-02 0:03:44 605
396 1.0210e-06 1.1207e-10 3.4270e-11 1.5985e-16 2.0471e-05 1.0059e-05 9.7960e-01 1.3795e-02 0:02:59 604

iter continuity x-velocity y-velocity energy k omega lift-force drag-coeff time/iter
397 1.0058e-06 1.1025e-10 3.3912e-11 1.6188e-16 2.0390e-05 1.0032e-05 9.7960e-01 1.3795e-02 0:04:23 603
398 1.0074e-06 1.1056e-10 3.3850e-11 1.6438e-16 2.0305e-05 9.9746e-06 9.7960e-01 1.3795e-02 0:03:30 602
! 399 solution is converged
399 9.9268e-07 1.0883e-10 3.3516e-11 1.6237e-16 2.0225e-05 9.9502e-06 9.7960e-01 1.3795e-02 0:02:48 601

Upper ks=0.0258 mm, Lower ks=0.19 mm at V=23 m/s

iter continuity x-velocity y-velocity energy k omega lift-force drag-coeff time/iter
323 1.2850e-06 1.4316e-10 4.2272e-11 1.5518e-16 2.7253e-05 1.3863e-05 9.8225e-01 1.3570e-02 0:04:02 677
324 1.2564e-06 1.3963e-10 4.1605e-11 1.5882e-16 2.7127e-05 1.3785e-05 9.8225e-01 1.3570e-02 0:03:13 676
325 1.2730e-06 1.4695e-10 4.4950e-11 1.5789e-16 2.7032e-05 1.3771e-05 9.8225e-01 1.3570e-02 0:04:49 675
326 1.3273e-05 3.3197e-10 1.7925e-10 1.5976e-16 2.6941e-05 1.3676e-05 9.8225e-01 1.3570e-02 0:03:51 674

327 1.0773e-05 2.8790e-10 1.3904e-10 1.5638e-16 2.6803e-05 1.3637e-05 9.8225e-01 1.3570e-02 0:03:05 673
328 8.8900e-06 2.6591e-10 1.0806e-10 1.5636e-16 2.6667e-05 1.3544e-05 9.8225e-01 1.3570e-02 0:04:42 672
329 7.5491e-06 2.5175e-10 8.9977e-11 1.5760e-16 2.6544e-05 1.3497e-05 9.8225e-01 1.3570e-02 0:03:45 671
330 6.3163e-06 2.3397e-10 7.6857e-11 1.5672e-16 2.6414e-05 1.3413e-05 9.8225e-01 1.3570e-02 0:05:14 670

iter continuity x-velocity y-velocity energy k omega lift-force drag-coeff time/iter
331 5.4295e-06 2.2357e-10 6.8679e-11 1.5879e-16 2.6295e-05 1.3366e-05 9.8225e-01 1.3570e-02 0:04:11 669
332 4.6435e-06 2.1534e-10 6.3626e-11 1.5521e-16 2.6170e-05 1.3286e-05 9.8225e-01 1.3570e-02 0:03:20 668
Done

Upper ks=0.0258 mm, Lower ks=0.19 mm at V=27 m/s

iter continuity x-velocity y-velocity energy k omega lift-force drag-coeff time/iter
193 2.8217e-06 3.1180e-10 8.0479e-11 1.5926e-16 5.2659e-05 2.7875e-05 9.8459e-01 1.3339e-02 0:05:49 807
194 2.8055e-06 3.0955e-10 8.0526e-11 1.6010e-16 5.2302e-05 2.7715e-05 9.8459e-01 1.3339e-02 0:04:39 806
195 2.7453e-06 3.0422e-10 8.0214e-11 1.6039e-16 5.1949e-05 2.7495e-05 9.8459e-01 1.3339e-02 0:03:43 805
196 2.7282e-06 3.0195e-10 8.0097e-11 1.5997e-16 5.1600e-05 2.7339e-05 9.8459e-01 1.3339e-02 0:05:39 804
197 2.6692e-06 2.9654e-10 7.9635e-11 1.6217e-16 5.1255e-05 2.7123e-05 9.8459e-01 1.3339e-02 0:04:31 803
198 2.6502e-06 2.9419e-10 7.9368e-11 1.6281e-16 5.0914e-05 2.6970e-05 9.8459e-01 1.3339e-02 0:03:36 802

iter continuity x-velocity y-velocity energy k omega lift-force drag-coeff time/iter
199 2.5909e-06 2.8887e-10 7.8776e-11 1.6164e-16 5.0576e-05 2.6759e-05 9.8459e-01 1.3339e-02 0:05:33 801
200 2.5728e-06 2.8657e-10 7.8383e-11 1.5868e-16 5.0243e-05 2.6609e-05 9.8459e-01 1.3339e-02 0:04:26 800

201 2.5165e-06 2.8141e-10 7.7662e-11 1.5993e-16 4.9913e-05 2.6402e-05 9.8459e-01 1.3339e-02 0:03:33 799
202 2.5011e-06 2.7930e-10 7.7154e-11 1.5814e-16 4.9586e-05 2.6257e-05 9.8459e-01 1.3339e-02 0:05:30 798
Done.

Upper ks=0.0258 mm, Lower ks=0.19 mm at V=30 m/s

iter continuity x-velocity y-velocity energy k omega lift-force drag-coeff time/iter
320 1.1248e-06 1.2343e-10 3.5898e-11 1.6238e-16 2.5428e-05 1.3513e-334 1.0605e-06 1.1592e-10 3.4028e-11 1.6164e-16 2.3928e-05 1.2696e-05 9.8599e-01 1.3207e-02 0:05:11 666
335 1.0298e-06 1.1259e-10 3.3506e-11 1.6515e-16 2.3827e-05 1.2654e-05 9.8599e-01 1.3207e-02 0:04:08 665
336 1.0524e-06 1.1499e-10 3.3798e-11 1.6460e-16 2.3725e-05 1.2586e-05 9.8599e-01 1.3207e-02 0:03:18 664
337 1.0219e-06 1.1168e-10 3.3277e-11 1.6181e-16 2.3625e-05 1.2544e-05 9.8599e-01 1.3207e-02 0:04:51 663
338 1.0444e-06 1.1408e-10 3.3566e-11 1.6301e-16 2.3524e-05 1.2476e-05 9.8599e-01 1.3207e-02 0:03:53 662
339 1.0140e-06 1.1079e-10 3.3046e-11 1.6725e-16 2.3426e-05 1.2435e-05 9.8599e-01 1.3207e-02 0:03:06 661
340 1.0364e-06 1.1317e-10 3.3330e-11 1.6793e-16 2.3326e-05 1.2369e-05 9.8599e-01 1.3207e-02 0:04:40 660
341 1.0061e-06 1.0990e-10 3.2812e-11 1.6743e-16 2.3229e-05 1.2328e-05 9.8599e-01 1.3207e-02 0:05:56 659

iter continuity x-velocity y-velocity energy k omega lift-force drag-coeff time/iter
342 1.0283e-06 1.1226e-10 3.3090e-11 1.6385e-16 2.3131e-05 1.2262e-05 9.8599e-01 1.3207e-02 0:04:44 658
! 343 solution is converged
343 9.9813e-07 1.0901e-10 3.2574e-11 1.6853e-16 2.3035e-05 1.2222e-05 9.8599e-01 1.3207e-02 0:03:47 657

Upper ks=0.0258 mm, Lower ks=0.19 mm at V=35 m/s

iter continuity x-velocity y-velocity energy k omega lift-force drag-coeff time/iter
312 1.0645e-06 1.1567e-10 3.4438e-11 1.6580e-16 2.4979e-05 1.3556e-05 9.8789e-01 1.3045e-02 0:04:18 688
313 1.0344e-06 1.1277e-10 3.3864e-11 1.6262e-16 2.4870e-05 1.3485e-05 9.8789e-01 1.3045e-02 0:05:43 687
314 1.0546e-06 1.1456e-10 3.4137e-11 1.6293e-16 2.4760e-05 1.3433e-05 9.8789e-01 1.3045e-02 0:04:34 686
315 1.0246e-06 1.1168e-10 3.3570e-11 1.6142e-16 2.4652e-05 1.3363e-05 9.8789e-01 1.3045e-02 0:05:56 685
316 1.0448e-06 1.1346e-10 3.3843e-11 1.6097e-16 2.4544e-05 1.3313e-05 9.8789e-01 1.3045e-02 0:04:44 684
317 1.0152e-06 1.1061e-10 3.3281e-11 1.5862e-16 2.4438e-05 1.3244e-05 9.8789e-01 1.3045e-02 0:06:04 683
318 1.0354e-06 1.1239e-10 3.3554e-11 1.6134e-16 2.4331e-05 1.3194e-05 9.8789e-01 1.3045e-02 0:04:51 682
319 1.0059e-06 1.0956e-10 3.2998e-11 1.6275e-16 2.4226e-05 1.3126e-05 9.8789e-01 1.3045e-02 0:03:52 681

iter continuity x-velocity y-velocity energy k omega lift-force drag-coeff time/iter
320 1.0261e-06 1.1133e-10 3.3268e-11 1.6098e-16 2.4121e-05 1.3077e-05 9.8789e-01 1.3045e-02 0:05:21 680
! 321 solution is converged
321 9.9668e-07 1.0852e-10 3.2719e-11 1.6367e-16 2.4018e-05 1.3010e-05 9.8789e-01 1.3045e-02 0:04:17 679

جامعة البحرين

كلية الهندسة



قسم الهندسة الميكانيكية

دراسة تأثير اختلاف خشونة السطحين الأعلى والأسفل على الخواص الديناميكية الهوائية لمقطع الجناح رقم ٤٤١٢

أطروحة لاستكمال متطلبات الحصول على درجة الدكتوراة في برنامج الهندسة الميكانيكية

إعداد

إبراهيم كمال صديق

الرقم الجامعي: ٢٠١٢١٠٠٣

إشراف

د. محمد نبهـــان
الأستاذ المشارك

د. عمر العباسي
الأستاذ المشارك

جـــامعة البحرين
ممـــلكة البحرين
يونيو, ٢٠٢٣